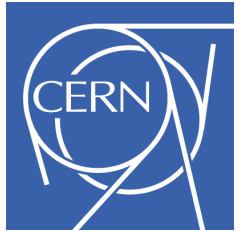
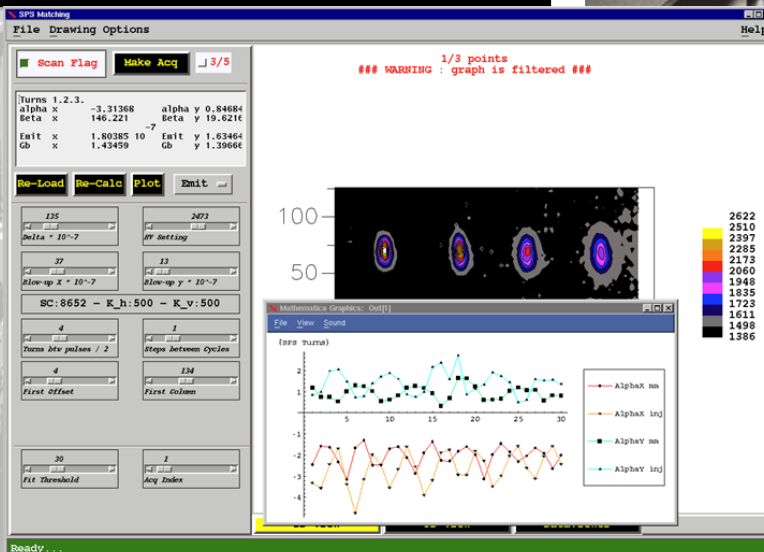
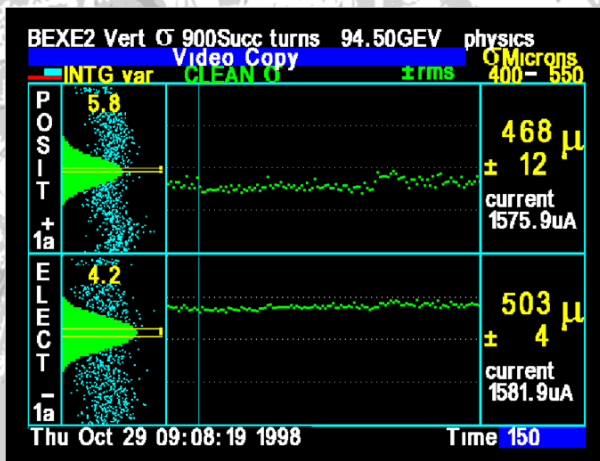


# CAS 2013



## Support Booklet for the Beam Instrumentation Course Trondheim—Norway



Prepared by:

Marek Gasior (CERN)  
Thibaut Lefevre (CERN)  
Rhodri Jones (CERN)  
Kay Wittenburg (DESY)  
Hermann Schmickler (CERN)

1. Beam position Monitors
2. Profile Monitors/Emittance
3. Tune and Phase Advance Measurements
4. Beam Loss Monitors
5. Bunch Length Measurements

# Contents

<b>1</b>	<b>Beam Position Monitors</b>	<b>2</b>
1.1	Problems to solve	2
1.2	Further Reading I: Overview of Recent Trends and Developments for BPM Systems M.Wendt, Proceedings of Beam Instrumentation Workshop DIPAC, DIPAC 2011	6
1.3	Further Reading II: Pickups P. Forck, JUAS Lecture Notes on Beam Instrumentation and Diagnostics	12
1.4	Further Reading III: Signal Processing for Beam Position Monitors G.Vismara, Proceedings of Beam Instrumentation Workshop BIW01	14
<b>2</b>	<b>Profile Monitors / Emittance Measurements</b>	<b>38</b>
2.1	Exercises and Literature: Profile Measurements	38
2.2	Exercises and Literature: Injection Mismatch	73
<b>3</b>	<b>Tune Diagnostics</b>	<b>81</b>
3.1	Exercises: Tune Measurements	81
3.2	Further Reading I: Diagnostics and Control of the Time Evolution of Beam parameters H.Schmickler, Proceedings of Beam Instrumentation Workshop DIPAC, DIPAC 1997	85
3.3	Further Reading II: High Sensitivity Tune Measurement by Direct Diode Detection M.Gasior (CERN), R.Jones (CERN), Proceedings of Beam Instrumentation Workshop DIPAC, DIPAC 2005	92
<b>4</b>	<b>Beam Loss Monitoring (BLM)</b>	<b>94</b>
4.1	Exercises	94
4.2	Further Reading	103
<b>5</b>	<b>Bunch Length Measurements</b>	<b>121</b>
5.1	Exercises	121
5.2	Further Reading: Bunch Length Measurements	126
<b>6</b>	<b>Writeup of instrumentation and diagnostics lectures: CAS2009</b>	<b>154</b>
6.1	Introduction to Beam Instrumentation and Diagnostics	154

# Chapter 1

## Beam Position Monitors

*M. Gasior (CERN), R. Jones (CERN)*

### 1.1 Problems to solve

# Chapter 1

## Beam Position Monitoring

*M. Gasior (CERN), R. Jones (CERN)*

### **General descriptions of basic BPM properties:**

- [1] M. Wendt, Proc. DIPAC Conference 2011, Hamburg, available at [www.jacow.org](http://www.jacow.org) (2011).
- [2] R.E. Shafer, *Proc. Beam Instr. Workshop BIW 89*, Upton, p. 26, available e.g. at [www.bergoz.com/products/MX-BPM/MX-BPM-downloads/files/Shafer-BPM.pdf](http://www.bergoz.com/products/MX-BPM/MX-BPM-downloads/files/Shafer-BPM.pdf) (1989).
- [3] S.R. Smith, *Proc. Beam Instr. Workshop BIW 96*, Argonne AIP 390, p. 50 (1996).
- [4] D.P. McGinnis, *Proc. Beam Instr. Workshop BIW 94*, Vancouver, p. 64 (1994).
- [5] J.M. Byrd, Bunched Beam Signals in the time and frequency domain, in *Proceeding of the School on Beam Measurement*, Montreux, p. 233 World Scientific Singapore (1999).
- [6] J. Hinkson, ALS Beam Instrumentation, available e.g. at [www.bergoz.com/products/MXBPM/MX-BPM-downloads/files/Hinkson-BPM.pdf](http://www.bergoz.com/products/MXBPM/MX-BPM-downloads/files/Hinkson-BPM.pdf) (2000).
- [7] R. Lorenz, *Proc. Beam Instr. Workshop BIW 98*, Stanford AIP 451, p. 53 (1998).
- [8] P. Forck, P. Kowina, D. Liakin, *Proc. CAS on Beam Diagnostics*, Dourdon, p. 187, CERN-2009-005 (2009).

# CAS2013 Course on Beam Position, Intensity and Tune and Measurement

## Trondheim - August 18<sup>th</sup>-29<sup>th</sup> 2013

### Purpose

The main aim of this course will be to give students the basic understanding of the measurement principles, fundamental concepts and related technological aspects of deriving beam position, intensity and tune. An interactive simulation tool will be available to all students for the generation and understanding of beam signals and the construction and understanding of their own virtual monitor and acquisition systems. A worksheet will also be provided to guide the student through the steps of creating their own accelerator diagnostic systems.

### Introduction to the Simulation Tool:

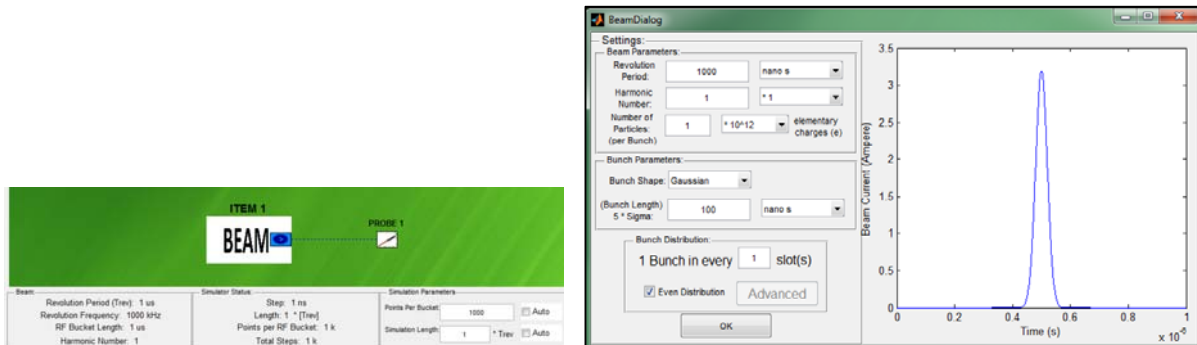
The simulation tool is comprised of a workspace and a results panel. The components to be simulated are put onto the workspace by selecting the appropriate circuit drawing block. The blocks are connected using wires, with the signals on any wire capable of being probed.



- Simulator workspace with circuit drawing *Block* open

The circuit drawing block contains most of the standard components required to simulate a beam and build a beam position or intensity monitor. Once selected and dropped onto the simulator workspace the properties of each component can be modified by right clicking on the block and selecting "properties" from the dropdown menu. For example the beam itself is represented by the "Beam" component in the "Sources" section of the circuit drawing "Block" menu. This allows the user to set all the parameters necessary to simulate most standard beam types. In the example below the beam is defined to be a single Gaussian bunch of length  $(5 \times \sigma) = 100\text{ns}$  containing

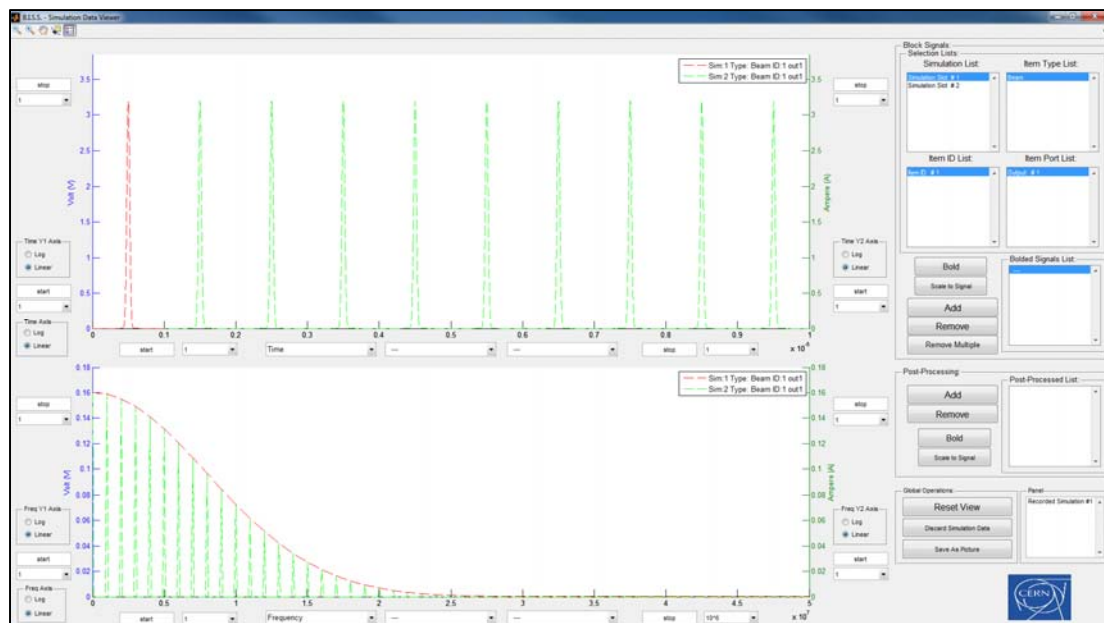
$10^{12}$  charges. The revolution frequency is 1 microsecond, with a harmonic number (number of RF buckets per revolution period) of 1, corresponding to an RF frequency of 1MHz. For higher harmonic numbers it is possible to further define how many bunches there are per turn and where these bunches are positioned, using the Bunch Distribution panel.



- Simulator workspace with Beam Properties panel open

The simulation parameters are defined in the task bar of the simulator workspace. Here the user can define the number of points to be used per RF bucket and the number of turns to be simulated.

Simulating the resulting signals observed at all probes located in a project is achieved by pressing the Simulate button. Once complete the results panel will automatically be opened to display all the probe results. All results are shown in both time and frequency domain.



- Results Panel showing Time and Frequency Domain Signals at each probe position

In the example above, two consecutive simulations show the difference in the time domain signal and frequency spectrum for a single bunch which performs one and ten revolutions past a stationary observer.

As all past simulations are stored until deleted, the results panel can be used to compare the output from multiple simulations, allowing the user to easily observe the influence of various parameters on the results, helping to optimise the system.

**1.2 Further Reading I:**

**Overview of Recent Trends and Developments for BPM Systems**

**M.Wendt, Proceedings of Beam Instrumentation Workshop DIPAC, DIPAC 2011**

# OVERVIEW OF RECENT TRENDS AND DEVELOPMENTS FOR BPM SYSTEMS\*

M. Wendt<sup>#</sup>, Fermilab, Batavia, IL 60510, U.S.A.

## Abstract

Beam position monitoring (BPM) systems are the workhorse of beam diagnostics for almost any kind of charged particle accelerator: linear, circular or transport-lines, operating with leptons, hadrons or heavy ions. BPMs are essential for beam commissioning, accelerator fault analysis and trouble shooting, machine optics, as well as lattice measurements, and finally, for accelerator optimization, in order to achieve the ultimate beam quality.

This presentation summarizes the efforts of the beam instrumentation community on recent developments and advances on BPM technologies, i.e. BPM pickup monitors and front-end electronics (analog and digital). Principles, examples, and state-of-the-art status on various BPM techniques, serving hadron and heavy ion machines, sync light synchrotron's, as well as electron linacs for FEL or HEP applications are outlined.

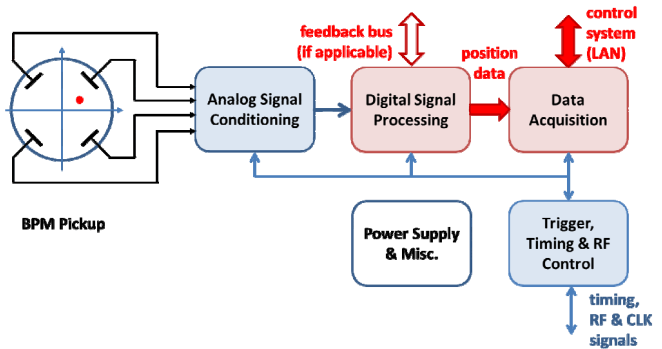


Figure 2: Schematics of a beam position monitor.

Each beam position monitor consists of a BPM pickup, with two or four symmetrically arranged electrodes, followed by a readout electronics system for signal conditioning and processing (Fig. 2). The pickup electrodes sense a part of the electromagnetic field of the passing beam and convert it to an electrical signal. The read-out electronics extract the beam position information out of the electrode signals by conditioning the analog signal, followed by digital signal processing techniques. The position data and other controls of the BPM read-out system are handled by a data acquisition interface, typically a CPU processor, which interfaces to the accelerator control system. The digital signal processing and data acquisition has to be supported by timing and clock signals, which are also used for time stamping, i.e. synchronizing BPM data across the entire system, as well as accelerator event and RF signals (for analog signal conditioning).

## INTRODUCTION

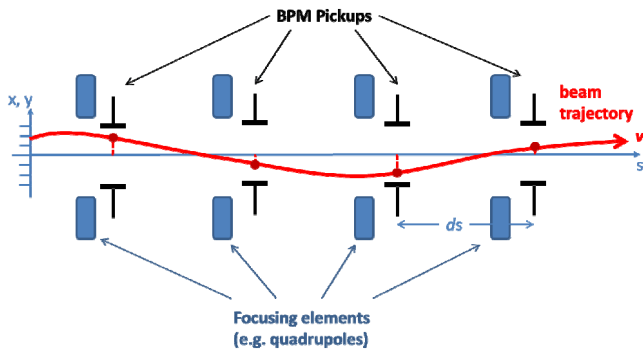


Figure 1: Measurement of the beam trajectory.

The observation of the beam trajectory

$$u(s) = A\sqrt{\beta} \sin(Q\varphi + \delta) \quad (1)$$

with  $u = (x, y)$  as the transverse coordinates,  $A$  the amplitude of the oscillation,  $\beta$  the beta-function,  $Q$  the betatron tune,  $\varphi = 0 \dots 2\pi$ , and  $\delta$  an initial condition, is one of the most fundamental beam measurements in any particle accelerator. A series of beam position monitors (BPM) are distributed along the beam-line, preferably near the focusing elements (e.g. quadrupole magnets), see Figure 1. The BPMs monitor the transverse beam displacement ( $x, y$ ) at their locations  $s_n$ , knowing the distance  $ds$  between two monitors we may also get the slope ( $x', y'$ ) of the beam trajectory – if no optical elements are in-between.

\* This work was supported by Fermi National Accelerator Laboratory, operated by Fermi Research Alliance, LLC under contract No. DE-AC02-07CH11359 with the United States Department of Energy  
<sup>#</sup>manfred@fnal.gov

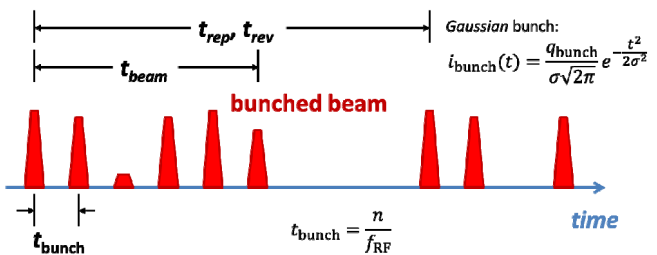


Figure 3: Beam structure.

The particle beam is a bunched stimulus signal for the BPM, with  $t_{\text{bunch}} = n/f_{\text{RF}}$ . As Figure 3 indicates, the beam bunches may have different intensities, sometimes even missing bunches. The beam structure spans  $t_{\text{beam}}$ , and typically repeats with  $t_{\text{rep}}$  in linacs and transport-lines, and  $t_{\text{rev}}$  in circular accelerators. Depending on the measurement or integration time of the BPM, we can resolve the beam position of single or all individual bunches, or the average over one or several beam pulses



With typical pickup dimensions, e.g.  $R=25$  mm,  $\phi=30^\circ$ , the sensitivity computes to 2.75 dB/mm around the beam pipe center. As eq. (2a) indicates, all broadband BPMs, suffer from a strong  $I_{\text{beam}}$  common mode term in the output signal, with a small amplitude modulation component due to the beam position  $(x,y)$ . The position sensitivity is basically fixed by the geometry and the related image current distribution, eq. (3), (4), (5).

Most prominent and widely applied member of the broadband BPM family is the electrostatic (capacitive) coupling so-called “button BPM” (different commercial button BPM feedthroughs are available). Also the stripline BPM (electromagnetic coupling) is popular, the length of the striplines, allows to match  $Z(\omega)$  to the bunch spectrum  $I_{\text{bunch}}(\omega)$ . Circular split-plane (“shoe-box”) BPMs have an almost linear position dependence, which also can be achieved with large capacitive electrodes, spanning  $\phi \approx 60^\circ$ . [9] uses BPMs with magnetic coupling loop antennas for beam position monitoring near the dump, and [10] gives further theoretical background on magnetic BPMs, also for detection of the beam angle. [11] developed a inductive BPM with single pass capability and sub-micrometer resolution.

While all broadband BPMs basically follow with their position characteristics the image current model, they differ in their frequency behavior  $Z(\omega)$ , which is discussed extensively [12], [13], [14]. The numerical solution of the Laplace equation allows a more precise approach to evaluate  $s(x,y)$ , also for non-circular cross-sections of the beam pipe. The results can be fitted with 2-D polynomials or look-up tables, allowing a linearization in the post-processing of the BPM data.

The effect of non-relativistic beams to the sensitivity of different BPM electrode shapes has been studied in great detail with help of numerical methods [15].

### Resonant BPM Pickups

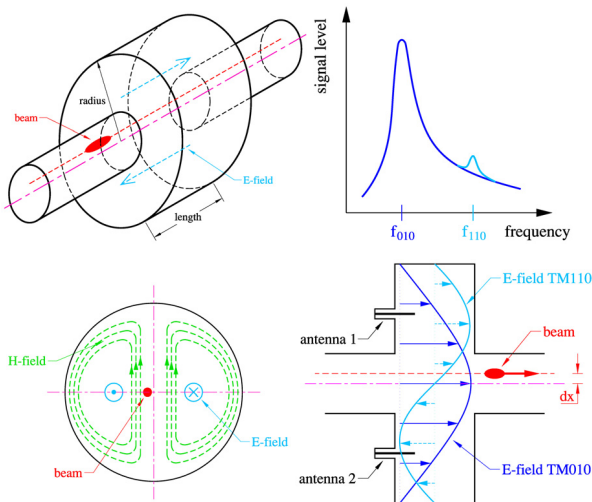


Figure 6: “Pillbox” cavity as BPM.

A cylindrical “pillbox” with conductive walls of length  $\ell$  and radius  $R$  resonates at its eigenfrequencies

$$f_{mnp} = \frac{1}{2\pi\sqrt{\mu_0\epsilon_0}} \sqrt{\left(\frac{j_{mn}}{R}\right)^2 + \left(\frac{p\pi}{\ell}\right)^2} \quad (6)$$

This resonator can be utilized as passive, beam driven cavity BPM by providing beam pipe ports (Fig. 6). A subset of the eigenmodes eq. (6) is excited by the bunched beam, for the application as BPM the lowest transverse-magnetic dipole mode  $TM_{110}$  is of interest. Its

$$E_z = C J_1\left(\frac{j_{11}r}{R}\right) e^{i\alpha z} \cos\varphi \quad (7)$$

field component couples to the beam with an almost linear dependence to the beam displacement  $r$ , and vanishes when the beam is in the center ( $r = 0$ ). Four symmetrically arranged pin antenna feedthroughs fix the polarization of  $TM_{110}$  to the horizontal and vertical axis, and provide the unnormalized difference signal  $\Delta = f(x,y,I_{\text{beam}})$ , the beam intensity is hidden in the constant  $C$ .

Resonant structures, e.g. “pill-box” or rectangular cavities, also coaxial resonators, and more complex waveguide-loaded resonators, became very popular to fulfil the high resolution, single-pass beam position monitoring demands of linear accelerators for the high luminosity final focus lattice [16], [17], or driving a SASE-FEL beam-line [18]. In [19] the operation of a simple cavity BPM inside a cryostat is presented. The discussion on the theoretical background was recently updated [20]. The x-y decoupling of the  $TM_{110}$  polarization is addressed in [21]. The high resolution potential of a BPM system with C-Band choke-mode resonators was demonstrated the first time at the SLAC final focus test beam, achieving 25 nm single-bunch, single-pass position resolution [22].

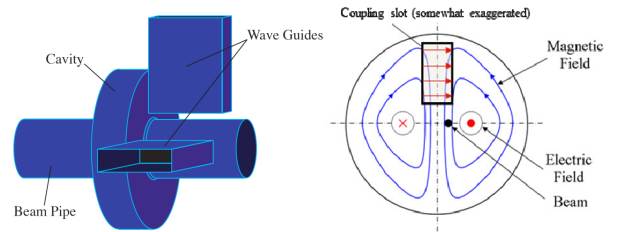


Figure 7: Waveguide-loaded cavity BPM.

The presence of the fundamental  $TM_{010}$  monopole mode adds a strong common mode component to the dipole-mode position signal, and even having a different frequency  $f_{010}$ , it limits the performance of the cavity BPM. A waveguide of width  $a$ , with a cut-off frequency

$$f_{010} < f_{10} = \frac{1}{2a\sqrt{\mu\epsilon}} < f_{110} \quad (8)$$

acts as very efficient, internal high-pass filter, and makes the cavity BPM quasi “common-mode free” (Fig. 7). The coupling slot between resonator and waveguide also helps to align the  $TM_{110}$  polarization planes, and minimizes the x-y coupling. However, the finite Q-value of the resonances still causes an unwanted leakage of the

monopole-mode at the frequency  $f_{110}$  of the dipole mode, thus limiting the resolution.

The first test of a system of three waveguide-loaded 14 GHz cavity BPMs was performed at BNL, demonstrating 150 nm beam position resolution [23]. Separate waveguide-loaded rectangular resonators (Fig. 8), operating at different C-Band frequencies achieved 8.7 nm resolution at the ATF2 final focus test beam-line [24].

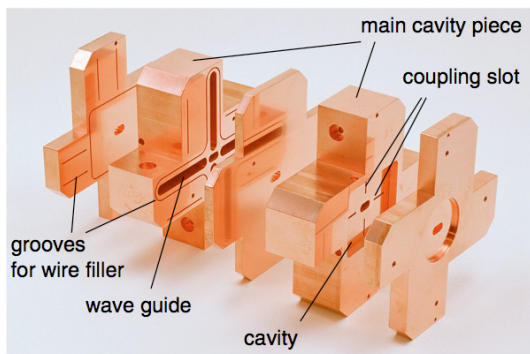


Figure 8: The ATF2 IP-BPM.

A magnetic waveguide-to-coaxial port coupling was introduced for the C-Band cavity BPMs at SPring-8 [25], a similar construction is tested for the XFEL [26]. The monopole-mode ( $TM_{010}$ ) reference resonator, required to deliver beam intensity and phase reference signals to the read-out electronics, is also used as beam arrival time monitor, showing a 25 fsec temporal resolution performance. A low-Q, mass-producible X-Band cavity BPM for the CLIC main linac is under development, targeting <50 nm spatial resolution at <50 nsec integration time. Details on the effects of tolerances are discussed, as well as performance limitations due to mode leaking, and a comparison between single vs. multi-bunch beam stimulus [27].

Beam position monitoring based on TEM coaxial resonators, the so-called re-entrant cavity BPM, has also been studied, and is proposed to operate inside the cryomodule at the European XFEL project [28]. A waveguide-loaded version demonstrated sub-micron resolution, when tested under single-bunch, single-pass beam conditions [29].

Beam excited dipole mode signals from the HOM-couplers of standing wave accelerating structures have been studied at the FLASH FEL facility. An online SVD algorithm was used to orthogonalize the signals, thus make HOM signals usable as beam position monitor [30].

## READ-OUT ELECTRONICS

The read-out system interfaces the BPM pickup to the accelerator data acquisition (control) system (Fig. 2). Signal conditioning, normalization and linearization of the position signals / data have to be provided for the time stamped beam position data. To achieve long term stability, calibration signals for gain-correction, or other correction methods are added to the system. The BPM data may also serve in beam orbit feedback systems, thus

a low latency of the signal processing is of important value.

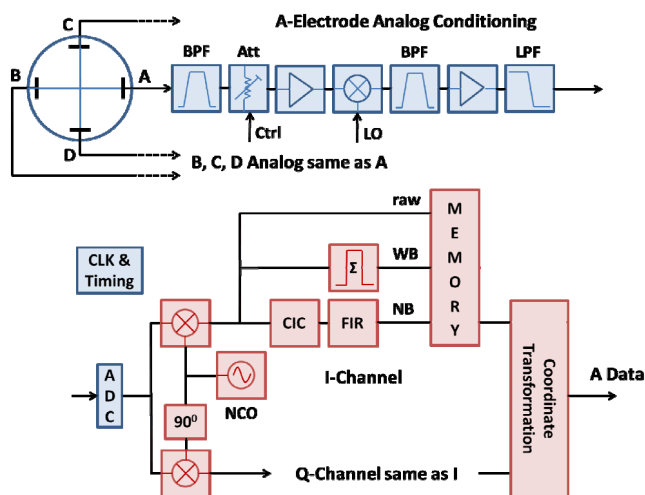


Figure 9: Key elements of the BPM read-out electronics.

An overview of “traditional” BPM read-out techniques was summarized in [31]. Today the BPM read-out electronics is typically based on frequency domain signal processing techniques, which were developed for the telecommunications market [32]. Bandpass filters in the analog section prepare the BPM pickup signals into sinewave-like burst signals, for waveform signal sampling and processing in the digital section. Microwave and RF analog components, 12-16 bit pipeline ADCs, FPGAs and clock distribution chips with sub-psec jitter are some of the key hardware elements. Figure 9 illustrates a typical electronics arrangement for a broad-band BPM pickup, 1-of-4 channels is shown. In some cases the analog down-mixer can be omitted, for cavity BPMs the schematics is similar, here the analog mixer is still required. The digital signal processing takes place in a FPGA, the I-Q down-conversion to baseband is required if the ADC clock is not locked to the accelerator RF.

As Figure 9 indicates, the measurement of the pickup electrodes signals (A, B, C, and D) is performed separately, normalization and linearization takes place in the FPGA or CPU. Drifts and aging effects have to be compensated by a calibration tone signal [33], or a channel switching scheme [34]. The effect of ADC clock jitter is discussed in various application notes [35], this becomes particularly critical in systems with heavy undersampling ( $f_{\text{signal}} \gg f_{\text{CLK}}$ ). The digital data stream can be filtered and decimated in various ways, Fig. 8 indicates how narrow-band, wide-band and raw signals can be handled simultaneously. We usually down-convert  $f_{\text{signal}} - f_{\text{NCO}}$  not exactly to DC, but to a low frequency with an integer number of oscillations over the measurement period, this avoids a crawling phase.

## ACKNOWLEDGEMENTS

Thanks to all the colleagues of the beam instrumentation community for their great help and support in preparing this document!

## REFERENCES

- [1] B. Banerjee, et.al., “Fermilab Main Injector Beam Position Monitor Upgrade,” BIW’06, Batavia, IL, USA, May 2006, AIP Conf. Proc. **868** (2006), pp. 540-548.
- [2] R. Brinkmann and M. Boege, “Beam-Based Alignment and Polarization Optimization in the HERA Electron Ring,” EPAC’94, London, UK, June/July 1994, pp. 938-940.
- [3] C. E. Adolphsen, et.al., “Beam-Based Alignment Technique for the SLC Linac,” PAC’89, Chicago, IL, USA, March 1989, Proc. of IEEE (1998), SLAC-PUB-4902
- [4] M. Boege, et.al., “The Swiss Light Source A “Test-Bed” for Damping Ring Optimization,” IPAC’10, Kyoto, Japan, May 2010, WEPE091, pp. 3560-62 (2010).
- [5] A. Hofmann, “Beam Diagnostics and Applications,” BIW’98, Stanford, CA, USA, May 1998, AIP Conf. Proc. **451** (1998), pp. 3-22.
- [6] J. Cuperus, “Monitoring of Particle Beams at High Frequencies,” CERN, Geneva, Switzerland, November 1976, CERN/PS/LIN 76-7.
- [7] K. Satoh, “New Beam Position Monitor by detecting Wall Currents,” Rev. Sci. Instr. **4** (1979), p. 450.
- [8] R. C. Shafer, “Characteristics of Directional Coupler Beam Position Monitors,” PAC’85, Vancouver, BC, Canada, May 1985, IEEE Trans. Nucl. Sci. **32** (1985), pp. 1933-37.
- [9] N. Baboi, et.al., “Magnetic Coupled Beam Position Monitor for the FLASH Dump Line,” BIW’10, Santa Fe, NM, USA, May 2010, TUPSM039, pp. 214-217 (2010).
- [10] X. He, et.al., “Direct Measurement of the Beam Deflection Angle using the axial B-dot Field,” APS Phys. Rev. 2011, to be published
- [11] I. Podadera, et.al., “Precision Beam Position Monitor for EUROTeV,” DIPAC’07, Venice, Italy, May 2007, TUPB03, pp. 57-59 (2007).
- [12] R. C. Shafer, “Beam Position Monitoring,” BIW’89, Uptown, NY, USA, October 1989, AIP Conf. Proc. **212** (1989), pp. 26-58.
- [13] D. P. McGinnis, “The Design of Beam Pickup and Kickers,” BIW’94, Vancouver, BC, Canada, October 1994, AIP Conf. Proc. **333** (1994), pp. 64-85.
- [14] F. Marcellini, et.al., “DAΦNE Broad-Band Button Electrodes,” INFN-LNF Frascati, January 16, 1996, Note: **CD-6**.
- [15] P. Kowina, et.al., “FEM Simulations – A Powerful Tool for BPM Design,” DIPAC’09, Basel, Switzerland, May 2009, MOOC03, pp. 35-37 (2009).
- [16] S. Walson, et.al., “Performance of a High Resolution Cavity Beam Position Monitor System,” NIM-A, **578** (2007), pp. 1-22.
- [17] S. T. Boogert, et.al., “Cavity Beam Position Monitor System for ATF2,” IPAC’10, Kyoto, Japan, May 2010, MOPE070, pp. 1140-42 (2010).
- [18] S. Smith, et.al., “LCLS Cavity Beam Position Monitors,” DIPAC’09, Basel, Switzerland, May 2009, TUOC03, pp. 285-287 (2009).
- [19] R. Lorenz, “Cavity Beam Position Monitors,” BIW’98, Stanford, CA, USA, May 1998, AIP Conf. Proc. **451** (1998), pp. 53-73.
- [20] D. Lipka, et.al., “Cavity BPM Designs, Related Electronics and Measured Performances,” DIPAC’09, Basel, Switzerland, May 2009, MOPD07, pp. 280-284 (2009).
- [21] V. Sargsyan, “Cavity Beam Position Monitor for the TESLA Cryomodule – Cross-Talk Minimization,” Ph. D. thesis, Technical University Berlin, Germany (2003).
- [22] T. Slaton, et.al., “Development of Nanometer Resolution C-Band Radio Frequency Beam Position Monitors in the Final Focus Test Beam,” SLAC-PUB-7921, August 1998
- [23] V. Balakin, et.al., “Experimental Results form a Microwave Cavity Beam Position Monitor,” PAC’99, New York, NY, USA, March/April 1999, IEEE Proc. (1999), pp. 461-464.
- [24] T. Nakamura, et.al., “High Resolution Cavity BPM for ILC Final Focus System (IP-BPM),” LCWS/ILC 2007, Hamburg, Germany, May/June 2007, arXiv:0709.2254v1, eConf C0705302.
- [25] H. Maesaka, et.al., “Development of the RF Cavity BPM of XFEL/Spring-8,” DIPAC’09, Basel, Switzerland, May 2009, MOPD07, pp. 56-58 (2009).
- [26] D. Lipka, et.al., “Orthogonal Coupling in Cavity BPM with Slots,” DIPAC’09, Basel, Switzerland, May 2009, MOPD07, pp. 44-46 (2009).
- [27] H. Schmickler, et.al., “Submicron Multibunch BPM for CLIC,” IPAC’10, Kyoto, Japan, May 2010, MOPE087, pp. 1185-87 (2010).
- [28] C. Simon, et.al., “Status of the Re-entrant Cavity Beam Position Monitor for the European XFEL Project,” BIW’10, Santa Fe, NM, USA, May 2010, TUPSM038, pp. 210-213 (2010).
- [29] J. Y. Ryu, et.al., “Development of a Re-entrant Cavity L-Band Beam Position Monitor for ILC,” to be published.
- [30] S. Molloy, et.al., “High Precision Superconducting Cavity Diagnostics with Higher Order Mode Measurements,” Phys. Rev. ST Accel. Beams **9**, 112802 (2006).
- [31] G. Vismara, “Signal Processing for Beam Position Monitors,” BIW’00, Cambridge, MA, USA, May 2000, AIP Conf. Proc. **546** (2000), pp. 36-60.
- [32] V. Schlott, et.al., “First Operational Experience with the Digital Beam Position Monitoring System for the Swiss Light Source,” EPAC’00, Vienna, Austria, June 2000, pp. 1809-11.
- [33] M. Wendt, et.al., “High Resolution BPMs with Integrated Gain Correction System,” DIPAC’09, Basel, Switzerland, May 2009, MOPD19, pp. 89-91 (2009).
- [34] Instrumentation Technologies, <http://www.i-tech.si>
- [35] Analog Devices, AN-282, AN-501.

**1.3 Further Reading II:**

**Pickups**

**P. Forck, JUAS Lecture Notes on Beam Instrumentation and Diagnostics**



# Lecture Notes on Beam Instrumentation and Diagnostics

Peter Forck

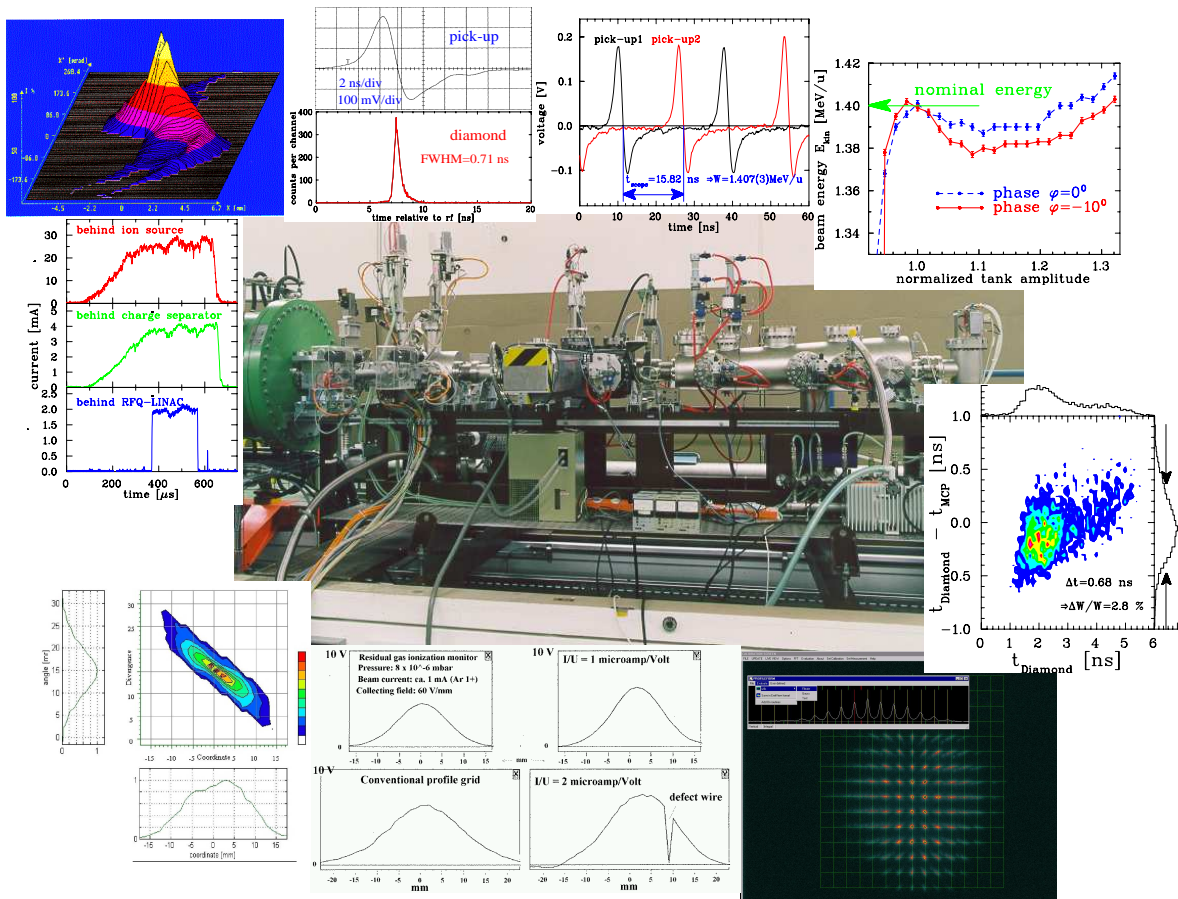
Gesellschaft für Schwerionenforschung (GSI)

Darmstadt, Germany

e-mail: p.forck@gsi.de

Joint University Accelerator School

January – March 2011



A picture of the mobile test bench including some measurements, as provided for the commissioning of the high current injector at GSI in 1999.

- 1.4 Further Reading III:**  
**Signal Processing for Beam Position Monitors**  
**G.Vismara, Proceedings of Beam Instrumentation Workshop BIW01**

**EUROPEAN ORGANIZATION FOR NUCLEAR RESEARCH  
CERN – SL DIVISION**

**CERN-SL-2000-056 BI**

# **SIGNAL PROCESSING FOR BEAM POSITION MONITORS**

**Vismara G.**

*Abstract*

At the first sight the problem to determine the beam position from the ratio of the induced charges of the opposite electrodes of a beam monitor seems trivial, but up to now no unique solution has been found that fits the various demands of all particle accelerators. The purpose of this paper is to help “instrumentalists” to choose the best processing system for their particular application, depending on the machine size, the input dynamic range, the required resolution and the acquisition speed. After a general introduction and an analysis of the electrical signals to be treated (frequency and time domain), the definition of the electronic specifications will be reviewed. The tutorial will present the different families in which the processing systems can be grouped. A general description of the operating principles with relative advantages and disadvantages for the most employed processing systems is presented. Special emphasis will be put on recent technological developments based on telecommunication circuitry. In conclusion, an application example will show how to choose the correct solution for a particular case

*Presented to the Beam Instrumentation Workshop in Boston - USA  
8 – 11 may 2000*

sl-2000-056  
10/07/2000



# Signals processing for Beam Position Monitors

Giuseppe Vismara

*CERN – Geneva-23 - Switzerland*

**Abstract.** At the first sight the problem to determine the beam position from the ratio of the induced charges of the opposite electrodes of a beam monitor seems trivial, but up to now no unique solution has been found that fits the various demands of all particle accelerators. The purpose of this paper is to help “instrumentalists” to choose the best processing system for their particular application, depending on the machine size, the input dynamic range, the required resolution and the acquisition speed. After a general introduction and an analysis of the electrical signals to be treated (frequency and time domain), the definition of the electronic specifications will be reviewed. The tutorial will present the different families in which the processing systems can be grouped. A general description of the operating principles with relative advantages and disadvantages for the most employed processing systems is presented. Special emphasis will be put on recent technological developments based on telecommunication circuitry. In conclusion, an application example will show how to choose the correct solution for a particular case.

## 1. INTRODUCTION

The beam position monitor (BPM) can be found in every accelerator and is by far the most popular instrument, particularly useful for machine setting-up and developments.

The BPM has largely evolved since the early days, from the simple scope visualization of coaxial multiplexed P.U. signals into a very complex system. They are now capable of digitizing individual bunches separated by a few tenths of ns, with spatial resolution in the micron range, while the resulting orbit or trajectory collected from several hundred PUs can be displayed in a fraction of a second.

To obtain such a performance the processing electronics have to be optimized to the machine and beam parameters.

A unique solution capable of covering all the possible combinations with satisfactory results seems almost impossible to realize. This is the reason for the wide spectrum of signal processing in use today.

The BPM applications are not only limited to orbit and trajectory measurements, they can also perform static and dynamic beam parameter measurements by exploiting the large amount of data collected and stored in their memories<sup>1</sup>.

By a “turn-by-turn” acquisition on a single monitor, it is possible to measure betatron oscillations, beam response and transfer function.

By a “turn-by-turn” acquisition using the whole monitoring system, it is possible to measure phase advance, local chromaticity, phase change versus beam current due to transverse reactive impedance and to perform optics checks.

By averaging over 1000 or more revolutions, high-resolution measurements can be obtained. The orbit response to local deflections is used for beam optics computing while machine impedance measurements are possible from the current dependence of the orbit.

A very recent application is energy calibration. In the LEP machine stable, polarized beam at 45 GeV is used to calibrate a spectrometer, which can then at >100 GeV measure the energy within a resolution of  $10^{-4}$ . Three X and Y monitors on each side of the deflecting magnet, with very high resolution ( $<1\mu\text{m}$ ) and long term and temperature stability, are required.

The BPM is also used for feedback applications to stabilize and align the beam; in this case, speed (loop bandwidth) is more important than linearity.

Another application (ESRF & SPS) for the BPM is the beam position interlock<sup>2</sup> which dump the beam when an excessive displacement is detected for a certain time.

These applications are much more performance demanding than for a simple position measurement. They require an excellent linearity over a large part of the chamber aperture, a high-resolution ( $\mu\text{m}$ ) to avoid large beam excitation and good position stability versus beam intensity, time and temperature variation.

## 2. SIGNAL ANALYSIS

### 2.1. Signal Source

The reference parameter used to define the input signal in a processing system is the beam current circulating in the machine. The beam current depends on the injected charge and the revolution period. The relation between current and charge is:

$$I_b = Q_b * N_b / t_{rev}$$

Where  $Q_b$  is the charge per bunch in Coulombs,  $N_b$  is the number of bunches and  $t_{rev}$  is the revolution period.

The beam current is the correct parameter when defining the sensitivity of the processing system if it will integrate over one or more revolution cycles. When using wide-band processing systems, capable of resolving individual bunches, it is much more convenient to talk about charges per bunch.

Another parameter defining the input signal is the longitudinal charge density of a bunch. It can be assumed to be almost gaussian for leptons and cosine-square for protons, hence the induced signals at the PU's output will have almost the same shape. The bunch length depends on the voltage gradient and the beam energy.

It is also assumed that the transverse beam size is negligible relative to the PU aperture but for  $\mu\text{m}$  resolution it must be taken into account<sup>3</sup>.

In order to translate the  $I_b$  or  $Q_b$ , into the electrical voltage seen by the signal processing system, it is very convenient to define, in analogy to Ohm's law, the following relation:

$$V(t) = Z_t * I_b(t)$$

Where  $Z_t$  is called the transfer impedance of the PU.

### 2.2. Beam Structure

Particle accelerators can be filled with beam in various ways; these determine the signal spectral content that the processing electronics can exploit.

It is possible to define 4 major beam structures.

**All rf buckets filled:** Beam is trapped by the rf cavities in such a way that a particle bunch is present in all rf buckets. This situation is the easiest to be treated since the induced signal presents an almost monochromatic frequency spectrum. This is a typical condition for machines optimized for the maximum beam current (e.g. PEP II, LEP fixed target operation).

**Few rf buckets filled:** (with longitudinal symmetry): Beam bunches are only present in a regular structure over N possible buckets. The bunch density is the highest possible. The harmonics content shows the revolution frequency and all the multiple frequencies of [1 / bunch spacing] (e.g. LEP).

**Variable buckets filled:** In some particular cases the machine is filled with a particular structure, which is not longitudinally symmetric. A large spectral harmonic content is present (e.g. LHC).

**Un-bunched beam:** This situation can only be present in the absence of an rf signal, exclusively for proton or heavy ions machines (e.g. Cebaf recirculating linac ). This is the most difficult structure to process, since an unstructured beam is almost impossible to treat by the processing systems discussed here.

Some authors summarize the above beam filling structures by introducing the notion of a beam-bunching factor. It is defined as the ratio between the bunch width and the bunch spacing.

### 2.3. Beam Position Monitors

Five PU families are nowadays employed: Electrostatic (Buttons, electrodes of various shapes,..), Electromagnetic (Couplers), Resonant cavity<sup>4</sup> (specially suited for H.F. linacs), Magnetic and Resistive (wall current).

I will briefly describe the most commonly used.

#### 2.3.1. Electrostatic (Capacitive)

Let us analyze the properties of buttons since they are the easiest and cheapest to build. The image current associated with a circulating beam will induce a charge directly proportional to the beam intensity and inversely proportional to the distance.

Their simplified equivalent circuit is the following:

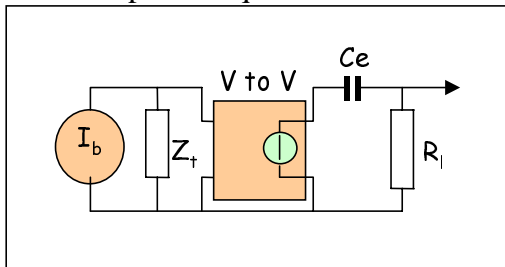


FIGURE 1. Simplified button's equivalent circuit

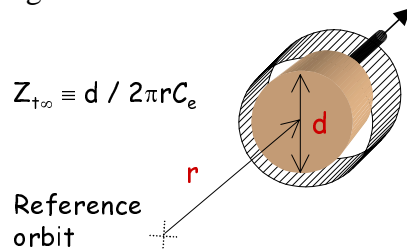


FIGURE 2. Button transfer impedance

where  $Z_t$  is the transfer impedance as defined above,  $C_e$  is the electrode capacitance and  $R_l$  is the load impedance.

The capacitive coupling is responsible for the low frequency cut-off, which depends on the PU time constant  $T = R_l C_e$ . Its value is in the hundreds of MHz range.

When designing button PUs special care should be taken to suppress unwanted parasitic signals due to the following phenomena:

- The button geometry determines a resonant cavity between the button and the body of the vacuum pipe; this resonator is usually tuned to GHz frequencies and can be excited by short bunches.
- The impedance variation on the transmission line from vacuum to air (ceramic or glass dielectric) will produce impedance mismatching, hence reflections, generating standing waves.

To attenuate these unwanted signals most processing systems have a front-end low-pass filter; in addition, the interconnection cables play a similar role as LP filters. The resulting global frequency response looks like a wide band-pass filter.

### 2.3.2. Electromagnetic (Strip Line Couplers)

Contrary to the electrostatic PU, here it is the electromagnetic field of the beam that induces a signal on the strip line:

$$Z_{t\infty} = 60 \ln[(r+h) / r] \equiv Z_0 [a / 2\pi(r+h)]$$

where  $Z_0$  is the characteristic impedance and  $a, r, h$  are the mechanical dimensions.

The amount of obtainable signal depends on the azimuthal coverage and on the strip-line length if it is comparable to the bunch length ( $2\sigma$ ).

The signal response versus frequency has a sinusoidal distribution and its maximum is obtained for a frequency corresponding to  $f_0 = 1/4 * t$ , where  $t$  is the electrical coupler length. On the other hand, for a frequency corresponding to  $f_0 = 1/2 * t$  the induced signal will be a minimum. This distribution repeats for all multiples of the fundamental base-band frequency.

Each strip-line has two termination ports and the designer can choose the output signal polarity on the downstream port by putting either a short circuit or an open end on the upstream port. When the upstream port is loaded with its characteristic impedance, no signal will appear on the downstream port, if the transverse electro-magnetic (TEM) wave and the beam speed are identical. In this case, the coupler is directional and it is possible to separate the signals of two beams circulating in opposite directions.

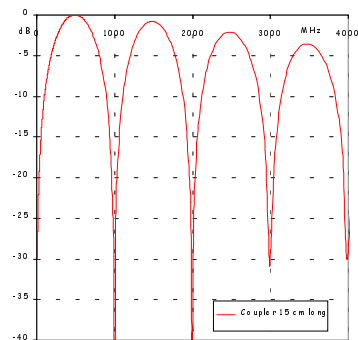


FIGURE 3. Coupler's frequency response

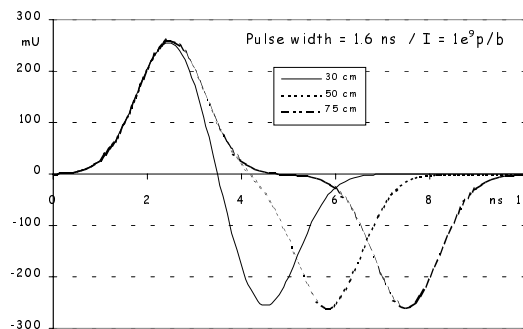


FIGURE 4. Coupler's time response

## 2.4. Beam position computing

The beam position is reconstructed from the signal difference of opposite PUs. The induced signals are intensity and position sensitive, hence the position can only be obtained by suppressing the intensity dependence; in other words, the signals should be normalized to the beam intensity:

$$\text{Position} = K_{x,y} * \Delta / \Sigma = K_{x,y} * N_p$$

where  $K_{x,y}$  is a scaling coefficient,  $\Delta$  the electrodes signal difference and  $\Sigma$  the beam intensity. For a BPM having a linear transfer function and the electrodes placed on a circular surface (of the vacuum pipe),  $K_{x,y}$  corresponds to its radius (Figure 5).

### 2.4.1. Normalized Position ( $N_p$ )

In the above equation,  $N_p$  represents the normalized position. It is dimensionless and can vary from  $-1$  unit ( $U$ ) to  $+1U$  passing through  $0$  for a centered beam.

$1U$  is called the “Normalized half aperture” ( $N_a$ ). All parameters defining the performance of an analog signal processing system should be specified relative to  $N_a$ .

Button or coupler monitors have strongly nonlinear transfer functions, with higher sensitivity at the center. In this case the effective  $K_{x,y}$  corresponds to the derivative at the center of the transfer function.

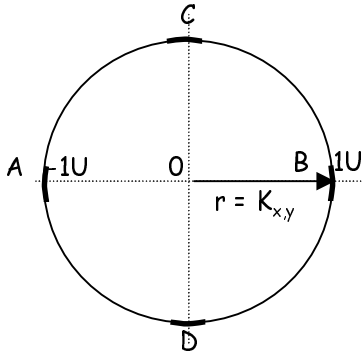


FIGURE 5. 4 PU's normalized representation

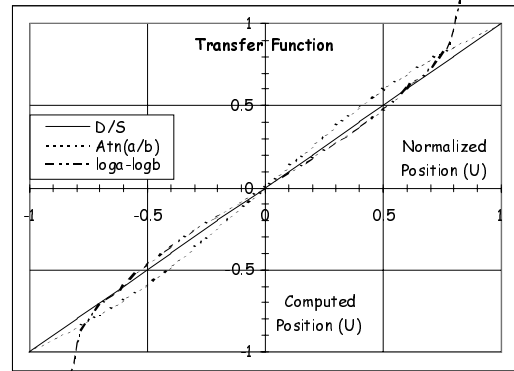


FIGURE 6. Normalized transfer functions

There are at least three methods to obtain a normalized signal.

### 2.4.2. Difference over Sum

As was explained above

$$N_p = (A-B)/(A+B)$$

where  $A, B$  are the induced voltage signals.

The difference and the sum can be obtained either in an analog way by the use of a  $0^\circ/180^\circ$  passive hybrid, a differential amplifier, or simply computed by software.

### 2.4.3. Amplitude to phase conversion (AM/PM)

The two input signals are converted, by the use of a  $90^\circ$  passive hybrid, into two signals having identical amplitude but different phase. Their phase relation is

$$N_p = \phi = 2 * \text{Arctangent} (A/B)$$

The transfer function is not linear, and shows an S shape (Figure 6).  
The slope at the center is higher, hence a large sensitivity or better S/N.

#### 2.4.4. *Logarithmic ratio*

The two input signals are converted into their logarithmic equivalents and subtracted from each other, which is equivalent to the logarithm of their ratio.

This is a pure active analog process.

$$N_p = [\log (A) - \log (B)] = \log (A/B)$$

The transfer function is non-linear, and shows a reversed S shape (Figure 6).

There is a very large deviation when exceeding > 70 % of the  $N_a$  and the sensitivity around the center is ~1.5 times smaller compared to the AM/PM function.

### **3. DESIGN PARAMETER SPECIFICATIONS AND THEIR DEFINITION**

When starting the design of analog signal processing electronics, one should first define all the parameter requirements indispensable to qualify the performance of the system.

Since engineers have adopted slightly different definitions according to the function of their systems, it is quite difficult to compare the performances of the different solutions.

In this chapter, I will try to define the way each fundamental parameter should be measured.

#### **3.1. Accuracy**

Accuracy is the ability to determine the absolute beam position.

This is limited by mechanical tolerances and alignment, the magnetic field distribution and the electronic errors. Beam based calibration techniques allow the global offset of a processing system to be determined for a particular condition, and so establish a reference point.

From here onwards it is the processing electronics that is responsible for the absolute position. The error sources are of various origin: the parasitic element on the PU itself (spurious resonances, impedance mismatching), interconnecting cables impedance mismatching and attenuation, electromagnetic interference and input stage noise, non-linearity and intensity dependence, gain difference between channels, calibration errors, and granularity errors on the digitizer.

#### **3.2. Resolution**

Resolution is the minimum position difference that can be resolved.

This parameter is particularly important in colliding machines, where luminosity depends on how accurately beams can be aligned.

Two resolutions can be defined:

### 3.2.1. Single shot resolution

This corresponds to the standard deviation (Stdev) of each individual position measurement. It applies to single beam passage (trajectory or transfer line) measurements.

### 3.2.2. Absolute resolution

This has the same definition as above but is obtained from the average over a certain time (e.g. 1 ms) when digitizing at the maximum acquisition rate. It applies to circulating or repetitive beam.

The measurements should be performed under conditions corresponding to a centered beam, at its nominal intensity.

The ADC resolution should be equal to or just below the rms. value of the output noise, measured within the input bandwidth of the digitizer.

At low input level, the absolute resolution depends on the input noise and the bandwidth of the analog processor. For large input signals, the limiting factor is mainly the ADC resolution (number of bits) and the uncertainty on electronic parameters such as the time jitter.

## 3.3. Stability

Stability is one of the most important parameters in a BPM since the main purpose of the system is to give a stable reference of the center. The uncertainty on the measurement stability will affect the global resolution of system.

The position measurement should be independent of the beam intensity, the bunch shape and the bucket filling.

**Stability versus input signal:** It is calculated as the Stdev from a series of digitized positions, measured over the whole dynamic range.

Reproducible intensity dependent errors can be compensated by the use of a polynomial fit when measuring the beam intensity.

The measurements should be averaged, in order to reduce the noise contribution to well below the error itself and are usually recorded for a centered position.

In addition, the position measurement should be stable with respect to the time and temperature at least during the time interval between two calibrations. This is extremely important for electron machines or in applications like energy calibration.

**Long term position stability (LTPS):** It is defined as the Stdev of the digitized values.

**Position temperature coefficient:** It is the slope of the position drift versus temperature.

The measurements should be done at the nominal input level, with all other parameters being fixed. The time interval for measuring the LTPS should range from at least one hour up to few days depending on the machine, with the temperature ranging from 0 to 40 C.

### 3.4. Non-conformity to the theoretical transfer function

This represents the measurement error relative to the theoretical transfer function.

Measurements on individual BPMs, high precision measurements (e.g. LEP spectrometer) and preservation of lepton beam spin polarization require processing systems with very low non-conformity.

Non-conformity is defined as the Stdev of the difference between the measured and the theoretical transfer function relative to  $2N_a$  ( $\pm 1U$ ). The reason for this choice is determined by the fact that it corresponds to the maximum possible excursion, which in turns equals the full scale of the ADC, in all the normalization process.

The measurement should be done at the nominal input level and for constant sum signals. Since the beam excursion never reaches the extremities, the measurement can in practice be limited to 80% of the full excursion.

### 3.5. Sensitivity

Sensitivity is the minimum input level at which beam position measurement still fulfills the accuracy specifications.

In order to be able to compare among different machines, the most adequate figure is the number of charges per bunch.

The present limit for standard orbit systems corresponds to a few  $10^7$  charges/bunch

### 3.6. Dynamic Range

The dynamic range determines the capability of the system to handle very different beam intensity conditions. Beam position measurements have to be possible, with reasonable accuracy, over the whole dynamic range.

During machine studies, circular machines are often filled with bunches of 1‰ (-60 dB) of the nominal intensity. The same is true for specific physics productions (e.g. Totem for LHC), and at the CERN anti-proton decelerating machine, where bunch intensity is reduced by 80 dB during the deceleration cycle. At GSI/Darmstadt bunch intensities can vary over several decades among proton and various ion beams.

The dynamic range is defined as the difference, expressed in dB, between the maximum input level before a large non-linearity on the output signal appears (saturation) and the minimum input level at which a pre-defined signal to noise ratio (S/N) is reached.

A practical figure to define when saturation is reached is a 1 dB signal compression (= 10% error in the position measurement) while a 20 dB S/N ratio could define the minimum input level.

Processors using a discrimination level will not be limited by the S/N ratio, the lower limit being determined by the discriminator's threshold.

### 3.7. Acquisition Time

This parameter defines the time required for the signal processor to store a full set of data into memory.

The importance of this parameter is related to the capability of resolving individual bunches and the absolute resolution of the processor, since the faster the system the larger the number of samples per time unit.

Some processor systems have the capability of digitizing individual bunches, others have turn by turn capability and finally some can only measure the integrated signal over several turns.

Several elements contribute to the acquisition time:

- ♣ The low-pass and band-pass filters selecting the useful frequency spectrum required for the signal processor.
- ♣ The switching and acquisition time of all channels (multiplexed signal treatment).
- ♣ The PLL time required to synchronize (synchronous detector).
- ♣ The set-up time for the automatic gain control AGC to stabilize (constant sum signal).
- ♣ The sample and hold circuit and the conversion time of the ADC.

#### 4. PROCESSING SYSTEM FAMILIES

The various signal-processing systems can be grouped into different families according to the employed techniques. At least three different criteria can be used to group them.

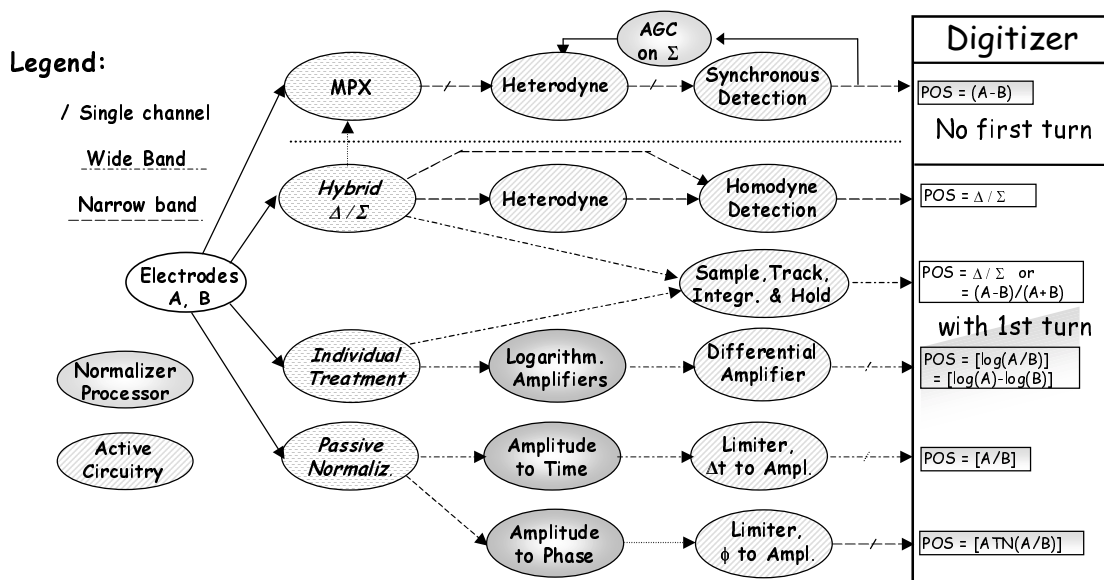


FIGURE 7. Schematic representation of the different families and their interconnections

## 4.1. Signal Recombination

Four main categories are nowadays employed:

- ◆ **Individual signal treatment:** The maximum signal information is still available, therefore a wide-band processing is the most suitable. Due to a very large Gain-Bandwidth, it offers a limited dynamic range.
- ◆ **Time MPX:** Electrode signals are sequentially time-multiplexed and processed by a single electronic system. It offers excellent long-term stability but cannot perform turn-by-turn measurements.
- ◆  **$\Delta/\Sigma$ :** The individual signals are immediately converted by the use of hybrids into  $\Delta$  and  $\Sigma$ . This offers excellent center position stability but requires switchable gain amplifiers.
- ◆ **Passive Normalization:** The signal's amplitude ratio is converted into a phase or time difference. This is amplitude independent but the intensity information is lost.

## 4.2. Normalization Processes

Normalization is an analog process that will produce a signal proportional to the position information and independent of the input signal level.

Three conditions apply to all normalization processes: 1) The intensity information is lost. 2) The digitization requires a smaller number of bits. 3) No gain selection is required.

Two active and two passive techniques are actually employed.

- ◆ **Constant Sum:** The Normalization is obtained by keeping constant the sum of the two electrode signals using AGC amplifiers. This approach applies to the time MPX process, where the signals exploit the same amplification chain and the digital receiver, where a permanent calibration on all channels will guarantee identical gains.
- ◆ **Logarithmic Conversion:** Since the ratio of the logarithm of two signals is equal to the difference of the logarithm, the signals can be converted by logarithmic amplifiers to give the normalized signal as the difference of the outputs. It offers a large dynamic range, but limited linearity.
- ◆ **Amplitude to Time:** This is based on the sum of a direct and a delayed signal coming from the two electrodes. The zero crossing of the sum signal varies with time proportionally to the signal ratio, and hence to the position. It offers large bandwidth but is limited to bunched beams.
- ◆ **Amplitude to Phase:** Is a similar process where time is replaced by phase and a single period by multiple oscillations. It is a simple solution but requires accurate phase matching (Filters).

All other processes that require computing software to extract the position information from the recorded data are known as un-normalized processes.

### 4.3. Acquisition Time

This is the time required for the BPM to supply a full set of data to the digital processor. Three categories can be created:

- ◆ **Wide-band:** It groups all processing systems capable of measuring individual bunches separated by  $>10$  ns down to a single bunch. The bandwidth can be as high as 100 MHz. Systems that belong to this group include: Sample/Track & Hold, Logarithmic amplifiers, Amplitude to Time normalizers.
- ◆ **Narrow-band:** It groups all processing systems capable of resolving one machine revolution period and in some cases can measure individual bunches separated by  $>100$  ns. The bandwidth ranges from a few 100 kHz up to a few MHz. The Heterodyne and Amplitude to Phase processors belong to this group.
- ◆ **Slow acquisition:** A special class is reserved for the Time MPX processing which, while having an equivalent bandwidth relative to other heterodyne systems, is penalized in the acquisition rate by the time multiplexing.

## 5. PROCESSING SYSTEM DESCRIPTIONS

### 5.1. Time Multiplexed Processor <sup>5</sup>

The processor is conceived for closed orbit measurement of stable stored beams.

The input MPX is usually built with a multiple configuration of Ga-As switches; the channel isolation should be  $>50$  dB for frequencies up to 1 GHz.

A band-pass filter is used to select the largest line of the signal spectrum; its selectivity is not critical.

The essential element is the pre-amplifier which should handle a very large dynamic range ( $>75$  dB) and compress it by  $>50$  dB. Its input admittance should be kept stable as a function of the gain to avoid a zero offset drift. The global noise figure is increased by different insertion losses and should be optimized for the largest gain.

An active mixer, making use of a frequency synthesizer to reduce the noise contribution, is used to down convert the signal to a standard intermediate frequency (IF usually 10.7 MHz or a multiple). The IF amplifier and the demodulator are usually integrated telecom circuits. The IF bandwidth is selective enough to suppress side bands at the revolution frequency (multiple bunches) but sufficiently wide to allow for

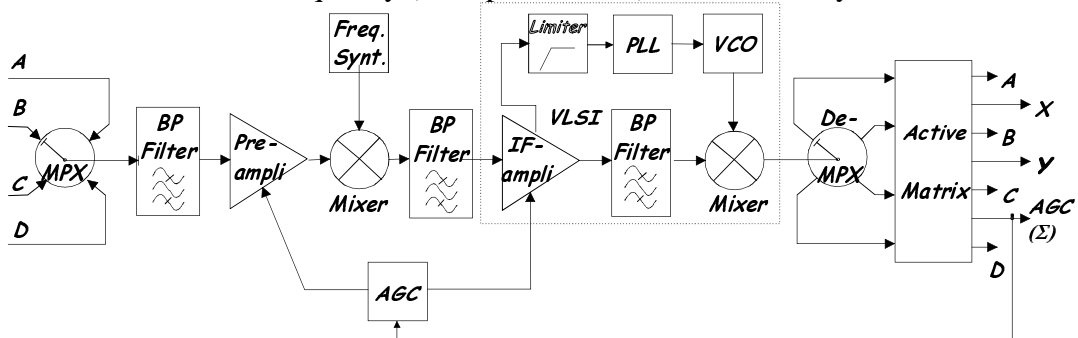


FIGURE 8. Block diagram of the time MPX processor.

fast switching among channels ( $100 \text{ kHz} > \text{BW} < 1\text{MHz}$ ). Synchronous detection is obtained by comparing the phase of a sample of the carrier frequency with a reference signal and driving a VCO in a phase locked loop. Synchronous detection offers a clean detected DC signal but it slows down the MPX switching time since the PLL has to relock after each switching (even with accurate phase adjustment).

The last part of the chain is composed of an output de-multiplexer, four track & hold amplifiers and an active matrix of video amplifiers to produce the AGC sum and X, Y positions <sup>6</sup>.

**TABLE 1: Time Multiplexed processor**

Advantages	Limitations
Normalization process	Requires a stable beam during the scanning
Reduced number of channels (x4)	No turn by turn acquisition
Identical gain for all the channels	Slow acquisition rate (MPX)
Large dynamic range (>80dB)	Reduced Noise Figure (gain matching & MPX insertion losses, AGC pre-ampli.)
Excellent position stability	Reduced linearity, for non-linear PU's since the $\Sigma$ is not constant
No temperature dependence and component aging	Complex engineering

## 5.2. $\Delta / \Sigma$ Processor

When using this approach it is convenient to convert the input signals into their equivalent difference and sum at the earliest possible stage. This is done by a simple and reliable passive element called the “180° hybrid”. The input signals should be in-phase, which means tight tolerances on the interconnection cables. Since the hybrid is radiation resistant, it can be connected directly to the electrodes.

**Wide-band:** The LP filters will just stretch the pulses. The pre-amplifiers have a large BW and programmable gain but a limited dynamic range. For long bunches, the S & H circuits are suppressed and FADCs (1 GS/s) digitize the signal directly <sup>7</sup>.

**Narrow Band:** In most of the cases, the hardware is similar to that of the time MPX. In some applications, the heterodyne conversion is suppressed. The pre-amplifiers have low noise figure ( $\text{NF} < 2\text{dB}$ ), programmable gain through pin diodes switches, and will absorb a large input dynamic range (> 90 dB). A fraction of the  $\Sigma$  signal is limited and used as a local oscillator in a homodyne detector. The  $\Delta$  &  $\Sigma$  signals are digitized by a track and hold circuit and externally triggered ADCs. This scheme is

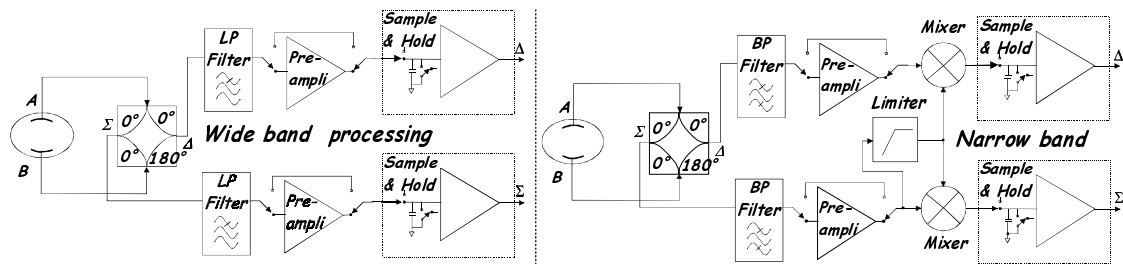


**FIGURE 9.** Block diagram of the  $\Delta / \Sigma$  processors

also used for single bunch measurement in complex injector machines (SPS)<sup>8</sup>, where the bunch excites the BP filter to resonate on its central frequency (see amplitude to phase normalizer). No hardware modifications are necessary but even tighter tolerances on the phase matching are required.

**TABLE 2.  $\Delta$  &  $\Sigma$  Processor**

Advantages	Limitations
The central position is independent of input intensity	Programmable gain amplifiers
Intensity measurement is available	Multiple calibration coefficients
Excellent Noise Figure	The absolute position is f(gain)
[Wide band allows measurements on multiple bunches ( $\Delta t < 20$ ns)]	{ Tight phase matching ( $\Delta$ , $\Sigma$ ) at all the gains required by the synchronous detection ( $\pm 5^\circ$ ) }
{ Large dynamic range $> 90$ dB }	{ Pedestal error on $\Sigma$ }

[W.B.] & {N.B.}

### 5.3. Logarithmic Amplifiers<sup>9, 10, 11</sup>

The processor makes use of logarithmic amplifiers to compress each signal. The outputs are at first demodulated, filtered and applied to a differential amplifier.

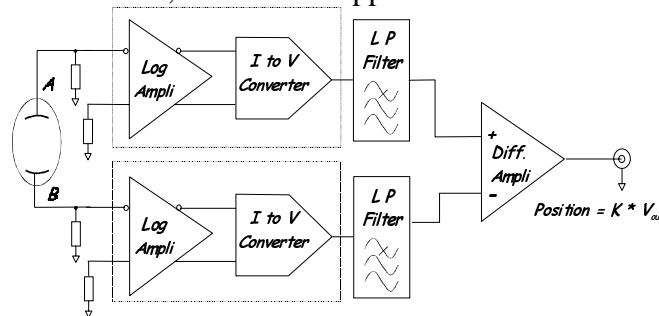


**FIGURE 10.** Block diagram of the logarithmic amplifier processor

The schematic is very simple but the hardware realization hides a very sophisticated electronic circuit in order to approach the ideal function. New generation circuits make use of several cascaded limiting amplifiers, with fixed gain and a wide bandwidth. Full wave rms. detectors are applied at each stage and by summing their output signals, a good approximation to a logarithmic transfer function is obtained.

**TABLE 3. State of the art parameters for Logamp.**

Input dynamic range	$> 90$	dB
Input noise	$< 1.5$	nV/ $\sqrt{\text{Hz}}$
Non conformance linearity	$< \pm 0.3$	dB
Limiter Bandwidth	D.C. to $> 2$	GHz
Video Bandwidth	D.C. to 30	MHz

The demand of the consumer market (primarily telecommunications) for these products has resulted in a wide variety of new circuits, each one optimized for a specific parameter.

**TABLE 4. Logarithmic amplifiers.**

Advantages	Limitations
Possible applications in the time and frequency domain (NB & WB)	State of the art performances are not simultaneously available
Very large dynamic range (>90 dB)	Poor position stability vs. input level, for peculiar conditions
Wide input bandwidth	Limited linearity ( few % of the $N_a$ )
No bunch shape dependency	Limited long term stability
Simultaneous digitization of + and - charges	Temperature dependence
Simple engineering	

## 5.4. Amplitude to Phase Normalization

This technique was first developed for RF signals working in the frequency domain and rapidly adapted to short pulses working in the time domain <sup>12</sup>.

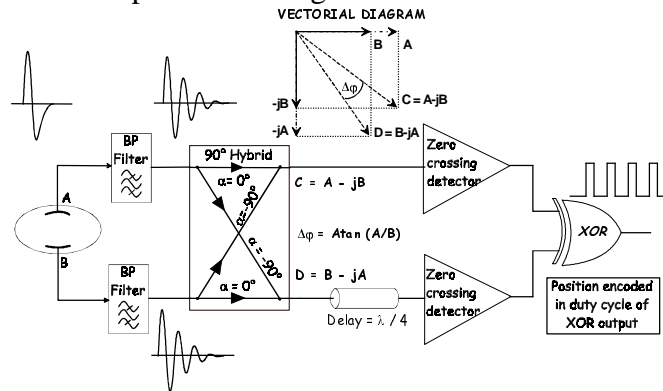


**FIGURE 11.** Block diagram of the amplitude to phase (AM/PM) processor

The two electrode signals are converted into a RF burst or a permanent RF signal, according to the beam shape, by the use of a BP filter. These in-phase signals are applied to the inputs of a “90° Hybrid”. Each signal is split into two branches; one of them is shifted by 90° and added to the opposite in-phase signal, and vice versa. The outputs are of equal amplitude and have a phase difference ( $\Delta\phi$ ) proportional to the position.

$$\text{Position} \equiv \Delta\phi = 2 * \text{Arc-tangent} (A / B) - \pi/2$$

This relation is valid for both a continuous wave or for a burst after proper settling time, which depends on the bandwidth. To avoid an ambiguity in sign, one output is also delayed by 90° degrees.

The two signals are applied to comparators that suppress the amplitude dependence. The phase difference is reconverted into an amplitude variation by the use of XOR logic. The position information has a variable duty cycle at twice the filter frequency, and is digitized by an ADC driven by a LP filter and a video buffer.

Two cases should be distinguished:

**Current modulated beam:** The BP filters are tuned to the largest line in the frequency spectrum. Their selectivity (BW) should suppress all spurious frequencies (rejection > 40 dB) but be wide enough to accept the small frequency changes that may occur during an acceleration cycle. The BP filters are not critical elements and the phase shift needs only be matched to within a few percent.

Frequency down conversion<sup>13</sup> : For frequencies above 150 MHz, comparators are less performant and the signal is therefore down converted using heterodyne conversion. The acquisition time is increased by the ratio  $f_{rf}/f_{if}$ .

**Bunch modulated beams** (single or multi bunches): The induced signals charge the BP filter, which in turn will start a free oscillation on its central frequency for a predetermined time. The pulse width should be shorter than the oscillation period ( $W_{(fwhm)} < 1/4 * f_0$ ) to obtain the maximum signal. The bunch spacing should be larger than the damping time of the filter to allow for individual measurements. Acquisition rates up to a few MHz can be achieved, so that turn-by-turn and individual bunch acquisition is feasible. Since the BP filter selectivity is not critical, a single resonator can be employed. However, this results in a longer damping time and therefore requires a longer bunch separation<sup>14</sup>. Several BP filter parameters should be accurately matched in order to preserve the relative phase over several oscillation periods.

**TABLE 5. Amplitude to Phase Normalization.**

Advantages	Limitations
Normalization process	Upper frequency limit < 150 MHz
Reduced number of channels (x2)	Tight phase adjustment
Input dynamic range > 50 dB	[Minimum bunch spacing (> 100 ns)]
~10 dB reduction on the position dependent dynamic due to signal recombination (90° sum)	[Matched pair BP filters (tight tolerances)]
[Dynamic range is independent of the number of bunches]	Hardware; limited technological improvements foreseen
Simultaneous digitization of + and - charges	
Simple & Reliable	

{ Current modulated beams }, [ Bunched beams ]

### 5.5. Amplitude to Time Normalization

This new normalization idea is derived from the “Amplitude to phase” principle where “phase” is replaced by “time” and the applied signal has a single oscillation period. It applies to bunched beams and works in the time domain<sup>15, 16</sup>.

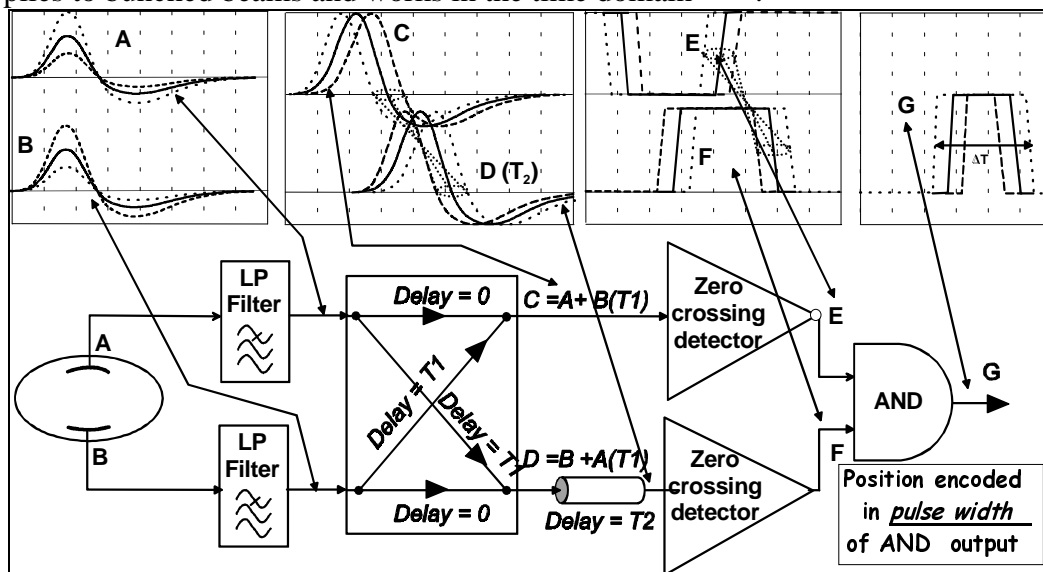


**FIGURE 12.** Block diagram of the amplitude to time processor

The LP filters produce the correct pulse shape. The signals from both electrodes are split in two and one branch is delayed by a time  $T_1$ . The delayed signal of one channel is then added to the direct signal of the other channel, and vice versa. At C, the time of the zero crossing varies according to the signal ratio, up to a maximum of  $T_1$ . At the output D, you have the same signal amplitude but the time variation has opposite sign.

The maximum time difference is therefore  $2 * T_1$ . The delay offset  $T_2$  is required to avoid sign ambiguity and should always be larger than  $T_1$ . The zero crossing is independent of amplitude and is easy to detect using fast comparator circuits. Their outputs drive an AND gate, which generates a pulse with a width proportional to the beam position.

$$\text{Position} \equiv \Delta t = 2 * T_1 * [(A - B) / (A + B)] + T_2$$

By integrating this pulse, the time variation is transformed into an amplitude that can be read by an ADC.

**TABLE 6. Amplitude to Normalization.**

Advantages	Limitations
Fastest normalization process (> 40 MS/s)	Can only be employed with bunched beams
Reduced number of channels (x2)	No Intensity information
Input dynamic > 50 dB	
~10 dB reduction on the position dependent dynamic due to signals recombination	Tight time adjustment
Dynamic is independent of the number of bunches	Propagation delay between comparators
Almost independent of the bunch length	

Remark: A specifically designed monolithic Ga-As chip would allow for a large speed breakthrough.

## 5.6. Digital Receiver <sup>17,18</sup>

The digital receiver is a new approach to the classical heterodyne receiver. This has become possible due to technological improvements in the telecommunication field.

In this new approach, the basic functionality is preserved but implementation is different. In fact, as processing and sampling technologies improve, digital moves from the baseband end (a) towards the pick-up sensor (b). The present situation allows the digital transition to take place just after the IF amplifier.

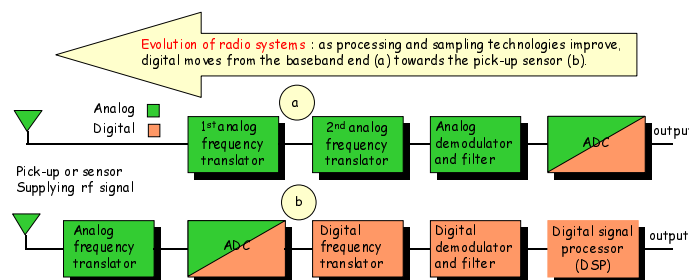


**FIGURE 13.** Block diagram of the evolution of the heterodyne receivers

The RF front-end circuit, while being identical to its analog counterpart, requires a specific design adapted to the digital world. A BP filter selects the useful signal while rejecting the image frequency and a Pin diode attenuator is used to avoid saturation.

A frequency down conversion then transposes the signal to the tens of MHz range (~36 MHz). A surface acoustic wave (SAW) filter with in-band flatness of  $\pm 0.1$  dB and a very linear amplifier with adjustable gain to ensure large dynamic range, are required.

The heart of the digital receiver is the analog to digital converter (ADC). Present performances for low cost ADC are: Input bandwidth (>100MHz); Sampling rate (> 40 MS/s); Resolution (12 bit); Linearity (<.5 LSB). The sampling rate should be chosen to be a few MHz below the IF frequency in such a way that the signal aliases down to the base band.

Once the IF signal is successfully digitized the next step is the data processing. This could be done by one or more digital signal processor (DSP), which implement the remaining functions (IF filtering, demodulation, data reduction). However, the total processing required in such a receiver may add up to several GFLOPS (giga floating operations per second), which is not a straightforward operation. For this reason specialized digital hardware, known as Digital Down-Converter (DDC) has been designed to perform these specific tasks.

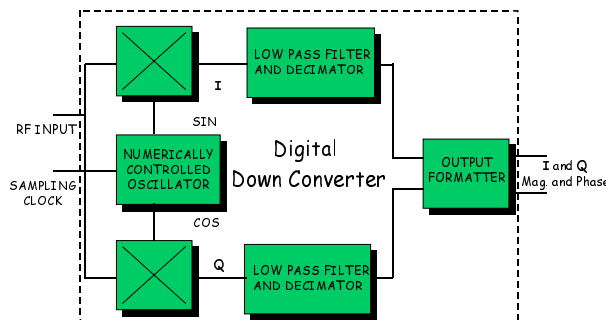


**FIGURE 14.** Block diagram of a digital down converter

The filtering action defines the processor bandwidth, which in turn affects the system resolution. Since the tuning frequency can easily be re-programmed, the same hardware allows for high speed / medium resolution and low speed high-resolution acquisition.

The data reduction (also called decimation) drastically reduces the downstream signal processing requirements.

The data flow is stored in a FIFO memory and accessed by a DSP that applies the correction factors, does additional filtering, calculates the position and the intensity and performs all other post-processing such as FFTs, etc.

Four identical channels are implemented, one for each electrode in the BPM block.

In order to guarantee an identical and stable gain in each channel, a pilot signal at a frequency shifted by -1.5 MHz and at a level of -10 to -20 dB relative to the beam signal is permanently injected via couplers.

By simply changing the tuning frequency of the digital IF filter, one can choose either the beam or the pilot signals. The digitized pilot signal is used to change the gain in the IF amplifier and keep the global four channel gain within the specified tolerance.

In the classical heterodyne receiver, the most critical parameter is the demodulator non-linearity. When using a digital processor, the demodulation action is done

digitally by the DDC, hence suppressing this error. Here it is mainly the ADC that defines the global non-linearity.

Another advantage of the digital receiver concerns the resolution. The signal to noise ratio is improved by the digital filtering and the over-sampling with respect to the base band. This factor corresponds to the square root of the ratio of the digital band-pass filter to the Nyquist bandwidth, expressed in dB.

**TABLE 7. Digital receiver.**

<b>Advantages</b>	<b>Limitations</b>
Programmability	No single shot measurement
Narrow & Wide band processing	No “plug and play” system
Identical gain for all channels due to possible permanent calibration	All problems related to a new inexperienced processing system
Resolution improved by over-sampling techniques	Complex engineering
Large dynamic range	
Excellent linearity (only limited by the ADC)	

## 6. APPLICATION EXAMPLE

The PS and SPS are versatile machines, capable of producing and accepting over 7 different types of beam. The transfer line between the two machines will be equipped with 20 BPMs, spread over 1.5 Km.

The purpose of this example is to choose the most suitable processing system.

### 6.1. Specifications

#### 6.1.1. Beam parameters

**TABLE 8. Beam parameters of the 4 most important cases for the PS to SPS transfer line**

<b>Beam</b>	<b>N° bunches</b>	<b>Spacing</b>	<b>Width</b>	<b>Intensity</b>	<b>Dynamic</b>	<b>Dynamic</b>
<b>Fixed target</b>	<b>2000</b>	<b>5</b>	<b>1.66</b>	<b><math>1 \cdot 10^9</math></b>	<b>30</b>	<b>42</b>
<b>LHC</b>	<b>1 to 84</b>	<b>25</b>	<b>2.1</b>	<b><math>3 \cdot 10^9</math></b>	<b>35</b>	<b>86</b>
<b>Special beam</b>	<b>1, 8, 16</b>	<b>131.2</b>	<b>4.8</b>	<b><math>5 \cdot 10^9</math></b>	<b>20</b>	<b>56</b>
<b>Heavy ions</b>	<b>16</b>	<b>131.2</b>	<b>6.2 / 15</b>	<b><math>2.6 \cdot 10^8</math></b>	<b>10</b>	<b>22</b>
	<b>N</b>	<b>ns</b>	<b>(fwhm) ns</b>	<b>Charge/bunch</b>	<b>(Bunch) dB</b>	<b>(Global) dB</b>

Analysis of the beam parameters (Table 8) reveals the following difficulties:

- A very wide dynamic range (>86 dB), which comprises bunch intensity variation, variable number of bunches and 12 dB of position dynamic range.
- A variable bunch width, of an order of magnitude.
- Bunch spacing from 5 ns to a single bunch.

### 6.1.2. Processing system specifications

The required accuracy and linearity should be contained in 2% of the  $N_a$  for a nominal beam, while resolution and stability versus intensity should be  $< 0.5\%$  of the  $N_a$ .

The PS extraction time is such that beam duty cycle is very low in the transfer line hence limiting the integrated radiation to an acceptable value.

Considering the long distances between the PUs and the electronics racks and taking into account the high frequency signal spectrum, it is advisable to place the processing electronics as near as possible to the PUs.

## 6.2. Pick-up choice

For a beam intensity of a few  $10^8$  p/b, the choice of a coupler offers a better sensitivity compared to buttons. The coupler length should be optimized to obtain a maximum response in the frequency range from a few MHz up to 200 MHz. This corresponds to a coupler length of 50 cm, with an azimuthal coverage of  $24^\circ$  and  $Z_t = 7 \Omega$

## 6.3. Spectral analysis

The variable frequency signal spectral content makes it difficult to choose whether a wide or narrow band processor is most suited to this application.

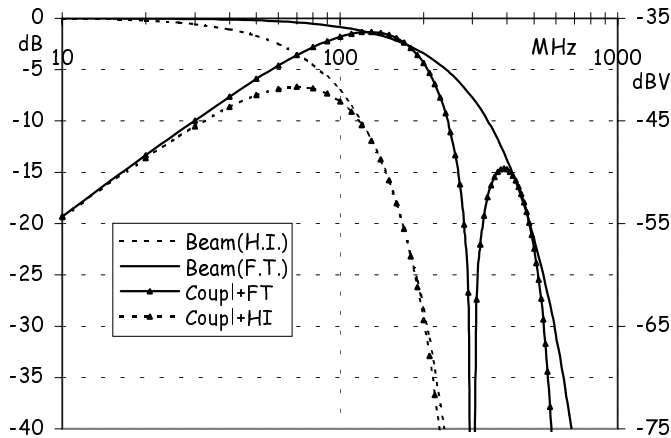


FIGURE 15. Beam and coupler signal frequency spectrum.

A “Spice” simulation of 3 particular cases (fixed target, LHC and single bucket filling) will help for a better understanding.

Let's take a wide-band system with a low-pass frequency of 200 MHz and a band-pass filter centered at 200 MHz, having a 12 MHz bandwidth. For a real narrow-band system ( $\approx 1$  MHz) you can linearly scale down the results of the above-simulated BP filter.

Figures 16, 17 and 18 show the frequency contents and the time domain response.

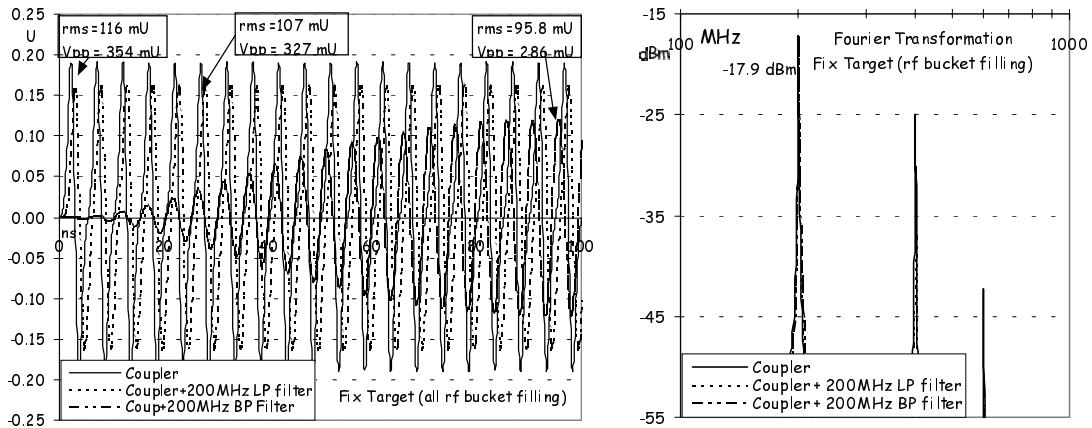


FIGURE 16. Fixed target (all rf buckets filled). Time response and spectral content

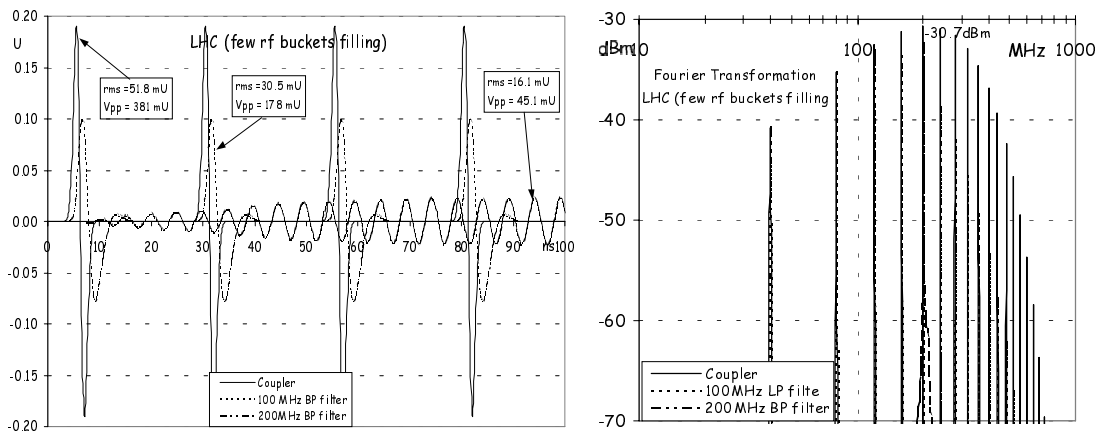


FIGURE 17. LHC (few rf buckets filling). Time response and spectral content

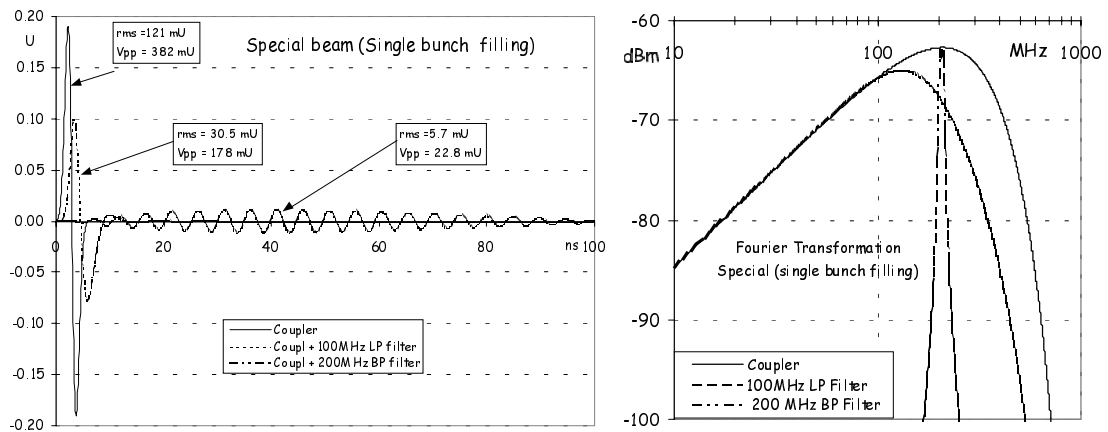


FIGURE 18. Single bunch. Time response and spectral content

## 6.4. Spectral content and time response.

Assuming an identical global input noise of  $1.6 \mu\text{V}/\sqrt{\text{MHz}}$ , the S/N ratio is indicated in the following table.

**TABLE 9. S/N considerations**

Processor	Wide-band	Narrow-band	
Band-width	200	12.0 (1.2)	MHz
Input noise	23.0	5.4 (1.7)	$\mu$ V (rms)
	<b>S / N</b>	<b>S / N</b>	
<b>Fixed Target</b>	76.8 [89.8]	86.4 (96.4)	dB
<b>LHC</b>	75.8 [82.6]	70.2 (80.2)	dB
<b>Single (4.8ns)</b>	67.1 [67.1]	39.8 (29.8)	dB

Values in [] correspond to the possible improvement one can obtain when averaging the collected data in a time interval equivalent to that required by a NB.

It should be noted that NB processing performs better for a limited frequency spectrum (Fixed Target) but as soon as the frequency spectrum becomes larger, WB processing becomes superior.

In the case of a single bunch, NB performance drops dramatically with the bunch length. The reason is that the first part of the bunch excites the filter but after half an oscillation period, the filter polarity changes and the input signal starts annihilating what has already been filled.

### 6.5. Processing system choice

**TABLE 10. Processing system comparison**

Processor type	Remarks	Solution =
<b>MPX heterodyne</b>	MPX, PLL and AGC don't work for single passage.	<b>Unfeasible</b>
<b>NB <math>\Delta / \Sigma</math></b>	200 MHz tune, cannot detect Heavy Ions at 7.6 or one of its harmonics.	<b>Unfeasible</b>
<b>Phase Normalizer</b>	200 MHz discriminator & logic is difficult to realize. Insufficient sensitivity for weak and long bunches.	<b>Unfeasible</b>
<b>Time Normalizer</b>	Not suitable for variable bunch widths. Electronics time jitter is too big relative to the possible time excursions.	<b>Unfeasible</b>
<b>WB <math>\Delta / \Sigma</math></b>	Requires several gain switching and scaling factors. Difficult to calibrate.	<b>Feasible</b>
<b>Digital receiver</b>	Easy switching from 200 down to 198.1 MHz tuning frequency. Adjustable BW. No AGC action, hence larger N° of bits	<b>Feasible</b>
<b>Log-amplifier</b>	Excellent dynamic range. Insensitive to bunch shape & length. Reduced N° of bits. Low cost. <i>Limited linearity</i>	<b>Feasible</b>

The above table collects the main advantages / disadvantages of the various processing systems. Three solutions appear to be feasible but just one offers almost no restrictions.

Since resolution and accuracy are not restrictive parameters for this application, the logarithmic processor is by far superior to all the others systems.

## 7. CONCLUSIONS

Experience has proved that every new machine requires a new approach to the same problem. This offers an excellent opportunity for new ideas.

Several different combinations among the currently available processing systems have still to be explored and this may provide solutions for particular cases.

The telecommunications field has similar needs and is expanding rapidly. Full advantage should be taken of its technological progress and of the reduced prices of components on the consumer market.

My personal feeling for the future is that two processing systems, capable of covering almost all possible applications, will coexist: the Amplitude to Time Normalizer and the Digital Receiver. Both have a bright future.

## 8. ACKNOWLEDGMENTS

I would like to thank Dr. Hermann Schmickler for his encouragement and precious advice for structuring this subject and my most faithful collaborator J.L. Pasquet who has built and tested most of the circuits described here.

## 9. REFERENCES

- 
- 1 A. Hofmann, "Beam diagnostics and applications", BIW 98, pg.3.
  - 2 F. Loyer, K. Scheidt, "Electron beam position monitor : performances considerations", Dipac 93 Proc, pg. 21.
  - 3 J. Matheson "Non-linearity in the response of BPM", same proceeding
  - 4 R. Lorentz, "Cavity beam position monitor", BIW 1998 Stanford CA, AIP Conf Proc. 451, pg 74
  - 5 R. Biscardi, J.W.Bitter, "Switched detector for Beam Position Monitor", Proc. IEEE Particle Accelerator Conference, San Francisco CA (1991) Cat N°89CH2669-0, Vol.3, pp.1154 – 1156.
  - 6 J.A.Hinkson, K.B. Unser, "Precision analog signal processor for BPM in electron storage ring", Dipac 95 Proc, Travemunde (D).
  - 7 M. Le Gras , D.J. Williams, "Trajectory measurement of bunches ejected from the CERN PSB", Dipac 97 Proc., pg.
  - 8 R. Bossart et al. "Synchronous receivers for beam position measurement", IEEE trans. Nucl. Sci. 32, 1899 (1985).
  - 9 R.E. Shafer, G. Swain et ali. "Beam position monitor upgrade for Los Alamos proton storage ring", U.S.PAC Conf. Proc.(1989), page 1562.
  - 10 G.Aiello, M.R.Mills, "Log-ratio technique for beam position monitor systems", BIW92, AIP Conf. Proc. xxx, page 301.
  - 11 R.E. Shafer, "Log-ratio signal processing technique for beam position monitors", BIW92, AIP Conf. Proc. xxx, page 120.
  - 12 G. Vismara SL/BI Note 1998.
  - 13 F.D. Wells, S.P. Jachim, "A technique for improving the accuracy and dynamic range of BPM", PAC Proc. 1989.
  - 14 J. Borer et al. "The second generation and optimized beam orbit measurement system of LEP. Hardware and performance description", 2<sup>nd</sup> DIPAC, Travemunde 1995.
  - 15 G. Vismara et al. "From narrow to wide band normalizer for orbit and trajectory measurements", BIW 98, AIP conference proceeding 451, page 246.
  - 16 D. Cocq " The wide band normalizer – a new circuit to measure transverse bunch position in accelerator and collider", NIM A 416 (1998) I-8.
  - 17 R. Ursic et al. "Digital receiver offer new solutions for beam instrumentation", PAC 1999 Proc., pg. 2253
  - 18 M. Dehler, et al. "BPM system for the swiss light source", Proceedings 1999 PAC, pg. 2087

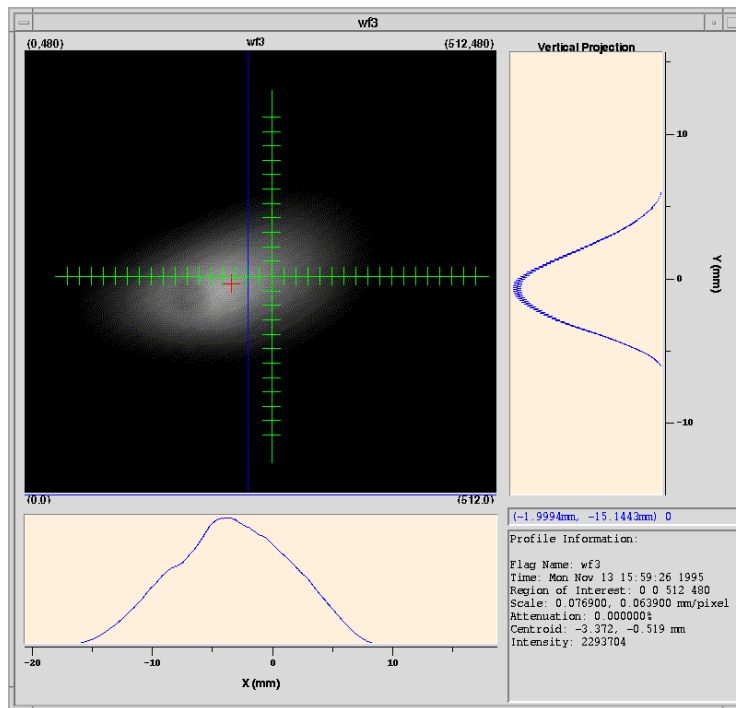
## **Chapter 2**

### **Profile Monitors / Emittance Measurements**

#### **2.1 Exercises and Literature: Profile Measurements**

## Exercises:

### LINACS/Transport Lines Emittance Measurement



by Kay Wittenburg, -DESY-

## LINACS/Transport Lines Emittance Measurement

In a transfer line (or Linac), the beam passes once and the shape of the emittance ellipse at the entry to the line determines its shape at the exit. Exactly the *same* transfer line injected first with one emittance ellipse and then different ellipses has to be accredited with *different*  $\alpha$  and  $\beta$ ,  $\gamma$  functions to describe the cases. Thus  $\alpha$  and  $\beta$ ,  $\gamma$  depend on the input beam and their propagation depends on the structure. Any change in the structure will only change the  $\alpha$  and  $\beta$ ,  $\gamma$  values downstream of that point. ... The input ellipse must be chosen by the designer and should describe the configuration of all the particles in the beam.

1) **Explain ways of measuring the emittance of a charged particle beam in a Linear accelerator or a transport line without knowing the beam optic parameters  $\alpha$ ,  $\beta$ ,  $\gamma$ .**

- a) Exercise L1: Which one is the preferable method for a high energy proton transport line ( $p > 5 \text{ GeV}/c$ )?
- b) Exercise L2: Assuming that the geometry between the measurement stations and the transport matrices  $M$  of the transport line are well defined (including magnetic elements), describe a way to get the emittance using the answer of L1 and the  $\sigma$ -matrix.

$$\sigma = \begin{pmatrix} \sigma_{11} & \sigma_{12} \\ \sigma_{21} & \sigma_{22} \end{pmatrix} = \begin{pmatrix} \sigma_y^2 & \sigma_{yy'} \\ \sigma_{yy'} & \sigma_{y'}^2 \end{pmatrix} = \epsilon_{rms} \begin{pmatrix} \beta & -\alpha \\ -\alpha & \gamma \end{pmatrix} = \sigma \text{ matrix}$$

Write down the equation how the beam width  $\sigma_y$  is transferred from  $s_0$  to the next location  $s_1$ .

- c) Exercise L3: In a transport line for  $p = 7.5 \text{ GeV}/c$  protons are two measurement stations. The first is located exactly in the waist of the beam and shows a beam width of  $\sigma_y = 3 \text{ mm}$ , the second at a distance of  $s = 10 \text{ m}$  shows a width of  $\sigma_y = 9 \text{ mm}$ . Assuming no optical elements in this part, calculate the emittance and the normalized emittance of the beam.

Additional exercise: Calculate  $\beta(s=0 \text{ and } s=10\text{m})$

What is the influence on the emittance  $\epsilon$  assuming at  $s = 10\text{m}$  this b, a dispersion of  $D = 1 \text{ m}$  and a momentum spread of  $\Delta p/p = 10^{-3}$ ?

## References

Ref. 1: S.Y. Lee, Accelerator Physics, World Scientific, pp 54-55 is attached.

Ref. 2: Emittance Measurements at the Bates Linac, *K.D. Jacobs, J.B. Flanz, T. Russ*  
[http://accelconf.web.cern.ch/accelconf/p89/PDF/PAC1989\\_1529.PDF](http://accelconf.web.cern.ch/accelconf/p89/PDF/PAC1989_1529.PDF), is attached.

Ref. 3: Basic accelerator course, like Schmüser and Rossbach in previous CAS CERN  
94-01 v 1; <http://doc.cern.ch/cgi-bin/tiff2pdf?/archive/cernrep/1994/94-01/p17.tif>.

Ref. 4: Beam-line instruments/ **Raich, U** ; *In: Joint US-CERN-Japan-Russia Particle Accelerators School on Beam Measurement, Montreux, Switzerland, 11-20 May 1998*  
- World Sci., Singapore, 1999. - pp.263-276

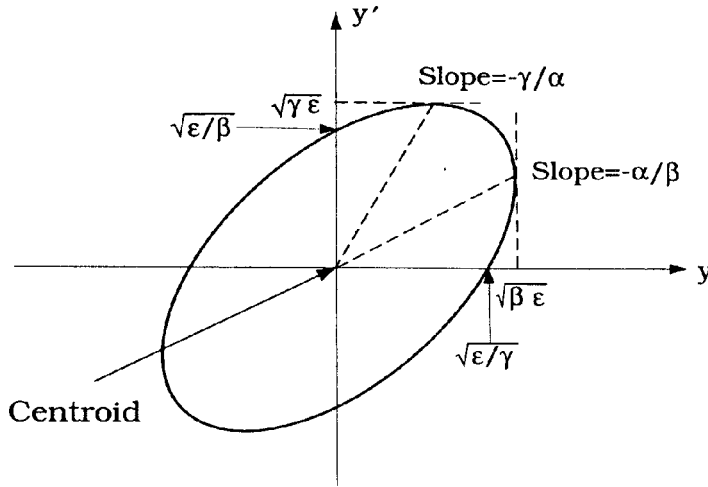


Figure 2.8: The Courant–Snyder invariant ellipse. The area enclosed by the ellipse is equal to  $\pi\epsilon$ , where  $\epsilon$  is twice the betatron action;  $\alpha, \beta$  and  $\gamma$  are betatron amplitude functions.

### A. The emittance of a beam

A beam is usually composed of particles distributed in the phase space. Depending on the initial beam preparation, we approximate a realistic beam distribution function by some simple analytic formula. Neglecting dissipation and diffusion processes, each particle in the distribution function has its invariant Courant–Snyder ellipse.

Given a normalized distribution function  $\rho(y, y')$  with  $\int \rho(y, y') dy dy' = 1$ , the moments of the beam distribution are

$$\langle y \rangle = \int y \rho(y, y') dy dy', \quad \langle y' \rangle = \int y' \rho(y, y') dy dy', \quad (2.94)$$

$$\sigma_y^2 = \int (y - \langle y \rangle)^2 \rho(y, y') dy dy', \quad \sigma_{y'}^2 = \int (y' - \langle y' \rangle)^2 \rho(y, y') dy dy', \quad (2.95)$$

$$\sigma_{yy'} = \int (y - \langle y \rangle)(y' - \langle y' \rangle) \rho(y, y') dy dy' = r \sigma_y \sigma_{y'}, \quad (2.96)$$

where  $\sigma_y$  and  $\sigma_{y'}$  are the rms beam widths,  $\sigma_{yy'}$  is the correlation, and  $r$  is the correlation coefficient. The rms beam emittance is then defined as

$$\epsilon_{\text{rms}} = \sqrt{\sigma_y^2 \sigma_{y'}^2 - \sigma_{yy'}^2} = \sigma_y \sigma_{y'} \sqrt{1 - r^2}. \quad (2.97)$$

If the accelerator is composed of linear elements such as dipoles and quadrupoles, the emittance defined in Eq. (2.97) is invariant. The rms emittance is equal to the phase-space area enclosed by the Courant–Snyder ellipse of the rms particle (see Exercise 2.2.16).

Although incorrect, the term “emittance” is often loosely used as twice the action variable of betatron oscillations. The betatron oscillations of “a particle” with an “emittance”  $\epsilon$  is

$$y(s) = \sqrt{\frac{\beta\epsilon}{\pi}} \cos[\nu\phi(s) + \delta]. \quad (2.98)$$

Figure 2.8 shows a Courant–Snyder invariant ellipse for a given emittance of a beam. For a beam with rms emittance  $\epsilon$ , the rms beam width is  $\sqrt{\beta(s)}\epsilon$ , and the beam rms divergence  $y'$  is  $\sqrt{\gamma(s)}\epsilon$ . Since  $\gamma = (1 + \alpha^2)/\beta$ , the transverse beam divergence is smaller at a location with a large  $\beta(s)$  value, i.e. all particles travel in parallel paths. In accelerator design, a proper  $\beta(s)$  value is therefore important for achieving many desirable properties.

### B. The $\sigma$ -matrix

The  $\sigma$ -matrix of a beam distribution is defined as

$$\sigma = \begin{pmatrix} \sigma_{11} & \sigma_{12} \\ \sigma_{12} & \sigma_{22} \end{pmatrix} = \begin{pmatrix} \sigma_y^2 & \sigma_{yy'} \\ \sigma_{yy'} & \sigma_{y'}^2 \end{pmatrix} = \langle (\mathbf{y} - \langle \mathbf{y} \rangle)(\mathbf{y} - \langle \mathbf{y} \rangle)^\dagger \rangle, \quad (2.99)$$

where  $\mathbf{y}$  is the betatron state matrix of Eq. (2.36),  $\mathbf{y}^\dagger = (y, y')$  is the transpose of  $\mathbf{y}$ , and  $\langle \mathbf{y} \rangle$  is the first moment. The rms emittance becomes (see also Exercise 2.2.14)

$$\epsilon_{\text{rms}} = \sqrt{\det \sigma} = \sqrt{\sigma_{11}\sigma_{22} - \sigma_{12}^2}. \quad (2.97)$$

Using the transfer matrix, we obtain

$$\sigma_2 = M_{21}\sigma_1 M_{21}^\dagger. \quad (2.100)$$

It is easy to verify that  $\mathbf{y}^\dagger \sigma^{-1} \mathbf{y}$  is invariant under linear betatron motion, thus the beam distribution is

$$\rho(y, y') = \rho(\mathbf{y}^\dagger \sigma^{-1} \mathbf{y}). \quad (2.101)$$

### C. Emittance measurement

The emittance can be obtained by measuring the  $\sigma$ -matrix. The beam profile of protons and ions is usually measured by using wire scanners or ionization profile monitors. Synchrotron light monitors are commonly used in electron storage rings. More recently, laser light has been used to measure electron beam size in the sub-micron range. Using the rms beam size and Courant-Snyder parameters, we can deduce the emittance of the beam.

## EMITTANCE MEASUREMENTS AT THE BATES LINAC\*

K. D. Jacobs, J. B. Flanz, and T. Russ.  
MIT Bates Linear Accelerator Center  
P.O. Box 846, Middleton, MA 01949

### Abstract

An emittance measuring system has been installed at the Bates Linear Accelerator Center. The system consists of three wire scanners used to measure the electron beam profile, plus a microcomputer for data acquisition and processing. The scanners are located in a drift space on a beam line. Each scanner measures the horizontal and vertical beam size with a possible resolution of 25  $\mu\text{m}$ . The horizontal and vertical beam phase spaces can then be determined. Results of measurements are presented here. Calculations relating the theoretical accuracy of the emittance measurements with the distance separating the scanners, and the location and size of the beam waist, are also presented.

Another technique for measuring emittance has also been employed. This technique involves using a wire scanner to measure the beam size at a fixed location, as a function of the strength of an upstream quadrupole.<sup>1</sup>

### Introduction

The transverse phase space of a particle beam can be characterized by three parameters. For example, knowing the extent of the beam phase ellipse in distance and in angle, plus the orientation of the ellipse, will fully determine the phase space. An equivalent set of parameters is the location of a beam waist, the waist radius, and the maximum particle divergence at the waist. Various techniques can be used to measure these parameters. Measuring the beam size at three different locations, with fixed machine optics, will determine the phase space,<sup>2</sup> as will measuring the beam size at one location for three different optics configurations.

In this paper, we describe the technique for measuring the beam phase space by using the measurements of the beam sizes at three different locations. Calculations regarding the precision of this technique are presented, as are results of experimental measurements of the beam phase space at the Bates Linac.

### Measurement Technique

Consider a beam in a field free region (drift space). If  $x_0$  is the horizontal beam size at a waist located at axial position  $z_0$ , and  $\theta_0$  is the maximum horizontal divergence angle any particle makes with the beam axis at the waist, then the beam size  $x$  at location  $z$  is given by

$$x^2 = x_0^2 + (z - z_0)^2 \theta_0^2 \quad (1)$$

To measure the beam phase space, we measure the beam size using three profile monitors, equally spaced by the distance  $L$ . Defining the origin to be at the center profile monitor, so that  $z_1 = -L$ ,  $z_2 = 0$ , and  $z_3 = +L$ , the beam sizes  $x_i$  at the monitors are given by

$$\begin{aligned} x_1^2 &= x_0^2 + (L + z_0)^2 \theta_0^2 \\ x_2^2 &= x_0^2 + z_0^2 \theta_0^2 \\ x_3^2 &= x_0^2 + (L - z_0)^2 \theta_0^2 \end{aligned} \quad (2)$$

Thus, knowing the beam sizes  $x_i$  and the profile monitor separation  $L$ , we can calculate the waist size

$$x_0 = \left\{ x_2^2 - \frac{1}{8} \left( \frac{x_1^2 - x_3^2}{x_1^2 - 2x_2^2 + x_3^2} \right) \right\}^{1/2}, \quad (3)$$

the divergence at the waist

$$\theta_0 = \frac{1}{\sqrt{2}L} (x_1^2 - 2x_2^2 + x_3^2)^{1/2}, \quad (4)$$

and the location of the waist

$$z_0 = \frac{L}{2} \left( \frac{x_1^2 - x_3^2}{x_1^2 - 2x_2^2 + x_3^2} \right). \quad (5)$$

The particle beam emittance  $\epsilon$  is given by the product  $x_0 \theta_0$ ,

$$\epsilon = \frac{1}{4L} [8x_2^2(x_1^2 - 2x_2^2 + x_3^2) - (x_1^2 - x_3^2)^2]^{1/2}. \quad (6)$$

A similar set of calculations holds in the vertical dimension.

These calculations are for the case of equally spaced profile monitors in a drift space. They can be extended to include unequal monitor spacing and the presence of intervening optical components.

### Measurement Error Analysis

In order to make meaningful emittance measurements using beam profile monitors of realistic resolution, it may be necessary to set up the beam and the profile monitors in a particular manner. The precision of the measurements depends on  $L$ ,  $x_0$ , and  $z_0$ . (For a beam of fixed emittance,  $\theta_0 \propto x_0^{-1}$ , and is not an independent variable.) In general, the precision of an emittance measurement increases with increasing  $L$ , and when the waist is located closer to the center profile monitor.

To quantitatively determine the uncertainty in the phase space measurements, standard propagation of error calculations have been made. In making these calculations, it has been assumed that the uncertainty in the measured beam sizes  $\sigma_{x_i}$  dominate, and that  $L$  is known to greater precision. The results are

$$\begin{aligned} \frac{\sigma_{x_0}}{x_0} &= \left\{ \sigma_{x_1}^2 x_1^2 (x_1^2 - x_3^2)^2 (x_1^2 - 4x_2^2 + 3x_3^2)^2 \right. \\ &\quad + 4\sigma_{x_2}^2 x_2^2 [4(x_1^2 - 2x_2^2 + x_3^2)^2 - (x_1^2 - x_3^2)^2]^2 \\ &\quad \left. + \sigma_{x_3}^2 x_3^2 (x_1^2 - x_3^2)^2 (3x_1^2 - 4x_2^2 + x_3^2)^2 \right\}^{1/2} \\ &\quad / 4\sqrt{2}x_0^2 (x_1^2 - 2x_2^2 + x_3^2)^2, \end{aligned} \quad (7)$$

$$\frac{\sigma_{\theta_0}}{\theta_0} = \sqrt{2} \frac{(\sigma_{x_1}^2 x_1^2 + 4\sigma_{x_2}^2 x_2^2 + \sigma_{x_3}^2 x_3^2)^{1/2}}{(x_1^2 - 2x_2^2 + x_3^2)}, \quad (8)$$

$$\begin{aligned} \sigma_{z_0} &= \frac{2L}{(x_1^2 - 2x_2^2 + x_3^2)^2} [\sigma_{x_1}^2 x_1^2 (x_2^2 - x_3^2)^2 \\ &\quad + \sigma_{x_2}^2 x_2^2 (x_1^2 - x_3^2)^2 + \sigma_{x_3}^2 x_3^2 (x_1^2 - x_2^2)^2]^{1/2}, \end{aligned} \quad (9)$$

\* Work supported by the U.S. Department of Energy

and

$$\frac{\sigma_\epsilon}{\epsilon} = \frac{4}{\sqrt{2}[8x_2^2(x_1^2 - 2x_2^2 + x_3^2) - (x_1^2 - x_3^2)^2]} \times [\sigma_{x_1}^2 x_1^2 (x_1^2 - 4x_2^2 - x_3^2)^2 + 16\sigma_{x_2}^2 x_2^2 (x_1^2 - 4x_2^2 + x_3^2)^2 + \sigma_{x_3}^2 x_3^2 (x_1^2 + 4x_2^2 - x_3^2)^2]^{1/2}. \quad (10)$$

Using Eq. (10), the beam configuration for making optimum emittance measurements can be found. For example, the effect of moving the location of the beam waist is shown in Fig. 1, for fixed monitor separation and different waist sizes.

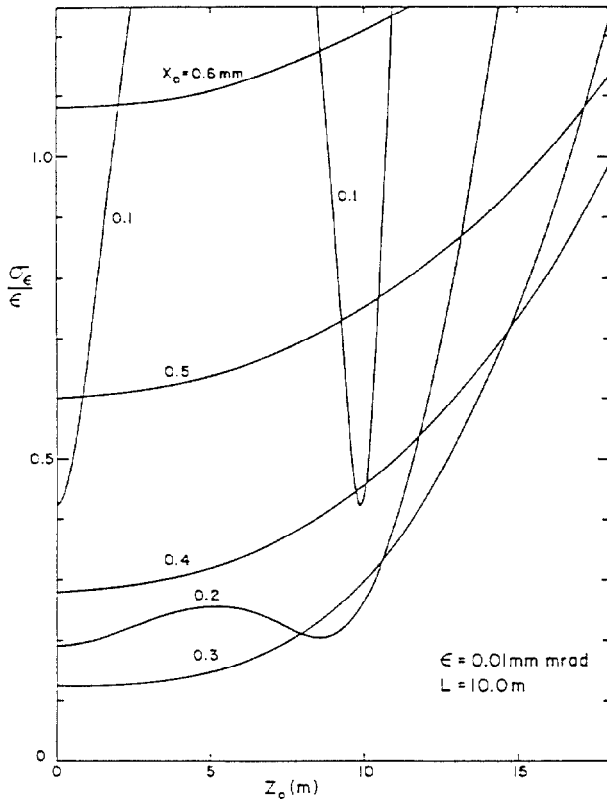


Fig. 1: Precision of emittance measurement  $\sigma_\epsilon$  vs. location of waist  $z_0$ , for different waist sizes  $x_0$ . Here  $L = 10$  m and  $\epsilon = 0.01$  mm · mrad. The precision of the beam width at each profile monitor is taken to be  $\sigma_{x_i} = 25$   $\mu$ m.

As can be seen, it is always best to have the waist near the center monitor ( $z = 0$ ), although for some  $x_0$  this requirement is not as critical. (When  $z_0 \approx 0$ , the precision of  $x_0$  is improved, which leads to a decrease in  $\sigma_\epsilon$ .) Figure 1 also indicates that for fixed  $z_0$ , there is a dependency of  $\sigma_\epsilon$  on  $x_0$ . This is shown explicitly in Fig. 2, which plots  $\sigma_\epsilon$  as a function of  $x_0$  for  $z_0 = 0$ , and several different  $L$ . The optimum value of  $x_0$  as a function of  $L$  is shown in Fig. 3. Finally, with  $x_0$  at its optimum value and  $z_0 = 0$ , the obtainable  $\sigma_\epsilon$  is shown as a function of  $L$  in Fig. 4. Here we see that the obtainable fractional precision  $\sigma_\epsilon/\epsilon$  scales as  $L^{-1/2}$ .

### Experimental Results

Emittance measurements at Bates, based on the above analysis, are made with an automatic emittance measuring system. The beam profiles are determined using high resolution wire scanners.<sup>3</sup> Data from the scanners are digitized, acquired,

and processed by the Linac Control System. The processing is done on a MicroVAX by programs written in a high level language, and includes fitting a Gaussian to the profile data to determine the beam size. Once the size is known at each scanner, the emittance, beam waist size and location, and beam divergence are calculated, along with estimates of their uncertainties.

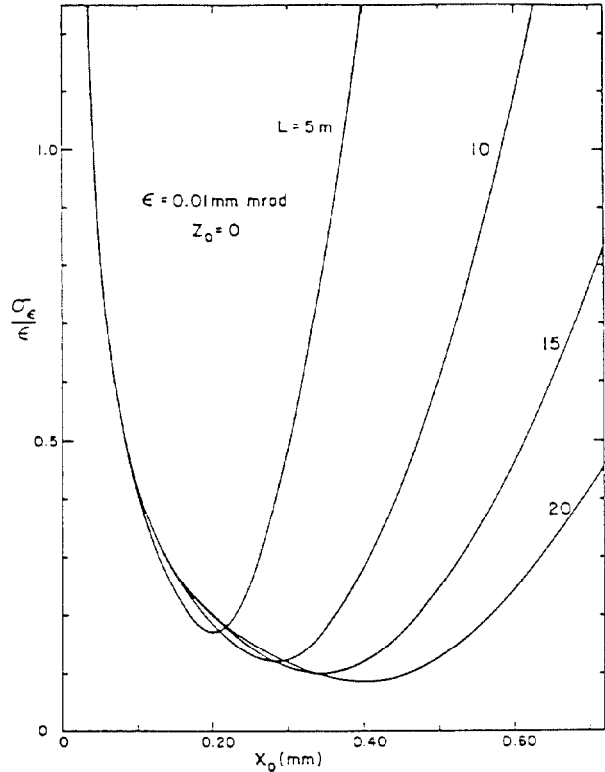


Fig. 2: Precision of emittance measurement  $\sigma_\epsilon$  vs. waist size  $x_0$ , for different profile monitor separations  $L$ . The waist is located at the center monitor ( $z_0 = 0$ ), and  $\epsilon = 0.01$  mm · mrad. The precision of the beam width at each profile monitor is taken to be  $\sigma_{x_i} = 25$   $\mu$ m.

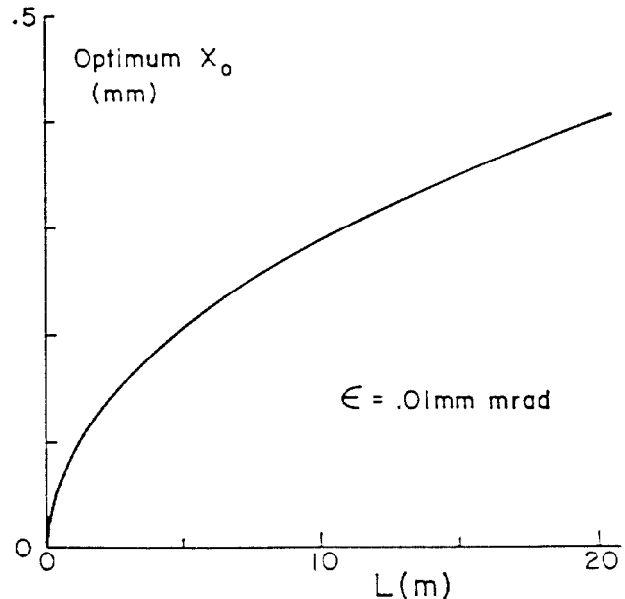


Fig. 3: Waist size  $x_0$  for optimum emittance measurement vs. profile monitor separation  $L$ , for  $\epsilon = 0.01$  mm · mrad.

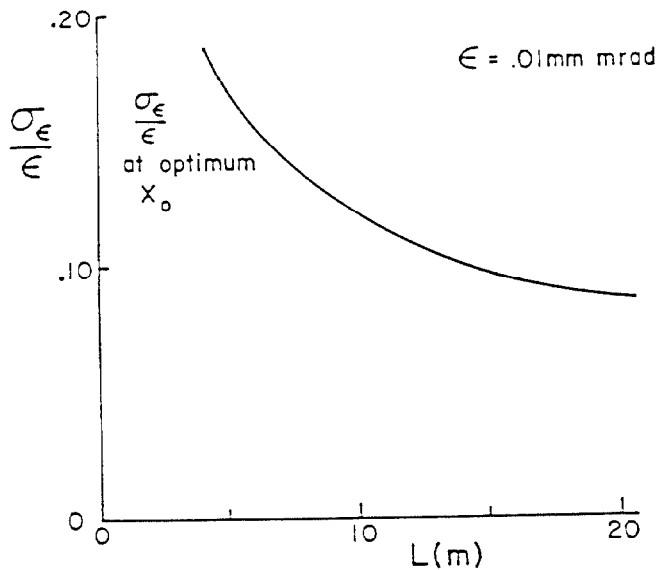


Fig. 4: Precision of emittance measurement  $\sigma_\epsilon$  at optimum  $x_0$  and  $z_0$  vs. monitor separation  $L$ , for  $\epsilon = 0.01$  mm · mrad. The precision of the beam width at each profile monitor is taken to be  $\sigma_{z_i} = 25 \mu\text{m}$ .

All data acquired and calculated are displayed on the MicroVAX workstation. These include plots of the raw data from the wire scanners, along with the fitted profiles. Finally, the beam phase space ellipse at the center scanner is calculated and displayed. Figure 5 shows a sample display. The time needed to acquire a complete set of data depends primarily on the speed of the wire scanners, with the data analysis taking much less time. The scanner speed is a function of several parameters such as the beam repetition rate and the range of scanner motion. Under typical conditions, an emittance measurement is completed in less than one minute.

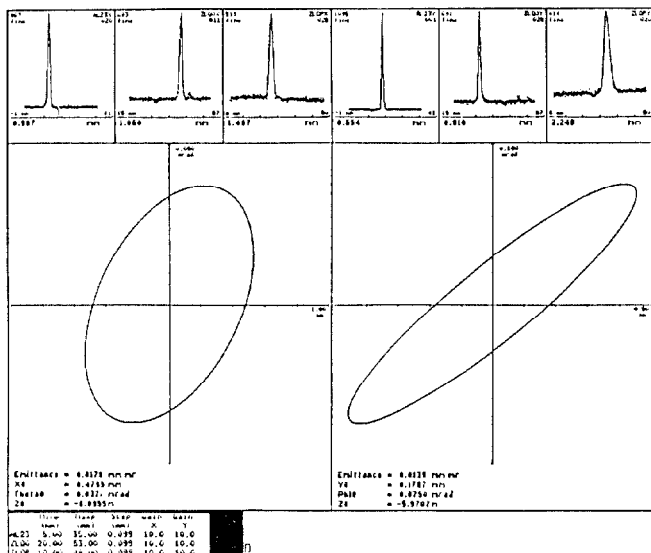


Fig. 5: Sample emittance measuring system display. The horizontal and vertical data are shown on the left and right halves, respectively. The small boxes at the top show beam profile data. The larger boxes show the calculated beam phase space ellipses.

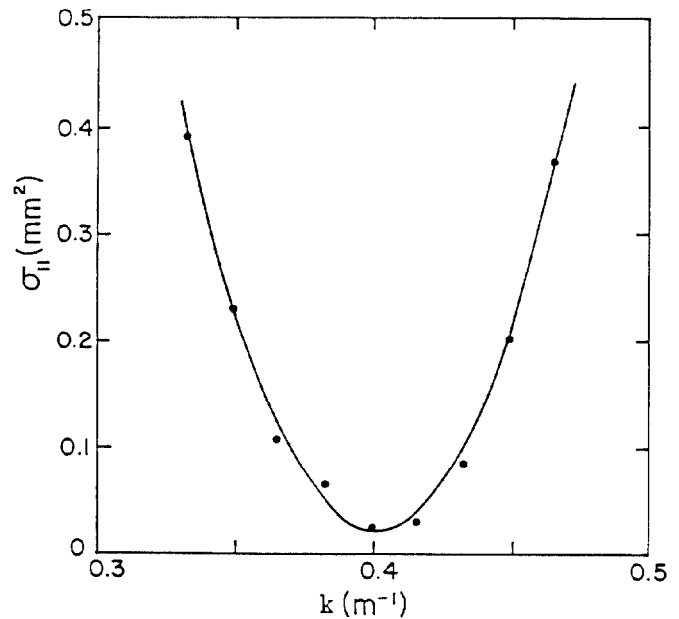


Fig. 6: Square of the horizontal beam size  $\sigma_{11}$  vs. strength  $k$  of a quadrupole singlet 8.03 m upstream from the measurement point. The points are experimental data, and the curve is the best fit parabola.

Preliminary results have been obtained with this system. The three wire scanners are located in a drift space where the beam emerges from the linac. The measured value of the horizontal emittance is  $0.04$  mm · mrad at a beam energy of 175 MeV, and  $0.02$  mm · mrad at 250 MeV. This is in good agreement with the expected value of  $10/\gamma$  mm · mrad. In addition, varying the strength of a quadrupole upstream from the emittance measuring system produces the expected rotation of the measured phase space ellipse. Similar results have been obtained in the vertical dimension. The uncertainties in these measurements, both statistical and systematic, are presently under study.

The emittance of the beam has also been measured using a different method.<sup>1</sup> In this technique, the size of the beam is measured at one location, as a function of the strength of an upstream quadrupole. The square of the beam size should have a parabolic dependence on quadrupole strength. Results of such a measurement in the horizontal dimension are shown in Fig. 6. From the parameters of the parabola fit to the data, shown in Fig. 6, the emittance is determined to be  $0.02$  mm · mrad at 250 MeV, in agreement with the emittance measured using the three scanner technique.

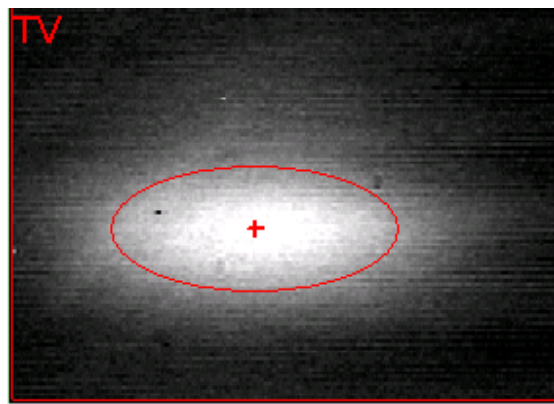
### Summary

Emittance measurements have been made at Bates using an automatic emittance measuring system, consisting of three beam profile monitors equally spaced in a drift region. The results obtained are in good agreement with the values expected at Bates. Measurement of the emittance by an independent technique has yielded similar results.

### References

- [1] M. C. Ross, *et al.*, SLAC-PUB-4278, March 1987.
- [2] R. I. Cutler, J. Owen, and J. Whittaker, Proc. of the 1987 IEEE Particle Accelerator Conference, p. 625, March 1987.
- [3] K. D. Jacobs, *et al.*, "The Beam Profile Measuring System at the Bates Linac," these proceedings.

# Synchrotron light profile monitor



## Exercises

by Kay Wittenburg, -DESY-

### Synchrotron light profile monitor

In electron accelerators the effect of synchrotron radiation (SR) can be used for beam size measurements. In this course we will focus on profile determination, but SR can also be used for bunch length measurements with e.g. streak cameras with a resolution of < 1 ps.

From classical electrodynamics the radiated power is given for a momentum change  $dp/dt$  and a particle with mass  $m_0$  and charge  $e$ :

$$P_{SR} = \frac{e^2 c}{6\pi\epsilon_0 (m_0 c^2)} \left[ \frac{dp}{dt} \right]^2$$

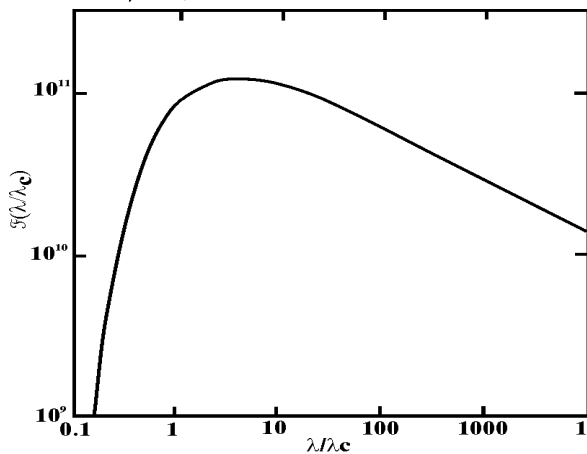
For linear accelerators  $dp/dt = dW/dx$ . For typical values of  $dW/dx = 10 - 20$  MeV/m the SR is negligible. In circular machines an acceleration perpendicular to the velocity exists mainly in the dipole magnets (field  $B$ ) with a bending radius  $\rho = \beta\gamma m_0 c / (eB)$ . The total power of  $N$  circulating particles with  $\gamma = E/m_0 c^2$  is then

$$P_{tot} = \frac{e^2 c \gamma^4}{6\pi\epsilon_0 \rho^2} N$$

This expression is also valid for a ring having all magnets of the same strength and field-free sections in between.

The critical wavelength  $\lambda_c$  divides the Spectrum of SR in two parts of equal power:

$$\lambda_c = \frac{4\pi\rho}{3\gamma^3}$$



flux integrated over all  $\psi$  (Krisinsky *et al.* 1983).

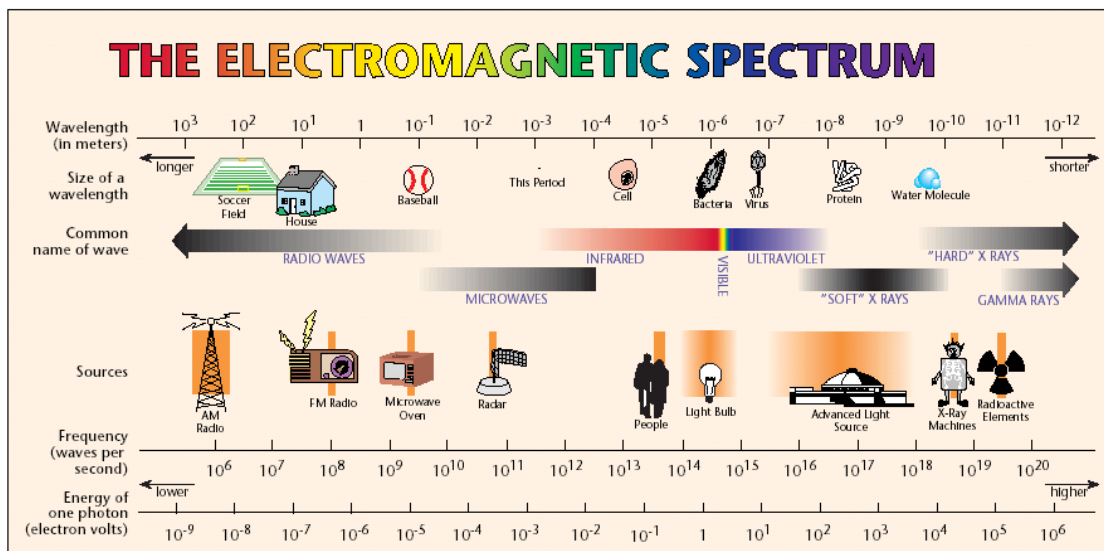
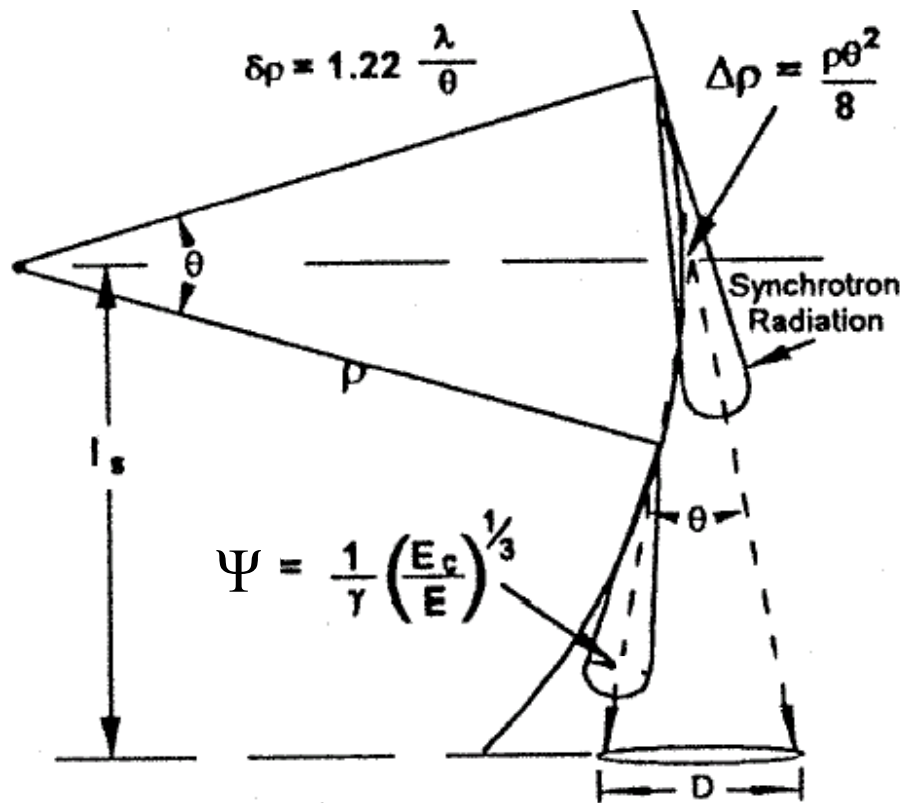
The opening angle  $\Psi$  of the SR (1/2 of cone!) for  $\lambda \gg \lambda_c$ :

$$\Psi = \frac{1}{\gamma} \left( \frac{\lambda}{\lambda_c} \right)^{1/3} = \left( \frac{3\lambda}{4\pi\rho} \right)^{1/3}$$

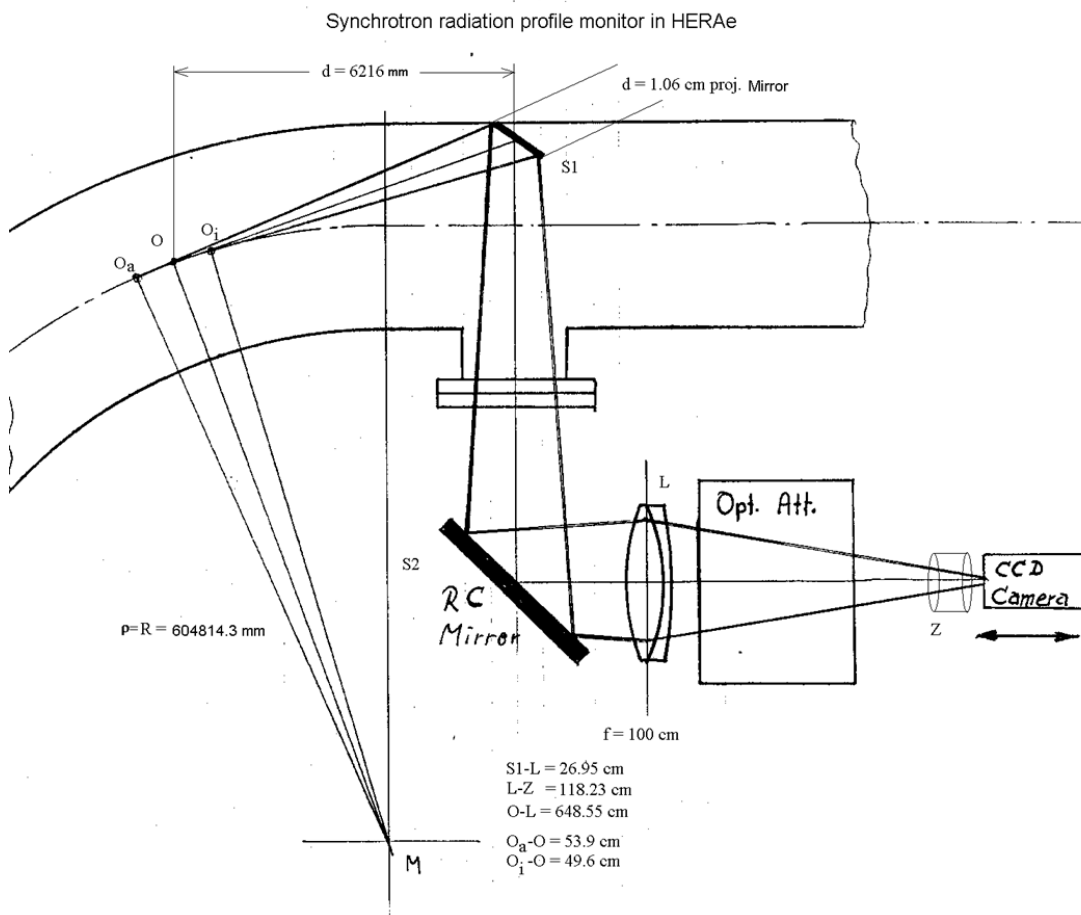
Path length  $s$ :

$$s = \rho\theta$$

$\rho$  = Bending radius of Dipole



## An Example: HERAe



$$R = \rho = 604814.3 \text{ mm}$$

$$G = O-L = 6485.5 \text{ mm}$$

$$B = L-Z = 1182.3 \text{ mm}$$

$$O-S1 = 6216 \text{ mm}$$

$$L = O_a-O_i = 1035 \text{ mm}$$

$$\text{opening angle (horizontal): } \tan\theta/2 = d/2/6216 \Rightarrow \theta/2 = \text{arc tan } d/2/6216 = \underline{0.85 \text{ mrad}}$$

$$\text{opening angle (vertikal): } \Psi(\lambda) = 1/\gamma (\lambda/\lambda_c)^{1/3}$$

with

$$\gamma = E/m_0c^2 = E [\text{MeV}]/0.511 = 23483 \text{ at } 12 \text{ GeV and } 52838 \text{ at } 27 \text{ GeV}$$

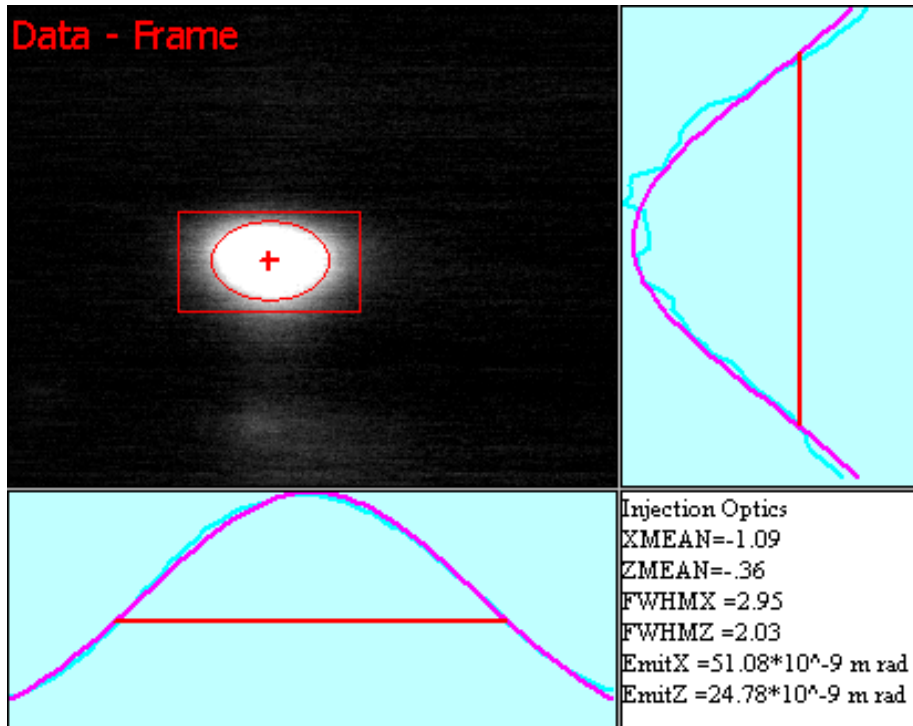
and

$$\lambda_c = \frac{4\pi\rho}{3\gamma^3} = 0.017 \text{ nm} \ll \lambda \approx 500 \text{ nm}$$

**Exercise SR1: Which problems with the setup can be expected?:**

**Exercise SR2: What limits the spatial resolution?**

Beam width  $\sigma_{\text{beam}} = (\sigma_{\text{fit\_measured}}^2 - \sigma_{\text{cor}}^2)^{1/2}$



**Exercise SR3: Discuss possible improvements**

## References attached

### **A Review of Optical Diagnostics Techniques for Beam Profile Measurements.**

J A Clarke

EPAC94

[http://accelconf.web.cern.ch/AccelConf/e94/PDF/EPAC1994\\_1643.PDF](http://accelconf.web.cern.ch/AccelConf/e94/PDF/EPAC1994_1643.PDF)

### **Further readings:**

**Characteristics of synchrotron radiation/ [Hofmann, A](#) ;**

*In:* CAS - CERN Accelerator School : Synchrotron Radiation and Free Electron Lasers, Grenoble, France, 22 - 27 Apr 1996 - CERN, Geneva, 1998. [[CERN-98-04](#)]

<http://doc.cern.ch/archive/cernrep//1998/98-04/p303.pdf>

### **DIAGNOSTICS FOR ULTRA-LOW EMITTANCE BEAMS\***

J.W. Flanagan, KEK, Tsukuba, 305-0801 Japan

IPAC2011

<http://accelconf.web.cern.ch/AccelConf/IPAC2011/papers/weyb01.pdf>

### **Optical resolution of beam cross-section measurements by means of synchrotron radiation,**

A. Hofmann, F. Meot, Nucl. Instr. Meth. 203 (1982) 483

### **Accurate and Efficient Computation of Synchrotron Radiation in the Near Field Region**

O. Chubar, P. Elleaume, ESRF, Grenoble, France

Proc. EPAC 1998 Stockholm, Sweden

<http://accelconf.web.cern.ch/AccelConf/e98/PAPERS/THP01G.PDF>

### **Synchrotron Radiation Profile Monitor for HERA Positron Beam**

G. Kube, Rainer Fischer, Kay Wittenburg - Deutsches Elektronen Synchrotron DESY

[11th Beam Instrumentation Workshop](#), May 3-6 2004, Knoxville, Tennessee, USA

[http://adweb.desy.de/mdi/downloads/Kube\\_BIW04.pdf](http://adweb.desy.de/mdi/downloads/Kube_BIW04.pdf)

### **Detailed Resolution Studies of the Synchrotron Radiation Profile Monitor for HERAe**

Gero Kube, Rainer Fischer, Kay Wittenburg (DESY, Hamburg)

Proc. DIPAC 2005 Lyon

<http://accelconf.web.cern.ch/AccelConf/d05/PAPERS/POT025.PDF>

### **Interferometer:**

**SPATIAL COHERENCY OF THE SYNCHROTRON RADIATION AT THE  
VISIBLE LIGHT REGION AND ITS APPLICATION FOR THE ELECTRON  
BEAM PROFILE MEASUREMENT.**

By T. Mitsuhashi (KEK, Tsukuba). KEK-PREPRINT-97-56, May 1997. 4pp. Talk given at 17th IEEE Particle Accelerator Conference (PAC 97): Accelerator Science, Technology and Applications, Vancouver, Canada, 12-16 May 1997.

<http://accelconf.web.cern.ch/accelconf/pac97/papers/pdf/3V016.PDF>

**Intensity Interferometer and its application to Beam Diagnostics,**

Elfim Gluskin, ANL,

PAC 1991 San Francisco

[http://accelconf.web.cern.ch/AccelConf/p91/PDF/PAC1991\\_1169.PDF](http://accelconf.web.cern.ch/AccelConf/p91/PDF/PAC1991_1169.PDF)

**MEASUREMENT OF SMALL TRANSVERSE BEAM SIZE USING  
INTERFEROMETRY**

T. Mitsuhashi

High Energy Accelerator Research Organisation, Oho, Tsukuba, Ibaraki, 305-0801 Japan  
*DIPAC 2001 Proceedings - ESRF, Grenoble*

<http://accelconf.web.cern.ch/AccelConf/d01/papers/IT06.pdf>

[Recent Progress in SR Interferometer](#)

Authors: T.M. Mitsuhashi [KEK, Ibaraki, Japan]

IBIC2012

<http://accelconf.web.cern.ch/AccelConf/IBIC2012/papers/weic02.pdf>

# A Review of Optical Diagnostics Techniques for Beam Profile Measurements.

J A Clarke

DRAL Daresbury Laboratory, Daresbury, Warrington WA4 4AD, UK

## Abstract

The measurement of beam profiles using optical detectors is widespread. This paper reviews the various optical techniques employed in the community and points out the advantages and disadvantages for each one, illustrated by practical examples including experience with systems at the Daresbury SRS. Fundamental imaging limitations will be discussed together with calibration methods.

## 1. INTRODUCTION

In every particle accelerator the beam profile is an important parameter. Many methods exist for determining the beam profile, including several destructive techniques. This paper deals only with methods which rely on emitted visible synchrotron radiation from bending magnets as the diagnostic means. A review of the imaging resolution is given, followed by a discussion of optical detectors in use in the accelerator community. Possible calibration methods are also highlighted.

## 2. IMAGING RESOLUTION

The resolution of profile measurements by synchrotron radiation (SR) is strictly limited by fundamental effects. It is important that these effects are minimised so that the best resolution is obtained for the profile measurement. The horizontal and vertical cases are not the same; they are dealt with separately below.

### 2.1 Horizontal Case

#### 2.1.1 Chromatic Error

In precise optical imaging of SR it is necessary to monochromate the light. This is most easily achieved with a bandpass filter. Typically a filter with a 500 nm centre wavelength and 30 nm bandwidth is used. However, as will be shown later, shorter wavelengths will improve the resolution.

#### 2.1.2 Depth of Field Error

By its very nature the electron beam is a long source of light. This means that the imaging of the SR will produce a significant depth of field error, dependent upon the acceptance angle. For the simple case, illustrated in figure 1, the depth of field error is given by:

$$df = \frac{L}{2}\theta \quad (1)$$

where L is the length of the source and  $\theta$  is the half-acceptance angle. Note that L is given by:

$$L = 2R(\theta + \theta_{SR}) \quad (2)$$

where R is the electron orbit radius and  $\theta_{SR}$ , the natural opening angle of the photon beam, is given by:

$$\theta_{SR} = \frac{3\lambda}{4\pi R}^{1/3} \quad (3)$$

for the case where  $\lambda$ , the wavelength of the light, is much longer than the critical wavelength. This is usually the case for visible wavelengths. Note that  $\theta_{SR}$  is the same in both planes.

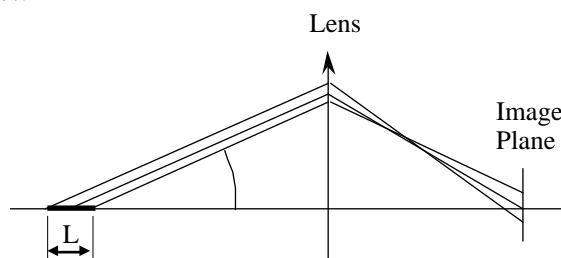


Figure 1. Depth of field error sketch.

#### 2.1.3 Diffraction Error

Any imaging problem that involves apertures will inevitably have a diffraction error. Contrary to the depth of field error in the previous section, this error increases as the aperture is decreased. It is usual to restrict the aperture with either a circular iris or a vertical slit. The formulae for the diffraction resolution for these two cases are given below [1]. For an iris,

$$diff = 0.61 \frac{\lambda}{\theta} \quad (4)$$

and for a slit,

$$diff = 0.5 \frac{\lambda}{\theta}. \quad (5)$$

Clearly, a vertical slit will give the better resolution.

#### 2.1.4 Curvature Error

Due to the nature of the source, the curvature of the electron beam also contributes an error term that limits the horizontal resolution. From the geometry shown in figure 2 it is straightforward to derive the apparent width of the source as:

$$curv = \frac{R\theta^2}{2}. \quad (6)$$

So, for a particular wavelength, the best resolution is found by minimising the sum of the squares of the three error terms described in equations (1), (5) and (6). For the SRS with  $R = 5.5$  m,  $\theta_{SR} = 2.8$  mrad and  $\lambda = 500$  nm, the optimum value of  $\theta$  is 2.6 mrad, defined by a vertical slit. This gives a combined value of 125  $\mu$ m for the apparent width of a negligible cross-section beam.

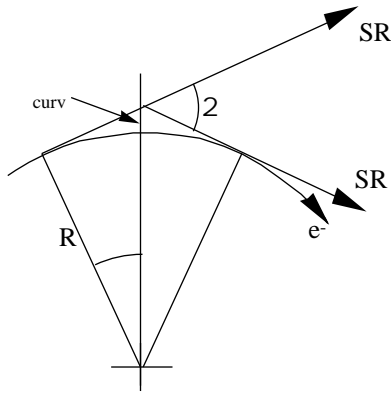


Figure 2. Curvature error sketch.

### 2.2 Vertical Case

For the vertical case the chromatic and depth of field errors are as for the horizontal. However, in the horizontal case the relevant diffraction effect and the depth of field error were both in the same plane. This is not true for the vertical case. Here the depth of field is again determined by the horizontal acceptance, but the diffraction is now only of consequence in the vertical plane. This means that the horizontal acceptance must be set to limit the depth of field and that any vertical acceptance limit will introduce unnecessary broadening due to diffraction. Therefore, in the vertical plane it is most advantageous to use a vertical slit instead of a circular iris. The minimum diffraction error is determined by the natural opening angle of the source. The diffraction limited resolution in the vertical plane can be estimated by replacing  $\lambda$  by  $\lambda_{SR}$  in equation (5). The difference between using a slit and an iris is illustrated in figure 3 for the SRS.

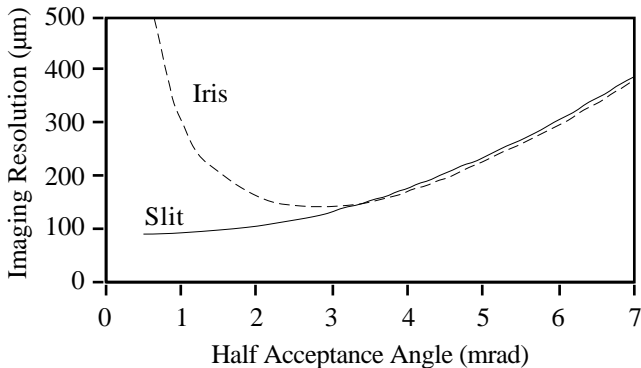


Figure 3. Apparent vertical width of a beam of narrow cross-section vs half acceptance angle for a slit and a circular iris.

Clearly the best vertical resolution is found by using a narrow vertical slit. However, since it is common to measure the profile of both planes with the same detector (eg a CCD camera) this is not always practical. Generally a compromise must be found between the resolution of the two planes in setting the horizontal acceptance, but since the vertical source size is usually much smaller than the horizontal it is normal to sacrifice some horizontal resolution in favour of the vertical. In fact, in modern 3rd generation light sources the vertical beam size may be significantly less than the diffraction limited resolution. In this case accurate profile measurements

can best be made with light of a significantly shorter wavelength.

## 3. CHARGE COUPLED DEVICES

The most common detector used for measuring beam profiles is the Charge Coupled Device (CCD). Such a device is a solid state detector that essentially consists of an array of discrete potential wells (known as pixels) that store accumulated charge. The charge, induced by incident photons, is read out sequentially. A complete description of CCDs is given in ref [2]. The CCD chip has a well defined geometry, which makes them ideal for metrology, with typical pixel sizes of  $20 \mu\text{m} \times 20 \mu\text{m}$ . Each chip will contain something like  $512 \times 512$  pixels.

CCDs can have two geometries, Frame Transfer and Inter-Line Transfer (figure 4). Both of these can be used for profile measurements. The difference between the two types relates to the method used for reading out the accumulated charge. Each CCD has a memory area that is light insensitive to which all of the stored charges are transferred after a fixed integration time. The Frame Transfer type has a better horizontal spatial resolution but the Inter-Line type has a faster image to memory shift [3].

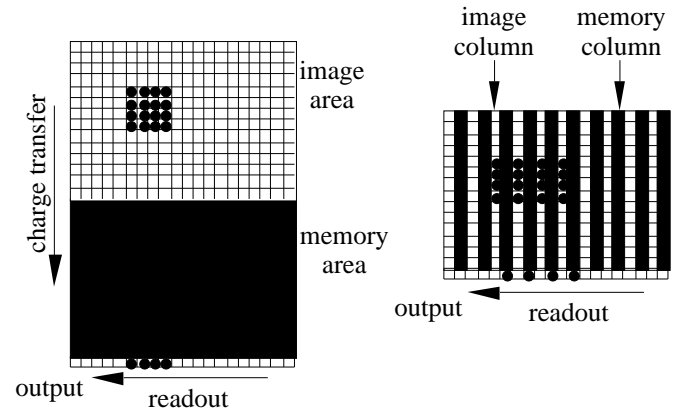


Figure 4. The two types of CCD detector. Frame Transfer on the left and Inter-Line Transfer on the right.

In order to use these devices for profile measurements it is necessary to connect the CCD camera to a framegrabber. A framegrabber is a device that interrogates the CCD and stores the reading for each pixel in buffer memory. It essentially consists of an Analogue to Digital Converter and some RAM (eg for an 8 bit ADC and  $512 \times 512$  pixel array, 256 kbytes are required).

The CCD and framegrabber each have their own internal clocks for controlling timing functions. To achieve the best resolution it is necessary to synchronise these internal clocks [4] although for most applications this would only prevent a small error.

The framegrabber is usually a plug-in computer card. The values in the framegrabber memory can be manipulated by the computer to find the beam profiles. Although the framegrabber generally comes with some commercial software, this is not normally sufficient. It is not uncommon to have to write software for controlling the framegrabber and for determining the beam profiles. This software will have to determine the

centre of the beam using some peak detection algorithm, and then select the appropriate pixels for each plane. This is not straightforward and may need to be optimised for each particular application. For example, at Elettra this has been resolved by averaging and smoothing [5].

It is important to remember when using CCD cameras that the output is not necessarily linear with light intensity. It is common for camera manufacturers to apply a so-called 'gamma correction' to the CCD output to compensate for the fact that TV monitors have a non-linear response. Although the optical detector itself is inherently linear, the electronics in most cameras applies a logarithmic scaling to the output. If this correction factor is not removed either by adjusting the camera hardware or software then the CCD will not give accurate beam profile measurements [6].

It is often desirable to measure several beam profiles rapidly, over a few ms say, to investigate beam damping or instability. Unfortunately CCDs are relatively slow, running at TV refresh rate speeds. By screening off 90% of the optical detector (Frame Transfer type) and using it as a memory area it has been shown that it is possible to measure a short burst of profiles at around 10 kHz [7].

It is also useful to be able to monitor beam profiles from linacs or synchrotrons at their repetition rates of typically 50Hz. This can best be achieved by using fast shutters locked to the beam cycle. Mechanical shutters are possible but electro-optical ones are preferred. These are a sandwich of a photocathode, micro-channel plate and phosphor screen. The shutter is controlled by gating the accelerating potential across the micro-channel plate. Such a shutter has been used to monitor profiles stroboscopically turn-by-turn in the SLC damping rings [8].

#### 4. PHOTODIODE ARRAYS

An alternative detector that can be used for measuring profiles is the Photodiode Array (PDA) [9]. This is a one dimensional strip of photodiodes (typically 25  $\mu\text{m}$  long) that have an output that is linearly dependent upon the light intensity. This is a purely analogue device, unlike the CCD and framegrabber. The photodiodes are read sequentially and the output can be observed on a scope.

Of course, since the arrays are one dimensional the profile of only one plane can be observed. Therefore two arrays are required to measure both horizontal and vertical profiles simultaneously. This does however have the advantage of allowing the optical system to be optimised for each plane unlike the two dimensional CCD. The other advantage of the one dimensional array is that the need to find the centre of gravity of the beam is removed, greatly simplifying the measurement procedure.

Unlike the CCD the PDA does not lend itself easily to computer control. One method of overcoming this is to control the scope observing the PDA output. This has been successfully demonstrated at Daresbury where the scope is controlled over the GPIB interface [10]. Here, the scope trace is captured by the computer and the profile determined.

Typical integration times for PDAs are 25 ms, so like the CCD they are not ideally suited to rapid profile measurements.

However the fast shutter that was mentioned in the previous section could equally well be applied to the PDA.

#### 5. CALIBRATION

An important requirement that must not be overlooked is proper calibration of the detector. In many cases the accuracy of the final measurement is limited by calibration error rather than by imaging resolution. Calibration here refers to the determination of the magnification of the optical system employed and so relates the measured profile width in the laboratory to the actual width in the storage ring.

Of course, if the focal lengths of the lenses used is well known then a theoretical calibration can be predicted. However it is always desirable to check this by experiment. This can best be achieved by moving the electron beam by a known amount and measuring how far the focussed image moves. The electron beam can be moved with local bumps or by varying the RF frequency, so long as the change in position of the beam is accurately known.

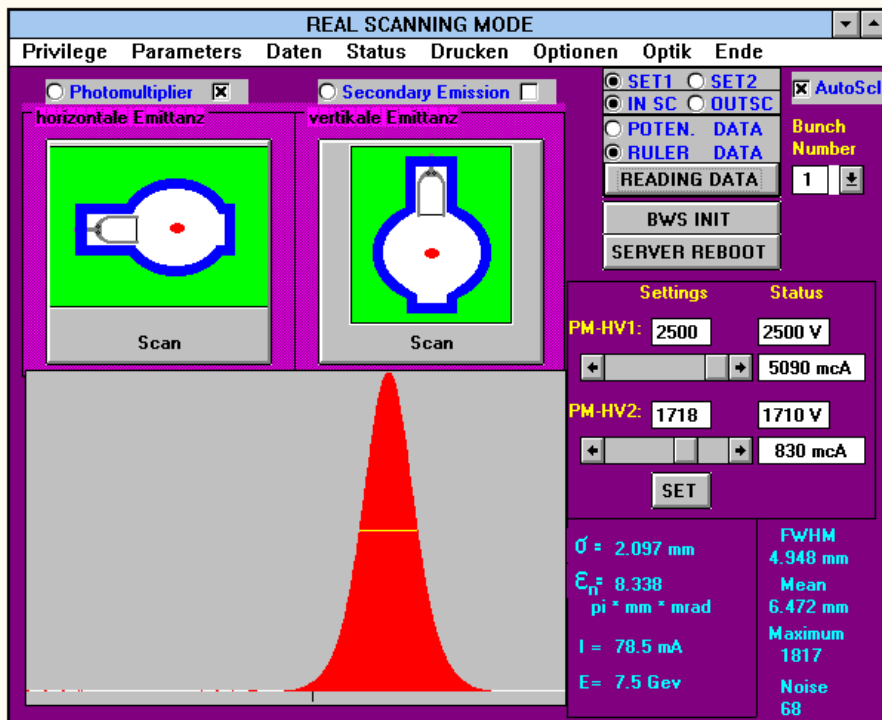
#### 6. SUMMARY

Measurement of beam profiles with synchrotron radiation is now commonplace. A review has been given of the points that need to be considered when deciding upon a particular technique. The simplest method to use is based upon a photodiode array detector. However, the most common method employed is with a CCD camera and framegrabber. This may take longer to commission because of software requirements but the final product has greater potential.

#### 7. REFERENCES

- [1] A. Hofmann and F. Meot, "Optical Resolution of Beam Cross-Section Measurements by means of Synchrotron Radiation", Nucl. Inst. Meth., 203 (1982), pp 483 - 493.
- [2] J.A. Hall, "Arrays and Charge-Coupled Devices", in Applied Optics and Optical Engineering, Academic Press, 1980, pp 349 - 400.
- [3] R. Jung, "Image Acquisition and Processing for Beam Observation", Proceedings of the First European Workshop on Beam Diagnostics and Instrumentation for Particle Accelerators, Montreux, Switzerland, May 1993, pp 54 - 63.
- [4] J.M. Raynor and P. Seitz, "The Technology and Practical Problems of Pixel-Synchronous CCD Data Acquisition for Optical Metrology Applications", SPIE vol. 1395, pp 96 - 103.
- [5] G.R. Aiello and F. Cavazzoni, "The Beam Profile Monitors for Elettra", Proceedings of the European Particle Accelerator Conference, Nice, France, June 1990, pp 747 - 749.
- [6] Y. Hashimoto et al, "Beam Profile Monitor using Alumina Screen and CCD Camera", Eighth Symposium on Accelerator Science and Technology, Japan, November 1991.
- [7] C. Bovet et al, "The LEP Synchrotron Light Monitors", Proceedings of the IEEE Particle Accelerator Conference, San Francisco, USA, May 1991, pp 1160 - 1162.
- [8] M. Minty et al, "Using a Fast-Gated Camera for Measurements of Transverse Beam Distributions and Damping Times", Proceedings of the 1992 Accelerator Instrumentation Workshop, Berkeley, USA, October 1992.
- [9] R.J. Nawrocky et al, "A Beam Profile Monitor for the NSLS VUV Ring Employing Linear Photodiode Arrays", IEEE Trans. Nucl. Sci., NS-32, 1985, pp 1893 - 1895.
- [10] J.A. Clarke and P.A. McIntosh, "The Application of LabVIEW for Data Acquisition at an Accelerator Laboratory", these proceedings.

# Wire Scanners



by Kay Wittenburg, -DESY-

## I. Introduction

Conventional wire scanners with thin solid wires (conventional compared with new techniques using, for example, Lasers) are widely used for beam size measurements in particle accelerators. The interaction of the wire with the beam generates a number of different interactions which can be used for the profile determination.

- ❖ Secondary emission current
- ❖ Bremsstrahlung, detection by Scintillators
- ❖ Scattering of beam particles, detection by Scintillators etc.
- ❖ creation of electromagnetic/hadronic showers, detection by shower counters.

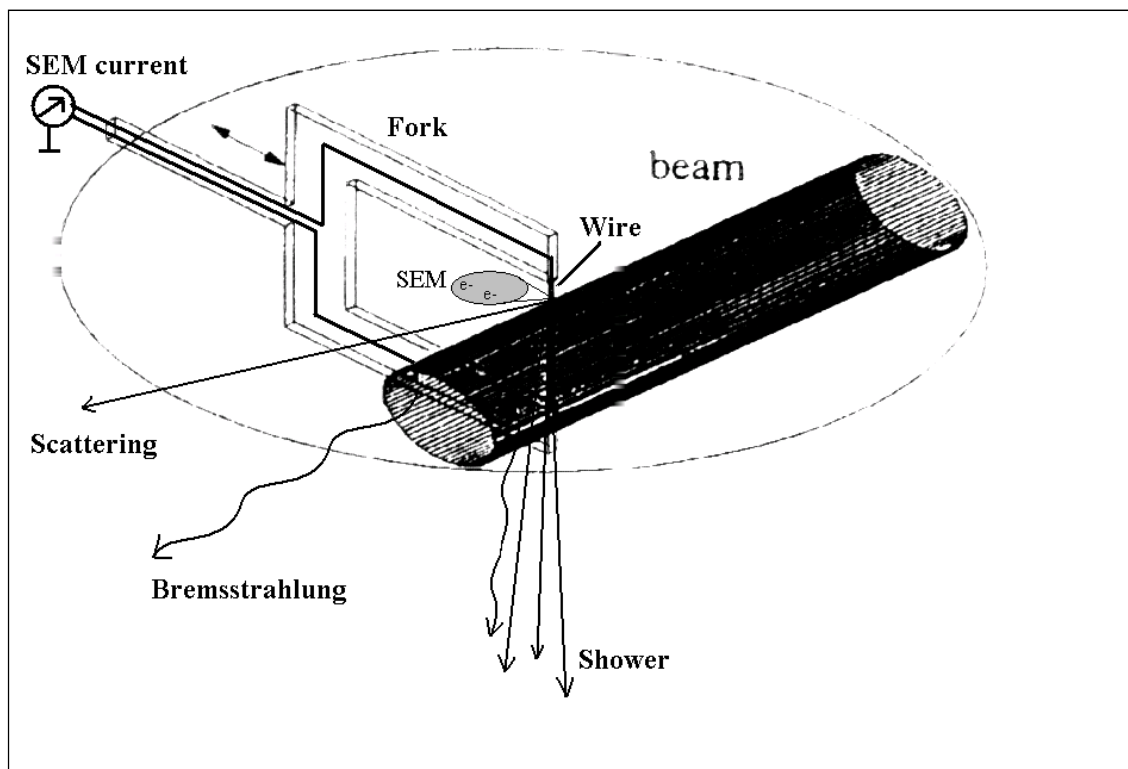


Figure WIRE1: Beam wire interactions

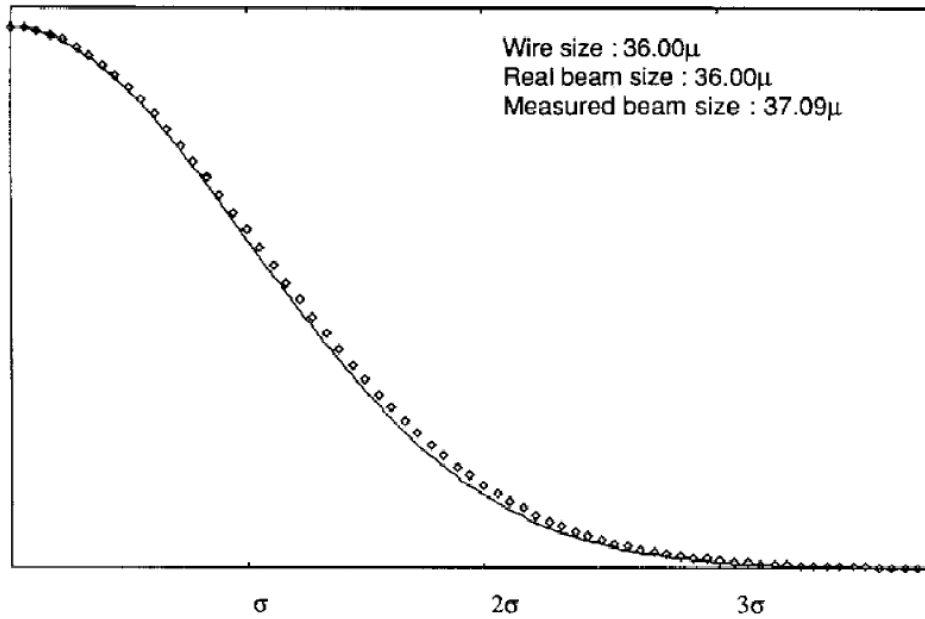
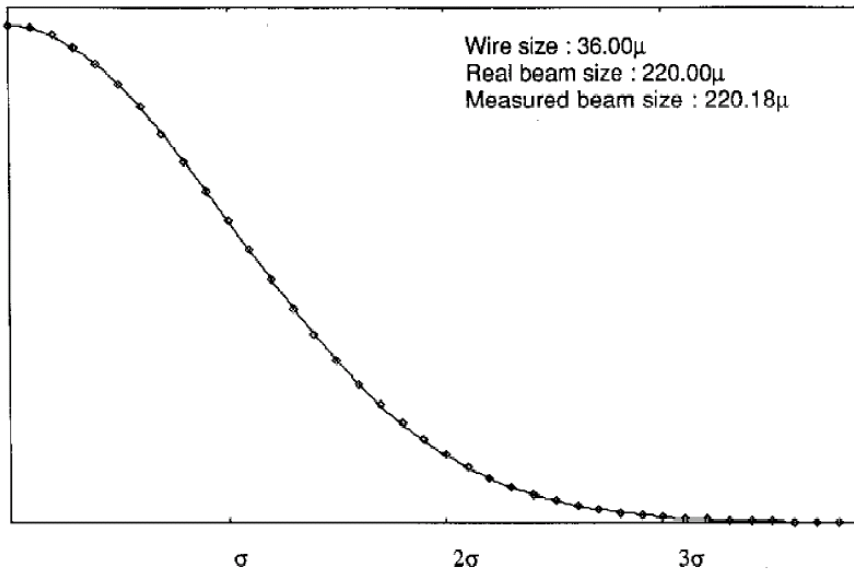
**Exercise WIRE: Discuss where one should locate the Scintillator in case of a proton and an electron accelerator?**

**Known limitations of wire scanners are?**

## II. Limitations:

### 1. Beam size

The smallest achievable wires have a diameter of about 5-6  $\mu\text{m}$ . This limits the use of wire scanners to beam sizes of a few microns. An example of the error in the beam width determination is shown in the next figures for a 36  $\mu\text{m}$  wire.



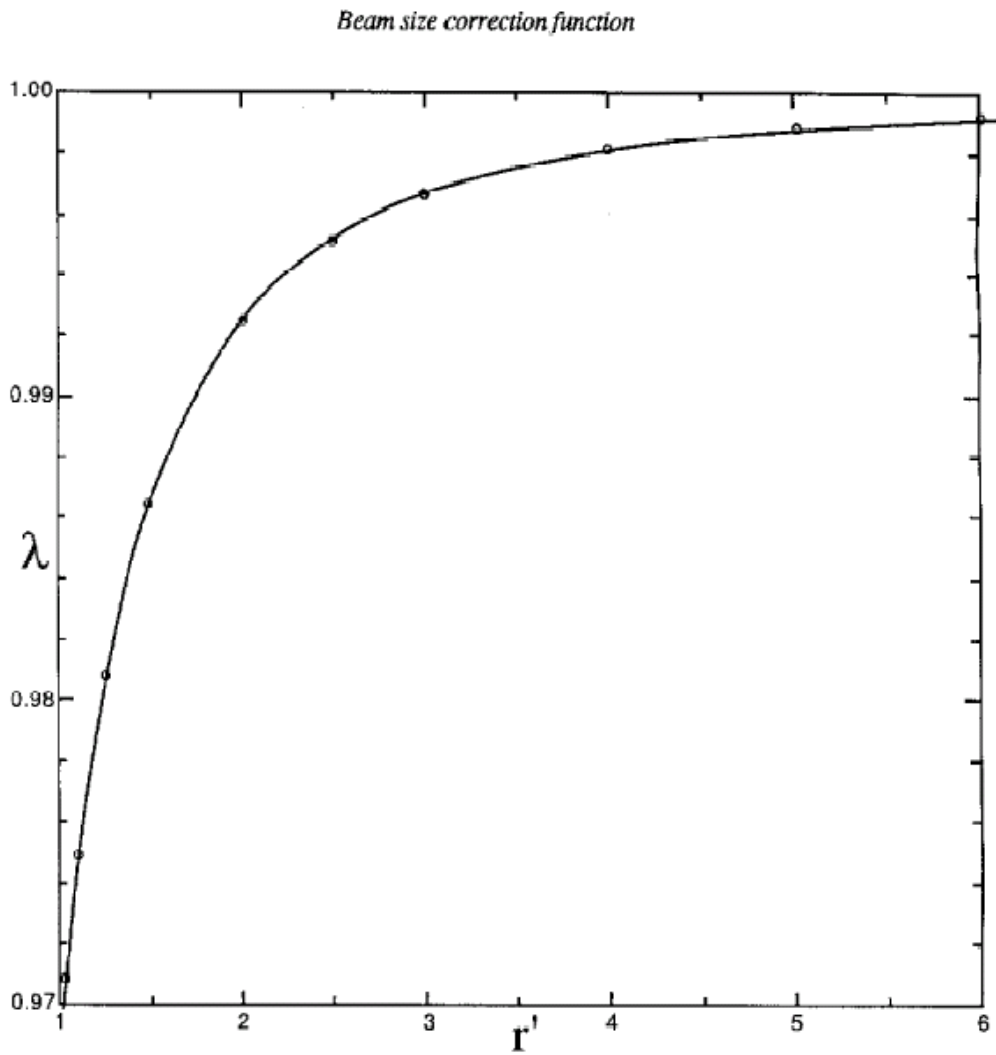


Figure WIRE 3 a-c: Influence of the wire diameter on the measured beam width (All figures from: Q. King; [Analysis of the Influence of Fibre Diameter on WireScanner Beam Profile Measurements](#), SPS-ABM-TM/Note/8802 (1988))

## 2. Higher Order Modes

An early observation (1972 DORIS) with wire scanners in electron accelerators was, that the wire was always broken, even without moving the scanner into the beam. An explanation was Higher Order Modes coupling into the cavity of the vacuum chamber extension housing the wire scanner fork. The wire absorbs part of the RF which led to strong RF heating.

**Exercise WIRE1: Discuss methods of proving this behavior. What are possible solutions against the RF coupling?**

## 3. Wire heat load

According to Bethe-Blochs formula, a fraction of energy  $dE/dx$  of high energy particles crossing the wire is deposit in the wire.  $dE/dx$  depends mainly on the material of the wire and its diameter, in the following we will assume  $dE/dx$  for minimum ionizing particles.

For simplification, a rectangular wire with a mean diameter of  $d'$  will be used in the calculation:

$$area = \frac{\pi d^2}{4} = d'^2 \Rightarrow d' = d / 2 \cdot \sqrt{\pi}$$

The following table shows parameters which can be used for some temperature estimations:

### Wire Parameters

Parameter	Symbol	Unit	wire material				
			AL	W	Carbon	Beryllium	Quartz (SiO <sub>2</sub> )
wire diameter	$d$ $= 7 \cdot 10^{-4}$	cm					
mean wire diameter	$d' = d/2 \cdot \sqrt{\pi}$ $= 5.5 \cdot 10^{-4}$	cm					
Conversion	0.239	cal/Joule					
Conversion factor	$C = 3.8 \cdot 10^{-14}$	cal/MeV					
Speed of wire	$v = 100$	cm/s					
specific heat capacity*	$c_p$	cal / g / °C	0.21	0.036	0.42 (>400 °C) 0.17 (< 400 °C)	0.43	0.18
Energy loss of min. ion. part. (MIPs)	$dE/dx$	MeV cm <sup>2</sup> / g	1.62	1.82	2.3	1.78	2.33
	$dE/dx_m$	MeV/cm	4.37	35.13	5.3	3.3	5.3
density	$\rho$	g/cm <sup>3</sup>	2.7	19.3	2.3	1.85	2.29
melting temp.	$T_m$	°C	650	3400	ca. 3500	1200	1700
Heat conductivity	$\lambda$	W/(m K)	230	100-160	30-3000	200	1.2-1.4
Radiation length	$l_{rad}$	cm	8.9	0.35	18.8	34.7	12.3
Nuclear coll length	$l_{nuc}$	cm	26	9.6	34	30	25.4

Table WIRE1: Parameters of wire materials. \* > 500 °C

### Beam Parameters

The beam parameters used in this exercise are shown in the following table:

Parameter	Symbol	Unit	Value
circumference of accel.	circ.	m	300
particle		Proton	
Beam particle momentum	p	GeV/c	0.3-7
Beta function	$\beta_h = \beta_v$	m	11.8
Emittance	$\epsilon_h = \epsilon_v$	$\pi$ mm mrad	15
revolution Frequency	$f_{rev}$	MHz	0.93
Bunch spacing	$t_{bunch}$	ns	98
	$f_{bunch}$	MHz	10.2
Number of bunches in accel.	NB		11
Bunch charge	$n_{bunch}$	1/e	$1.1 \cdot 10^{11}$
Beam width measurement <sup>1</sup>	$\sigma_h$	mm	1.5
Beam width perpendicular to meas. <sup>1</sup>	$\sigma_v$	mm	1

Table WIRE2: Parameters of Beam

Each beam particle which crosses the wire deposits energy inside the wire. The energy loss is defined by  $dE/dx$  (minimum ionization loss) and is taken to be that for a minimum ionizing particle. In this case the temperature increase of the wire can be calculated by:

$$T = C \cdot dE / dx_m \cdot d' \cdot N \cdot \frac{1}{c_p \cdot G} \quad [^{\circ}C],$$

where N is the number of particles hitting the wire during one scan,  $d'$  is the thickness of a quadratic wire with the same area as a round one and G [g] is the mass of the part of the wire interacting with the beam. The mass G is defined by the beam dimension in the direction of the wire (perpendicular to the measuring direction).

### **Estimation of the wire temperature after one scan with speed v (assume no cooling mechanisms):**

---

<sup>1</sup> Gaussian shape of width  $\sigma$

**Exercise WIRE2: Which kind of wire Material you will prefer for a wire scanner in this accelerator?**

Material
AL
W
C
Be
SiO2

**Exercise WIRE2a: Discuss cooling mechanisms which will cool the wire.**

**4. Emittance blow up**

**Exercise WIRE3: Calculate the emittance blowup of the proton beam after one scan at a position with  $\beta = 11.8$  m for  $p = 0.3$  and 7 GeV/c (Carbon wire):**

**Assume a position of the wire scanner very close to a quadrupole ( $\alpha=0$ )**

For small deflection angles a good approximation for average root mean square scattering angle is given by:

$$\delta \Theta = \frac{0.014 \text{ GeV}}{pc} \cdot \sqrt{\frac{d'}{L_{rad}}} \cdot \left( 1 + 1/9 \cdot \log_{10} \frac{d'}{L_{rad}} \right)$$

Remember:

$$\gamma(s)y^2 + 2\alpha(s)yy' + \beta(s)y'^2 = \varepsilon$$

## **References attached:**

### **High Resolution Measurements of Lepton Beam Transverse Distributions with the LEP Wire Scanners.**

J. Camas, G. Crockford, G. Ferioli, C. Fischer, J.J. Gras, R. Jung, J. Koopman, J. Mann  
CERN CH-1211 Geneva 23, Switzerland  
PAC93

[http://accelconf.web.cern.ch/AccelConf/p93/PDF/PAC1993\\_2504.PDF](http://accelconf.web.cern.ch/AccelConf/p93/PDF/PAC1993_2504.PDF)

### **Design of a High-precision Fast Wire Scanner for the SPS at CERN**

R. Veness, N. Chritin, B. Dehning, J. Emery, J.F. Herranz Alvarez, M. Koujili, S. Samuelsson, J.L. Sirvent Blasco; CERN, Geneva, Switzerland

International Beam Instrumentation Conference, IBIC2012, Tsukuba, Japan, Oct 1-4, 2012

<http://ibic12.kek.jp/prepress/papers/mopb79.pdf>

## **Further readings**

K. Wittenburg

### **Conventional Wire Scanners at TESLA**

Tesla Report 2000-18

[http://adweb.desy.de/mdi/downloads/conventional\\_wire\\_at\\_tesla.pdf](http://adweb.desy.de/mdi/downloads/conventional_wire_at_tesla.pdf)

### **SNS LINAC WIRE SCANNER SYSTEM, Signal Levels and Accuracy;**

M. A. Plum, et al,

LINAC2002

<http://cern.ch/AccelConf/102/PAPERS/MO458.PDF>

### **Analysis of the Influence of Fibre Diameter on Wire Scanner Beam Profile Measurements**

Q. King; SPS-ABM-TM/Note/8802 (1988)

[http://adweb.desy.de/mdi/documentation/wire\\_scanner\\_at/ttf\\_new/analysis.pdf](http://adweb.desy.de/mdi/documentation/wire_scanner_at/ttf_new/analysis.pdf)

### **OBSERVATION OF THERMAL EFFECTS ON THE LEP WIRE SCANNERS.**

J. Camas, C. Fischer, J.J. Gras, R. Jung, J. Koopman (CERN). CERN-SL-95-20-BI, May 1995. 4pp. Presented at the 16th Particle Accelerator Conference - PAC 95, Dallas, TX, USA, 1 - 5 May 1995.

Published in IEEE PAC 1995:2649-2651)

<http://accelconf.web.cern.ch/AccelConf/p95/ARTICLES/TPC/TPC21.PDF>

### **CAVITY MODE RELATED WIRE BREAKING OF THE SPS WIRE SCANNERS AND LOSS MEASUREMENTS OF WIRE MATERIALS**

F. Caspers, B. Dehning, E. Jensen, J. Koopman, J.F. Malo, CERN, Geneva, Switzerland

F. Roncarolo, CERN/University of Lausanne, Switzerland; DIPAC03)

<http://accelconf.web.cern.ch/AccelConf/d03/papers/PM12.pdf>

### **QUARTZ WIRES VERSUS CARBON FIBERS FOR IMPROVED BEAM HANDLING CAPACITY OF THE LEP WIRE SCANNERS.**

By C. Fischer, R. Jung, J. Koopman (CERN). CERN-SL-96-09-BI, May 1996. 8pp. Talk given at 7th Beam Instrumentation Workshop (BIW 96), Argonne, IL, 6-9 May 1996.

Thermal Load on Wire Scanners

Lars Fröhlich

37th ICFA Advanced Beam Dynamics Workshop on Future Light Sources; May 15-19, 2006 in Hamburg, Germany

[http://www.desy.de/~ahluwali/technicalnotes/2006\\_02.pdf](http://www.desy.de/~ahluwali/technicalnotes/2006_02.pdf)

### **Operational Limits of Wire Scanners on LHC Beam**

Mariusz Sapinski, Tom Kroyer (CERN, Geneva)

2008 Beam Instrumentation Workshop (BIW08) held on May 4-8, 2008 at the Granlibakken Conference Center and Lodge in Tahoe City, CA, USA, pp.383-388

<http://www.als.lbl.gov/biw08/papers-final/TUPTPF066.pdf>

### **Carbon Fiber Damage in Accelerator Beam**

CERN-BE-2009-028

DIPAC09

Sapinski, M ; Dehning, B ; Guerrero, A ; Koopman, J ; Métral, E ; DIPAC09, Basel

<http://dipac09.web.psi.ch/ppp/papers/tupd40.pdf>

## High Resolution Measurements of Lepton Beam Transverse Distributions with the LEP Wire Scanners.

J. Camas, G. Crockford, G. Ferioli, C. Fischer, J.J. Gras, R. Jung, J. Koopman, J. Mann  
CERN CH-1211 Geneva 23, Switzerland

### Abstract

A large number of improvements were carried-out on the LEP Wire-Scanners in preparation for the 1992 running period. They include modifications of the monitors mechanics to decrease the vibrations and the heating of the wire by the beam generated electromagnetic fields, improvements of the detector chain and a software re-organization at the various levels for better noise rejection, improved user interface and "off-line" data analysis capabilities. It is now also possible to acquire the profiles of each of the sixteen circulating bunches, electrons and positrons, during the same sweep. As a consequence of these actions the quality of the collected data is much improved. The results are presented and discussed.

### I. INTRODUCTION

Four wire-scanners are installed in LEP straight section 1 [1] to provide transverse distributions in both horizontal and vertical planes. Figure 1 gives the lay-out of the monitors together with their associated detectors.

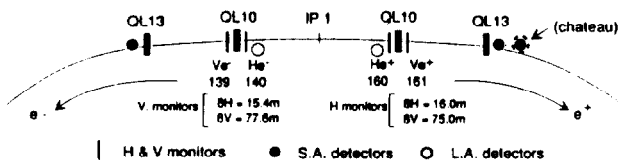


Fig 1: The LEP Wire-Scanners arrangement and Optics Parameters

One horizontal and one vertical monitor are symmetrically installed and are each associated with two detectors:

- a scintillator located behind a thin window, 75 meters downstream of the wire, receives the Bremsstrahlung resulting from the beam-wire interaction emitted at small angles (S.A.). It acquires the scan of the associated beam (i.e. e- profile from the monitors located on the e- injection side).

- a scintillator installed against the vacuum chamber near to the horizontal monitor collects the emission at large angles (L.A.) during the passage of the counter-rotating beam.

The signal received by the S.A. scintillators [1] is attenuated by 4 orders of magnitude before transmission to a photo-multiplier which has a gain 100 times smaller than that of the L.A. detectors.

### II. THERMAL AND MECHANICAL OBSERVATIONS

Fourteen wires have been destroyed from 1989 to 1992, most of them in 1989 and 1990. With the exception of two 50  $\mu\text{m}$  Beryllium wires, they were 36  $\mu\text{m}$  thick carbon wires. The Be wires showed clearly [1] that the wire had melted over its full length, excluding beam energy deposition as the only destruction mechanism. This is confirmed by previous measurements at the SPS where the wires survived higher intensities at comparable speeds. Moreover, permanent wire average temperature monitoring has shown several interesting features (Figure 2):

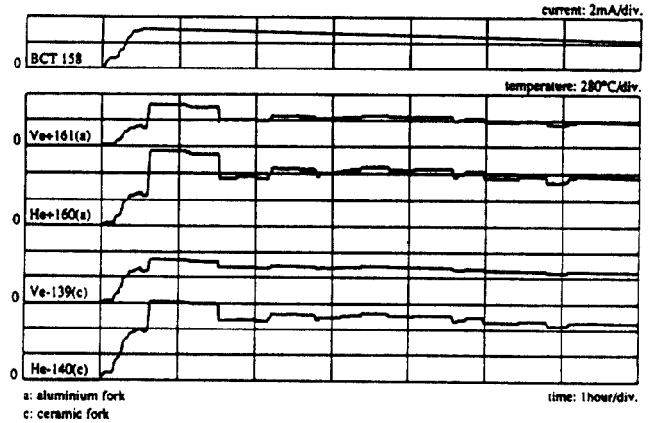


Fig. 2: Long term recording of wire resistance (temperature) and beam current with wires retracted in the parking position

The temperature of the wires increase with the stored current and the vertical wires temperature increases less than that of the horizontal ones. This indicates that the heating is of electromagnetic origin, due to the wake fields generated in the wire scanner tanks. The vertical wires heat up less because they are retracted in a rectangular tube functioning as a waveguide below cut-off. The second evidence in favour of electromagnetic heating is the fact that the wire temperature changes when beam manipulations modifying the bunch length take place at constant circulating beam intensity. Finally wire temperature recordings during scans provide other evidence of heating by electromagnetic coupling (Figure 3).

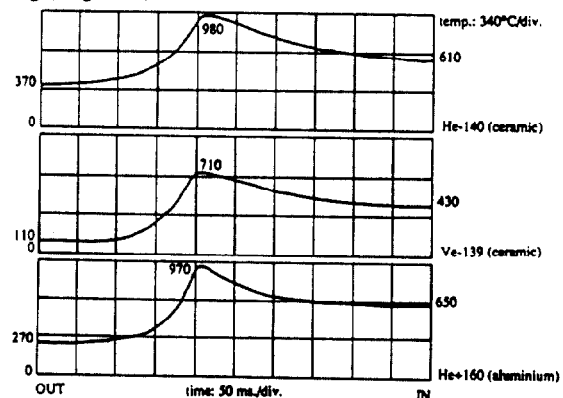


Fig. 3: Wire resistance change during scans of 300  $\mu\text{A}$  on 300  $\mu\text{A}$  circulating beams. Calculated temperatures are indicated.

As the wire approaches the beam, a temperature increase starts at approximately 40 mm from the beam centre, mainly due to coupling to the electric field. A steady state temperature is reached again when the wire is far from the beam. This results mainly from the magnetic field created by the beam passing in the loop formed by the wire and the supporting fork. The temperature increase of the

horizontal and vertical wires is inconsistent, the latter being too low compared to the former. Laboratory tests have shown that thermoemission starts at around 1000°C and shifts the resistance measurement towards lower equivalent temperatures. Electromagnetic heating of the wire being established, the fork construction was analysed for possible improvements. A coupling capacitance of a few pF was found between the wire and the fork; this was created between the aluminium arm, the wire supporting aluminium piece and the ceramic insulator (Figure 4). Two different types of supporting forks were installed in early 1991. The first design had a modified wire support piece and ceramic transition pieces to decrease the coupling capacitance (Figure 4).

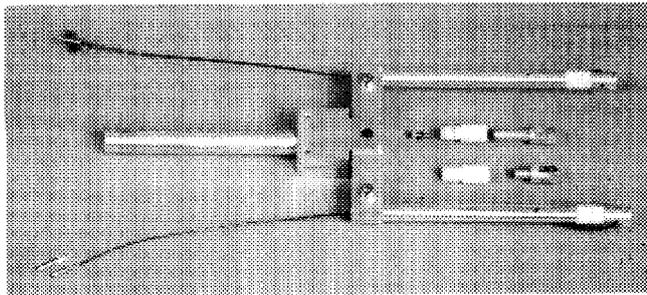


Fig. 4: Wire supporting fork with original (top) and modified (bottom) wire holding and ceramic isolating pieces.

A second design was implemented with the whole supporting tubes made of ceramic. In 1992, the wire length of the combined aluminium/ceramic forks was reduced from 55 to 29 mm. The vertical wire with this design broke twice in 1992. The temperature recording of the first incident showed that it happened at a circulating current of 2.8 mA; the temperature reached was 1280°C, uncorrected for thermoemission. For 1993, a 30  $\mu\text{m}$  quartz wire has been installed in place of the broken wire. The quartz wire will definitely break any current loop leading to heating but it may experience high voltage breakthroughs when passing through the beam. Since 1991, no wires with full ceramic arms were broken.

Scans taken in 1991 and 1992 are affected by a shift of the beam centre of charge between the IN and OUT directions of the order of 100  $\mu\text{m}$ . Laboratory tests have shown that it is due to an inertia induced movement of the driving screw [1]. This effect could be reduced in the laboratory from 70 to 10  $\mu\text{m}$  by using a counter-pin pushing on the free end of the driving shaft. This modification could not be implemented for the 1993 LEP start-up.

### III. LOW LEVEL AND APPLICATION SOFTWARE

The basic software design used in 1992 was unchanged from 1991. Amongst the various data structures exchanged between the local equipment server and the application, the PROFILE structures (one per profile) hold all the signals relative to a given bunch received from the photo-multiplier. If their initial analysis (sigma processing within the server) is successful, these data are trimmed to  $\pm 4$  sigmas; otherwise the entire profile is stored for more detailed "off-line" analysis. An analysis failure usually occurs when all signals are hidden within the noise. However, even with a good signal level the fit results (mainly the standard deviation) are noise dependent. In order to cope with this, two different methods have been tested :

- a simple rms calculation over the whole profile followed by a second iteration over a limited window
- a more refined gaussian fit providing a chi-squared minimization on all data above 10% of the maximum amplitude.

The later technique is less noise sensitive but is also less accurate when the distribution is not gaussian. For the future runs the results of both the rms processing and the gaussian fit will be forwarded to the application for systematic comparisons.

The application interface has also been upgraded for 1993 owing to the availability of more powerful graphic tools. It will be possible to display simultaneously up to eight circulating bunch profiles (of the same beam or of the two e+/e- beams) and to display IN and OUT profiles relative to a given scan on the same plot. These modifications added to better "off-line" analysis facilities will ease the interpretation of results.

### IV. RESULTS AND DISCUSSION

A scan is systematically performed in the IN (beam) and OUT (of beam) directions. As a result, two profiles are measured and can be compared each time a sweep is triggered in a given plane. The wire position (x axis) is in millimeters whereas the y scale unit is arbitrary and depends on the monitor gain setting.

#### HORIZONTAL PLANE:

In this plane the signal received by the S.A. detectors is excellent and provides good gaussian fits of the bunch profiles. This is illustrated on Figure 5 in the case of a positron bunch analysed with the monitor located on the positron side. Standard deviations from both scan directions are in agreement within  $\pm 1.3\%$ .

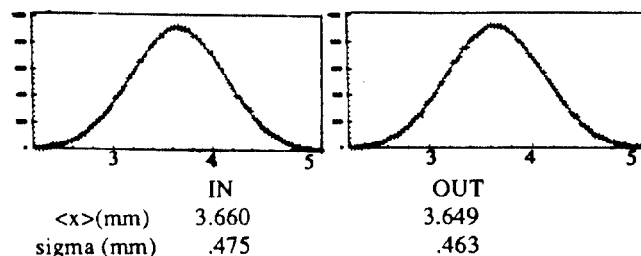


Fig 5: IN and OUT profiles and fit results of a positron bunch scanned with the He+ monitor and analysed with the S.A. detector at the window

Another S.A. detector (chateau) located fifteen meters downstream from the Bremsstrahlung radiation extraction window was also used in order to investigate eventual acceptance problems and effects of background close to the vacuum chamber. This detector was shifted radially which gave better shielding. Its response is given on Figure 6 for the same bunch .

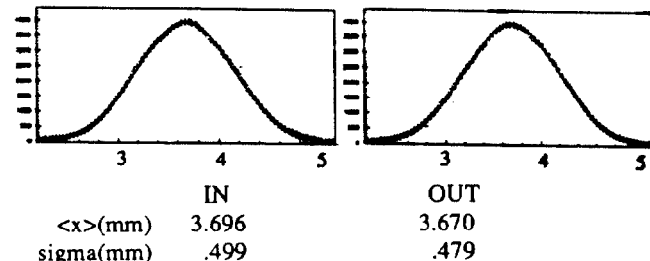


Fig 6: IN and OUT profiles and fit results of the same bunch from the S.A. detector located 15 meters downstream from the window

Between the IN and OUT directions the agreement is  $\pm 2\%$  and both S.A. detectors give the same standard deviation within  $\pm 2.1\%$

The response of the L.A. detectors is less good. The signal to noise ratio at large angle is less favourable and a compromise must be found between the shielding depth protecting the scintillator from background and the signal level to be analysed. In order to reduce the background noise 10 mm of Lead was necessary. However some saturation then started to affect the photomultiplier in the peak region (Figure 7)

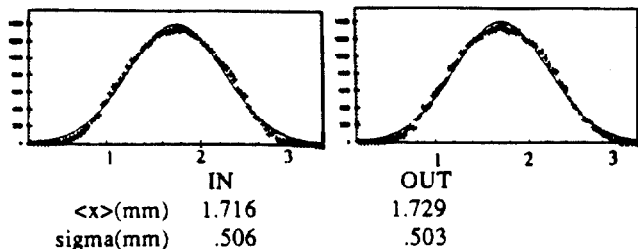


Fig 7: IN and OUT profiles and fit results of the same bunch scanned with the He- monitor and analysed with the L.A. detector.

The fit results provided by both directions agree very well but lead to standard deviations 5% higher than the S.A. detectors. The different average positions indicate that the beam trajectory is different at the e+ and at the e- monitors.

#### VERTICAL PLANE :

Typical profiles performed using the vertical monitors are shown on Figure 8 for the S.A. detectors.

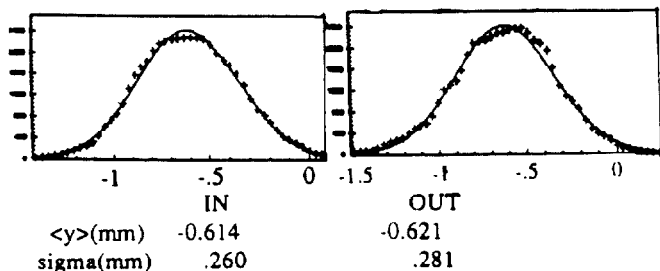


Fig 8: IN and OUT profiles and fit results of an electron bunch scanned with the Ve- monitor and analysed with the S.A. detector at the window.

Vertical profiles are usually affected by blow-up effects resulting from Coulomb Scattering of the beam through the wire. Taking the emittance ratio in LEP and the present monitor performances these effects can now be neglected in the horizontal plane at 46 GeV. They dilute mainly the second half of the vertical scan (positive and negative sides for respectively the IN and OUT directions) as can be seen on Figure 8. Hence, a direct gaussian fit provides a too pessimistic result. By modelling this effect and analysing the non-perturbed halves of the IN and OUT profiles [1], it is possible to reconstruct the initial distribution. An example of the results is given on Figure 9. A reduction of the rms value by 10% to 20% is then observed with respect to the fit of the entire measured distribution. However this method still suffers from the random mechanical effects (section II) and from timing imprecisions. Therefore it cannot be used systematically.

The L.A. detectors suffer from a lack of signal in the case of vertical profiles as they are located near to the H monitors (Figure 1) five meters downstream from the vertical ones.

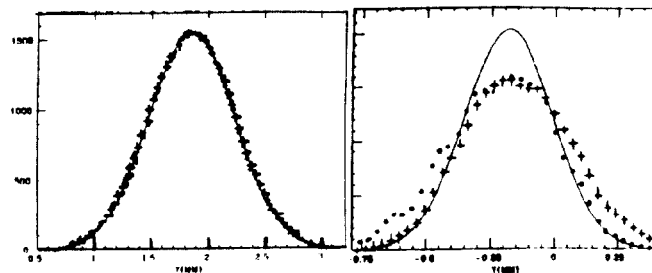


Fig 9: Initial distributions from IN and OUT profile analysis :  
+ : IN direction , o : OUT direction , — : fitted profile .

The gaussian fits of profiles from the S.A. detectors provide emittance values of 0.9nm to 1 nm in the vertical plane and 14nm to 15 nm horizontally. The precision achieved is a few per cent in the horizontal plane. Vertically the results are not so accurate as long as blow-up effects are not properly eliminated.

#### V. COMPARISON WITH S.R. MONITORS

These figures, can be used to calibrate the U.V. telescopes [2]. The agreement between the two devices is disturbed by parasitic effects which must be considered; they are at locations in the machine where the optics are not the same and where beam dynamical effects are different (for example coupling). This can account for discrepancies of around 20%. Some 50Hz noise also disturbs the two devices differently as they have different modes of acquisition

#### VI. FUTURE UPGRADES AND CONCLUSION

Several steps will be taken to improve wire-scanner performances in addition to the ones discussed in section II. The mechanics will be modified to reduce the shift between the two directions. It has also been considered to add to each monitor a wire rotated by 45 degrees. This will allow a better evaluation of the tilt effects. The electric noise level will be reduced in the wire scanners environment by installing filters on adjacent motorised devices. These improvements are foreseen for the 1994 runs. Both the S.A. and L.A. detectors have been modified. The former will have a better acceptance in particular close to the vacuum chamber whereas the shape of the later has been reconsidered to increase its acceptance and hence have better signal to noise ratio.

Several software modifications will be implemented apart from the availability of the new application (section III). An interlock will prevent any scans above a given circulating beam current and temperatures will be systematically recorded during wire sweeps. The timing will be upgraded so as to lower the uncertainty in the absolute position reference between IN and OUT scans from 50  $\mu$  m down to 10  $\mu$  m (rms). The wire status will also be monitored in permanence.

Resulting from these modifications we expect to have the same level of performance in both the horizontal and vertical planes.

#### VIII. REFERENCES

- [1] B.Bouchet et al., "Wire-Scanners at LEP", Proc. of the 1991 IEEE Part. Accel. Conf., San-Francisco, 6-9 May 1991 .
- [2] G. Burtin et al., "Performance and Operational Experience of the LEP Synchrotron Light Telescopes", these proceedings.

# DESIGN OF A HIGH-PRECISION FAST WIRE SCANNER FOR THE SPS AT CERN

R. Veness, N. Chritin, B. Dehning, J. Emery, J. Herranz Alvarez, M. Koujili, S. Samuelsson, J.L. Sirvent, CERN, Geneva, Switzerland

## Abstract

Studies are going on of a new wire scanner concept. All moving parts are inside the beam vacuum and it is specified for use in all the machines across the CERN accelerator complex. Key components have been developed and tested. Work is now focussing on the installation of a prototype for test in the Super Proton Synchrotron (SPS) accelerator.

This article presents the specification of the device and constraints on the design for integration in the different accelerators at CERN. The design issues of the mechanical components are discussed and optimisation work shown. Finally, the prototype design, integrating the several components into the vacuum tank is presented.

## INTRODUCTION

Wire scanners are installed in the LHC and all circular machines in the injector chain as a means to measure the transverse beam profile and hence emittance. The motivation for the development of a new scanner design has been described in a previous article [1], along with the concept with the rotor of the motor and wire position measurement system inside the beam vacuum [see Figure 1]. Development of key components, in particular the motor and control system, are well advanced [2]. Work is now focussing on the integration of all the required components with the aim of producing a scanner capable of 20 ms<sup>-1</sup> scanning speed combined with 2 μm position precision.

A number of mechanical components require careful optimisation. These include the motor housing, shaft, bearings, fork and wire. In addition, the design concept includes an in-vacuum optical position encoder in order to reach the required precision. Development of these components is described in the following sections.

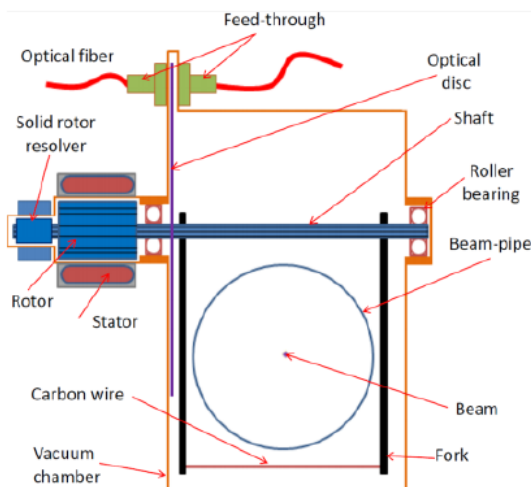


Figure 1: Fast Wire Scanner concept.

## INTEGRATION CONSTRAINTS

Wire scanners are currently installed in the PS, Booster, SPS and LHC at CERN. It would greatly simplify operation and maintenance if the same basic design could be implemented for all of these machines. To this end, the main constraints in terms of machine physics, operation and environment have been analysed for each machine. These are summarised in Table 1.

Table 1: Summary of Integration Constraints from the CERN Accelerator Complex

Machine	Scan aperture (mm)	RF Screen	Bakeout	Space Constraint
PS Booster	146x70	N	N	Axial, Transverse
PS	146x70	N	N	Axial
SPS	152x83	Y	N	-
LHC	65x65	Y	Y	Transverse

The scan aperture is the horizontal and vertical space that must be cleared by the wire. RF screens are required in some machines to minimise impedance and RF heating effects. Integration of new scanners into existing machines must take into account machine geometries and equipment. Axial space constraints occur in machines with a tight lattice whereas transverse constraints are seen with parallel equipment on the beamline (eg, the cryogenic distribution line in the LHC). It can be seen from table 1 that each of the machines brings constraints to the design. A solution has been adopted where the main components can be integrated into designs for the PS, SPS and LHC. Each machine will require a different fork geometry and a different flange interface, but other main components and principles will be common. The layout of the Booster with 4 rings in very close proximity mean that it has not yet been possible to integrate the design into this machine.

Combining these constraints leads to a design with aperture range up to 152 by 152, with the option to include RF screen and to be bakeable to 200°C in order to activate a low emission yield getter coating used in the LHC vacuum system.

## DESIGN OF COMPONENTS

### Motor Housing

The motor housing has the function of separating the rotor in-vacuum and stator on the atmospheric side of the

electric motor. The housing needs to be thin to fit in the relatively small air gap (approximately 0.8 mm) between the rotor and stator. The required wall thickness of the housing has been determined using finite element method (FEM) analysis. The analysis shows that elastic instability is the critical failure mode. The stability of the structure increases strongly with wall thickness. The dependence of stability on the length of the structure is weaker, where a shorter structure increases the stability. Furthermore, a thicker housing (within the limits of this problem) is easier to manufacture. When all the above mentioned considerations are put together, the optimum wall thickness of the motor housing is determined to be 0.4 mm.

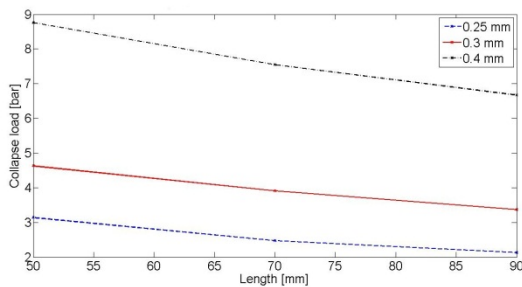


Figure 2: Graph of motor housing collapse load for different lengths and wall thicknesses.

*Shaft and Bearings*

One principal of this design is to support forks and position measurement system on one rigid structure to maximise precision. The shaft forms the core of the mechanical structure. It is driven by the motor and supports the rotor, forks and optical disc. The main constraint on the shaft is its deformation in torsion. The torsional deformation appears due to the acceleration of the shaft and the inertias of the components mounted on the shaft. This deformation must be kept small to ensure accuracy of the measurements. Although the shaft is not accelerating when the wire passes through the beam, the shaft will vibrate with a maximum amplitude corresponding to the torsional deformation due to the acceleration. The shaft needs to be hollow to be able to pass cables through it. Analysis of the shaft, using analytical calculations and FEM simulations, show that using a larger outer diameter has a strong effect on the stiffness. It is also shown that the stress in the shaft is low and the inertia of the shaft is of little importance compared to the inertias of the components mounted on the shaft. This means that the strength of the material is not critical and that a stiff, relatively heavy stainless steel is a better material choice compared to lighter, more flexible alternatives such as aluminium or titanium. The analysis also shows that it is the optical disc and the disc holder which give the largest contribution to the shaft twist. This is because they are mounted on the shaft end opposite to the motor. Therefore effort should be put into minimising the mass of these components. Figure 3 shows the offset of the wire position relative to the

encoder which the shaft vibrations give rise to. The calculations show that an outer diameter of 35 mm is needed to keep the deformation below the tolerated limit of 5  $\mu$ m.

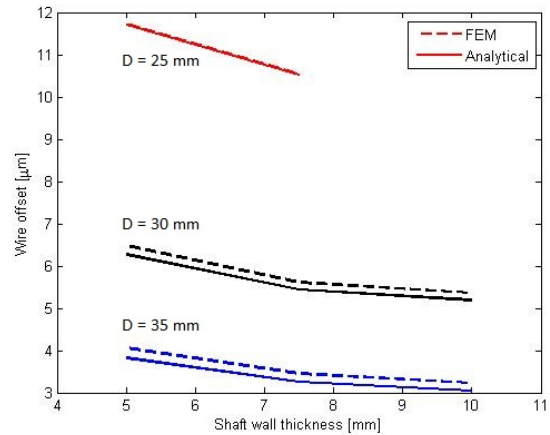


Figure 3: Graph of relative offset of wire vs. encoder for different shaft diameters and thicknesses.

The bearings need to assure high precision in terms of radial runout and the materials used must be UHV compatible and radiation and bake out resistant. This means that traditional lubricants such as oil and grease cannot be used [3]. Instead one must rely on running the bearings without any lubricant or possibly using solid lubricants (such as molybdenum disulphide or tungsten disulphide coatings). It is also recommendable to use different materials for the races and the rolling elements in the bearing, to avoid cold welding. One available alternative for this is hybrid bearings which use steel races and ceramic rolling elements.

*Optical Disc and Support*

The principle selected for the high precision determination of the beam size is an optical system based on a glass disc with a photo-lithographed  $\mu$ m pattern made of high reflectivity chrome, placed inside the vacuum chamber and fixed on the scanner shaft. This incremental angle encoder uses single-mode optical fibre and UHV fibre optic feedthrough (9/125 $\mu$ m) to drive 1310 nm laser light on a 1:1 lens system in-vacuum that focuses the light on the disc surface with a 10  $\mu$ m light spot size. Using the reflectivity of the chrome pattern, the reflected light is coupled back into the same fibre, and through an optical circulator directed to the photodiode. The laser diode, circulator, photodiode and subsequent electronics will be located in the surface building and only one optical fibre will go down to the accelerator tunnel (250 m). The performance of this single fibre angular position sensor has been tested and validated on the bench shown in Fig 4.

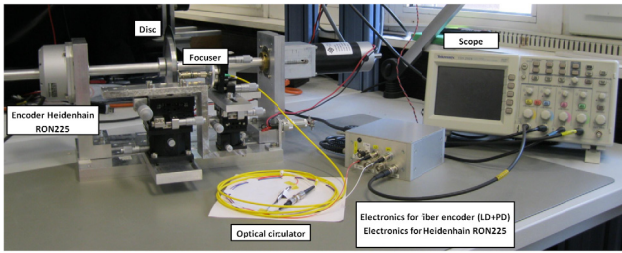


Figure 4: Test bench for the optical position sensor.

This fibre encoder provides a resolution of 157  $\mu$ Rad with a track of 10  $\mu$ m slits, and two position references using only one channel. An accuracy of  $\pm 25$   $\mu$ Rad is reached by angular calibration with a commercial encoder Heidenhain RON225 (Fig. 5). With this calibration, eccentricity errors, and partly grating errors can be minimized.

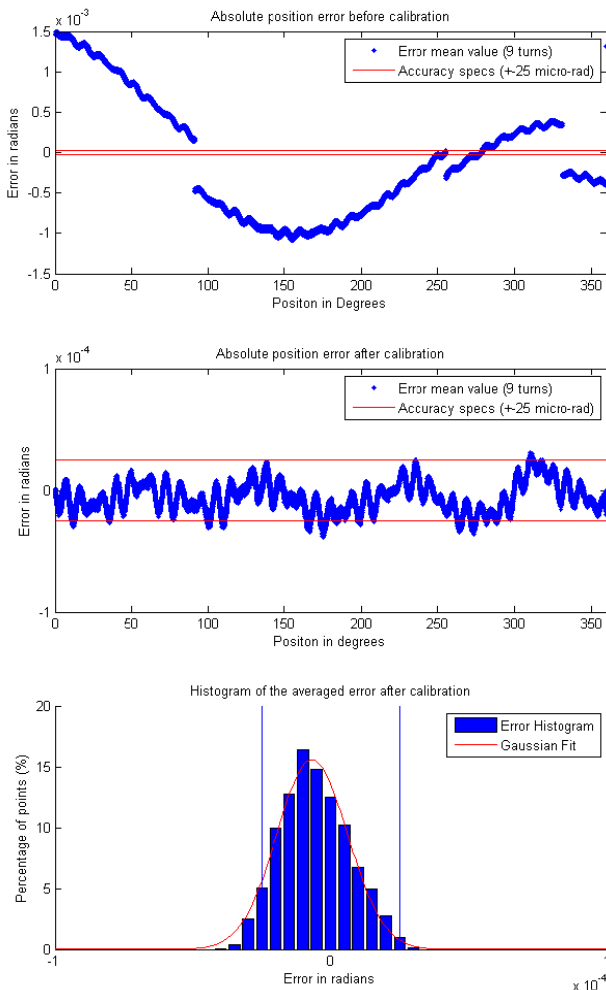


Figure 5: Error before calibration (top), calibration applied (center) and error histogram (bottom). Calibration made with Heidenhain RON225 angular position sensor.

The final system is UHV compatible with EMI immunity, works with temperatures up to 200°C, and it is radiation tolerant due the special fibre used. Studies are

on-going to verify the use of a 5  $\mu$ m track to reach better mechanical resolutions (around 70  $\mu$ Rad), and the incorporation of other calibration methods on the scanner working axis to perform a more reliable calibration procedure.

### Magnetic Restraint System

The design will integrate a magnetic restraint in order to prevent unplanned movements of the fork during transportation or installation and also during operation in case of power or control system failure.

Uncontrolled movement of the wire within the beam aperture could cause the melting of the wire and quenching of superconducting magnets (in the case of the LHC). This effect is enhanced as the wire speed due to its own unbalanced weight would be much slower than the nominal speed required for safe operation of the scanner.

The conceptual design of the restraint system consists of a magnetic circuit in two parts: One part outside of the vacuum has a permanent magnet and electrical coil; the other part inside the vacuum consists of a ferromagnetic piece fixed to the shaft. This has two poles that, when aligned with the external magnetic circuit, define an equilibrium position corresponding to the ‘parked’ fork positions. When the electric coil is energized it cancels the field of the permanent magnet allowing the shaft to rotate freely. This concept can be seen in Figure 6.

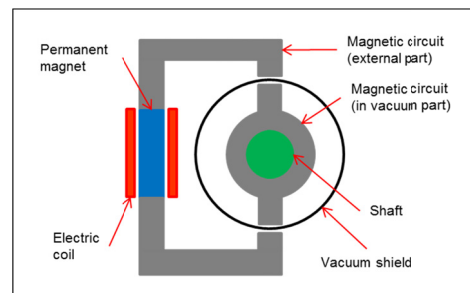


Figure 6: Conceptual design for the magnetic restraint system.

### Forks

The two forks which support the wire need to be carefully optimised. They need to be stiff enough to maintain the wire under tension and prevent excessive deformation and vibration during wire acceleration. However the forks are also a major component of the inertial load on the shaft and motor, so the mass and mass distribution need to be optimised. From the manufacturing viewpoint, there will be different designs for each machine due to the different apertures, so quantities will be small.

Considering all of these factors, it is logical to consider making these components using metal additive manufacturing [4] (also referred to as 3D printing). This method will allow complex geometries to be optimised using FEM, and produced directly in small quantities from 3D CAD models allowing for forms that cannot be produced with conventional machining.

Studies of the wire are on-going and will be presented separately.

### STATUS AND NEXT STEPS

All major components have been integrated into a 3D model with an envelope which would allow installation into the PS, SPS or LHC. Figure 7 shows a section through this model. The scanner is assembled as one self-contained ‘cartridge’ that will be inserted into the accelerator vacuum chamber. This will protect the wire from damage during insertion – a common problem with existing designs. A prototype will be constructed and tested in the coming months to verify the operation of the scanner assembly and performance. It is then planned to produce a first production model for test in the SPS accelerator. This will be installed in the forthcoming ‘Long Shutdown 1’ of all CERN accelerators in 2013-14. The plan is then to produce a series of scanners for installation in the second Long Shutdown scheduled for 2018-19.

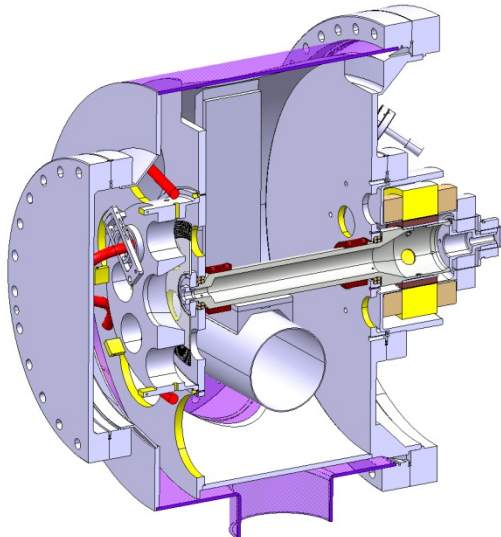


Figure 7: 3-D model section through the scanner.

### REFERENCES

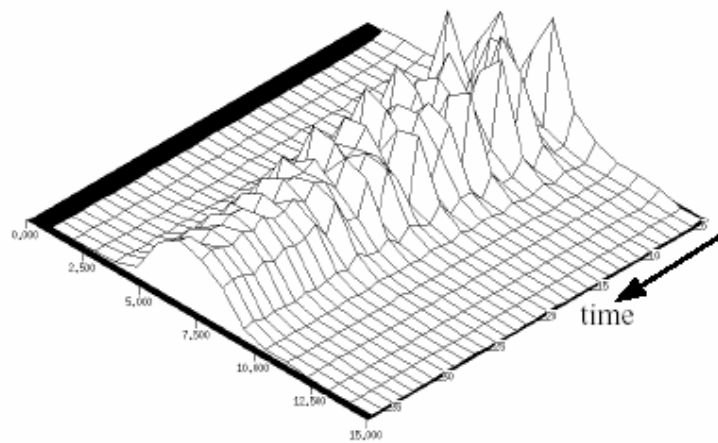
- [1] M.Koujili et al. ‘Fast and High Accuracy Wire Scanner’ DIPAC’09 Conference – 25-27 May 2009 /Basel-CH
- [2] B.Dehting et al. ‘Vacuum Actuator and Controller Design for a Fast Wire Scanner’ Proceedings of BIW2012, Newport News, Virginia, USA
- [3] D. Ramos ‘Bibliographic search on bearing technology for ultra-high vacuum applications’ Internal communication (2008).
- [4] L.E. Murr et al. ‘Metal Fabrication by Additive Manufacturing Using Laser and Electron Beam Melting Technologies’ J. Mater. Sci. Technol., 2012, 28(1), 1-14.

## 2.2 EXERCISES AND LITERATURE: INJECTION MISMATCH

### **2.2 Exercises and Literature: Injection Mismatch**

# Advanced Instrumentation

## Exercises: Injection mismatch



## Exercises: Injection mismatch

As a rule, proton/ion accelerators need their full aperture at injection, thus avoiding mismatch allows a beam of larger normalized emittance  $\epsilon^*$  and containing more Protons. In proton/ion ring accelerators any type of injection mismatch will lead to an emittance blowup. Off axis injection will lead to orbit oscillations. These oscillations can be detected easily by turn-by-turn BPMs in the ring (before Landau damping occurs). The orbit mismatch can be corrected by a proper setup of the steering magnets, kickers and septas. However, any mismatch of the optical parameters  $\alpha$ ,  $\beta$  (and therefore  $\gamma$ ) will also lead to an emittance blowup (and beam losses) and is not detectable by BPMs.

Fig. 1a shows the phase ellipse at a certain location in a circular accelerator. The ellipse is defined by the optics of the accelerator with the emittance  $\epsilon$  and the optical parameters  $\beta =$  beta function,  $\gamma = (1 + \alpha^2)/\beta$  and the slope of the beta function  $\alpha = -\beta'/2$ . Fig. 1b-d shows the process of filamentation after some turns.

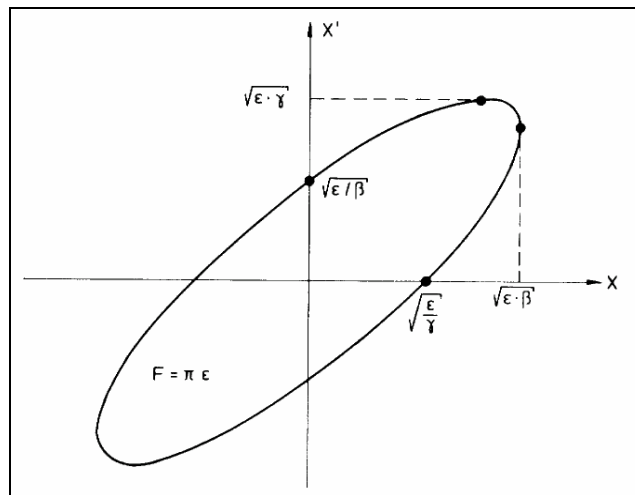


Fig 1a: A phase space ellipse of a circular accelerator, defined by  $\alpha$ ,  $\beta$ ,  $\gamma$ ,  $\epsilon$

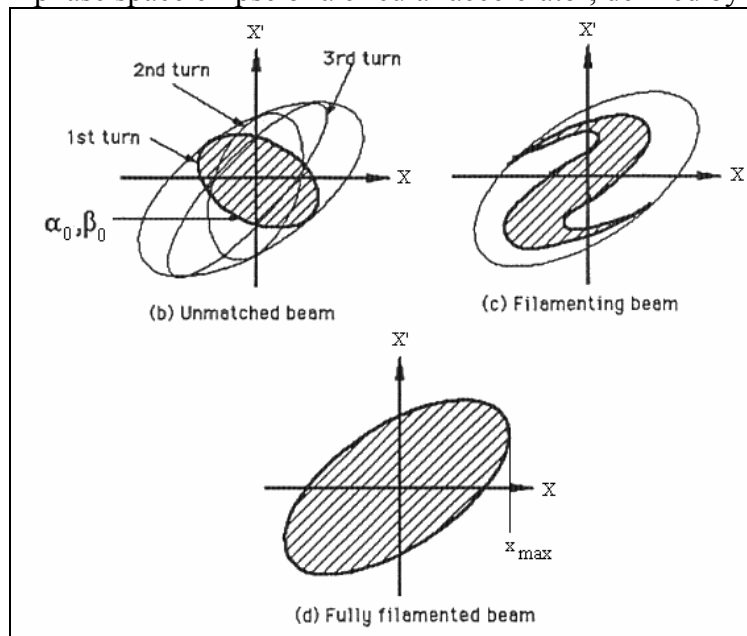


Fig. M1 b-d: Filamentation of an unmatched beam (from Ref. 2)

Assuming a beam is injected into the circular machine, defined by  $\beta_0$  and  $\alpha_0$  (and therefore  $\gamma_0$ ) with a given emittance  $\varepsilon_0$ . For each turn  $i$  in the machine the three optical parameters will be transformed by

$$\begin{pmatrix} \beta_{i+1} \\ \alpha_{i+1} \\ \gamma_{i+1} \end{pmatrix} = \begin{pmatrix} C^2 & -2SC & S^2 \\ -CC' & SC'+S'C & -SS' \\ C'^2 & -2S'C' & S'^2 \end{pmatrix} \cdot \begin{pmatrix} \beta_i \\ \alpha_i \\ \gamma_i \end{pmatrix} \quad (\text{Starting with } i = 0)$$

where  $C$  and  $S$  are the elements of the Twiss matrix ( $\mu = 2\pi q$ ,  $q = \text{tune}$ ):

$$\begin{pmatrix} C & S \\ C' & S' \end{pmatrix} = \begin{pmatrix} \cos \mu + \alpha_0 \cdot \sin \mu & \beta_0 \cdot \sin \mu \\ -\gamma_0 \cdot \sin \mu & \cos \mu - \alpha_0 \cdot \sin \mu \end{pmatrix} \quad (1)$$

and  $\gamma = (1 + \alpha^2) / \beta$

Without any mismatch, the three parameters will be constant while a mismatch will result in an oscillation of the parameters.

Some important machine parameters (here: HERAp)

Circumference  $\text{circ} = 6.3 \text{ km}$ ,  $f_{\text{rev}} = 47.3 \text{ kHz}$

Tune  $q = 0.31$  or  $f_{\text{tune}} = 14.6 \text{ kHz}$

Momentum  $E_p = 40 \text{ GeV}/c$  at injection

Normalized emittance  $\varepsilon_n = 20 \pi \text{ mm mrad}$ ,  $\varepsilon_0 = 5 \cdot 10^{-7}$

$\beta_0 = 238 \text{ m}$ ,  $\alpha_0 = -2.2$ ,  $\Rightarrow \gamma_0 = 0.0245$  at the injection point ( $\beta\gamma - \alpha^2 = 1$ ).  $\Rightarrow$  ring

$\beta = 214 \text{ m}$ ,  $\alpha_0 = \alpha$ ,  $\Rightarrow \gamma = 0.0272$  at the injection point.  $\Rightarrow$  injected beam

**Exercise M1: Show the beta-oscillation for the mismatch. What is the oscillation frequency? What are typical amplitudes?**

**Discuss how to measure a 10% betatron mismatch at injection between a transport line and a storage ring, for example in the HERAp accelerator.**

**Exercise M2: How large is the emittance blow-up?**

**Exercise M2a: What kind of measurement will you propose to determine the  $\beta$ -mismatch? Which monitor do you propose for this measurement?**

**Exercise M2b: What is the effect of the proposed monitor(s) on the beam?**

## References

- Ref. 1: P.J. Bryant; *Beam Transfer Lines, Proc. 5<sup>th</sup> CAS, 7-18. Sept. 1992, CERN 94-01 Vol. 1.*  
Ref. 2: M.J. Syphers, T. Sen; *Notes on Amplitude Function Mismatch. SSCL-604-mc, Oct 1992. 19pp.*  
Ref. 3: M. Syphers, T. Sen, D. Edwards; *Amplitude Function Mismatch.. SSCL-PREPRINT-438, Published in IEEE PAC 1993 (attached)*  
Ref. 4: Syphers, M.J.; *Injection mismatch and phase space dilution. Fermilab-FN-458, June 1987*

### **Monitors:**

- Ref. 4: **FIRST RESULTS FROM BETATRON MATCHING MONITORS INSTALLED IN THE CERN PSB AND SPS.**  
By C. Bovet, R. Colchester, C. Dutriat, G. Ferioli, J.J. Gras, R. Jung, P. Knaus, U. Raich, J.M. Vouillot (CERN). CERN-SL-98-037-BI, CERN-SL-98-37-BI, Jun 1998. 4pp. 6th European Particle Accelerator Conference (EPAC 98), Stockholm, Sweden, 22-26 Jun 1998.
- Ref. 5: **INJECTION MATCHING STUDIES USING TURN BY TURN BEAM PROFILE MEASUREMENTS IN THE CERN PS**  
M. Benedikt, Ch. Carli, Ch. Dutriat, A. Jansson, M. Giovannozzi, M. Martini, U. Raich, CERN, Geneva, Switzerland, DIPAC 2001
- Ref. 6: **SENSITIVITY STUDIES WITH THE SPS REST GAS PROFILE MONITOR**  
G. Ferioli, C. Fischer, J. Koopman, M. Sillanoli, CERN, Geneva, Switzerland  
DIPAC 2001 Proceedings - ESRF, Grenoble
- Ref. 7: *Noninvasive single-bunch matching and emittance monitor*  
**PHYSICAL REVIEW SPECIAL TOPICS - ACCELERATORS AND BEAMS, VOLUME 5, 072803, A.**  
Jansson; CERN, CH-1211 Geneva 23, Switzerland
- Ref. 8: **BETA-MATCHING AND DAMPING OBSERVATION BY SR MONITOR AT ATF DR**  
T. Naito, Y. Hashimoto, H. Hayano, K. Kubo, M. Muto, J. Urakawa  
KEK, High Energy Accelerator organization, Tsukuba, Japan

# Amplitude Function Mismatch

M.J. Syphers, T. Sen  
 Superconducting Super Collider Laboratory\*  
 2550 Beckleymeade Ave., Dallas, TX 75237  
 and

D. A. Edwards  
 DESY/Fermilab  
 P. O. Box 500, Batavia, IL 60510

## Abstract

We develop the general equation of motion of an amplitude function mismatch in an accelerator lattice and look at its solution for some interesting cases. For a free  $\beta$ -wave oscillation the amplitude of the mismatch is written in terms of the determinant of a single matrix made up of the difference between the new Courant-Snyder parameters and their ideal values. Using this result, once one calculates the mismatch of the amplitude function and its slope at one point in the lattice (at the end of a *nearly* matched insertion, for example), then the maximum mismatch downstream can be easily computed. The formalism is also used to describe emittance growth in a hadron synchrotron caused by amplitude function mismatches at injection.

While most of the content of this paper is not new to the accelerator physics community, we thought it would be useful to place this important, basic information all in one place. Besides the classic work of Courant and Snyder, our sources include other papers, internal reports, and numerous discussions with our colleagues. More details may be found in a related paper.[1]

## I. A STARTING POINT

The general solution for linear betatron oscillations in one transverse degree of freedom can be written as[2]  $x(s) = A\sqrt{\beta(s)}\cos[\psi(s) + \delta]$  where  $A$  and  $\delta$  are constants given by the particle's initial conditions. The phase advance  $\psi(s)$  and the amplitude function  $\beta(s)$  satisfy the differential equations  $\psi' = \frac{1}{\beta}$ ,  $2\beta\beta'' - \beta'^2 + 4\beta^2K = 4$ , where  $K = e(\partial B_y/\partial x)/p$ , with  $e =$  charge,  $p =$  momentum,  $\partial B_y/\partial x =$  magnetic field gradient, and  $\beta' = d\beta/ds$ , etc. When one considers the periodic solution of the amplitude function, the motion through a single repeat period can be described in terms of the Courant-Snyder parameters  $\beta(s)$ ,  $\alpha(s) \equiv -(d\beta(s)/ds)/2$ , and  $\gamma(s) \equiv (1 + \alpha^2)/\beta$ , using the matrix

$$\begin{pmatrix} \cos \psi_C + \alpha \sin \psi_C & \beta \sin \psi_C \\ -\gamma \sin \psi_C & \cos \psi_C - \alpha \sin \psi_C \end{pmatrix} \quad (1)$$

which operates on the state vector  $X$ , with  $X = (x, x')^T$ . Here, the phase advance is  $\psi_C = 2\pi\nu = \int_{s_0}^{s_0+C} \frac{ds}{\beta(s)}$ , where

\*Operated by the Universities Research Association, Inc., for the U.S. Department of Energy under Contract No. DE-AC35-89ER40486.

$C$  is the repeat distance of the hardware, which may be the circumference of the accelerator, and  $\nu$  is the *tune* of the synchrotron.

The matrix of Equation 1 is often written in compact form as  $M = I \cos \psi_C + J \sin \psi_C$  where

$$J \equiv \begin{pmatrix} \alpha & \beta \\ -\gamma & -\alpha \end{pmatrix}. \quad (2)$$

The amplitude function and its slope propagate through an accelerator section according to

$$J_2 = M(s_1 \rightarrow s_2)J_1M(s_1 \rightarrow s_2)^{-1}, \quad (3)$$

where  $J_1$  and  $J_2$  contain Courant-Snyder parameters corresponding to points 1 and 2, and  $M(s_1 \rightarrow s_2)$  is the transport matrix between these two points.

## II. PROPAGATION OF A THIN GRADIENT ERROR

We wish to see how the amplitude function downstream of a thin gradient error is altered. If  $J_0(s_0)$  is the matrix of unperturbed Courant-Snyder parameters at the location of the error and  $J_0(s)$  contains the unperturbed parameters at a point downstream, then, using Equation 3,

$$\Delta J(s) = M(s_0 \rightarrow s)\Delta J(s_0)M(s_0 \rightarrow s)^{-1}, \quad (4)$$

where

$$\Delta J(s) = J(s) - J_0(s) = \begin{pmatrix} \alpha - \alpha_0 & \beta - \beta_0 \\ -(\gamma - \gamma_0) & -(\alpha - \alpha_0) \end{pmatrix}; \quad (5)$$

$\beta$  is the new value of the amplitude function at  $s$ ,  $\beta_0$  is the unperturbed value, etc. Through a thin quad,  $\Delta\alpha = q\beta_0$ ,  $\Delta\beta = 0$ , and  $\Delta\gamma = 2\alpha q + \beta q^2$  and so

$$\begin{aligned} \frac{\Delta\beta(s)}{\beta_0(s)} &= -(\beta_i q) \sin 2\psi_0(s - s_0) \\ &\quad + \frac{1}{2}(\beta_i q)^2 [1 - \cos 2\psi_0(s - s_0)] \end{aligned} \quad (6)$$

where  $\psi_0(s - s_0)$  is the unperturbed phase advance between points  $s_0$  and  $s$  and  $\beta_i \equiv \beta_0(s_0)$ . The amplitude function perturbation oscillates at twice the betatron frequency and for  $(\beta_i q)$  sufficiently small, the perturbation describes simple harmonic motion. The change in  $\alpha$  also propagates at

twice the betatron frequency, it being given by

$$\begin{aligned} \Delta\alpha(s) = & \beta_i q [\cos 2\psi_0(s - s_0) - \alpha_0(s) \sin 2\psi_0(s - s_0)] \\ & - \frac{1}{2}(\beta_i q)^2 [\sin 2\psi_0(s - s_0) \\ & - \alpha_0(s)(1 - \cos 2\psi_0(s - s_0))] . \end{aligned} \quad (7)$$

Introducing this quad error also changes the phase advance across the lattice. The new phase advance  $\psi(s - s_0)$  across this section may be calculated using  $\sin \psi(s - s_0) = \bar{M}(s_0 \rightarrow s)_{12} / \sqrt{\beta_i \beta(s)}$  where  $\bar{M}(s_0 \rightarrow s)_{12}$  is the (1,2) element of the new ring matrix and  $\beta(s)$  is the new amplitude function at  $s$ . Using Equation 6, we obtain

$$\begin{aligned} \sin \psi(s - s_0) = & [1 - \beta_i q \sin 2\psi_0(s - s_0) \\ & + (\beta_i q)^2 \sin^2 \psi_0(s - s_0)]^{-1/2} \sin \psi_0(s - s_0) . \end{aligned} \quad (8)$$

An explicit result for the change in the phase advance may be obtained perturbatively in orders of the quad error  $q$  from the above exact expression. To second order in  $q$ , we find that the change  $\Delta\psi \equiv \psi(s - s_0) - \psi_0(s - s_0)$  is

$$\Delta\psi = \beta_i q \sin^2 \psi_0(s - s_0)$$

$$- (\beta_i q)^2 \sin 2\psi_0(s - s_0) \sin^2 \psi_0(s - s_0) + O(q^3) . \quad (9)$$

To first order in  $q$ , at a point  $\pi/2$  away from the location of the error, there is no change in the  $\beta$  function while the change in phase advance is at its maximum value of  $\beta_i q$ .

### III. EQUATION OF MOTION OF $\beta$ -WAVE

The equation of motion for an amplitude function mismatch is nonlinear when  $s$  is taken as the independent variable. A more congenial equation can be developed by using the reduced phase  $\phi \equiv \psi/\nu$  as the independent variable. For betatron oscillations the Floquet transformation, where the other variable is  $\zeta = x/\sqrt{\beta}$ , produces the equation of motion  $\frac{d^2 \zeta}{d\phi^2} + \nu^2 \zeta = 0$  which is pure simple harmonic motion with frequency (tune)  $\nu$ . For the amplitude function mismatch, we need to define the reduced phase in terms of the unperturbed functions. That is, let  $\phi \equiv \psi_0/\nu_0$ , where  $d\psi_0/ds = 1/\beta_0$ , and  $\nu_0$  is the unperturbed tune. The equation of motion for  $[\beta(\phi) - \beta_0(\phi)]/\beta_0(\phi) \equiv \Delta\beta/\beta_0$  in the absence of gradient errors is then

$$\begin{aligned} \frac{d^2}{d\phi^2} \frac{\Delta\beta}{\beta_0} + (2\nu_0)^2 \frac{\Delta\beta}{\beta_0} &= -2\nu_0^2 \det\Delta J \\ &= 2\nu_0^2 [\Delta\alpha^2 - \Delta\beta\Delta\gamma] \end{aligned} \quad (10)$$

where  $\Delta\alpha = \alpha(\phi) - \alpha_0(\phi)$ , etc. The quantity  $\det\Delta J$  is an invariant in portions of the lattice without gradient perturbations as can be seen with the aid of Equation 3.

So, the free amplitude function distortion oscillates with twice the betatron tune and with a constant offset given by the determinant of the  $\Delta J$  matrix at any point. This offset must be there since  $\beta > 0$  and hence  $\Delta\beta/\beta$  must always be greater than  $-1$ .

Rewritten in terms of the Courant-Snyder parameters,

$$\det\Delta J = - \frac{\left(\frac{\Delta\beta}{\beta_0}\right)^2 + \left(\Delta\alpha - \alpha_0 \frac{\Delta\beta}{\beta_0}\right)^2}{1 + \Delta\beta/\beta_0} < 0. \quad (11)$$

Thus,  $|\det\Delta J|^{1/2}$  can be interpreted as the amplitude of the  $\beta$  mismatch for small perturbations.

The solution to Equation 10 is just simple harmonic motion with a constant term added:

$$\frac{\Delta\beta}{\beta_0}(\phi) = A \cos 2\nu_0\phi + B \sin 2\nu_0\phi + \frac{1}{2}|\det\Delta J|. \quad (12)$$

The constants  $A$  and  $B$  are found from the initial conditions:

$$A = \frac{\Delta\beta}{\beta_0}(0) - \frac{1}{2}|\det\Delta J|, \quad (13)$$

$$B = \alpha_0 \frac{\Delta\beta}{\beta_0}(0) - \Delta\alpha(0). \quad (14)$$

Thus, the maximum value of  $\Delta\beta/\beta_0$  downstream of our starting point  $\phi = 0$  is given by

$$\begin{aligned} \left(\frac{\Delta\beta}{\beta_0}\right)_{max} &= \sqrt{A^2 + B^2} + \frac{1}{2}|\det\Delta J| \\ &= \frac{|\det\Delta J|}{2} + \sqrt{|\det\Delta J| + \left(\frac{|\det\Delta J|}{2}\right)^2} \end{aligned} \quad (15)$$

where use has been made of Equation 11. The maxima occur at phases where

$$\tan 2\nu_0\phi = \left( \frac{\alpha_0 \frac{\Delta\beta}{\beta_0} - \Delta\alpha}{\frac{\Delta\beta}{\beta_0} - |\det\Delta J|/2} \right)_0 . \quad (16)$$

The usefulness of the above result is, of course, that once one calculates the mismatch of the amplitude function and its slope at one point in the lattice (at the end of a *nearly* matched insertion, for example), then the maximum mismatch downstream can be computed immediately.

If we look once again at the perturbation downstream of a thin quadrupole error, we see that just after the quad,

$$\det\Delta J = \begin{vmatrix} q\beta_i & 0 \\ -\Delta\gamma & -q\beta_i \end{vmatrix} = -(q\beta_i)^2 \quad (17)$$

where  $\beta_i = \beta_0$  at the location of the quadrupole. Then,

$$\left(\frac{\Delta\beta}{\beta_0}\right)_{max} = q\beta_i \sqrt{1 + (q\beta_i)^2/4} + \frac{1}{2}(q\beta_i)^2 \quad (18)$$

$$\approx q\beta_i = \sqrt{|\det\Delta J|} \quad (19)$$

where the last line is valid for small perturbations.

#### IV. GENERAL EQUATION OF MOTION

To include the driving terms due to gradient errors in the equation of motion for  $\Delta\beta/\beta_0$ , we let  $\beta_0$  satisfy the differential equation  $K\beta_0 = \gamma_0 + \alpha'_0$ , and let  $\beta$  satisfy  $(K + k)\beta = \gamma + \alpha'$ , where  $\beta = \beta_0 + \Delta\beta$ , etc. Then, the relative  $\beta$  error satisfies

$$\begin{aligned} & \frac{d^2}{d\phi^2} \frac{\Delta\beta}{\beta_0}(\phi) + (2\nu_0)^2 \frac{\Delta\beta}{\beta_0}(\phi) \\ &= -2\nu_0^2 \left[ \beta_0^2(\phi) k(\phi) \left( 1 + \frac{\Delta\beta}{\beta_0}(\phi) \right) + \det\Delta J(\phi) \right]. \end{aligned} \quad (20)$$

Here, in general,  $\det\Delta J(\phi)$  is not invariant as it is altered by gradient perturbations:

$$\frac{d}{d\phi} \det\Delta J(\phi) = \beta_0^2 k \frac{d}{d\phi} \frac{\Delta\beta}{\beta_0} \quad (21)$$

For small perturbations we can drop quantities which are second order in the small quantities, e.g.  $k\Delta\beta$ . This reduces Equation 20 to

$$\frac{d^2}{d\phi^2} \frac{\Delta\beta}{\beta_0}(\phi) + (2\nu_0)^2 \frac{\Delta\beta}{\beta_0}(\phi) = -2\nu_0^2 \beta_0^2 k(\phi) \quad (22)$$

as appears in Courant and Snyder.[2]

Noting that  $\Delta\alpha - \alpha_0(\Delta\beta/\beta_0) = -(1/2\nu_0)d(\Delta\beta/\beta_0)/d\phi$ , one can easily exhibit Equation 20 entirely in terms of  $\Delta\beta/\beta_0$  and its derivatives with respect to  $\phi$ . Differentiating this resulting equation one obtains a *linear* differential equation for  $\Delta\beta/\beta_0$ :

$$\begin{aligned} & \frac{d^3}{d\phi^3} \frac{\Delta\beta}{\beta_0} + (2\nu_0)^2(1 + \beta_0^2 k) \frac{d}{d\phi} \frac{\Delta\beta}{\beta_0} \\ &+ 2\nu_0^2 \frac{d}{d\phi} [\beta_0^2 k] (1 + \frac{\Delta\beta}{\beta_0}) = 0. \end{aligned} \quad (23)$$

#### V. INJECTION MISMATCH

It is also of interest to look at the effects of mismatches of amplitude functions upon entrance to an accelerator. The treatment below may be followed in more detail in [3] and [4]. A beam which is described by Courant-Snyder parameters that are not the periodic parameters of the accelerator into which it is injected will tend to filament due to nonlinearities and hence have its emittance increased. Suppose  $\beta$  and  $\alpha$  are the Courant-Snyder parameters as delivered by the beamline to a particular point in an accelerator, and  $\beta_0$ ,  $\alpha_0$  are the periodic lattice functions of the ring at that point. A particle with trajectory  $(x, x')$  can be viewed in the  $(x, \beta x' + \alpha x) \equiv (x, \eta)$  phase space corresponding to the beamline functions, or in the  $(x, \beta_0 x' + \alpha_0 x) \equiv (x, \eta_0)$  phase space corresponding to the lattice functions of the ring. If the phase space motion lies on a circle in the beamline view, then the phase space motion will lie on an ellipse in the ring view. The equation of the ellipse in the "ring" system will be

$$\frac{(1 + \Delta\alpha_r^2)}{\beta_r} x^2 + 2\Delta\alpha_r x\eta_0 + \beta_r \eta_0^2 = \beta_0 A^2. \quad (24)$$

where  $\beta_r \equiv \beta/\beta_0$  and  $\Delta\alpha_r \equiv \alpha - \alpha_0(\beta/\beta_0)$ .

If the phase space coordinate system were rotated so that the cross-term in the equation of the ellipse were eliminated, the ellipse would have the form  $x_e^2/b_r + b_r \eta_{oe}^2 = \beta_0 A^2$  where  $b_r \equiv F + \sqrt{F^2 - 1}$  and  $F$  is given by

$$F \equiv \frac{1}{2} [\beta_0 \gamma + \gamma_0 \beta - 2\alpha_0 \alpha]. \quad (25)$$

Note that if  $\Delta\alpha_r = 0$ , then  $b_r = \beta_r$ .

There is a physical significance to the quantity  $b_r$ ; it is the ratio of the areas of two circumscribed ellipses which have shapes and orientations given by the two sets of Courant-Snyder parameters found in the matrices  $J$  and  $J_0$ . This might suggest that a beam contained within the smaller ellipse upon injection into the synchrotron (whose periodic functions give ellipses similar to the larger one) will have its emittance increased by a factor  $b_r$ . However, this would be an over-estimate of the increase of the average of the emittances of all the particles.

If in the beamline view the new phase space trajectory is  $x^2 + \eta^2 = b_r R^2$ , then in the synchrotron view, the equation of the ellipse would be  $\frac{x^2}{b_r R^2} + \frac{\eta_0^2}{R^2/b_r} = 1$ . A particle with initial phase space coordinates  $x_i$  and  $\eta_{oi}$  will commence describing a circular trajectory of radius  $a$  in phase space upon subsequent revolutions about the ring. The equilibrium distribution will have variance in the  $x$  coordinate

$$\sigma^2 = \langle x^2 \rangle = \frac{\langle a^2 \rangle}{2} = \frac{b_r^2 + 1}{2b_r} \sigma_0^2 = F \sigma_0^2, \quad (26)$$

where  $\sigma_0^2$  is the variance in the absence of a mismatch. This expression can be rewritten in terms of  $\det\Delta J$  which we found in Section III:

$$\frac{\sigma^2}{\sigma_0^2} = 1 + \frac{1}{2} |\det(\Delta J)|. \quad (27)$$

For the case where the slope of the amplitude function is matched and equal to zero, we have

$$\frac{\sigma^2}{\sigma_0^2} = 1 + \frac{1}{2} \left( \frac{\Delta\beta/\beta_0}{\sqrt{1 + \Delta\beta/\beta_0}} \right)^2. \quad (28)$$

This says that a 20%  $\beta$  mismatch at injection, for example, would cause only a 2% increase in the rms emittance.

#### VI. REFERENCES

- [1] T. Sen, M. J. Syphers, "Notes on Amplitude Function Mismatch," SSC Report SSCL-604, October 1992.
- [2] E.D. Courant and H.S. Snyder, "Theory of the Alternating-Gradient Synchrotron," *Annals of Physics*, vol. 3, No. 1, p.26 (1958).
- [3] M. J. Syphers, "Injection Mismatch and Phase Space Dilution," Fermilab FN-458, June 1987.
- [4] D. A. Edwards and M. J. Syphers, *An Introduction to the Physics of High Energy Accelerators*, John Wiley, and Sons, New York, 1993.

## **Chapter 3**

### **Tune Diagnostics**

#### **3.1 Exercises: Tune Measurements**

## Tune Measurements including time resolved tracking of tunes

### Summary:

The students are confronted with the different ways of measuring betatron tunes. The importance of time resolved measurements is illustrated, which is well achieved with a PLL circuit. A simple analog model of a PLL circuit is developed.

### Problems to be solved:

Neglecting betatron oscillations after the injection process or beam instabilities we can assume that the particle beam will circulate on a stable closed orbit in the accelerator. In order to measure the betatron tune a transverse oscillation of the beam has to be excited and then observed with one or several position sensitive instruments. Depending on the choice of the excitation method and the observation instrument many different ways of measuring the tune with different qualities can be imagined. The following table gives a brief summary.

Beam Excitation Signal	Treatment of measured oscillation	Comments
Consecutive random noise kicks	Fourier transform	Work horse of operational tune measurement, precision 10 <sup>-3</sup> ...10 <sup>-4</sup>
Single kick	Fourier transform, sliding Fourier transform, wavelet analysis	Observation of damped oscillation, large initial amplitude (emittance dilution in hadron machines after filamentation), access to non-linearities Precision depends on damping time
Sin wave excitation with slowly varying frequency (CHIRP)	Synchronous detection of beam motion	Measurement of full beam transfer function (network analyser) Precision only limited by beam stability and measurement time, precision typical typical 10 <sup>-4</sup>
Continuous sin wave excitation on beam resonance	Phase locked loop (PLL) circuit keeps beam exciter on resonance	Best tool to trace tune changes during machine transitions (acceleration...) Information of full beam spectrum not available, precision depends on bandwidth of PLL. 10 <sup>-6</sup> can be
“AC-dipole”excitation Sin wave excitation OUTside frequencies of beam resonance	Fourier transform of beam motion	acts like a fast orbit changing dipole magnet, can create large amplitudes for diagnostics, no emittance blowup

**Question 1)** Discuss the table with your tutor and draw the time envelope of the beam excitation signal and the beam response for the first 3 methods:

- a) broad band noise excitation and frequency analysis of the resulting oscillation.
- b) single kick stimulus and frequency analysis of resulting oscillation
- c) swept sine wave excitation and vector analysis of resulting oscillation

For a) What happens in case one does not use broad band (white) noise? Imagine the extreme case that the bandwidth of the “noise” spectrum is reduced to a single sinusoidal line.

Another way of looking at tune measurements is in frequency domain:

One considers the beam as a linear resonating oscillator, which responds to a stimulus like a filter. One can hence draw the spectral intensity of the beam exciter and the spectral density of the resulting beam oscillation. The ratio of both functions corresponds to the transfer function of the beam (as resonator) and the betatron tune can be measured as the maximum of this transfer function.

**Question 2)** Repeat the discussion as in 1, but this time produce qualitative drawings in frequency domain for the input spectra and the output spectra. Indicate in the ratio of these spectra (i.e. in the “measured beam transfer functions”) the betatron tune.

We refer to the more rigorous mathematical treatment of a beam as damped harmonic oscillator as done for the transverse feedback.

**Question 3)** Draw the transfer function of the beam as resonator as amplitude and phase as function of frequency. What physics parameters determine the resonance frequency and the width of these functions?

One can build a simple electronic circuit (called **PLL** for **Phase Locked Loop**), which excites the beam (via an electromagnetic deflection element) permanently with a sin-wave. In the return path the beam oscillation is measured with a position sensitive pickup. The phase detector measures the phase between beam exciter and beam response. The phase information is feed back to the frequency of the driving exciter, such that the circuit maintains an oscillation on the center of the resonance, even if this resonance changes as a function of time.

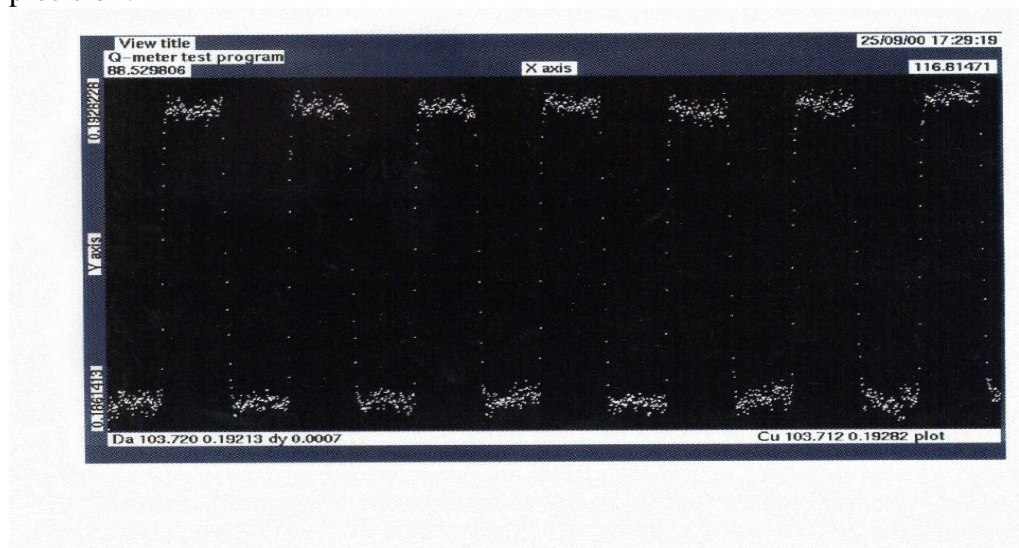
**Question 4)** Please draw a block diagram of the above circuit.

**Question 5)** If the phase detector of the above circuit is made, such that its output is proportional to  $\cos\Phi$ , then there will be no action on the frequency of the oscillator for  $\Phi=90$ . Use the answer of question 3 to indicate to what frequency the PLL circuit will lock in this case. If you had to build such a phase detector, how would you do that? By taking a second output of the controlled oscillator, which is 90 degrees shifted in phase (called a “quadrature oscillator” in the literature), one can construct another observable, which is proportional to  $\sin\Phi$ . This variable is at a maximum, in case the PLL has locked to the resonance.

**Question 6)** Draw a sketch, how the signal proportional to  $\sin\Phi$  could be used in order to regulate the amplitude of the beam exciting signal. Hint: Insert a 4-quadrant analog multiplier in to the output of the oscillator.

At last a practical measurement example (from LEP) is given: The measurement of the tunes in LEP during a rectangular current modulation in a LEP quadrupole.

**Question 7:** Knowing the amount of current modulation in the quadrupole and looking at the measured tune change, what beam quantity can be measured with this experiment? What precision does one need in the tune measurement, to measure the observable to 1% precision?



} 10<sup>-4</sup>

3.2 FURTHER READING I:

...

**3.2 Further Reading I:**

**Diagnostics and Control of the Time Evolution of Beam parameters**

**H.Schmickler, Proceedings of Beam Instrumentation Workshop DIPAC, DIPAC 1997**

**EUROPEAN ORGANIZATION FOR NUCLEAR RESEARCH**

**European Laboratory for Particle Physics**

CERN - SL DIVISION

CERN-SL-97-68 (BI)

**Diagnostics and Control of the  
Time Evolution of Beam Parameters**

Hermann Schmickler

**Abstract**

Measurement tools for the betatron tunes, chromaticity and coupling exists in every circular accelerator. This article reviews diagnostic tools for the time evolution of these beam parameters in view of potential online feedbacks on magnetic elements in the LHC. For chromaticity measurements a new development made at CERN based on the detection of the phase difference between head and tail betatron oscillations is presented.

*Paper presented at the Third European Workshop on Beam Diagnostics and  
Instrumentation for Particle Accelerators (DIPAC 97),  
Frascati, Italy, 12-14 October 1997*

Geneva, Switzerland  
December, 1997

# Diagnostics and Control of the Time Evolution of Beam Parameters

Hermann Schmickler, CERN, CH-1211 Geneva 23, (Switzerland)

**Abstract:** Measurement tools for the betatron tunes, chromaticity and coupling exists in every circular accelerator. This article reviews diagnostic tools for the time evolution of these beam parameters in view of potential online feedbacks on magnetic elements in the LHC. For chromaticity measurements a new development made at CERN based on the detection of the phase difference between head and tail betatron oscillations is presented.

**Introduction:** The following work has been stimulated by the participation in a working group called “*Dynamic Effects Working Group*” at CERN. In this working group various aspects of time varying magnetic fields and their control are studied for the LHC [1]. In particular at the beginning of the acceleration large variations of the betatron tunes, the chromaticities and coupling over a few seconds can be anticipated.

The author has collected experience from FNAL (Tevatron) , DESY (HERA-P), from older proton machines at CERN (SPS, ISR, PS) and from LEP on the subjects of measurement tools and eventual online feedback loops.

## 1. TUNE MEASUREMENTS

### 1.1 Fourier Transform (FFT) of beam motion:

The most common method for tune measurements is the excitation of a beam motion (in most cases broad band excitation with white noise) and the computation of the power density spectrum in frequency domain. The betatron tunes are determined as the frequency with the highest amplitude peak. The frequency resolution  $\Delta f$  is inversely proportional to the number of oscillation samples ( $N_{\text{samp}}$ ). One can write:  $\Delta f = 2/N_{\text{samp}}$ . So if for example one needs a tune resolution of  $10^{-3}$ , at least 2000 samples have to be acquired. A modern computer can perform the time frequency transform (FFT) of 2048 samples in about 1 msec. For typical signal to noise ratios about a factor 4 can be gained in tune resolution by interpolation between the measured amplitude values [2]. If there is enough external excitation from other sources (ground motion, power supply ripple) or the beam is slightly unstable by itself the method also gives useful information without specific beam excitation. The signal to noise ratio can be improved by averaging several spectra into one measurement display.

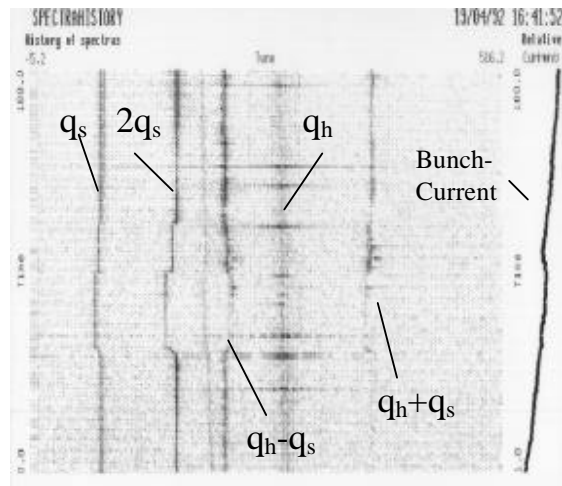


Fig.1: Accumulated spectra during LEP injection.

The time evolution of the tunes can be measured by accumulating many spectra and presenting them in a mountain range display. Figure 1 gives an example measured in LEP during injection. This figure nicely illustrates the diagnostic power of accumulated spectra. Apart from the horizontal tune multiples of the synchrotron tune and the synchrotron sidebands of the horizontal tune are visible. During a certain period two Rf-cavities had tripped (visible as shift in the synchrotron tunes). Such a tool is indispensable for machine set up and the study of many dynamic processes.

### 1.2 Chirp Excitation

As a variant of the previous method the beams are excited with a sine wave of time variable frequency. If one sends the excitation signal to a loudspeaker one gets the impression of a singing bird (at least at large machines!). For this reason the excitation is called “chirp” excitation. The chirp range is set around the expected betatron tunes and the length is taken corresponding to the requested time resolution and precision of the tune measurements. Data analysis of the resulting beam motion is either via sliding window Fourier transform or via a wavelet analysis [3]. The advantage of this method compared to noise excitation is that the phase information between excitation and beam motion is easier obtained and hence due to the better signal to noise ratio smaller excitation

amplitudes can be used. Figure 2 shows the result of a chirp measurement in the SPS. The sweep length is 20 msec and the repetition rate is 30 msec. In total 150 chirp measurements cover acceleration. More details can be found in [4].

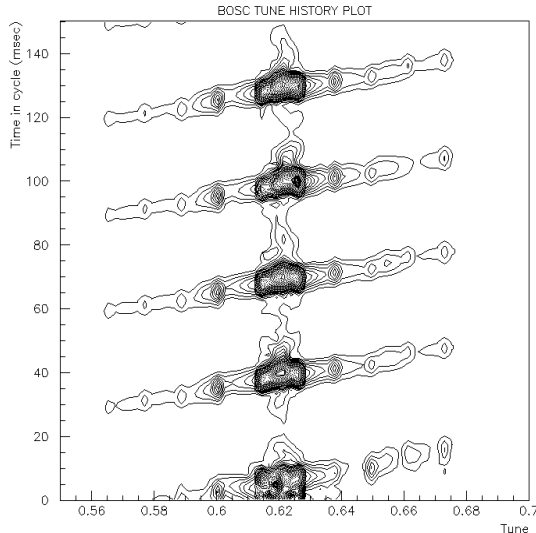


Fig. 2: Chirp tune measurement in the SPS. The horizontal scale is tune, the vertical scale is time (msec). The amplitude of the beam motion is encoded as grey scale.

### 1.3 Swept Frequency Analysis

For this method (often called “Network Analysis”) the beams are excited with a steady sinusoidal wave. Amplitude and Phase of the resulting oscillation are precisely determined by means of harmonic analysis. Thereafter the excitation frequency is increased in steps until the range of interest is covered. This represents a very precise measurement yielding the full information of the beam transfer function. The disadvantage is the long measurement time, which renders the method of little use for the study of dynamic phenomena. Details can be found in [5].

### 1.4 Phase Locked Loop Tune Tracker (PLL)

Most tune measurements use the amplitude peak of the beam oscillation as signal for tune measurements. This is somewhat odd, since the amplitude information with “0-slope” at its maximum suffers much more from noise than the phase information, which has its maximum slope at the tune resonance. Phase Locked Loop Circuits instead make use of the phase slope. The beams are excited with a continuous sine wave. By changing the frequency of the exciting oscillator an analog or digital circuit assures that the phase difference between excitation and beam motion is  $90^\circ$ . The tune measurement simply consists in a readout of the (filtered) frequency of the oscillator. In reality the design of such a PLL is more complicated, in particular the lock-in procedure and additional regulation circuits for constant amplitude of the beam oscillation. Many

details can be found in [6]. As the readout of the oscillator frequency can be made almost continuous a PLL circuit is the ideal tool for tracking the time evolution of the betatron tunes during machine transitions. Good measurement examples can be found in chapter 2.1 and 3.1 of this report.

### 1.5 Discussion

Common to all tune measurements is an exciter and an oscillation detector. The most natural approach is to implement the data treatment and the synthesis of the beam stimulus as a digital process of a system located “between” the monitor and the exciter. With the computing power of modern digital signal processors this should be a possible concept even for machines with revolution periods down to the microsecond. In that case the change in functionality is realised by a software reload.

The following functionalities are imported for the study of dynamic machine processes:

- Accumulated FFT spectra. Apart from the betatron tune lines other important spectral information is contained in the measurements. Beam excitation is done with random kicks or chirp signals.
- PLL tune tracking. In contrast to the previous method only the values of the betatron tunes are measured. With a good compromise in time resolution versus measurement noise a new tune reading is obtained every 100 machine turns.

The **Emittance Blowup** due to the beam excitation is of little importance for lepton machines, but this aspect is the key question for a proton machine. For machine studies and measurements during the setting up emittance blowup to a certain level can be tolerated, but on the operational beams for luminosity production one will only occasionally use a measurement with large (mm) oscillations. Accumulated or integrated spectra are very useful as they can be done without any excitation. In case the beams are quiet or kept quiet with a transverse feedback the use of chirp excitations can be considered, as the beam stimulus is centred around the region of interest. PLL tune tracking is on the first sight the worst one can do, as the beams are continuously excited on the resonance. On the other hand the very good signal to noise ratio of a PLL allows to work with sub micron beam oscillation amplitudes. Although not yet completely operational it has been shown at HERA-P that an online PLL tune measurement on two of the bunches of an operational beam was used for long periods without significant blowup [7].

## 2. Chromaticity Measurements

### 2.1 Variation of beam momentum

The commonly used method works by measuring directly the quantities involved in the definition of the chromaticity  $\xi$ . The definition is:

$$\Delta q = \alpha \cdot \frac{\Delta p}{p} = \alpha \cdot a \cdot \frac{\Delta f_{RF}}{f_{RF}} \quad (1)$$

( $\alpha$  = momentum compaction factor)

i.e. one measures the tune dependence  $\Delta q$  on beam momentum ( $\Delta p/p$ ), which is very often done by varying the Rf-frequency ( $\Delta f_{RF}/f_{RF}$ ).

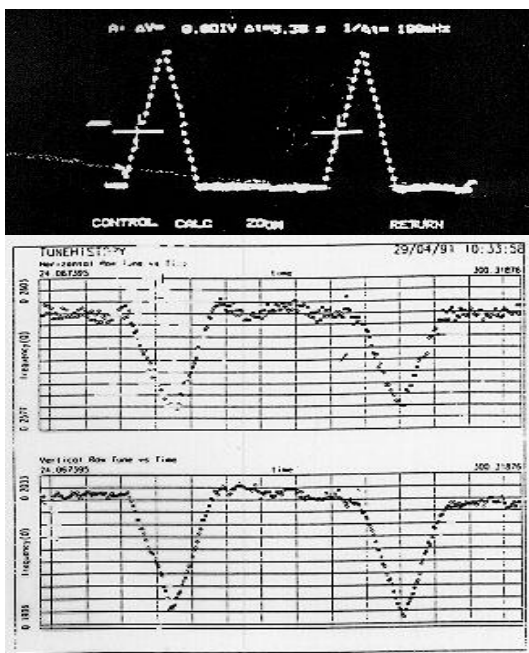


Fig. 3 Dynamic Chromaticity Measurement in LEP. Rf-frequency modulation measured on the tuning system (top trace) and tunes measured in PLL mode (bottom traces).

Figure 3 illustrates the measurement procedure implemented for LEP [8]. The tunes are measured in PLL mode (bottom traces) and the Rf-frequency is modulated in a three second long cycle with an asymmetric wave shape. The asymmetry of the modulation is important, as it allows to identify the sign of the chromaticities from the tune measurements. This is nicely visible in figure 4, which shows a chromaticity measurement during a beta squeeze of LEP. The top trace shows a diminishing horizontal chromaticity, which changes sign and then returns back to nominal sign and magnitude. The vertical chromaticity stays almost constant.

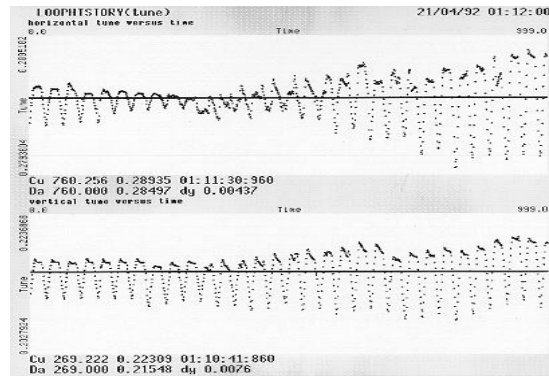


Fig.4: Horizontal (top trace) and vertical (bottom trace) chromaticity measurements during the beta squeeze in LEP.

### 2.2 Amplitude of Synchrotron Sidebands

The amplitude ratio of the betatron lines to their synchrotron side bands contains information on the chromaticity of the machine. This could well be used on accumulated tune spectra during machine transitions in order to get chromaticity information, but if the betatron tunes change a lot, it is not clear whether systematic lattice resonances influence the observed amplitude ratio. Studies have been made in LEP [9], but the issue has not been continued. In particular in proton machines the measurements are quite difficult, as the synchrotron tune is low and the signals of the side bands are often swamped in the spectral leakage of the main line.

### 2.3 Width of Tune Resonance

Using again equation (1) one can see that the momentum spread of the beam will result in a width of the betatron lines. Hence measuring the width of the resonance (best via swept frequency analysis (see chapter 1.3)) could be used as a measure of chromaticity. But there are other effects contributing to the line width (radiation damping, transverse feedbacks...), such that one normally looks only for variations in the width in order to deduce chromaticity changes. But in particular during acceleration this analysis is quite complicated, as the momentum spread changes during the measurement.

### 2.4 Frequency Shift in Bunch Spectrum

The longitudinal bunch profile generates a certain frequency spectrum in an electromagnetic coupler. If one excites betatron oscillations the longitudinal shape of the bunch changes depending on the chromaticity and hence will result in a different bunch spectrum. A detailed analysis yields that in frequency domain the measurable quantity is a shift in the peak of the bunch spectrum [10]. Experiments with this method are quite difficult and are at present not exploited for routine operation.

## 2.5 Phase of Head and Tail Betatron oscillations

This method is presently under development at CERN and has been stimulated by the ideas of the previous method. Rather than measuring in frequency domain the shift in bunch spectrum, the betatron oscillations of head and tail are individually sampled in time domain. The observable linked to the chromaticity is the phase difference between the head and tail oscillations. By the exciting kick this phase difference is initially forced to zero, evolving to a maximum after half a synchrotron period and then the oscillations rephase again after one complete synchrotron period. Figure 5 shows a computer simulation of the head tail motion for non zero chromaticity for illustration. The vertical axis is time (in [ns] along the longitudinal bunch profile), the horizontal axis is the revolution number after the kick stimulus and the amplitude of the betatron oscillation is encoded as grey scale. The head and tail oscillations are sampled in time slices indicated by the horizontal lines.

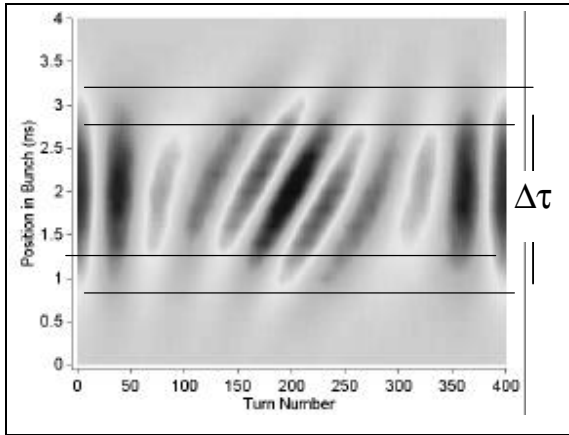


Fig. 5: Computer simulation of head-tail motion.

The chromaticity can be expressed as follows:

$$\chi = \frac{-\eta \cdot \Delta\Psi_i}{Q_0 \omega_0 \Delta t (\cos(2p \cdot i Q_s) - 1)} \quad (2)$$

with:  $\eta=1/\gamma^2-\alpha$ ;  $Q_s$  = synchrotron tune,  $\omega_0$  = angular revolution frequency;  $\Delta\Psi_i$  = head-tail phase difference,  $\Delta t$  = sampling time interval (see figure 6),  $Q_0$  = betatron tune and  $i$  turn index since initial kick

Practically the measured chromaticity does not depend on the betatron tune, as  $Q_0$  in equation 2 is the total tune of the machine. A first series of measurements have been performed in the SPS in order to validate the basic idea. The results are very good. For instance an agreement within 15% of the chromaticity measured via momentum change and the new method could be found over a wide

range of chromaticities. One dataset from these measurements is reported in figure 7. It shows the measured head-tail phase shift turn by turn for 3 different values of the sampling time interval  $\Delta t$ . As expected from equation 2 the dependence is linear. Any explanation of experimental details would leave the scope of this paper, but can be found in [11]

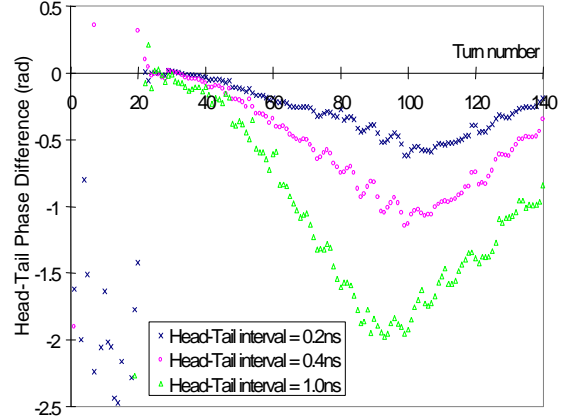


Fig. 6: Measured phase difference of head-tail betatron oscillations for 3 different sampling time intervals.

## 2.6 Discussion

By variation of the beam momentum and tune tracking a solid operational tool is available for dynamic chromaticity measurements. By extending the range of momentum variation even the non linear part of the chromaticity curve can be examined. But still the method has some limitations: The rate by which the beam momentum is changed can not be made extremely short, for example in LEP the modulation cycle is limited to a 3 second interval. This is certainly too long for a chromaticity measurement during the start of acceleration, were a time resolution as short as 100 msec would be of interest. The LHC will require for the nominal beam currents tight control of the orbit, in particular in the collimation region. Periodic momentum changes and hence orbit changes in dispersive regions will be a problem. Secondly if one imagines the use of an online tune regulation loop a chromaticity measurement based on tune differences is very unfavourable. In that case the chromaticity would have to be deduced from the trims that the regulator has send to the quadrupoles in order to keep the tunes constant. With some sense for practical implementations one feels that this would not work!

For these reasons the development work on the head-tail sampling has been launched. The method provides a chromaticity reading independent of the betatron tunes and a measurement time of one synchrotron period (15 to 50 msec in case of the LHC). Further analysis will show the influence of octupolar fields, the limit in signal to noise ratio and consequently the amount of emittance growth that is linked with a single measurement.

### 3. Coupling Measurements

Coupling Measurements and Control are also important for the LHC. As the working point will be very close to the diagonal a bad compensation of betatron coupling will make tune and chromaticity measurements almost impossible. A very good and comprehensive summary of linear betatron coupling can be found in [12].

#### 3.1 Closest Tune Approach

For this method both betatron tunes are measured during a linear power converter ramp, which crosses the values of the horizontal and vertical tunes. The remaining separation of the tune traces is a direct measure for the total coupling coefficient  $|c|$ . A measurement example from is shown in figure 7. In order to ensure that the PLL keeps tracking both tunes even when they approach each other the measurements are done on two different bunches.

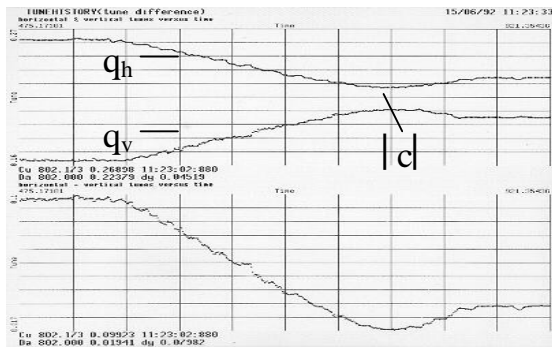


Fig. 7: PLL tune tracking during a swap of the tunes. The two top traces show the tunes, the bottom trace the tune difference reading.

#### 3.2 Kick Method

The above method does not allow diagnostic during machine transitions. A better tool, although demanding quite large beam excitations for the measurement of small coupling coefficients, consists in applying a single kick in one plane and observing the time evolution of the betatron oscillations in both planes. The method is described in [12].

### Summary

Comprehensive tools for tune, chromaticity and coupling measurements will be available for the diagnostic of dynamic phenomena in the LHC. The major development effort over the next years will be to improve the signal to noise ratio of the oscillation detectors for minimising the emittance blowup during the measurement. Control of the time evolution of these beam parameters will first of all be achieved by feed forward techniques, i.e. beam and magnetic measurements on one acceleration cycle and then incorporation of the necessary trims into the power converter functions.

In case the reproducibility of the machine is not good enough to comply with tight tolerances an online feedback on magnetic correction elements has to be implemented. It should be noted that none of the big present hadron storage rings make operationally use of an online feedback on tune, chromaticity or coupling. The implementation of online feedbacks demands an effort on two additional fronts: The design of the feedback itself taking into account the dynamic behaviour of all involved elements and secondly the design of reliable measurement systems, which deliver signals for the betatron tunes, chromaticities and eventually coupling, without the need of human interpretation of the results.

### References:

- [1] R. Bailey et al., "Dynamic Effects and their Control at the LHC", PAC97, Vancouver, 12-16 May 1997, LHC Project Report 124
- [2] H. Schmickler, "Study of the Accuracy and Computation Time requirements for a FFT based Measurement of Betatron Oscillations in LEP", LEP/BI/Note 87-10
- [3] - K.H. Mess, "Time and Frequency Domain Measurements", Presentation MOI2, this workshop.
- [4] A. Stillman, "Wavelet Analysis and Accelerator Signals", Proc. of the BIW94, Vancouver (Canada)
- [5] C. Boccard et al., "Tune Measurements in the SPS as Multicycling machine", Proc. of EPAC96, pp. 1600-1602, Sitges (Barcelona), 10-14 June 1996.
- [6] I. Farago et al., "Performance of the LEP Q-Meter during Operation and Machine Studies", Proc. of EPAC90, Nice (France), June 12-16, 1990, CERN/SL/90-40(BI)
- [7] K.D.Lohmann et al., "Design and Functionality of the LEP Q-Meter", Proc. of EPAC90, Nice (France), June 12-16, 1990, CERN/SL/90-32(BI)
- [8] J. Klute, "A New Tune Measurement System for the HERA Proton Ring", Contribution TUP11, this workshop.
- [9] G. Buur et al., "Dynamic Tune and Chromaticity Measurements in LEP", CERN SL/92-15(DI), paper presented at the 3<sup>rd</sup> EPAC, Berlin, 24 March 1992
- [10] K. Cornelis et al., "Resonant behaviour of head-tail modes", SL-MD Note 145 (CERN).
- [11] A. Hofmann, "Diagnostics and Cures for Beam Proc. of the 8<sup>th</sup> international conference on high energy accelerators, CERN 1971
- [12] D Cocq, R. Jones and H. Schmickler, "Chromaticity Measurements from Head-Tail Phase-Shift", internal CERN publication in preparation and abstract submitted to EPAC98.
- [13] P.J.Bryant, "A simple theory for weak betatron coupling", CERN accelerator school, CERN 89-03, pp 50ff.

**3.3 Further Reading II:**

**High Sensitivity Tune Measurement by Direct Diode Detection**

**M.Gasior (CERN), R.Jones (CERN), Proceedings of Beam Instrumentation Workshop DIPAC, DIPAC 2005**

### 3.3 FURTHER READING II:

...

`%includepdf[pages=1-4]Hermann/BBQ.pdf`

## **Chapter 4**

### **Beam Loss Monitoring (BLM)**

#### **4.1 Exercises**

# **Beam Loss Monitors**

## CAS Afternoon Course

### Exercises



by Kay Wittenburg, -DESY-

# 1 Introduction

Beam loss monitor systems are designed for measuring beam losses around an accelerator or storage ring. A detailed understanding of the loss mechanism, together with an appropriate design of the BLM-System and an appropriate location of the monitors enable a wide field of very useful beam diagnostics and machine protection possibilities.

Beam losses can be divided into two different classes:

## **1) Irregular losses.**

sometimes called “fast or uncontrolled losses”: These losses may be distributed around the accelerator and not obviously on a collimation system. They are very often a result of a misaligned beam or a fault condition, e.g. operation failure, trip of the HF-system or of a magnet power supply. Losses should be avoided and should be kept to low levels.

### **Discuss why it should be avoided?**

Sometimes such losses have to be tolerated even at a high level at low repetition rates during machine studies. However, a beam loss monitor system should define the allowed level of those losses. The better protection there is against these losses, the less likely is down time due to damage of components. A post mortem event analysis is most helpful to understand and analyse the faulty condition.

## **2) Regular losses.**

sometimes called “slow” or “controlled” losses: Those losses are typically not avoidable and are localized on the collimator system or on other (hopefully known) aperture limits. They might occur continuously during operational running and correspond to the lifetime/transport efficiency of the beam in the accelerator. The lowest possible loss rate is defined by the theoretical beam lifetime limitation due to various effects.

### **Discuss which effects?**

It is clearly advantageous to design a BLM-System which is able to deal with both loss modes.

In addition measurements of injection-, ejection- or collimator- efficiencies can be performed using BLMs or beam current monitors, as well as background measurements in the detectors. This survey concentrates on BLM systems which cover the entire accelerator.

## 1.1 Principles of loss detection

### **What should a Beam Loss Monitor monitor?**

...

**Exercise BLM 1a:**

Assuming a high energy accelerator, what is the main physical process in a BLM-detector to produce a useful signal?

Solution:

---

**Exercise BLM 1b:**

What is important for a BLM (System)? Why?

Discussion in plenum

---

**Exercise BLM 1b:**

Which types of BLMs do you know?

Discussion in plenum

---

## **2 Measuring Beam Losses**

### **2.1 Regular losses**

**Exercise BLM 2a:**

**HERAp is a proton storage ring (920 GeV/c) with 6.3 km circumference.**

**How many beam particles are lost within a second ( $N_{\text{Lost}}$ ), assuming a proton beam current of  $I_0=70$  mA and a lifetime of  $\tau = 50$  hours?**

**$I = I_0 \cdot \exp(-t/\tau)$**

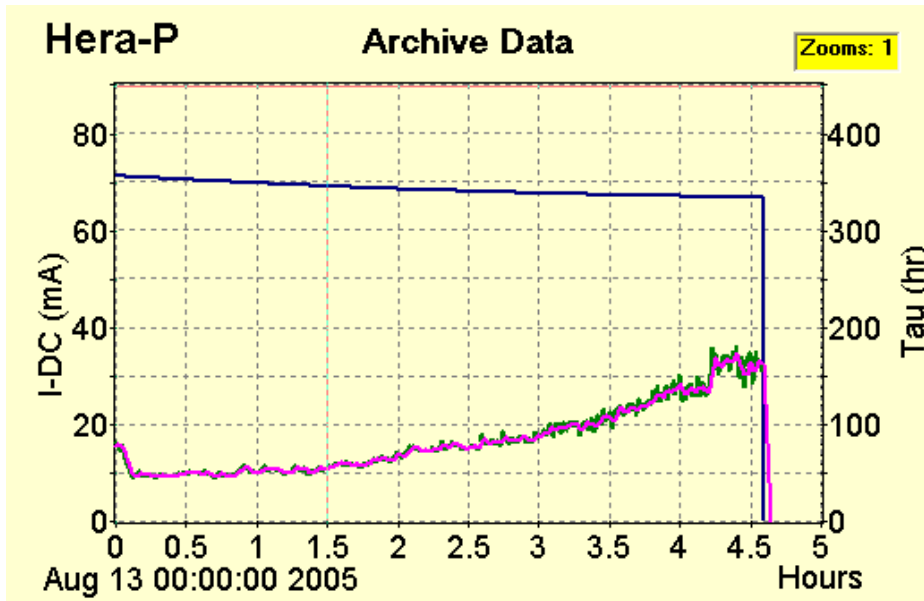


Fig. 1: Beam current [mA] vs time

*Solution*

---

**Exercise BLM 2b: 920 GeV protons,  $dE/dx = 11.6$  MeV/cm for Fe**

- 1) **Assuming all protons are lost in a  $1 \text{ cm}^3$  block of iron (penetration length  $L = 1$  cm). Calculate the deposit power  $P$  [W] in the block ( $1 \text{ J} = 6.241 \cdot 10^{18} \text{ eV}$ ):**
- 2) **Assume that all protons are absorbed in a collimator. Calculate the absorbed power:**
- 3) **The whole beam (70 mA) is absorbed in a collimator within 1 s. Calculate the absorbed power:**

*Solution:*

---

This number gives a macroscopic feeling of the measurable power due to beam losses during a bad luminosity run in HERAp with worse lifetime. Possible reasons for these losses are: Beam-beam kicks, transversal and longitudinal dispersion, residual gas scattering, halo scraping, instabilities... These losses can be used for beam diagnostics (see e.g. Ref. 3). But note that typically losses might not be concentrated at one location only!

### **Where to put the BLMs to measure beam losses?**

Each BLM at different locations needs its special efficiency-calibration in terms of signal/lost particle. This calibration can be calculated by use of a Monte Carlo Program with the (more or less) exact geometry and materials between the beam and the BLM. For the simulation it might be important to understand the (beam-) dynamics of the losses and the loss mechanism.

-----

### **Exercise BLM 2c:**

At a certain location of a BLM in HERA (collimator), the efficiency to beam losses is about  $\varepsilon = 0.1 \text{ MIP} / (\text{cm}^2 \cdot \text{lost proton})$  (at 300 GeV/c) at the BLM location.

**Calculate the resulting current  $I_{\text{ion}}$  of a 1 litre air filled ionization chamber BLM. Assume that 1/10 of the losses above (Exercise BLM 2a) occur here. About  $E_{\text{pair}} = 22 \text{ eV/pair}$  is needed to create an electron / ion pair in air. Hint:  $dE/d_{\text{xair}} = 2.2 \cdot 10^{-3} \text{ MeV/cm}$ .**

*Solution:*

-----

## **2.2 Quench Protection**

A serious problem for high current and high brilliance accelerators is the high power density of the beam. A misaligned beam is able to destroy the beam pipe or collimators

and may break the vacuum. This fact makes the BLM-System one of the primary diagnostic tools for beam tuning and equipment protection in these machines.

Superconducting accelerators need a dedicated BLM-system to prevent beam loss induced quenches. Such a system has to detect losses fast enough before they lead to a high energy deposition in the superconducting material.

**Exercise BLM 2d:**

**Which design criteria are important for a BLM system to prevent beam loss induced quenches (Discussion in plenum)?**

Solution:

-----

**Exercise BLM 2e:**

**What is a “critical loss rate”? How to define it**

Discussion in plenum

-----

**Calculation from the following table and figure (note the time scale of the losses) the current  $I_{ion}$  in a 1 liter air filled ionization chamber at the critical loss rate at 40 and 820 GeV/c (at that particular location):**

Momentum [GeV/c]	efficiency $\varepsilon$ [MIP/cm <sup>2</sup> /proton]
40	$3.25 \cdot 10^{-4}$
100	$4.47 \cdot 10^{-4}$
400	$1.53 \cdot 10^{-3}$
820	$2.20 \cdot 10^{-3}$

Tab. 1: Efficiency  $\varepsilon$  vs beam momentum for the BLMs at the superconducting magnets in HERA

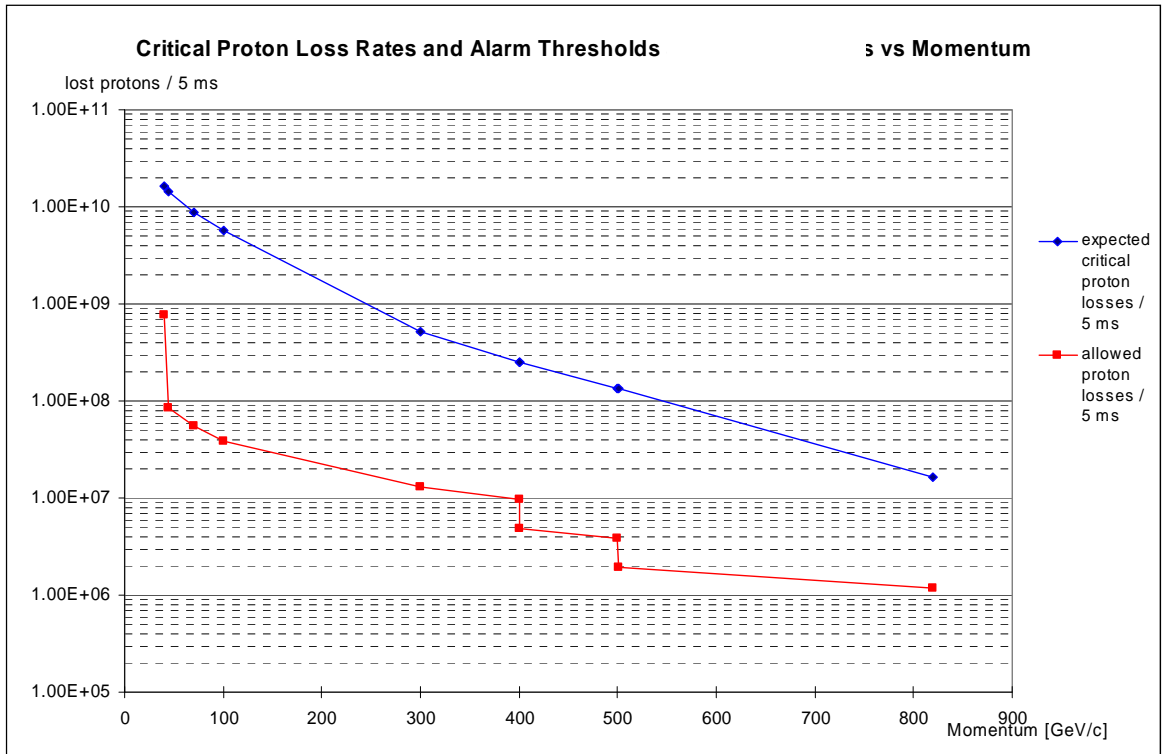


Fig. 2: Critical proton loss rate (above a quench occur) vs. momentum for the superconducting magnets in HERAp

Follow the calculations on the slides...

Note that regular losses at this location ( $\epsilon \approx 1 \cdot 10^{-3}$ ) give an ion-chamber current of  $8.16 \cdot 10^{-2}$  nA (exercise 2c). Therefore the dynamic range of a BLM system should exceed  $10^6$  to measure regular losses (diagnostic) as well as dangerous losses.

How to design a readout system with such a huge dynamic range?

See R. Jones talk (CAS: Beam Instrumentation) or Ref. [4] for the LHC solution to cover the whole range: =>

-----

# **BLMs in LINACs**

## **Exercise BLM 3a:**

**Calculate electron loss rate/bunch of 60fA/m at a bunch rate of 1 MHz**

Solution:

-----

## **Exercise BLM 3b:**

**Calculate electron loss rate/bunch of 1W/m loss-power at a bunch rate of 1 MHz**

Solution:

-----

## **Exercise BLM 3c:**

**What's the required dynamic range?**

Solution:

-----

## **Exercise BLM 3d:**

**Which type of BLM do you recommend for LINACs?**

Discussion in Plenum

-----

## 4.2 FURTHER READING

### **4.2 Further Reading**

## **References attached:**

### **Beam Loss Detection**

K. Wittenburg

Deutsches Elektronen Synchrotron, DESY

Proc. 1st European Workshop on Beam Diagnostics and Instrumentation for Particle Accelerators, Montreux, Switzerland, 3-5.5.1993,

CERN PS/93-35 (BD)

<http://adweb.desy.de/mdi/downloads/BLM-DET.pdf>

### **Beam Loss Monitoring and Control**

Kay Wittenburg,

Deutsches Elektronen Synchrotron DESY, Hamburg, Germany

Proc. Eighth European Particle Accelerator Conference, La Villette – PARIS, 3 - 7 June 2002

<http://accelconf.web.cern.ch/AccelConf/e02/PAPERS/THYGB001.pdf>

## **References to download:**

K. Wittenburg

### **Beam loss monitors**

CERN Accelerator School 2008 Specialised Beam Diagnostics School in [Dourdan](#), France,

CERN-2009-005; pp 249 ff.: <http://cdsweb.cern.ch/record/1071486/files/cern-2009-005.pdf>

#### **Abstract**

This lesson discusses the fundamental aspects of measuring beam losses including their use for beam diagnostic and safety issues. Also the detailed functionality and detection principle of various common beam loss monitors are presented, with a focus on their intrinsic sensitivity.

R.E. Shafer

### **A Tutorial on Beam Loss Monitoring**

Proc. 10th Beam Instrumentation Workshop

Brookhaven National Laboratory, Upton, NY

May 6 - 9, 2002

[http://ab-div-bdi-bl-blm.web.cern.ch/ab-div-bdi-bl-blm/Beam\\_loss\\_detectors/Literature/schaefer\\_biw02\\_tutorial.pdf](http://ab-div-bdi-bl-blm.web.cern.ch/ab-div-bdi-bl-blm/Beam_loss_detectors/Literature/schaefer_biw02_tutorial.pdf)

**Abstract.** The beam loss monitoring system is one of the two most widely distributed beam diagnostic systems at most particle accelerator facilities. This tutorial reviews the characteristics of the ionizing radiation from beam losses, and the properties of beam loss radiation detectors.

E.B. Holzer et al.,

### **Beam loss monitoring system for the LHC.,**

CERN-AB-2006-009, Feb 2006. 2005 IEEE Nuclear Science Symposium and Medical

Imaging Conference, El Conquistador Resort, Puerto Rico, 23-29 Oct 2005. , IEEE, Volume

2:1052 – 1056, <http://weblib.cern.ch/abstract?CERN-AB-2006-009>

L. Fröhlich,

### **Beam Loss Monitors,**

ERL Instrumentation Workshop, Cornell University, 2-3 June 2008

[http://tesla.desy.de/~lfroehli/download/ERL\\_instrumentation\\_ws\\_2008\\_BLMs.pdf](http://tesla.desy.de/~lfroehli/download/ERL_instrumentation_ws_2008_BLMs.pdf)

## 6. ATOMIC AND NUCLEAR PROPERTIES OF MATERIALS

**Table 6.1.** Revised May 2002 by D.E. Groom (LBNL). Gases are evaluated at 20°C and 1 atm (in parentheses) or at STP [square brackets]. Densities and refractive indices without parentheses or brackets are for solids or liquids, or are for cryogenic liquids at the indicated boiling point (BP) at 1 atm. Refractive indices are evaluated at the sodium D line. Data for compounds and mixtures are from Refs. 1 and 2. Further materials and properties are given in Ref. 3 and at <http://pdg.lbl.gov/AtomicNuclearProperties>.

Material	Z	A	$\langle Z/A \rangle$	Nuclear collision length $\lambda_T$ {g/cm <sup>2</sup> }	Nuclear interaction length $\lambda_I$ {g/cm <sup>2</sup> }	$dE/dx _{\min}^b$ { $\frac{\text{MeV}}{\text{g/cm}^2}$ }	Radiation length <sup>c</sup> $X_0$ {g/cm <sup>2</sup> } {cm}		Density {g/cm <sup>3</sup> } {g/ℓ} for gas	Liquid boiling point at 1 atm(K)	Refractive index $n$ {(n-1)}×10 <sup>6</sup> for gas
H <sub>2</sub> gas	1	1.00794	0.99212	43.3	50.8	(4.103)	61.28 <sup>d</sup>	(731000)	(0.0838)[0.0899]		[139.2]
H <sub>2</sub> liquid	1	1.00794	0.99212	43.3	50.8	4.034	61.28 <sup>d</sup>	866	0.0708	20.39	1.112
D <sub>2</sub>	1	2.0140	0.49652	45.7	54.7	(2.052)	122.4	724	0.169[0.179]	23.65	1.128 [138]
He	2	4.002602	0.49968	49.9	65.1	(1.937)	94.32	756	0.1249[0.1786]	4.224	1.024 [34.9]
Li	3	6.941	0.43221	54.6	73.4	1.639	82.76	155	0.534		—
Be	4	9.012182	0.44384	55.8	75.2	1.594	65.19	35.28	1.848		—
C	6	12.011	0.49954	60.2	86.3	1.745	42.70	18.8	2.265 <sup>e</sup>		—
N <sub>2</sub>	7	14.00674	0.49976	61.4	87.8	(1.825)	37.99	47.1	0.8073[1.250]	77.36	1.205 [298]
O <sub>2</sub>	8	15.9994	0.50002	63.2	91.0	(1.801)	34.24	30.0	1.141[1.428]	90.18	1.22 [296]
F <sub>2</sub>	9	18.9984032	0.47372	65.5	95.3	(1.675)	32.93	21.85	1.507[1.696]	85.24	[195]
Ne	10	20.1797	0.49555	66.1	96.6	(1.724)	28.94	24.0	1.204[0.9005]	27.09	1.092 [67.1]
Al	13	26.981539	0.48181	70.6	106.4	1.615	24.01	8.9	2.70		—
Si	14	28.0855	0.49848	70.6	106.0	1.664	21.82	9.36	2.33		3.95
Ar	18	39.948	0.45059	76.4	117.2	(1.519)	19.55	14.0	1.396[1.782]	87.28	1.233 [283]
Ti	22	47.867	0.45948	79.9	124.9	1.476	16.17	3.56	4.54		—
Fe	26	55.845	0.46556	82.8	131.9	1.451	13.84	1.76	7.87		—
Cu	29	63.546	0.45636	85.6	134.9	1.403	12.86	1.43	8.96		—
Ge	32	72.61	0.44071	88.3	140.5	1.371	12.25	2.30	5.323		—
Sn	50	118.710	0.42120	100.2	163	1.264	8.82	1.21	7.31		—
Xe	54	131.29	0.41130	102.8	169	(1.255)	8.48	2.87	2.953[5.858]	165.1	[701]
W	74	183.84	0.40250	110.3	185	1.145	6.76	0.35	19.3		—
Pt	78	195.08	0.39984	113.3	189.7	1.129	6.54	0.305	21.45		—
Pb	82	207.2	0.39575	116.2	194	1.123	6.37	0.56	11.35		—
U	92	238.0289	0.38651	117.0	199	1.082	6.00	≈0.32	≈18.95		—
Air, (20°C, 1 atm.), [STP]			0.49919	62.0	90.0	(1.815)	36.66	[30420]	(1.205)[1.2931]	78.8	(273) [293]
H <sub>2</sub> O			0.55509	60.1	83.6	1.991	36.08	36.1	1.00	373.15	1.33
CO <sub>2</sub> gas			0.49989	62.4	89.7	(1.819)	36.2	[18310]	[1.977]		[410]
CO <sub>2</sub> solid (dry ice)			0.49989	62.4	89.7	1.787	36.2	23.2	1.563	sublimes	—
Shielding concrete <sup>f</sup>			0.50274	67.4	99.9	1.711	26.7	10.7	2.5		—
SiO <sub>2</sub> (fused quartz)			0.49926	66.5	97.4	1.699	27.05	12.3	2.20 <sup>g</sup>		1.458
Dimethyl ether, (CH <sub>3</sub> ) <sub>2</sub> O			0.54778	59.4	82.9	—	38.89	—	—	248.7	—
Methane, CH <sub>4</sub>			0.62333	54.8	73.4	(2.417)	46.22	[64850]	0.4224[0.717]	111.7	[444]
Ethane, C <sub>2</sub> H <sub>6</sub>			0.59861	55.8	75.7	(2.304)	45.47	[34035]	0.509(1.356) <sup>h</sup>	184.5	(1.038) <sup>h</sup>
Propane, C <sub>3</sub> H <sub>8</sub>			0.58962	56.2	76.5	(2.262)	45.20	—	(1.879)	231.1	—
Isobutane, (CH <sub>3</sub> ) <sub>2</sub> CHCH <sub>3</sub>			0.58496	56.4	77.0	(2.239)	45.07	[16930]	[2.67]	261.42	[1900]
Octane, liquid, CH <sub>3</sub> (CH <sub>2</sub> ) <sub>6</sub> CH <sub>3</sub>			0.57778	56.7	77.7	2.123	44.86	63.8	0.703	398.8	1.397
Paraffin wax, CH <sub>3</sub> (CH <sub>2</sub> ) <sub>n≈23</sub> CH <sub>3</sub>			0.57275	56.9	78.2	2.087	44.71	48.1	0.93		—
Nylon, type 6 <sup>i</sup>			0.54790	58.5	81.5	1.974	41.84	36.7	1.14		—
Polycarbonate (Lexan) <sup>j</sup>			0.52697	59.5	83.9	1.886	41.46	34.6	1.20		—
Polyethylene terephthalate (Mylar) <sup>k</sup>			0.52037	60.2	85.7	1.848	39.95	28.7	1.39		—
Polyethylene <sup>l</sup>			0.57034	57.0	78.4	2.076	44.64	≈47.9	0.92–0.95		—
Polyimide film (Kapton) <sup>m</sup>			0.51264	60.3	85.8	1.820	40.56	28.6	1.42		—
Lucite, Plexiglas <sup>n</sup>			0.53937	59.3	83.0	1.929	40.49	≈34.4	1.16–1.20		≈1.49
Polystyrene, scintillator <sup>o</sup>			0.53768	58.5	81.9	1.936	43.72	42.4	1.032		1.581
Polytetrafluoroethylene (Teflon) <sup>p</sup>			0.47992	64.2	93.0	1.671	34.84	15.8	2.20		—
Polyvinyltoluene, scintillator <sup>q</sup>			0.54155	58.3	81.5	1.956	43.83	42.5	1.032		—
Aluminum oxide (Al <sub>2</sub> O <sub>3</sub> )			0.49038	67.0	98.9	1.647	27.94	7.04	3.97		1.761
Barium fluoride (BaF <sub>2</sub> )			0.42207	92.0	145	1.303	9.91	2.05	4.89		1.56
Bismuth germanate (BGO) <sup>r</sup>			0.42065	98.2	157	1.251	7.97	1.12	7.1		2.15
Cesium iodide (CsI)			0.41569	102	167	1.243	8.39	1.85	4.53		1.80
Lithium fluoride (LiF)			0.46262	62.2	88.2	1.614	39.25	14.91	2.632		1.392
Sodium fluoride (NaF)			0.47632	66.9	98.3	1.69	29.87	11.68	2.558		1.336
Sodium iodide (NaI)			0.42697	94.6	151	1.305	9.49	2.59	3.67		1.775
Silica Aerogel <sup>s</sup>			0.50093	66.3	96.9	1.740	27.25	136@ρ=0.2	0.04–0.6		1.0+0.21ρ
NEMA G10 plate <sup>t</sup>				62.6	90.2	1.87	33.0	19.4	1.7		—

# Beam Loss Detection

K. Wittenburg

Deutsches Elektronen Synchrotron, DESY; Hamburg

## 1 Abstract

A review of Beam Loss Monitor Systems (BLM systems) used in accelerators since about 1960 is given, with emphasis on systems suitable for measuring and localizing beam losses over an entire accelerator. Techniques presented include: Long and Short Ionization Chambers, Scintillation Counters, Electron Multipliers, Cryogenic Calorimeters and PIN Photodiodes.

## 2 Introduction

### 2.1 Uses of BLM systems

The usual goal of particle accelerators is to deliver high luminosity to experiments. The information from BLMs helps in the tuning of the machines for the high beam currents and long lifetimes necessary for improved luminosity.

Beam loss may result in damage to accelerator components or the experimental detectors. A task of the BLM system is to avoid such damage; in some accelerators it is an integral part of the protection system, signaling a beam abort system to fire if a certain loss rate is exceeded (Ref. 1, 2, 3). This is of vital importance to the Generation of superconducting accelerators, for which beam losses in the superconducting components may lead to a quench, resulting in a shut-down of accelerator operation during the quench recovery procedure, as well as possible damage to the components. Another task of BLM systems is to identify of the position (and time) of unacceptable losses. This often indicates the source of the problem in the machine. A BLM system provides a fast way to determine the position of aperture restrictions and semitransparent obstacles in the accelerator, and helps to keep the radiation level in the accelerator and its surroundings as low as possible.

### 2.2 Principles of loss detection

In case of a beam loss, the BLM system has to establish the number of lost particles in a certain position and time interval<sup>1</sup>. All BLM systems discussed here are mounted outside of the vacuum chamber, so that the detector normally observes the shower caused by the lost particles interacting in the vacuum chamber walls or in the material of the magnets. The number of detected particles (amount of radiation, dose) and the signal from the BLM should be proportional to the number of lost particles. This proportionality depends on the position of the BLM in respect to the beam, type of the lost particles and the intervening material, but also on the momentum of the lost particles, which may vary by a large ratio during the acceleration cycle. Together with the specification for acceptable beam losses as a function of beam momentum, this defines a minimum required sensitivity and dynamic range for BLMs. Additional sensitivity combined with a larger dynamic range extend the utility of the system for diagnostic work.

One has to distinguish between two types of losses:

#### FAST LOSSES:

Total beam loss during one or very few turns. In most cases there is no need of a BLM system to localize the error in the machine. Often it is a easily detectable error like a closed vacuum valve, a broken power supply, a

---

<sup>1</sup> I exclude from my talk beam current monitors, which give the amount of losses but not the position

fired (or not fired) kicker, etc. Nevertheless it could be dangerous for accelerator components (especially superconducting components) and a BLM system may warn if an intolerable dose occurs.

#### SLOW LOSSES:

Partial beam loss over a time (circular machines) or distance (LINAC, transport lines) interval. In storage-rings, the lifetime is defined by slow losses. There are many reasons for these losses and a BLM system is very helpful for finding out what is happening in the machine. In superconducting accelerators a BLM system may prevent from beam loss induced quenches caused by slow losses.

In addition measurements of injection-, ejection- or collimator- efficiencies can be performed using BLMs (e.g. Ref. 4), as well as background measurements in the detectors (e.g. Ref. 27, 28). This survey concentrates on BLM systems which cover the entire accelerator.

### 3 Long Ionization-Chambers

In 1963, Panowsky (Ref. 5) proposed for SLAC a BLM system consisting of one long (3.5 km) hollow coaxial cable. It is an industrial RG-319/U cable with a diameter of 4.1 cm, filled with Ar (95%) + CO<sub>2</sub> (5%) and used as an ionization-chamber (Panowski's long ionisation chamber, PLIC). It is mounted on the ceiling along the LINAC, about 2 m from the beam.

Position sensitivity is achieved by reading out at one end the time delay between the direct pulse and the reflected pulse from the other end. The time resolution is about 30 ns ( $\approx 8$  m), for shorter PLICs about 5 ns are achieved. This BLM system has been working for more than 20 years and was upgraded for the SLC (Ref. 6). Nearly the entire SLC is covered with a few PLICs

This principle of space resolution works for one-shot (-turn) accelerators (and transport lines) with a bunch train much shorter than the machine and with relativistic particles. For particles travelling significantly slower than the signal in the cable ( $\approx 0.92c$ ) the resolution of multiple hits in the cable becomes difficult. In this case and for circular machines it is necessary to split the cable. Each segment has to be read out separately, with spatial resolution approximately equal to the length of the unit. This was done in the BNL 200 MeV LINAC, where 30 cables, each 7-9 m long, are used (Ref. 7). They are installed at 1.5 - 3 m from the beam.

In the AGS ring, Booster and transport lines about 200 monitors with a length of about 5 m are installed (Ref. 8, 9). To improve the sensitivity of the BLM system in the AGS ring for ion acceleration the cables were moved from a position below the magnets to the median plane on the open side of the magnets (Ref. 10). The dynamic range of the BLMs is about  $10^3$ .

In the KEK-PS 56 air-filled cables with a length of about 6 m are installed. Using amplifiers with a variable gain, a dynamic range of  $10^4$  is archived (Ref. 11).

### 4 Short Ionisation Chambers

Short ionization chambers are used in many accelerators. They are more or less equally spaced along the accelerator with additional units at special positions such as aperture restrictions, targets, collimators, etc. An early example of an Air filled Ionisation Chamber is the AIC proposed in 1966 in Ref. 12 (Fig. 1). 100 AICs were installed in the CERN-PS. Each chamber had a volume of about 8000 cm<sup>3</sup> and used a multi-electrode layout to reduce the drift path, and hence the recombination probability, of the ions and electrons, with the goal of improved linearity. A dynamic range of  $10^3$  was obtained.

The idea of AIC was renewed in 1992 in Ref. 14. The authors propose an AIC with a  $2\pi$  geometry around the beam pipe. The goal is to measure the loss in the vacuum wall independent of azimuth angle and with high sensitivity.

The TEVATRON relies on 216 Argon filled glass sealed coaxial ionization chambers to protect the superconducting magnets from beam loss induced quenches (Ref. 1). The volume of each chamber is 190 cm<sup>3</sup> (Fig. 2). Most are positioned adjacent to each superconducting quadrupole. An Ar-filled chamber has the advantage of a better linearity because of a lower recombination rate than in AICs. A dynamic range of  $10^4$  has been reached.

A new idea is proposed in Ref. 15 for the UNK superconducting magnets. The ionization chamber is an integral part of the magnet and uses the liquid Helium as an ionization medium. A  $2\pi$  geometry close to the beam pipe is foreseen, with predicted dynamic range of  $10^5$ , but additional investigations are necessary to determine the linearity in this range, which may be restricted by the recombination rate.

## 5 Scintillation counters

In case of losses in a machine without a BLM system, a temporary installation of plastic scintillator with photomultiplier readout is often made. These counters have a well known behavior but the strong radiation damage of the plastic scintillator restricts their long term use. Liquid scintillators avoid this damage and were installed in some accelerators, e.g. Ref. 16, 17. Fig. 3 shows the device at LAMPF with a dimension of  $500\text{ cm}^3$ . A photomultiplier (PM) inside a oil filled paint can detects the scintillation light from the oil. This BLM is very fast, the pulse rise time is about 10 ns and a dynamic range of  $10^5$  was obtained. The gain of the photomultipliers varies within a factor of 10. Therefore a careful intercalibration of the BLM sensitivities was necessary by adjusting the high voltage (HV). The drift of the gain is a well known behavior of PMs. A stabilized HV-source and continuous monitoring of the photomultiplier gain over the run period keep the calibration error small.

## 6 Aluminum Cathode Electron Multipliers

An enhanced sensitivity of photomultipliers to ionized radiation is achieved by replacing the photocathode by an aluminum foil. This foil works as secondary electron emitter when irradiated. A BLM system consisting of this Aluminum Cathode Electron Multipliers (ACEM) was proposed in Ref. 18 and installed in the CERN-PS (100 units) and in the PS-Booster (48 units). They are located on top of the magnets behind each straight section plus 32 additional positions for specific applications (PS). The dimensions of the tube are 4 cm in diameter and 9 cm length plus the adjacent HV-divider (Fig. 4). This BLM is very fast; the rise time of the signal is about 10 ns. For the dynamic range a value of  $10^6$  was exceeded by adjusting the HV. A careful selection of the ACEMs had led to gain variations of 10 %, but intercalibration and gain monitoring was performed nevertheless. This BLM system is rather expensive because the ACEM is not a standard tube of PM-suppliers (Ref. 20).

## 7 Cryogenic Microcalorimeters

A new system called the Cryogenic Microcalorimeter was proposed and tested in 1992 for LEP (Ref. 21). It is designed to detect beam loss induced quenches in the superconducting quadrupoles of LEP. This detector is different from all the other BLMs presented here because it does not make use of the charge created by the lost particles. A carbon resistor thermometer measures the temperature rise of the liquid Helium in the cryostat produced by beam losses. It is a very small device with dimensions of about  $3 \times 3 \times 1.5\text{ mm}$  (see Fig. 5). Its position is restricted to the cryostat of superconducting magnets.

No values for the linearity and the dynamic range are available up to now but first measurements indicate an easily detectable signal with a rise time of about 20 ms in case of a beam induced quench. The signal occurs well before the quench and it should give enough time for the quench protection system to take action. The dynamic range is limited by the critical (quench-) temperature of the liquid Helium and by the noise of the monitor. One can expect that, with a known correlation between losses and temperature, this detector will work in a BLM system for superconducting accelerators. For quantitative loss measurements the temperature increase due to synchrotron radiation has to be taken into account.

## 8 PIN Photodiodes

Most of the existing BLM systems are installed in hadron accelerators or in Linacs. Circular electron accelerators emit hard synchrotron - radiation (SR). The radiation interacts with the BLMs and a separation between SR-background and the beam loss distributions using the traditional BLM techniques is practically impossible. HERA is an accelerator with an electron and a proton ring in the same tunnel, operating at the same time. Protection of the superconducting proton magnets from beam loss induced quenches must rely on a BLM

system which sees only the proton beam losses and not the SR-background. The (hadronic) shower created by beam losses includes a large number of charged particles, in contrast to the photons of the SR. The HERA BLM system consists of two PIN Photodiodes, mounted close together (face to face) and read out in coincidence (Ref. 22). Thus charged particles crossing through the diodes give a coincidence signal, while photons interact in only one diode do not.

In contrast to the charge detection of most other BLM systems, coincidences are counted, with the count rate is proportional to the loss rate so long as the number of overlapping coincidences is small.

The Photodiodes ( $2 \times 2.5 \times 2.5 \text{ mm}^3$ ) and the preamplifier ( $5 \times 5 \times 5 \text{ cm}^3$ ) are shielded by a hat of 3 cm of lead (Fig. 6). The overall reduction of SR signals is about  $10^4$ , resulting in a count rate of  $\approx 1 \text{ Hz}$  with 25 mA current at 30 GeV/c in the electron ring (Ref. 23). The system has very low noise, with a dark count rate of less than 0.01 Hz. The pulse length is adapted to the 96 ns bunch spacing in HERA, so that the maximum count rate is 10.4 MHz. Therefore a dynamic range of more than  $10^9$  is available.

The radiation resistance of the BLMs is adequate for long term use in HERA. A dose of  $5 \times 10^5 \text{ rad}$  leads to a small and tolerable reduction in gain (Ref. 24, 25), while the dose reaching the monitor below the lead shield will be about  $10^4 \text{ rads/year}$ . BLMs are mounted on top of each of the superconducting quadrupoles. At this position the showering of the lost protons give a count rate which is independent of the radial position of the loss, and, within 5 m, also of the longitudinal position (Ref. 23). Additional BLMs are mounted on collimators, and on some of the warm quadrupole magnets, for a total of 250 units.

The BLM system has been operating since the 1992 running period and their good performance is indicated by some measurements:

- 1) The loss rates calculated from lifetime and measured by the BLMs agree to within 25 % (Ref. 26)<sup>2</sup>.
- 2) The counts are integrated over a time period of 5.2 ms to match the cryogenic time constant of the superconducting magnets (>20 ms). The predicted coincidence rate corresponding to the critical loss rate for a quench at 820 GeV/c is about 860 counts/5.2 ms. The only beam induced quench of a HERA quadrupole in 1992 showed a count rate of 1258 counts/5.2 ms for the quenched quadrupole. A nearby quadrupole which did not quench showed a rate of 893 counts/5.2 ms. The critical rate must be somewhere in between and is not far away from the predicted one. The critical rate was detected about 100 ms before the magnet quenched.
- 3) A lifetime problem in the HERA electron ring was solved using the BLMs. All monitors were moved from the proton ring to the electron ring to find the problematic section. A high count rate, inversely proportional to the beam lifetime, was measured in one of the straight sections. The problem vanished after a part of the vacuum-chamber in this section was replaced. This result demonstrates that the BLM system is also useful in high energy electron rings. It is planned to install about 250 additional monitors in the HERA electron ring.

## 9 Summary

Some Beam Loss Monitors techniques for measuring losses along an entire accelerator have been presented.

A long ionization chambers using a single coaxial cable works well for one-shot accelerators or transport lines. To achieve spatial resolution of losses along an entire accelerator two conditions must be fulfilled: 1) The machine must be much longer than the bunch train, and 2), the particles must be relativistic.

The most common BLM now in use is a short ionization chamber. Whether a simple air filled chamber is adequate, or an Argon or Helium filled chamber, with superior higher dynamic range, must be used, depends on the conditions of the particular accelerator. Ionisation chambers are radiation resistant but respond to synchrotron radiation.

A very sensitive system for measuring beam losses is an electron multiplier in combination with a photocathode and scintillator or with an Aluminum cathode acting as secondary electron emitter. Because of the adjustable gain the dynamic range can be large, but the calibration of each device must be adjusted and monitored over time. These systems are also sensitive to synchrotron radiation and relatively expensive.

The Cryogenic microcalorimeter measures the temperature rise of the liquid Helium in superconducting magnets resulting from beam loss. The temperature rise corresponding to beam loss sufficient to cause a quench

---

<sup>2</sup> Please note that the efficiency of the BLM to charged particles is about 20 time higher than previously assumed (Ref. 27). Correct the loss-rate in Ref. 26 by 1/20.

is readily observed. Some additional investigations must be made of the dynamic range and the linearity of this device but first measurements indicate its suitability for quench prevention and loss measurements. The temperature rise due to synchrotron radiation must be taken into account when using Cryogenic Microcalorimeters for loss diagnostics in electron machines. The application of the calorimeter is limited to superconducting magnets.

The combination of two PIN-Photodiodes in a coincidence counting results in a detector with very large dynamic range and extremely effective rejection of synchrotron radiation. The small dimensions permit simple shielding and easy installation at any position. The measured radiation resistance permits long term use also in high energy electron machines with a high radiation background. The monitor with its simple accompanying electronic is inexpensive, which may be of great importance in very big machines with a large number of loss monitors. A (present) limitation is the inability to distinguish overlapping counts, so that the response is linear only for losses for which there is significantly less than one count per coincidence interval.

### **Acknowledgements**

Many thanks to Steve Herb, who made some very useful comments on the manuscript.

## **10 References**

- Ref. 1:** R.E. Shafer et al.; The TEVATRON Beam Position and Beam Loss Monitoring System. Int. Conf. on High Energy Accelerators, Fermilab, (1983)
- Ref. 2:** M. Fishman, D. Reagan; The SLAC Long Ion Chamber System for Machine Protection. IEEE Trans. on Nucl. Science Vol. 14 (1967), p.1096 - 1098
- Ref. 3:** SSC Central Design Group; Conceptual Design of the Superconducting Super Collider. SSC-SR-2020, (1986)
- Ref. 4:** F. Hornstra; The System for precise Measurement of Accelerator Extraction Efficiency. Nucl. Instr. & Methodes 128, (1975), p. 435 - 440
- Ref. 5:** W.K.H. Panofsky; SLAC Internal Report TN-63-57, (1963)
- Ref. 6:** J. Rolfe et al.; Long Ion Chamber System for the SLC. SLAC-PUB-4925, (1989)
- Ref. 7:** J. Balsamo et al.; Long Radiation Detector System for Beam Loss Monitoring. IEEE Trans. on Nucl. Science Vol.NS-24, No. 3, (1977), p. 1807-1809
- Ref. 8:** R.L. Witkover; Microprocessor Based Beam Loss Monitor System for the AGS. IEEE Trans. on Nucl. Science, Vol. NS-26, No. 3, (1979), p. 3313-3315
- Ref. 9:** E.R. Beadle et al.; The AGS Beam Loss Monitor System. Proc. Part. Accel. Conf., San Francisco, (1991), p. 1231-1233
- Ref. 10:** G.W. Bennett et al.; The Upgraded Ring Loss Radiation Monitoring System at the AGS. Proc. Part. Accel. Conf., Chicago, (1989); BNL-41824
- Ref. 11:** N. Nahagawa et al.; Beam Loss Monitoring System with Free - Air Ionisation Chambers. Nucl, Instr. & Meth. 174, (1980), p. 401 - 409
- Ref. 12:** V. Agoritsas; Air Ionisation Chamber as Detector of the Beam Losses in the CPS Ring. Internal Report CERN MPS/Int.CO 66-23, (1966)

- Ref. 13:** J.J. Merminod; Le System d'Obvseration des Pertes du Fraisceau Interne du PS.  
CERN MPS/Int. CO 68-6, (1968)
- Ref. 14:** S.N. Lapitsky et al.; The Concept of Beam Loss Monitors Design and their Implementation at IHEP.  
Proc. 15th Int. Conf. on high Energy Accel., Hamburg, (1992), p.242-244
- Ref. 15:** I.A. Kurochkin et al.; Beam Loss Monitor for Superconducting Accelerators.  
IHEP 91-168, (1991), Protvino
- Ref. 16:** J.R. Parker et al.; A Beam-Spill Monitor for LAMPF.  
IEEE Trans. on Nucl. Science Vol. 18 No. 3, (1971), p. 825-826
- Ref. 17:** R.A. Lundy and D.F. Sutter; A System for Monitoring Proton Losses from the NAL Main Accelerator.  
IEEE Trans. on Nucl. Science Vol. 20 No. 3, (1973), p. 596-598
- Ref. 18:** V. Agoritsas and C. Johnson; EMI Aluminum Cathode Electron Multipliers: CERN TESTS.  
CERN MPS/CO Note 71-51, (1971)
- Ref. 19:** V. Agoritsas et al.; A Microprocessor-Based System for Continuous Monitoring of Radiation Levels  
around the CERN PS and PSB Accelerators.  
CERN PS/ 85-60 (CO), (1985)
- Ref. 20:** Thorn EMI, Technical Data sheet; Nuclear Radiation Detector Type 9841 (Aluminum Cathode Electron  
Multiplier), (1989)
- Ref. 21:** Ph. Lebrun et al.; Cryogenic Microcalorimeters for Measurement of Energy Deposition by Beam Losses  
in Superconducting Accelerator Magnets.  
15th Int. Conf. on high Energy Accel., Hamburg, (1992), p. 592-595
- Ref. 22:** K. Wittenburg; Strahlverlustmonitore für den HERA Protonen-Ring.  
DESY HERA 89-23, (1989)
- Ref. 23:** S. Schlögl; Einsatz von PIN-Photodioden als Protonen-Strahlverlustmonitore bei HERA.  
DESY HERA 92-03, (1992)
- Ref. 24:** K. Wittenburg; Radiation Damage in PIN - Photodiodes.  
Nucl. Instr. & Meth. A270, (1988), p. 56 - 61
- Ref. 25:** K. Wittenburg; Strahlenschäden am Photodioden Verstärker.  
Interner Bericht, PKTR note No. 9, (1987)
- Ref. 26:** S. Schlögl and K. Wittenburg; A Beam Loss Monitor System for HERA.  
Proc. 15th Int. Conf. on high Energy Accel., Hamburg, (1992), p. 254-256
- Ref. 27:** E. Morre; Ein Untergrundmonitor für das ZEUS-Experiment.  
Diploma Thesis, (1992), University Hamburg
- Ref. 28:** J. Wear; The ALEPH Rapid Beam Loss Interlock- System.  
This proceedings

## 11 Figures

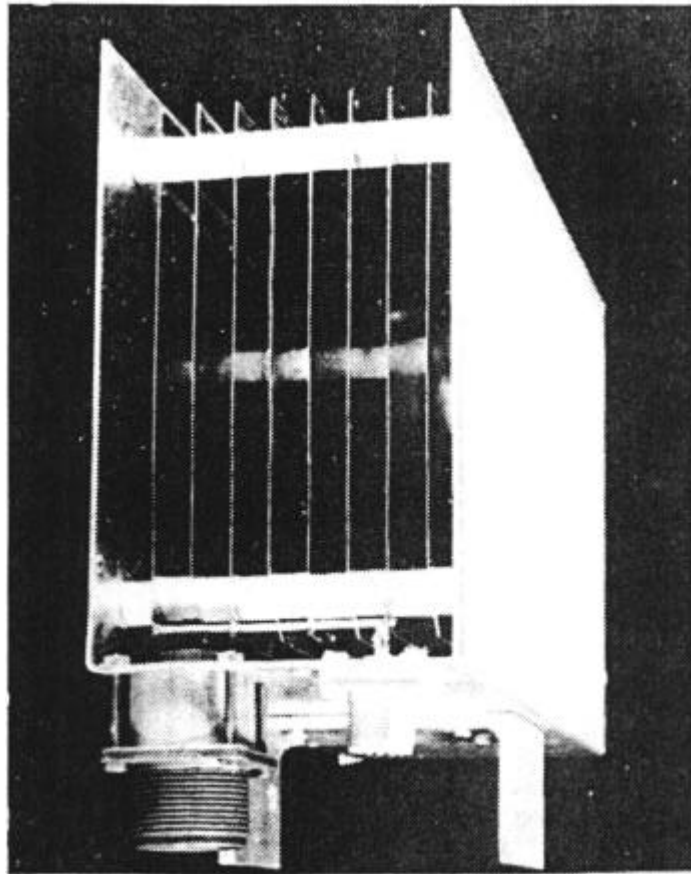


Figure 1: Air Ionisation Chamber at the PS (1968). The cover is removed (from Ref. 13).



Figure 2: The TEVATRON Argon filled Ionization Chamber (1983)

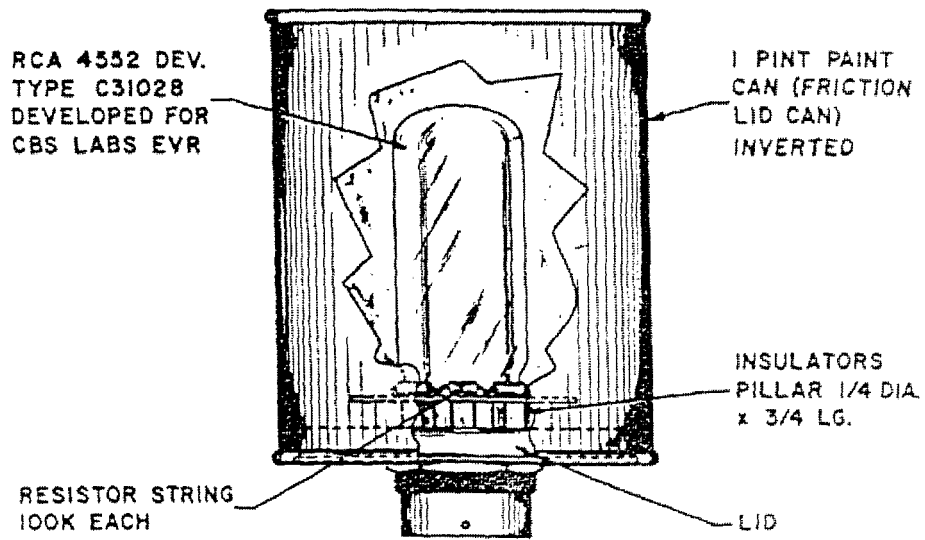


Figure 3: The Liquid Scintillator BLM at LAMPF (1971), (from Ref. 16)

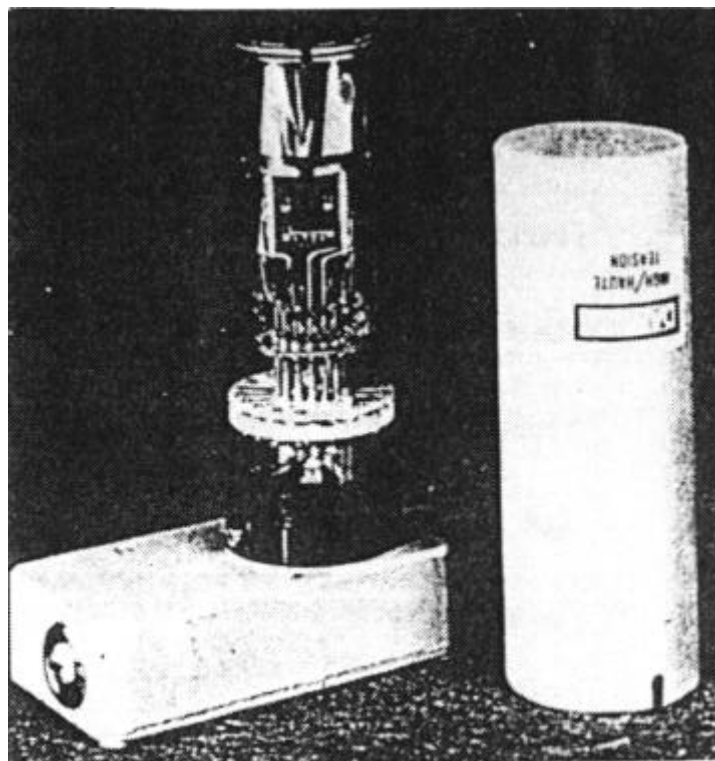


Figure 4: The Aluminum Electron Multiplier at CERN PS (1985), (from Ref. 19).

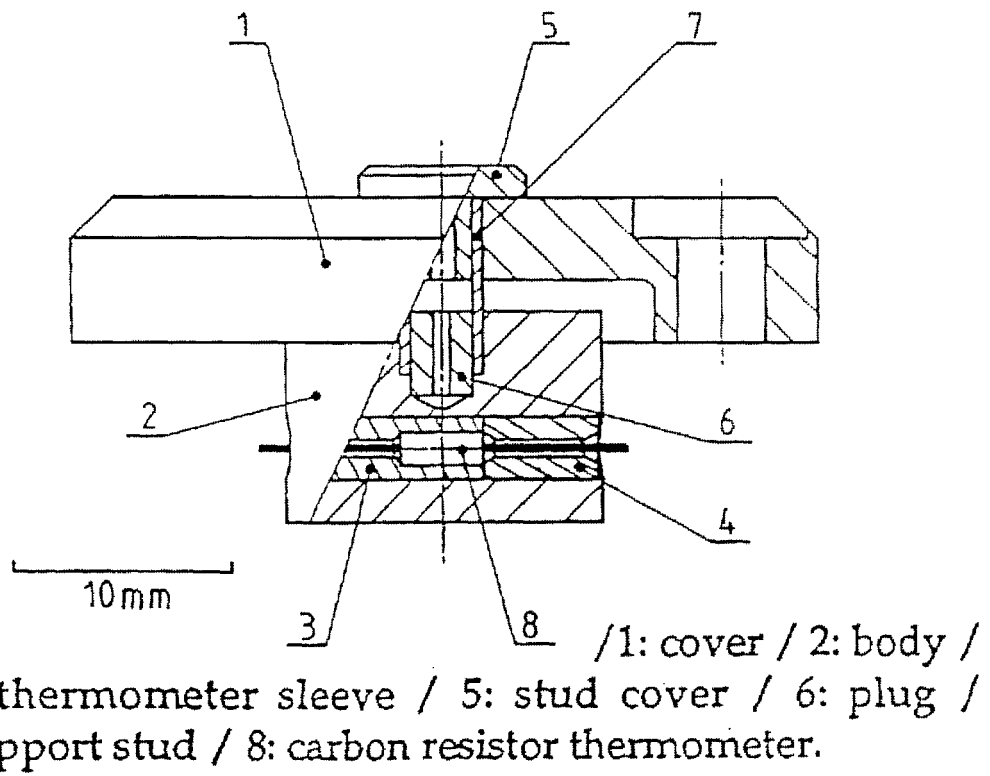


Figure 5: Cut-away view of the microcalorimeter (1992), (from Ref. 21).

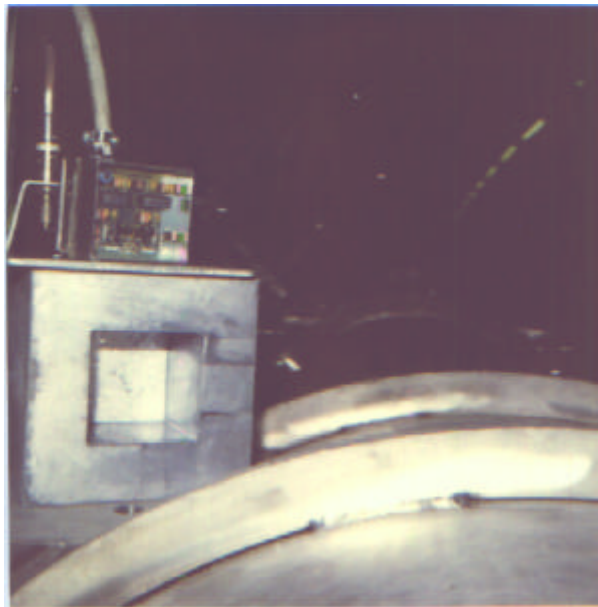
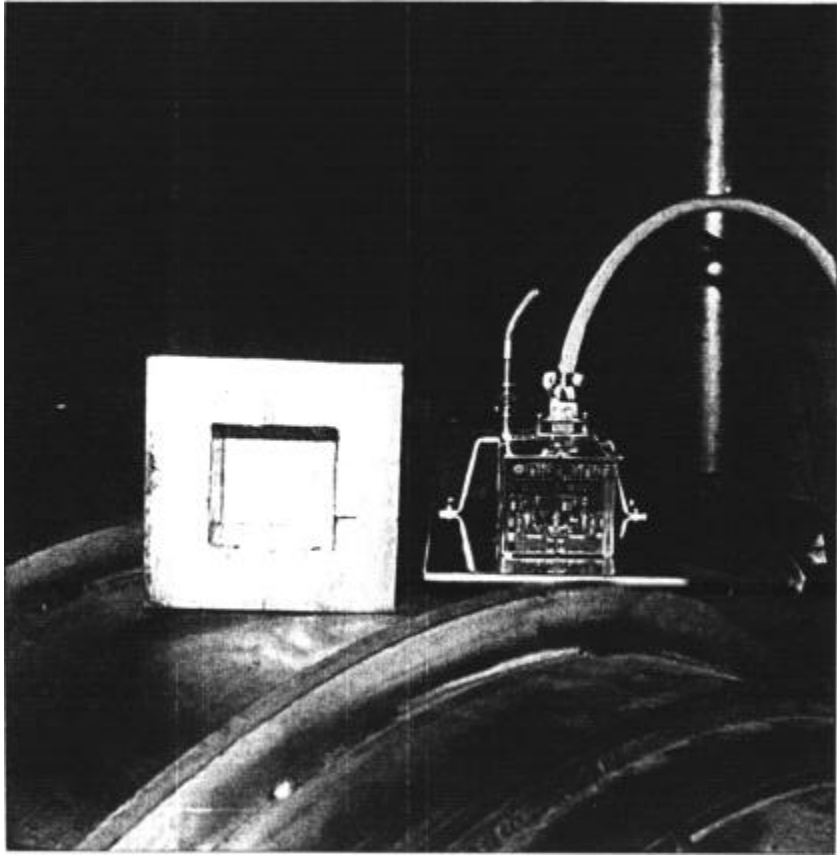


Figure 6: The PIN Photodiode BLM on top of a HERA magnet (1991). The lead hat is removed



# BEAM LOSS MONITORING AND CONTROL

Kay Wittenburg, Deutsches Elektronen Synchrotron DESY, Hamburg, Germany

## Abstract

The use of Beam Loss Monitors (BLMs) as sensitive tools for various beam diagnostic applications will be discussed as well as their tasks in machine protection and loss location detection. Examples will illustrate that an appropriate design of a BLM-system and a proper understanding of loss events can improve machine performance.

## 1 INTRODUCTION

“You do not need a BLM-System as long as you have a perfect machine without any problems. However, you probably do not have such a nice machine, therefore you better install one.”

Beam loss monitor systems are designed for measuring beam losses around an accelerator or storage ring. A detailed understanding of the loss mechanism, together with an appropriate design of the BLM-System and an appropriate location of the monitors enable a wide field of very useful beam diagnostics and machine protection possibilities.

Beam losses can be divided into two different classes:

1) **Irregular losses**, sometimes called “fast or uncontrolled losses”: These losses may be distributed around the accelerator and not obviously on a collimation system. They are very often a result of a misaligned beam or a fault condition, e.g. operation failure, trip of the HF-system or of a magnet power supply. Losses should be avoided and should be kept to low levels

- to keep activation low enough for hands-on maintenance, personal safety and environmental protection,
- to protect machine parts from beam related (radiation) damage. This includes quench protection of superconducting magnets and acceleration structures and protection of detector components,
- to achieve long beam lifetimes or an efficient beam transport to get high integrated luminosity for the related experiments.

Sometimes such losses have to be tolerated even at a high level at low repetition rates during machine studies. However, a beam loss monitor system should define the allowed level of those losses. The better protection there is against these losses, the less likely is down time due to damage of components. A post mortem event analysis is most helpful to understand and analyse the faulty condition.

Some examples of such a functionality of beam loss monitor systems will be given in this paper.

2) **Regular losses**, sometimes called “slow” or “controlled” losses: Those losses are typically not avoidable and are localized on the collimator system or on other (hopefully known) aperture limits. They might occur continuously during operational running and correspond to the lifetime/transport efficiency of the beam in the accelerator. The lowest possible loss rate is defined by the theoretical beam lifetime limitation due to various effects, like residual gas, Touschek effect, etc.

Some examples will be discussed, where, with the help of a beam loss monitor system, the measurement of losses can be used for machine diagnostic purposes.

It is clearly advantageous to design a BLM-System which is able to deal with both loss modes.

## 2 SOME COMMON ASPECTS

There are some common aspects, which are valid for every beam loss monitor system:

- a) Type of loss monitor
- b) Positioning of the loss monitor

### 2.1 Type of Loss Monitor

Typical beam loss monitors detect beam losses by measurement of ionising radiation produced by lost beam in real-time and with a certain position resolution. Other systems, like differential beam current measurements, have a very rough position resolution, or have a very long time constant (e.g. dose measurements or activation) and are not the subject of this talk.

The produced radiation consists mainly of electromagnetic particles (electron-, positron- and gamma- shower), while the loss of a hadron (proton, ion) produces some hadronic particles (protons, neutrons), too. However, the signal source of beam loss monitors is mainly the ionizing capability of the charged shower particles.

Different types of such loss monitors exist and detailed descriptions of most types can be found in [1, 2]. Options for beam loss monitors might be: long and short Ion chambers, Photomultipliers with scintillators (incl. Optical Fibers), PIN Diodes, Secondary Emission Multiplier-Tubes, Microcalorimeters, Compton Diodes, etc. A nice list of “considerations in selecting a beam loss monitor” is discussed in [2]:

- Sensitivity
- Type of output (current or pulse)
- Ease of calibration (online)
- System end-to-end online tests
- Uniformity of calibration (unit to unit)
- Calibration drift due to aging, radiation damage, outgassing, etc.
- Radiation hardness (material)

- Reliability, Availability, Maintainability, Inspect ability, Robustness
- Cost (incl. Electronics)
- Shieldability from unwanted radiation (Synchrotron Radiation)
  - Physical size
  - Spatial uniformity of coverage (e.g. in long tunnel, directionality)
  - Dynamic range (rads/sec and rads)
  - Bandwidth (temporal resolution)
  - Response to low duty cycle (pulsed) radiation
  - Instantaneous dynamic range (vs. switched gain dynamic range)
    - Response to excessively high radiation levels (graceful degradation)

Consideration of these parameters gives a good guide to find (or design) the best monitor type for a particular beam loss application.

## 2.2 Positioning of the Loss Monitor

The loss of a high-energy particle in the wall of a beam pipe results in a shower of particles, which leak out of the pipe (Low energy beam particles, which do not create a shower leakage outside the vacuum pipe wall, will be hardly detectable by a loss monitor system). The signal of a loss detector will be highest, if it is located at the maximum of the shower. Refs. [3, 4, 5] are using Monte Carlo simulations to find the optimum locations for the monitors, as well as to calibrate the monitors in terms of ‘lost particles/signal’. The length of the shower depends on the energy of the lost particle and ranges from some meters for very high proton energies [4] to a few cm for medium electron energies [5]. Therefore the expected location of lost particles has to be studied in advance to locate the monitors at the right location, especially at electron accelerators. But this means, that an understanding of the loss mechanism and dynamics in the accelerator is necessary to predict the typical positions of losses. For example, Refs [5, 6] had done detailed particle tracking studies to follow the trajectory of an electron in the accelerator after an energy loss due to scattering on a residual gas molecule or on a microparticle.

There are many different reasons for beam losses and a complete beam loss system has to be carefully designed for a detection of a specific loss mechanism.

In the following, some examples for different loss mechanisms, their detection and their use for beam control and diagnoses will be presented.

## 3 SOME EXAMPLES FOR IRREGULAR, UNCONTROLLED LOSSES

### 3.1 Radiation Damage

A serious problem for high current and high brilliance accelerators is the high power density of the beam. A misaligned beam is able to destroy the beam pipe or collimators and may break the vacuum. This fact makes the BLM-System one of the primary diagnostic tools for

beam tuning and equipment protection in these machines. Such a system must have enough sensitivity and dynamic range to measure low-level losses at low current (test-) beams, as well as high local losses of short duration. Together with well-designed collimation and machine interlock systems, the BLM-System should prevent harmful accidents by switching off the beam in time in case that the loss rate exceeds a certain threshold at any position. But it should also serve as a sensitive diagnostic tool during the set-up periods of the accelerator to prevent high losses at nominal currents [7, 8]. This will help to prevent excessive activation of the environment and equipment damage. Especially for high-current proton and ion accelerators, this became a very important for hands-on maintenance as well as for ground water and air activation [9].

### 3.2 Obstructions

The set-up periods of a new accelerator or after a reconstruction of an existing machine are always associated with beam losses, before the machine goes into normal operation. Unexpected losses can be caused by a various number of reasons, and a BLM-System may help to find them. A ‘beautiful’ example is discussed in [10], where an RF-finger pointing in the beam line prevented the beam from circulating in Rhic. The loss pattern showed an apparent obstacle in the ring at a certain location. The losses there went away as the beam was steered locally around an obstacle after which the beam began circulating for thousands of turns.

Other obstacle-like obstructions are vacuum-crashes and trapped microparticles [11]. They caused in more or less sudden drops in the lifetime due to scattering of the electrons on the additional particles in the beam pipe. The lifetime is reduced because beam particles lose energy by bremsstrahlung both in the field of the atomic nuclei and in the macroscopic field of the highly charged microparticle or ‘dust’. The deviation of the electron orbit from the nominal orbit depends on the dispersion function in the accelerator and on the energy loss. Therefore the electrons may be lost behind the following bending magnet on the inside wall of the vacuum chamber. Beam loss monitors located at this location are sensitive to these effects and therefore can measure the vacuum-distribution, vacuum leaks (Fig. 1) and the existence, location and even the movement of microparticles [6, 12].

### 3.3 Quench Protection

Superconducting accelerators need a dedicated BLM-system to prevent beam loss induced quenches. Such a system has to detect losses fast enough before they lead to a high energy deposition in the superconducting material. A time constant of a few ms is adequate for the main loss system. HERA has shown, that the BLM-system is very often the last chance to recognize a doomed beam and to dump it before it is lost uncontrollably, possibly quenching magnets [3, 13]. Care has to be taken, to set-up

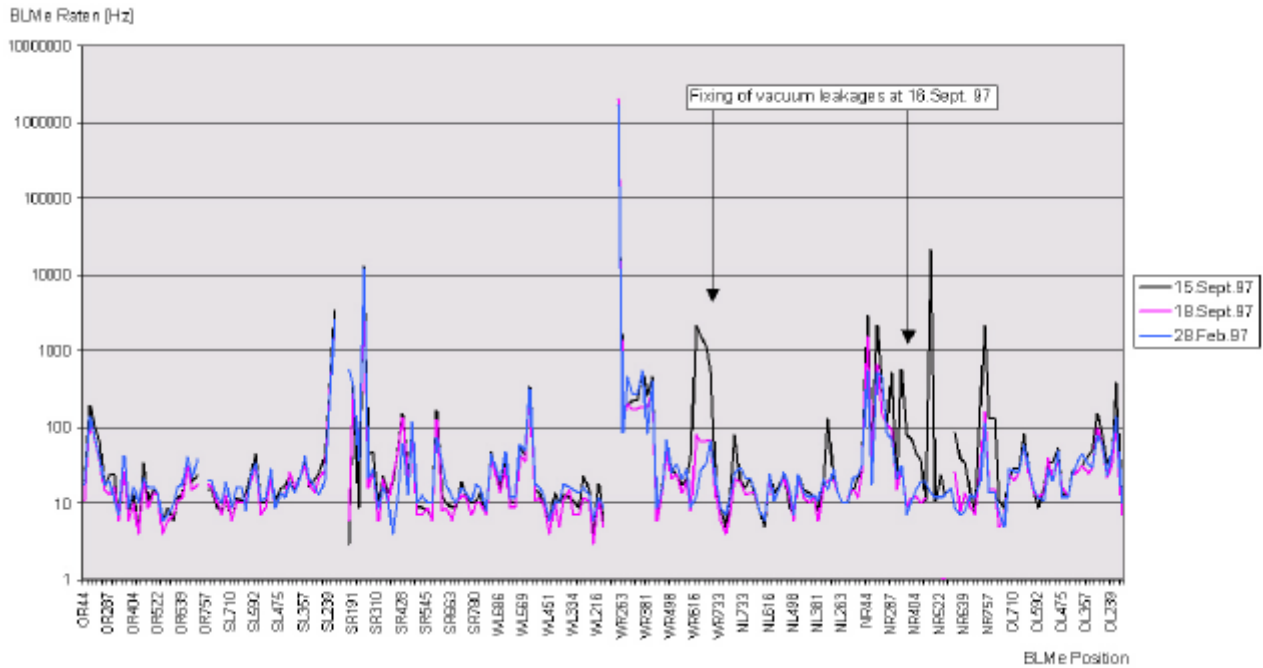


Figure 1: Beam loss monitor signals versus their location along HERAe at different dates during 1997. The two vacuum leaks on the 15.Sept. are clearly visible, as well as their repair on the next day. Note the reproducibility of the rates.

such a system properly, so that it is not overly active (dumping too often) and also not too relaxed, allowing dangerous loss rates. Typical locations for the protection system monitors are the quadrupoles of the accelerator, where the beam has its largest dimensions. The quadrupoles act as local aperture limits and therefore the chance for a loss is larger there. It might turn out, that some special locations are more sensitive to losses than others, e.g. global aperture limits and collimators. For such locations a special treatment of the alarm-threshold, timing constant (faster) and sensitivity is applicable. Even an additional type of monitor might be the right choice.

In all cases of fast beam losses, an event archive is most helpful for a post mortem analysis of the data, to find out the reason for the loss. Certainly this will improve the operational efficiency of the accelerator.

#### 4 SOME EXAMPLES FOR REGULAR, CONTROLLED LOSSES

##### 4.1 Injection Studies

The injection of beam into the next accelerator of a chain should work with the highest possible efficiency. Keeping the loss rate of adjacent BLMs as low as possible is a very simple way of tuning the injection schema. BLMs measure the loss directly and with better sensitivity and resolution than the differential beam current measurement. This became important, if low injection (test-) currents are required as a result of radiation safety issues. Additional, a distributed BLM-system shows the areas of losses during the injection process as well as the loss timing behaviour (Fig. 2). By placing BLMs at

betatron and dispersion aperture limits, one can distinguish between transversal mismatch (betatron oscillations) and energy mismatch (dispersion) at injection [15].

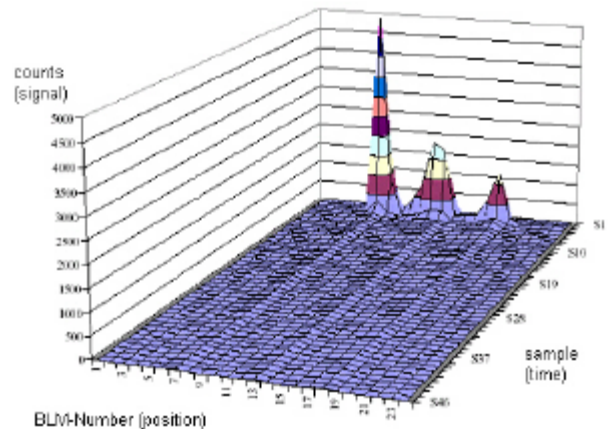


Figure 2: Surface plot of beam loss at injection and afterwards (from [14]).

##### 4.2 Lifetime Limitations

Beside of unwanted conditions, there are unavoidable effects which limit the beam lifetime in an accelerator, e.g. vacuum lifetime (Coulomb scattering), Touschek effect, quantum lifetime, etc.:

**Touschek Effect:** Particles inside a bunch perform transverse oscillations around the closed orbit. If two particles scatter, they can transform their transverse momenta into longitudinal momenta. If the new momenta are outside the momentum aperture the particles are lost.

Good locations for the detection of Touschek scattered particles are in high dispersion sections following sections where a high particle density is reached. Since the two colliding particles lose and gain an equal amount of momentum, they will hit the in- and outside walls of the vacuum chamber. In principle the selectivity of the detection to Touschek events can be improved by counting losses at these locations in coincidence.

Coulomb Scattering etc.: Particles scatter elastically or inelastically with residual gas atoms or photons (Compton) or emit a high energy synchrotron radiation photon (Quantum). This leads to betatron or synchrotron oscillations and increases the population of the tails of the beam. If the amplitudes are outside the aperture the particles are lost. Losses from elastic scattering occur at aperture limits (small gap insertions, septum magnet, mechanical scrapers and other obstructions). If the energy carried away by the emitted photon is too large, the particle gets lost after the following bending magnet on the inside wall of the vacuum chamber.

A BLM-System with good selectivity to the different loss mechanisms is a very useful tool for various kinds of beam diagnostics, especially in Touschek limited (electron-) accelerators: The Touschek loss rate depends on the 3-dimensional electron density and on the spin of the scattering particles. Therefore any change of one or more of these parameters has an influence on the loss rates at the selected monitors. The BLM-System at BESSY was used to determine the (desired) vertical beam blow up due to a resonant head-tail mode excitation [16]. At ESRF the BLM-System was used to study the beam coupling between the transversal planes [17]. At ALS and BESSY the BLM-System was used to calibrate precisely the beam energy and observing its variation in time by using resonant depolarization of the beam [16, 18].

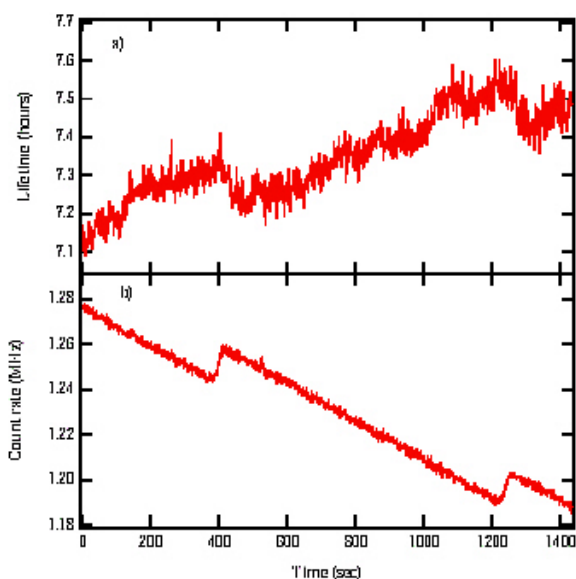


Figure 3: Beam lifetime derived from current monitor and count rate from beam loss monitor showing two partial spin depolarizations over a 25 minute period (from [18]). Note the much clearer signal from the BLM.

One useful applications of the energy measurement is the precise determination of the momentum compaction factor [18].

### 4.3 Tail Scans

Non-Gaussian tails in the transverse and longitudinal beam distribution produce lower beam lifetimes and background in experimental detectors. With beam profile monitoring, these tails are difficult to detect because of their small population in respect to the core of the beam. A combination of scrapers and BLMs is a good choice to measure the tail population and to get rid of it. Transverse tails are best measured at scraper positions with a large  $\beta$ -function and with no dispersion, while for longitudinal tail scraping scraper positions at small  $\beta$ -function and large dispersion are best. The measurement and scraping can be done by moving the scraper in small steps closer to the beam core measuring at each step the response of the adjacent BLM. This procedure does not affect the lifetime because the particles in the tails will get lost anyhow (as long as the scraper doesn't reach the beam core). Coulomb or Touschek scattering are the dominant processes for creating tails in lower energy electron rings, while at the very high energy ring LEP the dominant processes are Compton scattering on thermal photons (horizontal) and beam-beam bremsstrahlung (vertical) [19].

In the high-energy proton accelerator HERAp, the lifetime limitation arises from proton diffusion due to beam-beam interaction and tune modulation due to ground motion. The ground motion frequencies can be measured with BLMs at the scrapers [20, 21]. The loss spectrum of a very stable machine corresponds very well with the ground motion spectrum. The diffusion parameters at different tune modulation settings are measured by retracting the scraper from the beam tail and observing the time constants of the adjacent loss rate decrease and slow increase afterwards [20].

### 4.4 Tune Scans

Any change of the 3-dimensional phase space of a particle beam will effect the loss rates. By observing these losses as a function of the tune, the phase space area of the lattice can be investigated, as well as the influence of insertion devices that may cause non-linearities [16, 22]. The examination of the tune area might be somewhat lengthy, when only measuring the small changes of the beam lifetime. With the help a BLM-System, this procedure can be done very fast because the change of the loss rate can be measured immediately. [23] had shown, that a combination of a collimator and a BLM is a very sensitive tool to make fast tune scans of the area around the working point even at very long lifetimes and very small lifetime-changes.

## 5 CONCLUSIONS

It has been shown, that a beam loss monitor system is a multi-faceted beam instrumentation tool, which opens a

wide field of applications. A precondition is a proper understanding of the physics of the beam loss to place the monitors at their adequate positions.

BLM-systems are frequently used to minimise irregular, uncontrolled losses to protect the environment and equipment of the accelerator from radiation damage; in superconducting accelerators also from beam loss induced quenches. They also serve as a sensitive tool to localise and study any kind of physical obstruction in the accelerator, from abominably RF-fingers down to different vacuum problems. Also a BLM-system helps to study and optimise the injection scheme of an accelerator. BLM-systems play an important role in investigating and optimising the beam lifetime, which is defined by different, but regular losses. A BLM-System with a good selectivity to the different loss mechanisms is a very useful tool for various kinds of beam diagnostics and beam control, e.g. controlled beam blow-up, coupling studies and tune scans. Even a precise energy calibration of the beam can be done with signals from a BLM-system. The combination of a scraper and a BLM offers additional useful applications for lifetime studies, e.g. ground motion observation, beam diffusion measurements and tail scans.

## 6 REFERENCES

- [1] K. Wittenburg, "Beam Loss Detection", 1st European Workshop on Beam Diagnostics and Instrumentation for Particle Accelerators, Montreux, Switzerland, 3-5.5.1993, CERN PS/93-35 (BD)
- [2] R. E. Shafer, "A tutorial on Beam Loss Monitoring," 10<sup>th</sup> Beam Instrumentation Workshop 2002, Brookhaven, Mai 2002.
- [3] K. Wittenburg, "The PIN-Diode Beam Loss Monitor System At HERA" Beam Instrumentation Workshop 2000, Boston, USA, Mai 2000
- [4] A. Arauzo et al., "LHC Beam Loss Monitors", DIPAC2001, Grenoble
- [5] L. Yuxion et al., „The beam loss monitoring system for the HLS storage ring", Nucl. Instr. & Meth. A467-468, 2001
- [6] F. Ridoutt, K. Wittenburg, "Experience with the Electron and Proton Beam Loss monitor System at HERA", EPAC 1996, Stiges
- [7] D. Gassner et al., „Spallation Neutron Source Beam Loss Monitor System"; 9th Beam Instrumentation Workshop, Boston, USA; May 2000
- [8] M. C. Ross, D. McCormick, "A Coaxial Cable Beam Loss Monitor Ion Chamber System for High Power Multi-Bunch Beams", 19<sup>th</sup> International Linear Accelerator Conference (Linac 98), Chicago, IL, Aug 1998.
- [9] O. E. Krivosheev, N. V. Mokhov, "Tolerable Beam Loss at High-Intensity Proton Machines", Proce ICFA Beam Halo and Scraping Workshop, Lake Como, WI, 1999
- [10] P. Thompson et al., "RHIC Beam Loss Monitor System Commissioning in RHIC Year 00 Run", 9th Beam Instrumentation Workshop (BIW 2000), Cambridge, Massachusetts, May 2000. and: [http://www.rhichome.bnl.gov/RHIC/YearZero/early\\_beam.html](http://www.rhichome.bnl.gov/RHIC/YearZero/early_beam.html)
- [11] Zimmermann, F. et al., "Trapped macroparticles in electron storage rings", 16<sup>th</sup> Particle Accelerator Conference : PAC '95, Dallas, TX, USA, May 1995
- [12] B. Joly, U. Weinrich, G. A. Naylor, "Beam Loss Monitors at the ESRF", 4<sup>th</sup> DIPAC, 1999, Chester, UK, May 1999.
- [13] M. Lomperski: "Beam losses at HERA - is everything understood?", 11<sup>th</sup> Chamonix workshop 2001 <http://cern.web.cern.ch/CERN/Divisions/SL/publications/chamx2001/PAPERS/8-2-ml.pdf>
- [14] J. Hinkson, "ALS Beam Instrumentation, Beam Loss Monitoring", not published, Feb. 1999
- [15] A. Pietryla, W. Berg, "A Cerenkov Radiation Detection System for the Advanced Photon Source Storage Ring", PAC 2001, Chicago, USA, 2001
- [16] P. Kuske "Accelerator Physics Experiments with Beam Loss Monitors at BESSY", 5<sup>th</sup> DIPAC2001, Grenoble, 2001
- [17] Weinrich, Udo, "Mastering beam losses on small gap vacuum chambers in synchrotron light sources", ESRF 1999, Dortmund, Univ., thesis, 2000
- [18] C. Steier, J. Byrd, P. Kuske, "Energy Calibration of the Electron Beam of the ALS Using Resonant Depolarisation", EPAC2000, Vienna, Austria, 2000
- [19] H. Burkhardt, I. Reichel, G. Roy, "Transverse Beam Tails due to Inelastic Scattering", Phys. Rev. Spec. Top. Accel. Beams : 3 (2000)
- [20] Brüning, O ; Mess, K H ; Seidel, M ; Willeke, F , "Measuring the effect of an external tune modulation on the particle diffusion in the proton storage ring of HERA" DESY-HERA-94-01, DESY, Jan 1994.
- [21] K.H. Mess, M. Seidel, "Measurement of Proton Beam Oscillations at low Frequencies", EPAC 94, Vol. 2, London 1994
- [22] K.T. Hsu et al. „Real-Time Beam Loss Monitoring and its Applications in SRRC" Particle Accelerator Conference, Vancouver, B.C., Canada, May 1997
- [23] O. Kaul, B. Sarau, K. Wittenburg , "Fast Measurement of Lifetime Changes and Beam Losses in DORIS by the use of Bremsstrahlung from a Collimator", DIPAC 97, Frascati, Italy, 1997

## **Chapter 5**

### **Bunch Length Measurements**

#### **5.1 Exercises**



## Excercises on Bunch Length Measurements

by T. Lefevre

### Problem 1:

You have just been hired to work on a 5MeV electron gun – 4ps bunch length. Your first job is dedicated to the design of a bunch length monitor using Cherenkov radiation and a streak camera.

As a reminder, Cherenkov light is emitted when a charge particle travels inside a transparent medium with a velocity higher than the speed of light in this medium. The Cherenkov photons are emitted all along the material thickness

- Speed of light inside the material :  $v = \frac{c}{n}$  with  $n$  is the index of refraction of the material
- $\beta$  is the relative particle velocity
- $\gamma$  is the particle relativistic factor :  $\gamma = \frac{1}{\sqrt{1-\beta^2}}$
- $d$  the thickness of the Cherenkov radiator

### Questions:

- What is the minimum index of refraction of the given material so that Cherenkov effect occurs?
- Assuming that you will use fused silica as a Cherenkov radiator (index of refraction is 1.46), How thick must be the crystal to keep the time resolution below 1ps? You can neglect the effect of light dispersion and multiple scattering inside the radiator

---

## Problem 2:

You have been promoted and are now in charge of the bunch length measurement at the end of the Linac for electrons energy of 50GeV (4ps bunch length). Your boss specifically asks for a non destructive method and you are considering Optical Diffraction Radiation.

ODR is a pure high relativistic phenomenon (contraction of length), where a charged particle emits radiation when it passes close to the edge of a dielectric medium. To produce ODR, there is a condition to fulfill between the distance from the edge to the beam ( $h$ ), the beam energy ( $\gamma$ ) and the wavelength ( $\lambda$ ) of the radiation you like to produce.

$$h \leq \frac{\gamma\lambda}{2\pi}$$

### Questions:

- What will be the required minimum distance from the edge of the slit to the beam in order to produce visible photons (550nm wavelength)
- Is that distance looks reasonable, Would you think it can be used at lower beam energies

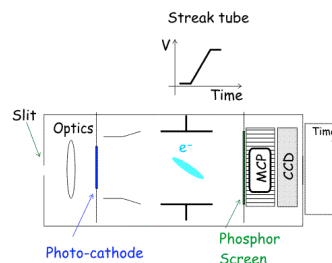
---

## Problem 3:

You are responsible for the purchase of the streak camera and you should define what the parameters of the streak camera to buy are. This is an expensive device and the performance of the camera should match precisely your needs. You were told that you need a minimum of 2points per sigma in order to clearly measure a Gaussian bunch length.

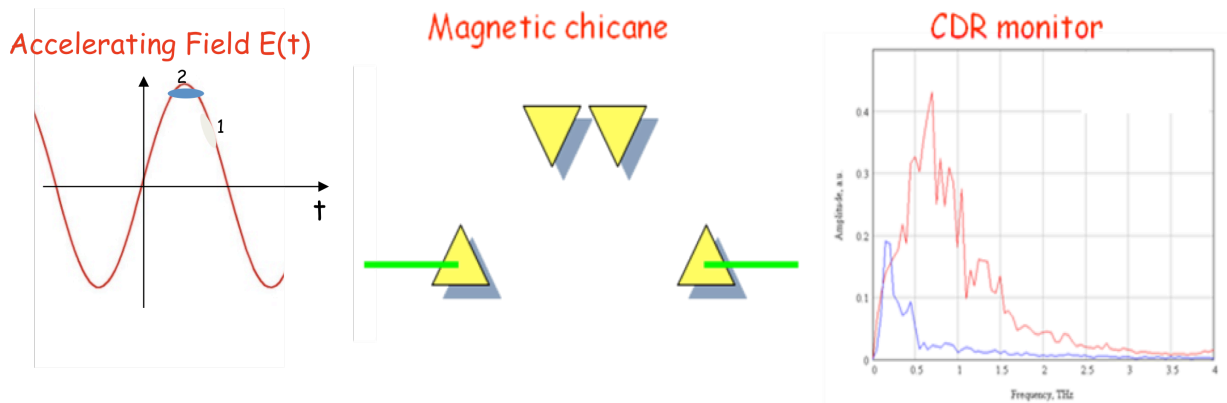
### Questions:

- Assuming that your mcp-ccd system is 1cm wide in vertical and have 500pixels, what will be the minimum sweep speed (in ps/mm) of the streak tube in order to measure the 4ps bunch length in your linac



### Problem 4:

You did so well for the bunch length measurement in the linac that you are asked to provide some support to operate of the bunch compressors. The bunch compression is done using an accelerating structure and a magnetic chicane. A coherent diffraction radiation monitor is measuring the bunch frequency spectrum just downstream of the chicane. Coherent radiation monitor relies on the fact that the shorter the bunch the broader the bunch frequency spectrum.



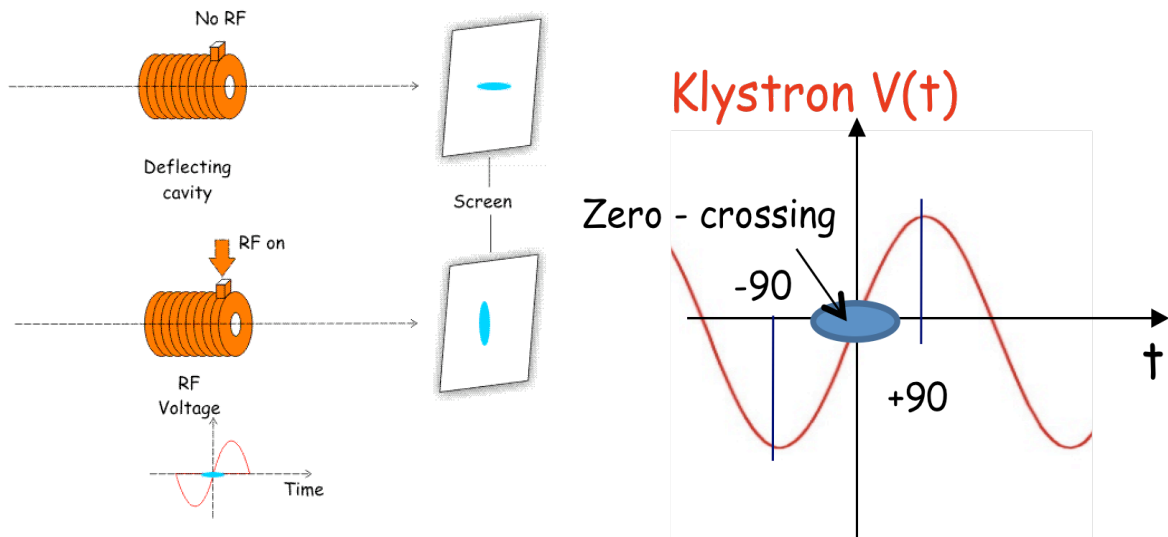
### Questions:

- On the figure, there are two different settings of the klystron phase. For these two cases, draw what will be the trajectory of electrons sitting at the head and at the tail of the bunch for each case?
- On the CDR monitor, two different bunch frequency spectra have been measured. Choose which spectra corresponds to which phase settings
- Are you happy with the performance of the bunch compressor? if not what will you modify to have a better result

---

### Problem 5:

With your new success, you really become a well recognized expert. In the meanwhile, the calibration of the RF deflector has changed during the replacement of a Klystron. You have been asked to calibrate the monitor. By changing the phase of your klystron with respect to the beam, the beam position changes on the screen. The RF deflector is working at 3GHz and for a maximum deflection ( $\pm 90^\circ$  phase difference) the beam position on the screen changes by 5mm.



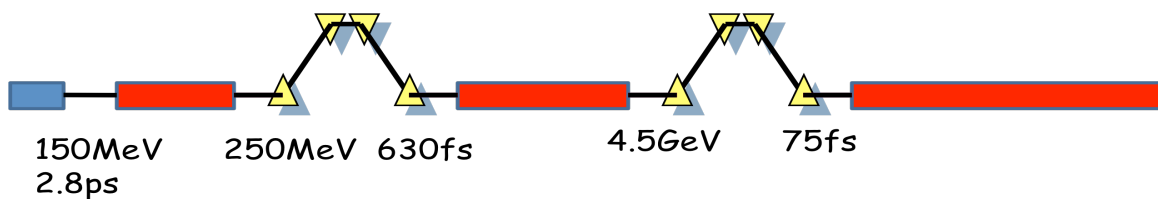
Questions:

- If the bunch is placed at the zero-crossing of the RF deflector. What happens to the beam position and to the beam size?
- If the natural beam size (no RF) on the screen is  $10\mu\text{m}$ , what will be approximately the size increase for zero-crossing if the bunch is  $1\text{ps}$  long. The relation between the bunch length, the beam size on the screen with and without RF power is given by the following expression.

$$\sigma_y^2 = \sigma_{y_0}^2 + \sigma_z^2$$

Problem 6:

You are now working on the design of 4<sup>th</sup> generation light source and you have been asked to define the several techniques to measure bunch length all along the machine. The layout of the machine is presented here.



Questions:

Choose at least one location where the following detector could be used along the machine.

- ODR with a streak camera
- RF deflector
- Coherent diffraction radiation
- EO spatial decoding

## 5.2 Further Reading: Bunch Length Measurements



# Lectures on Bunch Length Measurements

by T. Lefevre, CERN

## Abstract

This lecture gives an introduction to the main techniques used to measure the longitudinal structure of particle beams. It is composed of two distinct parts. The first is a short introduction to the production of particle bunches, like we can observe them in most accelerators. The second part reviews the different techniques classically used to measure bunch length and presents their performances and limitations.

## More..

In accelerators, the time structure of the beam is governed by the characteristic of the accelerating field. On one side of the present technology, electrostatic accelerators produce DC particle beams that have no variation in time. On the opposite side, Radio-Frequency (RF) accelerators generate beams with a time microstructure extremely well defined. The sinusoidal time behavior of the RF field only provides stable conditions for acceleration during a time that is small compared to the electric field period, noted  $T$ . Therefore, a typical beam accelerated in an RF cavity is composed of a succession of particle bunches, spaced by a time equal to  $T$  with a duration, called bunch length, equivalent to a fraction of  $T$  (Typically,  $T/200$ ). Nowadays RF accelerators may have operating frequency up to tens of Gigahertz, which means that particle bunches can naturally be as short as few picoseconds. For some applications, like in Free Electron Lasers [1,2] or TeV Linear Colliders [3,4], the bunch length is even shorter, typically 10-100 femtoseconds long. In order to produce particle bunches as short, they have to be compressed. Two techniques, based on RF manipulations, have been developed, namely ballistic bunching [5] and magnetic compression [6]. Moreover, since the late 90's, the development of ultra-short intense laser pulses has contributed to the development of innovative acceleration schemes, i.e. Laser Plasma Wakefield Acceleration (LPWA) [7]. Here the accelerating field is generated by the interaction of a laser beam with a gas cell. The resulting plasma wave has a very high electric field that may oscillate at frequency up to Terahertz. The corresponding bunch length is of the order of femtoseconds.

In order to measure the longitudinal behavior of the particle beams, a lot of instruments have been developed during the last three decades. They can be regrouped in different categories: Direct Beam Observation, Detection of Coherent Radiation, Radio-Frequency Manipulation and Sampling Techniques.

Direct Beam Observation means that the longitudinal structure of the beam is directly measured by means of fast detectors. For example, the beam current can be measured using Wall Current Monitors [8] and then digitalized using a fast oscilloscope. Wall Current Monitors have already proven their performances up to 10GHz and state of the art oscilloscopes are improving their specifications every year with sampling rate as high as 20-50GSa/s. Another very popular method since 20years relies on the use of

Streak Cameras [9]. In this case an optical replica of the beam longitudinal distribution is first generated using an adequate technique like Synchrotron Radiation [9], Transition Radiation [9], Diffraction Radiation [10], Cherenkov Radiation [11], ... This light pulse is then analyzed by the Streak Camera, with time resolution down to 200fs.

The observation of Coherent Radiation can also provide information on the bunch length [12]. Let's consider a bunch, consisting of many particles, classically  $10^9$  to  $10^{11}$ , that radiates light through one of the effect listed in the previous paragraph. For wavelength shorter than the bunch length, the particles radiate incoherently, not being affected by the radiation of the neighbors. And the power emitted is proportional to the number of particles. For wavelength longer or equal to the bunch length, every particle emits radiation in phase, in a coherent way and the emitted power scales with the number of particles squared. In this condition, the bunch length can be obtained by measuring the power spectrum of the beam radiation. This technique, applicable to any kind of radiation has in theory no resolution limit. In practice, the method is relatively simple to implement and has already demonstrated its performances for the measurement of extremely short bunches. One limitation resides in the fact that it cannot directly provide a profile but just an estimate of the bunch length.

In order to measure the longitudinal profile of the bunch, physicists have also conceived beam diagnostics based on Radio-Frequency manipulation. Here the main idea is to encode, using RF devices, longitudinal structure of the beam into spatial information, which is easier to measure. For example, one can use an RF deflecting cavity [13] that will kick the head of the bunch in one direction and the tail of the bunch in the opposite direction. By measuring the transverse beam size downstream, one can reconstruct the longitudinal bunch profile. A similar technique exists if using an RF accelerating structure combined with a profile monitor in a dispersive region. RF deflectors become a standard instrument for femtosecond bunches [14] with the only disadvantage that this is a destructive and expensive method.

The last category of instruments presented here are basing on sampling with very short laser pulses. Electro-optic sampling [15] is the most developed technique. It is based on the conversion of the coulomb field of the bunch into an optical intensity variation. An electro-optic crystal is placed close to the beam. The field of the particle induces a polarization change of the laser beam passing through the crystal at the same time. Other sampling techniques have been tested using different processes, like Compton scattering [16] or Laser photo-neutralization [17]. Whatever is the process involved, sampling techniques always need laser pulses shorter than the particle bunch length and extremely precise laser-beam synchronization.

Since few years, single shot electro-optic techniques have been proposed and tested and are becoming the reference for non-destructive short bunch length monitoring [18].

---

<sup>1</sup> <http://xfel.desy.de/>

<sup>2</sup> <http://lcls.slac.stanford.edu/>

<sup>3</sup> <http://www.linearcollider.org/cms/>

<sup>4</sup> <http://clic-study.web.cern.ch/CLIC-Study/>

<sup>5</sup> B. Beutner *et al*, "Velocity Bunching at FLASH", EPAC conference, Genoa, (2008), 113

- 
- <sup>6</sup> M. Borland, "Design and Performance simulations of the bunch compressor for the Advanced Photon Source Low-Energy Undulator Test Line Free-Electron Laser", *Physical Review Special Topics – Accelerators and Beams*, 4 (2001), 074201
- <sup>7</sup> W. Leemans *et al*, "Laser-driven plasma based accelerators: Wakefield excitation, channel guiding and laser triggered particle injection", *Physics of Plasma*, 5 (1998), 1615
- <sup>8</sup> P. Odier, "A New Wide Band Wall Current Monitor", *Proceeding of DIPAC 2003*, Mainz, Germany, pp.216
- <sup>9</sup> C. Welsch *et al*, "Longitudinal Beam Profile Measurements at CTF3 Using a Streak Camera", *Journal of Instrumentation*, 1, (2006), P09002
- <sup>10</sup> P. Karatev *et al*, "Beam-Size Measurement with Optical Diffraction Radiation at KEK ATF", *Physical Review Letters*, 93, 244802 (2004)
- <sup>11</sup> J. Bähr *et al*, "Silica Aerogel Radiators for Bunch Length Measurements", *Nuclear Instruments and Methods in Phys. Res. A*, 538 (2005), 597
- <sup>12</sup> O. Grimm, "Coherent Radiation Diagnostics for Short Bunches", *Particle Accelerator Conference (PAC 07)*, Albuquerque, New Mexico, (2007) p.2653
- <sup>13</sup> P. Emma *et al*, "A Transverse RF Deflecting Structure for Bunch Length and Phase Space Diagnostics", LCLS-TN-00-12, (2000)
- <sup>14</sup> M. Huening *et al*, "Observation of Femtosecond Bunch Length Using a Transverse Deflecting Structure", *Free Electron Laser Conference*, Stanford, California, (2005) p.538
- <sup>15</sup> S.P. Jamison *et al*, "Femtosecond Resolution Bunch Profile Measurement", *EPAC Conference*, Edinburgh (2006), 915
- <sup>16</sup> W.P. Leemans *et al*, "X-ray Based subpicosecond Electron Bunch Characterization using 90° Thomson Scattering", *Physical Review Letters* 77, (1996), 4182
- <sup>17</sup> R. Connolly *et al*, "A Transverse Phase-Space Measurement Technique for High Brightness H- Beams", *Nuclear Instruments and Methods in Phys. Res A* 312, (1992), 415
- <sup>18</sup> B. Steffen *et al*, "Electro-Optic Time Profile Monitors for Femtosecond Electron Bunches at the soft X-ray Free Electron Laser FLASH", *Physical Review Special Topics – Accelerators and Beams* 12 032802 (2009)



# Silica aerogel radiators for bunch length measurements <sup>☆</sup>

J. Bähr<sup>a</sup>, V. Djordjadze<sup>a</sup>, D. Lipka<sup>a,\*</sup>, A. Onuchin<sup>b</sup>, F. Stephan<sup>a</sup>

<sup>a</sup>DESY Zeuthen, Platanenallee 6, 15738 Zeuthen, Germany

<sup>b</sup>Budker Institut of Nuclear Physics, Novosibirsk 630090, Russia

Received 8 March 2004; received in revised form 11 August 2004; accepted 12 August 2004  
Available online 11 September 2004

## Abstract

Cherenkov radiators based on silica aerogel are used to measure the electron bunch length at the photo injector test facility at DESY Zeuthen (PITZ). The energy range of those electrons is 4–5 MeV. In this paper, the time resolution defined by the usage of aerogel is calculated analytically and Monte Carlo simulations are performed. It is shown that silica aerogel gives the possibility to reach a time resolution of about 0.1 ps for high photon intensities and a time resolution of about 0.02 ps can be obtained for thin silica aerogel radiators.

© 2004 Elsevier B.V. All rights reserved.

PACS: 06.60.Jn; 07.60.Rd; 29.27.Fh; 42.72.Bj

Keywords: Silica aerogel; Bunch length; Time resolution; PITZ

## 1. Introduction

Successful optimization of the photo injector test facility at DESY Zeuthen (PITZ) requires beam diagnostics, allowing to measure electron beam properties with high resolution. To measure the temporal properties at electron energies of 4–5 MeV by optical means a radiation process is needed at which a photon bunch is produced with the same time properties as the electron bunch.

Optical transition radiation which is widely used for accelerator diagnostics produces a low number of photons per electron. In addition, those photons are produced with a wide angular distribution at these energies. Using Cherenkov radiation a significantly larger number of photons is obtained. In order to produce these photons in a Cherenkov cone with small opening angle, a material with small index of refraction is required. Therefore, silica aerogel is studied as alternative in this paper. For convenience of writing, only the short form aerogel is mainly used hereafter.

In the following section the basic properties of aerogels are summarized. In Section 3 analytical calculations on the expected degradation of the

<sup>☆</sup>Partially supported by Russian Foundation for Basic Research, Grant 02-02-16321.

\*Corresponding author.

E-mail address: [dirk.lipka@desy.de](mailto:dirk.lipka@desy.de) (D. Lipka).

time resolution are presented. In Section 4 GEANT 4 simulations are compared with the analytical calculations. Finally, the results are summarized.

## 2. Aerogel radiators

### 2.1. Optical properties

The main optical properties of aerogel [1–8] are characterized by three parameters:

(1) Index of refraction  $n$ .

It is determined by the density  $\rho$ . The correct dependence [1] is  $n = \sqrt{1 + \alpha\rho}$  where  $\alpha = (0.438 \pm 0.001) (\text{g/cm}^3)^{-1}$  for a wavelength  $\lambda = 400 \text{ nm}$ . For low densities it is possible to use  $n \approx 1 + k\rho$ , where  $k \approx 0.21 (\text{g/cm}^3)^{-1}$ . The chemical composition of aerogel is  $\text{SiO}_2$ , therefore the aerogel dispersion can be calculated from the quartz dispersion. Aerogels are produced in a range of index of refraction of 1.006–1.13 [1–3].

(2) Light scattering length  $L_{\text{sc}}$ .

This quantity is defined as the path length after which a fraction  $1/e$  of the photons is not scattered. This effect is caused by Rayleigh scattering, for which  $L_{\text{sc}} \sim \lambda^4$ . Usually  $L_{\text{sc}}$  is cited at  $\lambda = 400 \text{ nm}$ . For good aerogels the scattering length is  $L_{\text{sc}} = 1\text{--}2 \text{ cm}$ , for best aerogels  $L_{\text{sc}} = 4\text{--}5 \text{ cm}$ . The dependence of  $L_{\text{sc}}$  on the refractive index  $n$  is weak [1,4].

(3) Light absorption length  $L_{\text{ab}}$ .

The light absorption length is defined as the path length after which a fraction  $1/e$  of photons is not absorbed. It mainly depends on an admixture contained in the aerogel. The  $L_{\text{ab}}$  dependence on  $\lambda$  is a complicated relation [1,5]. For good aerogels  $L_{\text{ab}} = 1 \text{ m}$  at  $\lambda = 400 \text{ nm}$  and for best aerogels it reaches a value of  $10 \text{ m}$ .

### 2.2. Maximum thickness of aerogel

The maximum thickness of an aerogel sample is mainly limited by the scattering length  $L_{\text{sc}}$ . Let us

denote the number of Cherenkov photons per unit length of the electron path by  $N_{\text{ph},1}$ . The number of photons, which do not suffer from Rayleigh scattering, in dependence on the aerogel thickness, has the form

$$N_{\text{ph}} = N_{\text{ph},1} L_{\text{sc}} (1 - e^{-l/L_{\text{sc}}}). \quad (1)$$

The maximum number of photons  $N_{\text{phmax}} = N_{\text{ph},1} L_{\text{sc}}$  is reached at  $l \gg L_{\text{sc}}$ . A good choice of aerogel thickness is  $0.5 L_{\text{sc}}$ . In that case about 80% of the produced photons will be collected and 20% will be scattered. The ratio of the background to the effect is around 0.25. Therefore, the maximum thickness used in this paper is  $l_{\text{max}} \approx 2 \text{ cm}$ .

### 2.3. Number of photoelectrons

It is convenient to express the number of Cherenkov photons per unit length of the particle path and per unit wavelength interval in the following form [9]

$$\frac{d^2 N_{\text{ph}}}{dl d\lambda} = 2\pi\alpha \frac{1}{\lambda^2} \left(1 - \frac{1}{n^2 \beta^2}\right), \quad (2)$$

where  $\alpha = \frac{1}{137}$  and  $\beta = v/c$ .

Let us express the quantum efficiency of the photon detector in a form  $Q(\lambda) = Q_0 f(\lambda)$ , where  $Q_0$  is the quantum efficiency at the maximum of the spectral distribution. Let us denote the collection efficiency of the Cherenkov photons on the photo cathode of the detector by  $G(\lambda)$ . Then the photo electron number can be written as

$$\begin{aligned} N_{\text{pe}} &= \left(1 - \frac{1}{n^2 \beta^2}\right) Q_0 l 2\pi\alpha \int \frac{1}{\lambda^2} f(\lambda) G(\lambda) d\lambda \\ &= \left(1 - \frac{1}{n^2 \beta^2}\right) Q_0 l B(\lambda), \end{aligned} \quad (3)$$

where  $B(\lambda) = 2\pi\alpha \int \frac{1}{\lambda^2} f(\lambda) G(\lambda) d\lambda$ .

Taking  $f(\lambda)$  for a borosilicate glass window and a bialkali photo cathode [10] with  $Q_0 = 20\%$  and  $G = 1$ , particles with  $\beta = 1$  in matter with  $n = 1.5$  gives  $N_{\text{pe}} = 165$  photo electrons, where  $l$  is the path length in cm. In Table 1, the corresponding data are presented for electrons with  $pc = 4.0 \text{ MeV}$  ( $\beta = 0.9919$ ) and  $pc = 4.5 \text{ MeV}$  ( $\beta = 0.9936$ ).

### 2.4. Multiple scattering

The mean squared angle of the electron multiple scattering can be calculated using the Rossi formula including a correction [11]:

$$\theta_{MS} = \sqrt{\overline{\theta^2}} = \frac{21 \text{ MeV}}{p\beta c} \sqrt{\frac{l}{X_0}} \left( 1.0 + 0.038 \ln \frac{l}{X_0} \right). \quad (4)$$

Aerogel is SiO<sub>2</sub>, therefore  $X_0 = 27 \text{ g/cm}^2$ , the same as for quartz [2,11]. For refractive indices of  $n = 1.01$ ,  $n = 1.03$  and  $n = 1.05$  the corresponding radiation length is  $X_0 = 570 \text{ cm}$ ,  $X_0 = 190 \text{ cm}$  and  $X_0 = 115 \text{ cm}$ , respectively.

In Table 2, the data for Cherenkov angle  $\theta_C$ , radius of the Cherenkov cone at the exit of the aerogel plate  $r_C = l \tan \theta_C$  and the multiple

scattering angle  $\theta_{MS}$  are presented for different aerogels.

### 3. Time resolution

#### 3.1. Reference plane

At PITZ, the Cherenkov light will be transmitted over 26 m to the entrance slit of the streak camera by an optical transmission line. In general, the optical system will have an influence on the time dispersion. This effect is not considered in this article. To analyze the influence of the radiator itself, the streak camera entrance slit is considered to be virtually back imaged near to the exit plane of the aerogel radiator.

In this article, we assume that this reference plane (RP) is located parallel to the exit plane of the aerogel (see Fig. 1). All the questions concerning the resolution discussed in this article are only considered up to this RP.

#### 3.2. Thickness of aerogel

Besides the refractive index  $n$  also the thickness of the aerogel  $l$  is an important parameter for the time resolution. The optimal thickness in a real experiment has to be chosen as a compromise between two contradictory requirements. To improve the signal-to-noise ratio of the Cherenkov light detection taking into account light losses along the optical transmission line, the radiator

Table 1

Number of photo electrons per 1 cm path length of electrons with  $p = 4.0 \text{ MeV}/c$  and  $p = 4.5 \text{ MeV}/c$  in materials with different index of refraction

$n$	$p = 4.0 \text{ MeV}/c$	$p = 4.5 \text{ MeV}/c$
1.008	0.034	0.36
1.01	0.53	0.82
1.03	5.3	5.3
1.05	9.5	9.5
1.5	65	65

A bialkali photo cathode with  $Q_0 = 20\%$  and a light collection efficiency of  $G = 1$  was assumed.

Table 2

The parameters Cherenkov angle  $\theta_C$ , Cherenkov cone radius  $r_C$ , angle of multiple scattering  $\theta_{MS}$ , time difference because of path length differences  $\Delta_{pl}$ ,  $\sigma_{pl}$  of time difference, the time difference caused by multiple scattering  $\Delta_{MS}(\delta)$  and the corresponding  $\sigma_{MS}(\delta)$  for three aerogel radiators with  $n = 1.01$ ,  $n = 1.03$  and  $n = 1.05$  and for two incident electron momenta at different thickness  $l$

$n$	1.01	1.01	1.03	1.03	1.05	1.05	1.01	1.01
$l$ (mm)	20	20	2	2	1	1	2	2
$p$ (MeV/c)	4.0	4.5	4.0	4.5	4.0	4.5	4.0	4.5
$\theta_C$ (dg)	3.5	4.8	11.8	12.3	16.2	16.6	3.5	4.8
$r_C$ (mm)	1.22	1.69	0.42	0.44	0.29	0.30	0.12	0.17
$\theta_{MS}$ (dg)	14.1	12.5	7.3	6.5	6.6	5.8	4.0	3.5
$\Delta_{pl}$ (ps)	0.25	0.48	0.30	0.32	0.29	0.30	0.025	0.048
$\sigma_{pl}$ (ps)	0.072	0.14	0.085	0.092	0.082	0.086	0.0072	0.014
$\Delta_{MS}(\delta)$ (ps)	1.5	1.8	0.42	0.43	0.37	0.37	0.047	0.072
$\sigma_{MS}(\delta)$ (ps)	0.45	0.51	0.12	0.13	0.11	0.11	0.014	0.021

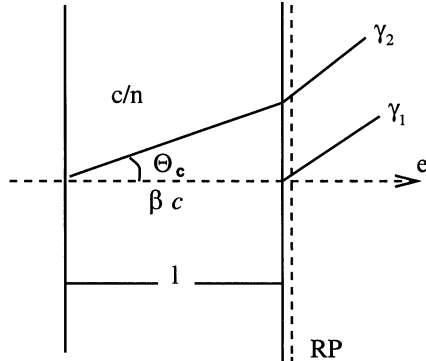


Fig. 1. Schematic view of the Cherenkov radiator system and the reference plane (RP, dashed line). The reference plane is meant to coincide with the downstream boundary of the Cherenkov radiator.

thickness has to be increased to produce more photons. But for improving the time resolution the radiator thickness is preferred to be small, as it will be shown in the next paragraphs. Two cases are considered:

- (A) Large thickness: for comparison of aerogel samples with different  $n$ , the thickness will be chosen such that the number of Cherenkov photons is equal. It means that

$$l \left( 1 - \frac{1}{n^2 \beta^2} \right) = \text{const.} \quad (5)$$

Aerogels with  $n = 1.01$ ,  $n = 1.03$ ,  $n = 1.05$  will be considered. For  $n = 1.01$  the optimal thickness is chosen to be about  $l = 20$  mm (see Section 2.2). According to Eq. (5) the rounded thickness for the other radiators was chosen accordingly: for  $n = 1.03$   $l = 2$  mm and for  $n = 1.05$   $l = 1$  mm.

- (B) Small thickness (for comparison): calculations for aerogel with  $n = 1.01$  and  $l = 2$  mm will be performed. The number of Cherenkov photons will be 10 times smaller in this case compared to case (A).

Modern technology allows to produce aerogel of such thicknesses.

### 3.3. Particle and light velocity

In Fig. 1 the electrons move perpendicular to the aerogel plate. The RP coincides with the second

boundary of the aerogel. The time interval between the arrival of the Cherenkov photons on the RP is

$$\Delta_{\text{pl}} = \frac{ln}{c \cos \theta_C} - \frac{l}{\beta c} = \frac{n^2 \beta}{c} \left( 1 - \frac{1}{n^2 \beta^2} \right) l. \quad (6)$$

This effect is caused by the time difference of the particle and light arrival at the RP plane.

For  $n = \text{const}$   $\Delta_{\text{pl}}$  is proportional to  $l$ . This means that one can improve the time resolution by decreasing the thickness.

The time distribution of the Cherenkov photon bunch has a rectangular shape (see Fig. 2, where  $t_1 = l/\beta c$  and  $t_2 = ln/c \cos \theta_C$ ), therefore the mean squared dispersion in time is  $\sigma_{\text{pl}} = \Delta_{\text{pl}}/\sqrt{12}$ .

The numerical values of the  $\Delta_{\text{pl}}$  and  $\sigma_{\text{pl}}$  are summarized in Table 2.

### 3.4. Dispersion of refractive index

To study the dependence of the time resolution on the wavelength, it is convenient to write Eq. (6) in the form

$$\Delta_{\text{pl}} = \frac{\beta l}{c} \left( n^2 - \frac{1}{\beta^2} \right). \quad (7)$$

The relative change for two different wavelengths is given by

$$\delta(\lambda_1, \lambda_2) = \frac{\Delta_{\text{pl}}(\lambda_1) - \Delta_{\text{pl}}(\lambda_2)}{\Delta_{\text{pl}}(\lambda_1)} = \frac{n^2(\lambda_1) - n^2(\lambda_2)}{n^2(\lambda_1) - (1/\beta^2)}. \quad (8)$$

One can see that  $\delta(\lambda_1, \lambda_2)$  does not depend on  $l$ . Some results of the calculation for aerogel with

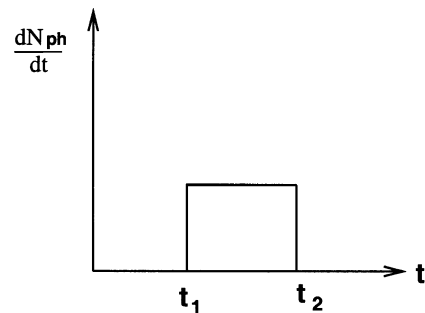


Fig. 2. Schematic view of the Cherenkov photon time distribution.

Table 3  
 $\delta(\lambda_1, \lambda_2)$  in % is the relative change of  $\Delta_{pl}$  as a result of the dispersion of  $n$

$\lambda_1$ (nm)	$\lambda_2$ (nm)	$\beta$	$n$		
			1.05	1.03	1.01
300	550	1	7	7	7
		0.9936 <sup>a</sup>	8	9	18
		0.9919 <sup>b</sup>	8	9	30
200	700	1	20	20	20
		0.9936 <sup>a</sup>	23	25	40
		0.9919 <sup>b</sup>	23	26	50

<sup>a</sup>For  $p = 4.5 \text{ MeV}/c$ .

<sup>b</sup>For  $p = 4.0 \text{ MeV}/c$ .

Eq. (8) are presented in Table 3 basing on quartz data from [12]. If one works far from the threshold for Cherenkov radiation  $\beta \gg 1/n$  and one uses

$$n^2 = 1 + \alpha\rho \quad (9)$$

one will obtain

$$\delta(\lambda_1, \lambda_2) = \frac{\alpha(\lambda_1) - \alpha(\lambda_2)}{\alpha(\lambda_1)}. \quad (10)$$

In this case one can see that  $\delta(\lambda_1, \lambda_2)$  does not depend on  $n$  and  $l$ .

The region  $\lambda = 300\text{--}550 \text{ nm}$  is the sensitive region of a bialkali photo cathode with borosilicate glass. It is seen that the dispersion is small enough for  $n = 1.05$  and  $n = 1.03$  but is 30% for  $n = 1.01$ ,  $p = 4.0 \text{ MeV}/c$ .

The region of  $200\text{--}700 \text{ nm}$  is presented for a dispersion estimation as an example for a photon detector with a wider sensitivity region.

### 3.5. Transverse dimensions and angular distribution of the electron beam

The arrival time of light on the chosen plane RP does not depend on the transverse coordinates of the electron, that is why there is no dispersion connected to the transverse size of the electron beam.

Two electrons  $e_1$  and  $e_2$  cross simultaneously the plane 1 (see Fig. 3). The electron  $e_1$  is moving perpendicular to the aerogel plate and electron  $e_2$  is moving at an angle  $\alpha$  to it. In this case the time

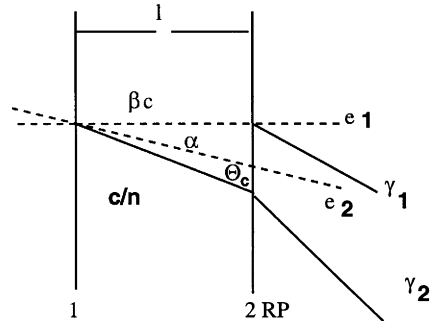


Fig. 3. Schematic view of the Cherenkov photon emission with different incident angles of the incoming electrons.

interval of the Cherenkov photons on the RP plane increases to

$$\Delta_x = \frac{l}{c} \left( \frac{n}{\cos(\alpha + \theta_C)} - \frac{1}{\beta} \right). \quad (11)$$

A typical value of  $\alpha$  at the position where the Cherenkov radiator will be used at PITZ is  $0.1^\circ$ . The resulting contribution of  $\alpha$  to the time resolution is negligibly small because  $\alpha \ll \theta_C$ .

### 3.6. Multiple scattering

Multiple scattering in aerogel creates an angular spread of the electron beam, therefore it leads to a time dispersion as given by the Eq. (11). The analytical calculation of this effect is complicated. One could put  $\alpha = \theta_{MS}$  in Eq. (11). In this case, one will do an overestimation of the multiple scattering influence, because the angle  $\theta_{MS}$  refers only to the electrons at the exit of the aerogel. The photons produced in the first part inside of the aerogel will have more narrow distribution than the photons produced in the last part.

The mean squared value of the trajectory shift is  $r_{MS} = \frac{1}{\sqrt{3}}\theta_{MS}l$  [11] (see Fig. 4). Let us introduce an angle  $\delta$ , so that  $tg\delta = r_{MS}/l = \frac{1}{\sqrt{3}}\theta_{MS}$  and let us assume that  $\alpha = \delta$ . The value of  $\Delta_{MS}(\delta) = l/c((n/\cos(\delta + \theta_C)) - (1/\beta))$  is presented in Table 2. It is seen that thin aerogel radiators and the use of aerogel with high index of refraction is preferred.

In Table 2 an estimation of  $\sigma_{MS}(\delta)$  which is defined as  $\sigma_{MS}(\delta) \approx \Delta_{MS}(\delta)/\sqrt{12}$  is included. For

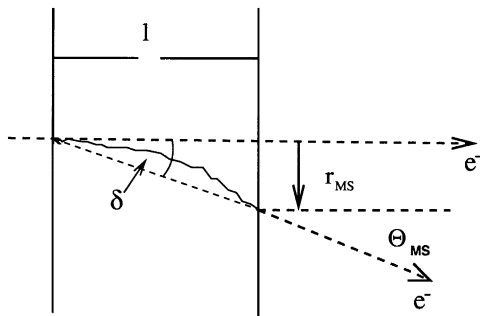


Fig. 4. Schematic view of the electron angular spread and shift due to multiple scattering.

$n = 1.05$ ,  $n = 1.03$ , and  $n = 1.01$  with  $l = 2$  mm the influence of multiple scattering is small, therefore the shape of the time spectrum is approximately rectangular. For  $n = 1.01$  with  $l = 20$  mm it is a rough estimation.

The data from Table 2 shows, that aerogel with  $n = 1.01$ ,  $l = 2$  mm gives the possibility to reach a time resolution  $\sigma_{MS}(\delta) = 0.02$  ps. Aerogel with  $n = 1.05$ ,  $l = 1$  mm gives 10 times more photons and  $\sigma_{MS}(\delta) = 0.1$  ps, whereas aerogel with  $n = 1.05$ ,  $l = 10$  mm would give 100 times more photons and  $\sigma_{MS}(\delta) = 2$  ps.

### 3.7. Other effects

Rayleigh scattering of Cherenkov photons inside aerogel is not considered. The scattered photons would have a wide angular distribution and only a small part of them would be within the acceptance of an optical transmission line.

The effect of energy loss due to ionization and Bremsstrahlung is negligibly small. Compton scattering of Cherenkov photons is much smaller than Rayleigh scattering, therefore this effect gives a negligible contribution to the time resolution. Scattering of photons at the boundary of aerogel is not considered because the index of refraction is small.

In addition to the effects on the time resolution of the aerogel radiator itself, other important sources contribute to the time resolution of a bunch length measurement system which are not considered in this article, e.g. dispersion of the

optical transport system, streak camera resolution and time jitter of the facility.

## 4. Time resolution: Monte Carlo results

### 4.1. Simulation conditions

Simulations of the electron beam passage through aerogel for the PITZ set-up were performed using the GEANT 4 [13] code. The simulation setup consists of a vacuum tube with the electron beam, an aluminium entrance window, the aerogel piece and the corresponding RP (see Fig. 5). The thickness of the aerogel plate  $l$  is chosen as it is described in Section 3.2. Aerogel materials ( $\text{SiO}_2$ ) with index of refraction of 1.01, 1.03 and 1.05 are investigated. In front of the aerogel a  $20 \mu\text{m}$  thick aluminium window can be positioned. This window will be used in the experiment to protect the rest of the PITZ vacuum system from outgasing particles from aerogel. An ideal photon detector is placed behind the aerogel at the reference plane as described above (see Section 3.1).

Electrons produce Cherenkov photons inside the aerogel in a wavelength range of 350–800 nm. The GEANT program was configured to perform a Cherenkov light simulation without wavelength dependence of the refractive index and assuming a photon detection efficiency of 100 percent. The physical processes include Cherenkov effect, Rayleigh scattering, multiple scattering, ionization and Bremsstrahlung. These processes are switched on one after another. No absorption and reflection of

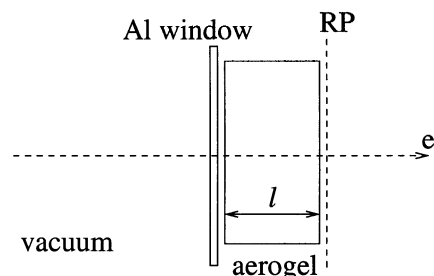


Fig. 5. Schematic view of the geometry of the GEANT 4 input.

the Cherenkov light at the boundaries of the aerogel were considered.

#### 4.2. Acceptance model of the optical transmission line

To estimate the needed acceptance of the optical transmission line behind the aerogel plate, the transverse distribution of the photon emission points from the aerogel backplane and the angular distribution of the emitted photons are calculated for different processes. Both distributions are calculated with respect to the incident electron position and direction.

Fig. 6 shows the distribution of the photon output angle with respect to the incident electron direction for two examples:  $n = 1.01$  and thickness  $l = 20$  mm (figure top) and  $n = 1.05$  and  $l = 1$  mm (figure bottom) for an electron momentum of  $4.5$  MeV/ $c$ . The processes described above are applied one after another. The Cherenkov effect alone results in an angle  $\theta_C$  equally to that shown in Table 2. By adding Rayleigh scattering an almost constant background is produced, the peak at  $\theta_C$  is still very clear. The electron scattering in the aerogel and the aluminium window causes smearing of the distribution and a strong increase of the tail of the distribution. The behavior is similar for aerogel of different refractive indices and thicknesses except that the Cherenkov angle peak occurs at different angles.

Fig. 7 shows the distribution of the photon output radius  $r$  with respect to the incident electron position for  $n = 1.01$  and thickness  $l = 20$  mm (upper figure) and  $n = 1.05$  and  $l = 1$  mm (lower figure) for an electron momentum of  $4.5$  MeV/ $c$ .  $r$  is the distance between the exit point of photons in the aerogel exit plane relative to the incident electron beam position. In these figures different processes were added one after another. For the Cherenkov effect alone a radiation intensity edge occurs corresponding to  $r_C$  as shown in Table 2. Rayleigh scattering results in photons with larger radii but small intensities. By adding multiple scattering and the aluminium window the probability for larger radii increases and for smaller radii decreases. The effect of multiple

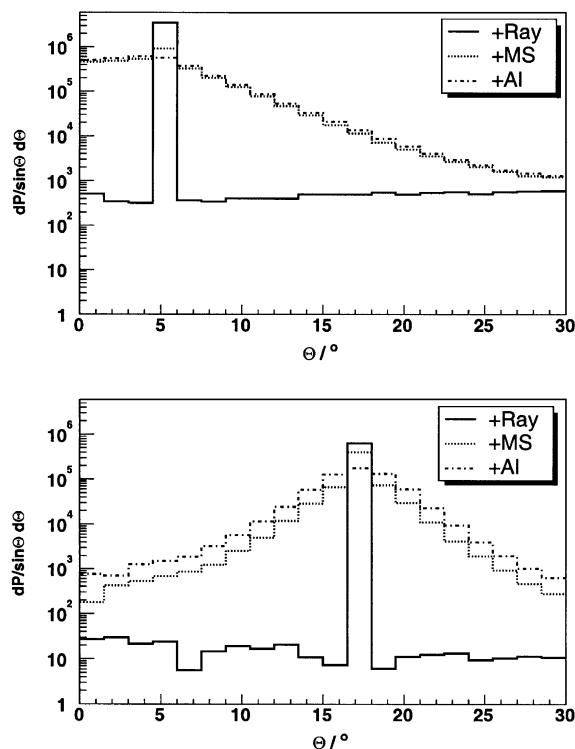


Fig. 6. Distribution of the Cherenkov photon bunches output angle with respect to the incident electron direction for  $n = 1.01$  and thickness  $l = 20$  mm (upper figure) and  $n = 1.05$  and  $l = 1$  mm (lower figure) for an electron momentum of  $4.5$  MeV/ $c$ . +Ray means just considering the Cherenkov effect and Rayleigh scattering. +MS means the inclusion of multiple scattering and +Al that of the aluminium window. Here the processes are added one after another.

scattering is much stronger for aerogel with low index of refraction.

For a realistic experimental design an acceptance angle for the optical transmission line between radiator and streak camera has to be chosen. Adding  $\theta_C$  and  $\theta_{MS}$  for the first three cases in Table 2 leads to a choice of an acceptance angle of about  $20^\circ$ . In addition, all photons inside of a  $5$  mm radius around the initial electron direction are accepted, because the typical electron beam size at PITZ is smaller than this transverse size. This choice of cuts in angle and radius includes the peaks and edges seen in the Figs. 6 and 7, therefore most photons are collected. The following simulations are shown assuming these acceptance cuts.

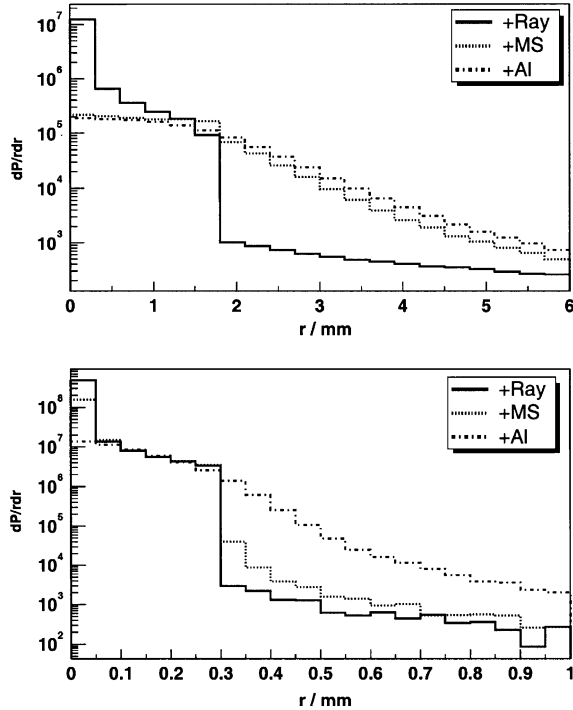


Fig. 7. Distribution of the Cherenkov photon bunches output radius with respect to the incident electron position for  $n = 1.01$  and thickness  $l = 20$  mm (upper figure) and  $n = 1.05$  and  $l = 1$  mm (lower figure) for an electron momentum of  $4.5 \text{ MeV}/c$ . Here the processes are added one after another. +Ray means the inclusion of Rayleigh scattering, +MS the inclusion of multiple scattering and +Al that of the aluminium window. The calculated values of  $r_C$  for pure Cherenkov effect are  $r_C = 1.69$  mm and  $r_C = 0.30$  mm respectively.

#### 4.3. Particle and light velocity

To study the influence of different effects on the time resolution, simulations were performed step by step adding new phenomena to be considered in the simulation. The simplest case is when the bunch length is set to be zero and all electrons are assumed to have the same momentum, no aluminium window is in front of the aerogel and neglecting all electron interactions except the Cherenkov radiation. The electron incident angle is perpendicular to the aerogel plate.

Fig. 8 shows the time distribution of Cherenkov photons produced by electron bunches of  $4.5 \text{ MeV}/c$  momentum and arriving at the photon

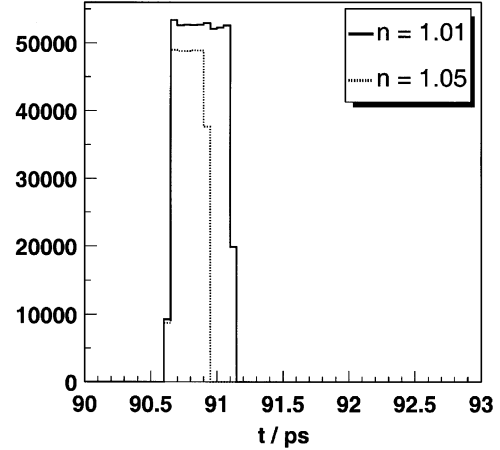


Fig. 8. Time distribution of Cherenkov photon bunches produced by electron bunches of  $4.5 \text{ MeV}/c$  momentum, fixed electron direction and point-like source, no consideration of Rayleigh scattering, multiple scattering and aluminium window. The thickness of the aerogel samples is  $20$  mm for  $n = 1.01$  and  $1$  mm for  $n = 1.05$ .

receiver plane for aerogels with  $n = 1.01$  and  $n = 1.05$  within the acceptance angle. The simulation time clock starts when the electrons start to move and ends when the photons, produced by the electrons, reach the photon receiver. This time distribution has a rectangular shape as expected from Fig. 2. The FWHM of these distributions is in agreement with the theoretical calculation of  $\Delta_{PI}$  (see Table 2.). The simulated Cherenkov angle  $\theta_C$  and cone radius  $r_C$  coincide with the expected values (see Figs. 6 and 7).

The integral of the distribution shown in Fig. 8 is proportional to the amount of emitted Cherenkov photons. These integrals are not equal for both distributions because the thickness was optimized for a momentum of  $4 \text{ MeV}/c$ .

#### 4.4. Rayleigh scattering

To study the influence of Rayleigh scattering on the time resolution, a scattering length of  $40$  mm at  $400$  nm wavelength is assumed, using the proportionality mentioned in Section 2.1 (2). The resulting time distributions for an electron momentum of  $4.5 \text{ MeV}/c$  are shown in Fig. 9. The FWHM does not change compared to Fig. 8. A small

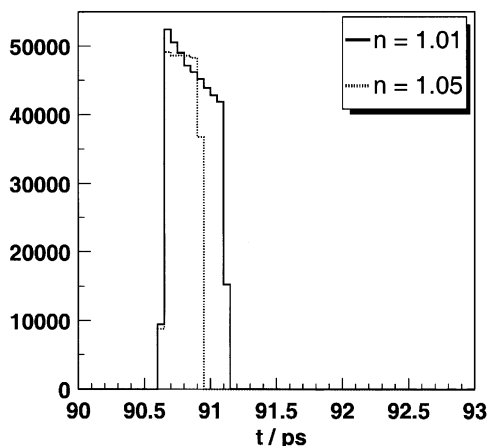


Fig. 9. Time distribution of Cherenkov photon bunches considering Rayleigh scattering produced by an electron bunch of  $4.5 \text{ MeV}/c$  momentum, without multiple scattering and aluminium window. The thickness of the aerogel samples is 20 mm for  $n = 1.01$  and 1 mm for  $n = 1.05$ .

decrease of intensity with time can be observed because of a longer way of the photons inside of the aerogel compared to photons which are produced near to the RP. The scattered photons have a large angle and radius (see Figs. 6 and 7) and therefore are mainly outside of the acceptance range.

#### 4.5. Multiple scattering

To study the influence of multiple scattering, this process was included in the simulation. The processes ionization and Bremsstrahlung are added, too. Fig. 10 shows the time distributions of photons reaching the photon receiver for an electron momentum of  $4.5 \text{ MeV}/c$ . For a refractive index of  $n = 1.01$  the shape of the distribution is changed completely compared to Fig. 9, it now has a long tail. The shape for  $n = 1.05$  is mainly conserved, only for a logarithmic scale a small tail can be observed too. The reduction of the photon intensity at the beginning of the distribution compared to Fig. 9 is explained by the fact that due to multiple scattering the electron direction is changed. This results in a wider angular distribution of the emitted photons yielding longer path length.

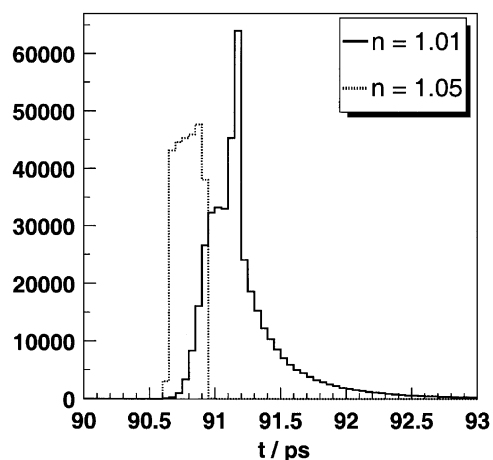


Fig. 10. Time distribution of Cherenkov photon bunches produced by electron bunches with a zero electron bunch length. Rayleigh and multiple scattering, ionization and Bremsstrahlung in aerogel are considered. No aluminium window is used, the momentum is  $4.5 \text{ MeV}/c$ . The thickness of the aerogel samples is 20 mm for  $n = 1.01$  and 1 mm for  $n = 1.05$ .

#### 4.6. Aluminium window

An aluminium window of  $20 \mu\text{m}$  thickness is placed in front of the aerogel. This causes scattering of the electrons before they enter the aerogel. Fig. 11 shows the resulting time distributions for an electron momentum of  $4.5 \text{ MeV}/c$ . The tails are increased and longer. This is significant for  $n = 1.01$ . For  $n = 1.05$  the tail is smaller by a factor of  $10^3$ . Therefore it is not visible in this linear plot.

#### 4.7. Resolution

The described time distributions are calculated assuming a point-like electron source. The RMS time duration is a measure of the RMS time resolution of the system. These values are shown in Table 4. The RMS values are increased and decreased with adding one effect after another. The reason is that some photons can be scattered away out of the acceptance cone and give no contribution to the RMS value. The last line of Table 4 is comparable with  $\sigma_{\text{MS}}(\delta)$  of Table 2.

The refractive index 1.01 is preferred for a small acceptance angle of an optical transmission line,

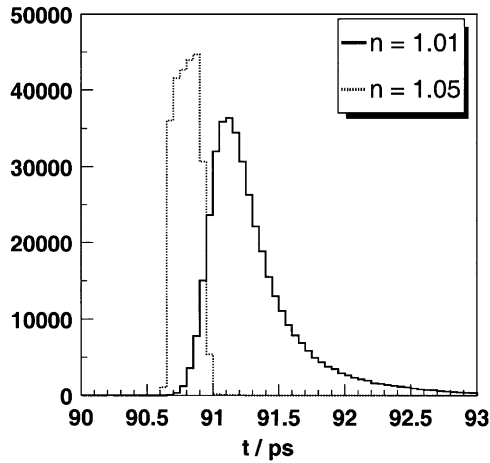


Fig. 11. Time distribution of Cherenkov photon bunches produced by electron bunches with zero electron bunch length. Rayleigh and multiple scattering, ionization and Bremsstrahlung and a 20  $\mu\text{m}$  thick aluminium window are considered for an electron momentum of 4.5 MeV/c. The thickness of the aerogel samples is 20 mm for  $n = 1.01$  and 1 mm for  $n = 1.05$ .

Table 4

RMS time resolution in ps for different refractive indices and different thicknesses of aerogel samples for an electron momentum of 4.5 MeV/c

$l$ (mm)	$n = 1.01$	$n = 1.03$	$n = 1.05$	$n = 1.01$
	20	2	1	2
Cherenkov	0.14	0.092	0.086	0.014
+ Ray	0.60	0.104	0.090	0.014
+ MS	0.80	0.094	0.084	0.012
+ Al	0.58	0.110	0.091	0.017

From top to bottom the processes are added to each other.

but due to the large thickness of 20 mm to obtain the same photon yield a worse time resolution is caused by multiple scattering. By using a smaller thickness, as it is described in Section 3.2(B), the number of photons is decreased by a factor of 10. Fig. 12 shows the time distribution for different processes, the time range is much smaller than for the thicker aerogel with  $n = 1.01$ . The corresponding time resolutions are also shown in Table 4. One can see that aerogel gives the possibility to reach a time resolution of 0.02 ps. This time resolution can

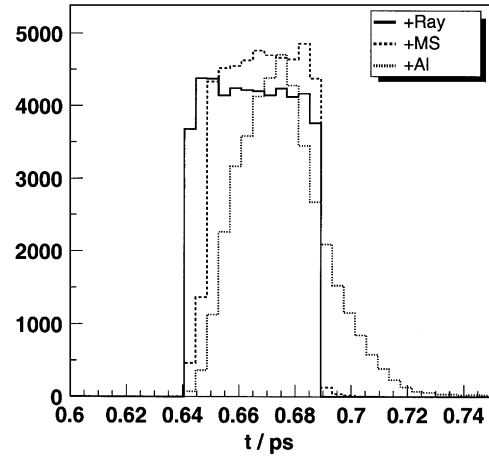


Fig. 12. Time distribution of Cherenkov photon bunches produced by electron bunches in aerogel with refractive index of 1.01 for a momentum of 4.5 MeV/c for different effects, the effects are added after another. The thickness of the aerogel sample is 2 mm.

be reached if the detector is able to detect the weak signal.

To determine how the proposed system will measure the bunch length distribution, an electron beam simulated with ASTRA [14] is used as input for the GEANT 4 simulation. The beam has a transverse size of  $\text{RMS}_{x,y} = 2.3$  mm and an angle distribution of  $\text{RMS}_{x',y'} = 1.6$  mrad with a mean momentum of 4.54 MeV/c and a momentum spread of 1.4%.

The example shown in Fig. 13 is for the worst case of time resolution for  $n = 1.01$  and thickness  $l = 20$  mm. The thick solid line represents the time distribution of the electron beam, the thin line shows the time distribution produced by Cherenkov photons in aerogel. Only small differences can be seen. The distributions for the other considered aerogels match even better the electron beam time distribution.

## 5. Summary

The time resolution of aerogel radiators used for the measurement of the electron bunch length at the PITZ facility is analytically calculated and simulated with GEANT 4. It was shown, that for

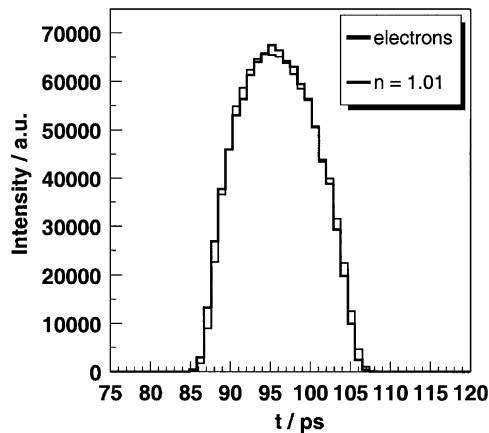


Fig. 13. Time distribution of a simulated electron beam and its corresponding Cherenkov photon beam produced in aerogel (refractive index  $n = 1.01$ , thickness 20 mm). The distributions are normalized to their areas.

aerogel of refraction index  $n = 1.05$ , 1 mm thickness and an aluminium window of  $20\ \mu\text{m}$  thickness, the time system response has a rectangular shape with the RMS resolution of  $\sim 0.1\ \text{ps}$ . The tails are at the level of  $10^{-3}$ . Such a radiator will allow to study the bunch structure of electrons. In addition, it is shown that with aerogel of  $n = 1.01$  and 2 mm thickness a time resolution of  $\sim 0.02\ \text{ps}$  could be reached if photon detectors with a corresponding time resolution and sensitivity would be available.

## Acknowledgements

We would like to thank A. F. Danilyuk, S. A. Kononov, E. A. Kravchenko and P. V. Logachev for the fruitful discussion.

## References

- [1] A.F. Danyliuk, et al., Nucl. Instr. and Meth. A 494 (2002) 491.
- [2] A.R. Buzykaev, et al., Nucl. Instr. and Meth. A 433 (1999) 396.
- [3] T. Iijima, et al., Nucl. Instr. and Meth. A 453 (2000) 321.
- [4] A.R. Buzykaev, et al., Nucl. Instr. and Meth. A 379 (1996) 465.
- [5] M.Yu. Barnyakov, et al., Nucl. Instr. and Meth. A 453 (2000) 326.
- [6] A.F. Danyliuk, et al., Nucl. Instr. and Meth. A 433 (1999) 406.
- [7] M.Yu. Barnyakov, et al., Nucl. Instr. and Meth. A 494 (2002) 424.
- [8] T. Iijima, et al., Nucl. Instr. and Meth. A 502 (2003) 231.
- [9] I.M. Frank, I.E. Tamm, Dokl. Akad. Nauk, SSSR 14 (3) (1937) 109.
- [10] Photomultiplier Tubes, Catalog TPM0003E02, Hamamatsu, October 1998.
- [11] K. Hagiwara, et al., Particle data group, Phys. Rev. D 66 (2002) 010001.
- [12] F. Kohlrausch, Teubner Verlag, ISBN 3-519-23000-3, 1996.
- [13] GEANT 4, <http://wwwasd.web.cern.ch/wwwasd/geant4/geant4.html>.
- [14] K. Flöttmann, A space charge tracking algorithm, [http://www.desy.de/~mpyflo/Astra\\_dokumentation](http://www.desy.de/~mpyflo/Astra_dokumentation).

# COHERENT RADIATION DIAGNOSTICS FOR SHORT BUNCHES

O. Grimm\*, University of Hamburg, Germany

## Abstract

Investigating the longitudinal charge distribution of electron bunches using coherent radiation has become an important diagnostic technique at many accelerators. The principle of the method and some example applications from the FLASH free-electron laser in Hamburg will be described in this article.

## INTRODUCTION

The longitudinal charge distribution in an electron bunch is an important characteristic for many particle accelerators and storage rings: the gain length of a free-electron laser (FEL) depends on the peak current of the bunch, and thus, for a given charge, on the bunch length (a typical value is  $15 \mu\text{m}/50 \text{fs}$ ); the slicing-technique for producing ultra-short x-ray pulses at third-generation light sources relies on producing and controlling a very short longitudinal structure in the bunch through interaction with a laser ( $90 \mu\text{m}/300 \text{fs}$ ); high-energy physics machines need to achieve a sufficiently short bunch to avoid luminosity degradation due to the hourglass-effect ( $600 \mu\text{m}/2 \text{ps}$ ).

Manipulating the bunch to get a desirable and short charge distribution is a complicated procedure and typically requires, for an FEL, several bunch compression steps involving complex longitudinal dynamics. Stable lasing is only achieved for a well-tuned machine. Measuring the longitudinal profiles, and thus guiding the tuning, is a very important ingredient for efficient machine running, as is the preservation of a once-found good machine setup using feedbacks.

Time-domain methods for measuring the longitudinal structure with resolutions in the 50 fs range exist, though typically require involved set-ups, for example high-power transverse deflecting cavities (that need special optics to attain maximum resolution and are thus not parasitic to normal machine operation), or techniques based on electro-optic principles. Coherent radiation diagnostics (CRD) allows a different approach to this measurement task by working in the frequency domain. No individual technique is currently giving all the information that is needed, and therefore several approaches to longitudinal diagnostics are often employed in parallel.

The notion that the bunch charge distribution affects the emission spectrum is known for a long time, though only starting around 1990 the application for beam diagnostics

has been investigated.<sup>1</sup> See [2] for further references on original works.

This article will give a brief introduction to the principle of the diagnostic technique, followed by an overview of some of the experimental arrangements that are currently employed. By no means a complete coverage is intended or possible. The focus will be on studies and results from the FLASH free-electron laser at DESY, Hamburg.

## PRINCIPLE OF CRD

The basic relation of coherent radiation diagnostics connects the radiation emission spectrum of a bunch of electrons,  $dU/d\lambda$ , to that of a single-electron,  $(dU/d\lambda)_1$ , by

$$\frac{dU}{d\lambda} = \left( \frac{dU}{d\lambda} \right)_1 \left( N + N(N-1) |F(\lambda)|^2 \right). \quad (1)$$

$N$  is the number of electrons in the bunch,  $F(\lambda)$ , the *form factor*, the Fourier transform of the normalized bunch charge distribution  $S(z)$ ,

$$F(\lambda) = \int_{-\infty}^{\infty} S(z) e^{-2\pi i z/\lambda} dz. \quad (2)$$

Here, charge distribution and form factor are considered only for a line charge. A non-vanishing transverse extend influences the emission spectrum, although only weakly due to the strong collimation of the radiation for highly relativistic particles, unless the transverse extend is very large with respect to the wavelength. Transverse effects are studied in [3, 4].

The effect of coherent enhancement is illustrated in Fig. 1. For wavelengths comparable to the bunch length or larger, the spectral intensity is strongly amplified, as a large part of the bunch electrons emits coherently. The enhancement of the spectrum extends to shorter wavelengths for shorter bunches, and the shape of the spectrum depends on the shape of the charge distribution. Coherent radiation diagnostics uses this effect to deduce information about the bunch length or bunch shape. The derivations of the basic relations are given in detail in [5].

## EXPERIMENTAL BASICS

Any setup that uses coherent radiation as a diagnostic tool includes as a minimum a source of some kind, some

<sup>1</sup>The first description of coherent effects is made, to the authors knowledge, in an originally unpublished paper in 1945 by Schwinger within the context of synchrotron radiation, including also a discussion on shielding. The paper has been reissued in [1].

\* oliver.grimm@desy.de

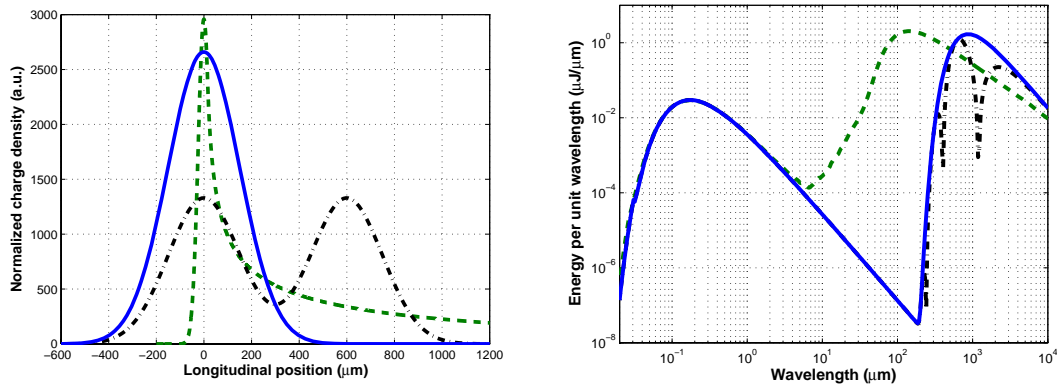


Figure 1: Example for coherent enhancement. On the left, three different bunch shapes are shown, on the right the effect on the emission spectrum after Eq. 1 for 1 nC bunch charge. As single-electron spectrum, synchrotron radiation for circular motion is taken.

beam line to transport the radiation, and a detector. Additional components for a more detailed analysis of the radiation, like spectrometers, are often added, some of which are mentioned in subsequent sections.

*Radiation sources*

All processes that result in the emission of radiation from an electron are in principle suitable for the purpose of CRD. At FLASH, for example, synchrotron, transition and diffraction radiation are used so far, and a dedicated tunable electromagnetic infrared undulator is currently being installed [6]. The choice of source depends very much on the desired application, as the spectral characteristics and the influence on accelerator operation vary.

A fully parasitic source, not influencing accelerator operation at all, is synchrotron radiation if taken from an existing bunch compressor or bending magnet. This source covers a wide wavelength range. The emission spectrum, especially at long wavelengths, is complicated, as the usual spectrum derived for circular motion in free space is not valid for the comparatively short bending magnets in a bunch compressor (edge effect) and the typically flat vacuum chambers (cut-off) [7, 8]. Also the coherent enhancement can be affected if a bunch only moves on an arc instead of a circle [9].

Transition radiation is significantly more intensive and can be reasonably well calculated for realistic geometries [10]. It is, however, destructive (even for a thin radiator, the emittance is degraded strongly). A fast kicker is used at FLASH to extract a single bunch for beam diagnostics with transition radiation, allowing quasi-parasitic operation if longer bunch trains are used.

Diffraction radiation is parasitic if the gap in the radiator is sufficiently wide to prevent wake fields from disturbing subsequent bunches. Due to the gap, however, short wavelengths are strongly suppressed [10], and this source is thus not suitable for investigations of short bunch structures.

Smith-Purcell radiation essentially combines the source

with a spectrometer [11], as the emitted frequency depends on the observation angle. It requires, similar to diffraction radiation, a radiator close by the beam, rising the question of wake fields and the emission of short wavelengths.

Undulator radiation is a narrow-band, high-intensity source, in principle rendering a spectrometer for analysing the radiation obsolete. Attention has to be paid to higher harmonics if a wiggler-like spectrum is obtained from a high-K device.

*Radiation transport*

The emitted radiation has inevitably to be coupled out from the accelerator vacuum into a measurement setup, requiring some form of radiation transport beam line. To avoid absorption from water vapour that is prominent in the infrared, evacuation of the whole setup is desirable, though only a fore vacuum on the order of 0.1 mbar is needed for distances up to several 10m. A window then has to separate the fore-vacuum from the ultra-high accelerator vacuum. Thin foils of polyethylene have a good wide-band transparency, though often are considered to be too fragile from a machine safety point-of-view. Other plastic materials, like for example TPX that has the advantage of being transparent in the visible, have also been used. Crystalline quartz (cut perpendicular to its optical axis to avoid birefringence) is frequently used, but its useful transmission range extends only down to 80μm. The only fully satisfactory material with almost constant transmission of 70% from the visible up to at least millimeter waves is diamond. It is also a strong material, so that 0.5 mm thick windows of 20 mm aperture withstand atmospheric pressure. To avoid etalon interference, such a window is typically wedged with an angle of up to 1°.

As the design of the beam line usually requires full attention to diffraction effects, Fourier optics codes (for example ZEMAX) are used. Although the application and working of such a code is in principle straightforward, care must be taken to implement the source correctly.

## Detectors

Broad-band infrared detectors are bolometric, that is their primary detection mechanism is heating due to absorption of radiation. A subsequent effect then converts the temperature change into an electric signal.

Widespread use is made of pyroelectric detectors that use a change of polarization of certain materials like  $\text{LiTaO}_3$  with temperature. Such a detector is essentially a capacitor of a few square millimeter area and a thickness between  $30\ \mu\text{m}$  and  $100\ \mu\text{m}$ . Radiation enters through the transparent top electrode, is absorbed, and the resulting surface charge or voltage from the polarization change is detected. Etalon interferences due to the relatively weak absorption in the far infrared are pronounced, as shown in a measurement in Fig. 2. Wedged crystals could overcome this problem, but have so far not been made.

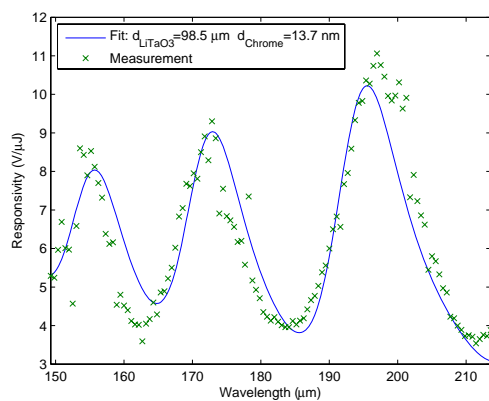


Figure 2: Response of a pyroelectric detector. The fit describes absorption in a stack of a thin Chrome top electrode, a  $\text{LiTaO}_3$  crystal and a thick gold back electrode. The optical constant of  $\text{LiTaO}_3$  are not known precisely, limiting the quality of the fit.

Pyroelectric detectors are intrinsically fast, and are used at FLASH with suitable read-out electronics to measure infrared radiation in long trains of up to 600 bunches with 1 MHz repetition rate. Response speeds exceeding 1 ns have been demonstrated elsewhere [12]. Since all pyroelectric crystals are also piezoelectric, mechanical vibrations excited by the absorption of short, intense infrared pulses result in ringing, typically at frequencies of several 100 kHz, depending on crystal geometry [12].

Another broad-band, room-temperature detector that is used frequently is the Golay cell, an opto-acoustic detector. The heating of a closed gas volume and subsequent pressure increase is detected optically via the flexing of a thin membrane. It is expected to have a much flatter response, showing no resonance structures like a pyroelectric detector, as the Golay cell has some similarity to a black body cavity. Measurements similar to those from Fig. 2 support this for the wavelength range  $100\ \mu\text{m}$  to  $160\ \mu\text{m}$ , though indicate non-uniform response around  $3\ \text{mm}$  [13].

06 Instrumentation, Controls, Feedback & Operational Aspects

1-4244-0917-9/07/\$25.00 ©2007 IEEE

Orders of magnitude more sensitivity are possible with cooled bolometers, essentially due to the decreased heat capacity of materials at low temperatures (liquid Helium) and the fast change of resistivity with temperature in the transition region from normal to superconducting state. A superconducting hot-electron bolometer was shown in [14] to have a time constant faster than 25 ps. Wide bandwidth operation of such a detector into the mid-infrared is usually not possible due to the steeply increasing heat load from room-temperature black body radiation. Cold filters are employed to limit thermal radiation from reaching the detecting element.

## BUNCH COMPRESSION MONITOR

The simplest application of coherent radiation diagnostics uses the frequency-integrated intensity as a relative measure of bunch length. An example from FLASH is shown in Fig. 3: Transition or diffraction radiation from a screen is coupled out through a crystalline quartz window and transported to a pyroelectric detector.

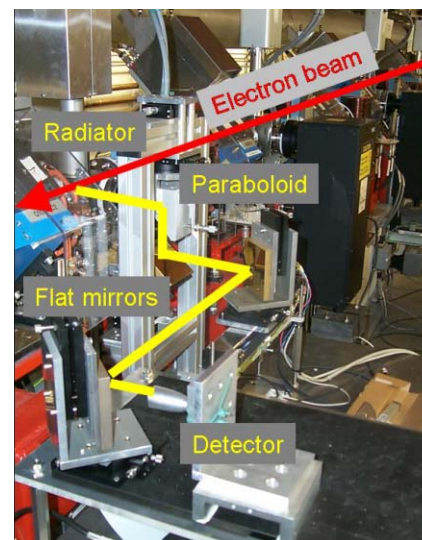


Figure 3: Bunch compression monitor setup at FLASH.

This compression monitor is installed after the first magnetic bunch compressor of FLASH. According to Fig. 1, the total radiation intensity increases with shorter bunches. The degree of bunch compression is adjusted by changing the acceleration phase of the acceleration module in front of the bunch compressor. A scan of this phase versus the intensity registered by the pyroelectric detector is shown in Fig. 4. Note that the curves obtained with synchrotron radiation from the last bunch compressor dipole magnet and with diffraction radiation from the set-up Fig. 3 are very similar except for the amplitude. Different pyroelectric detectors, different optics and only a simple alignment have been used, indicating the robustness of the method for determining maximum compression.

Such a scan, especially the deduced maximum compression phase, is used routinely at FLASH to establish the

T03 Beam Diagnostics and Instrumentation

2655

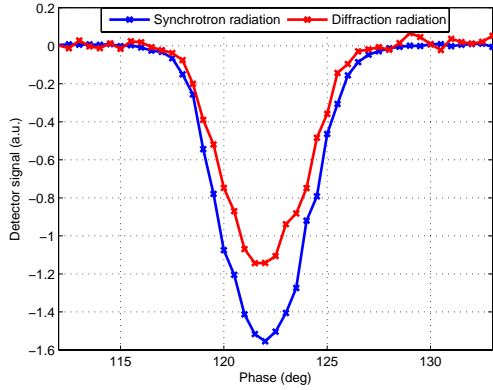


Figure 4: Phase scan with two bunch compression monitors at FLASH. The varied phase is that of the accelerating module in front of the bunch compressor.

*per se* arbitrary setpoint phase scale. A typical phase for SASE operation is several degrees away from maximum compression, thus allowing a simple feedback algorithm to stabilize the compression by regulating the module phase. This is an indispensable tool at FLASH to counteract drifts on the time-scale of some 10 seconds or longer. Despite the restricted wavelength range due to a crystalline quartz window, the phase found for maximum compression agrees well with the value expected from simulations.

A compression monitor based on using a ceramic gap as radiation source and diode detectors working up to several hundred GHz is proposed for the first bunch compressor of LCLS [15].

### BUNCH SHAPE RECONSTRUCTION

By using the full spectral information instead of the frequency-integrated intensity, a more complete determination of the bunch profile is possible. Through knowledge of the single-electron spectrum and the bunch charge, at first the magnitude of the form factor  $|F(\lambda)|$  can be deduced from (1). Inverting the Fourier transformation (2) to get the charge distribution is then possible if both amplitude and phase of the complex form factor are available. Although a strict solution of this phase-reconstruction problem is not possible, the Kramers-Kronig relation gives a handle to solve the problem from a practical point of view satisfactorily [2, 5, 16]. If the complex form factor is expressed as  $F(\nu) = |F(\nu)| \exp(i\Theta(\nu))$ , then

$$\Theta(\nu) = \frac{2\nu}{\pi} \int_0^\infty \frac{\ln(|F(\nu')|/|F(\nu)|)}{\nu'^2 - \nu^2} d\nu' \quad (3)$$

yields a phase, the so-called *minimal phase*, that is compatible with the measured form factor amplitude. Although this solution is not necessarily unique, in practice the requirement to extrapolate the measured data to zero and infinite frequency, and the measurement errors are a more

serious problem of the reconstruction process than the non-rigorous mathematics.

It is usually difficult to assess the single-electron spectrum precisely. It requires detailed knowledge of not only the radiation generation process in the actual experimental setup, but also of the distortions of the spectrum by the beam line and by the response of the instrument used to measure the spectrum. In some cases it has been possible to measure the incoherent spectrum over a certain wavelength range by assuring that the bunch is long enough to suppress coherent effects [17], but otherwise it is necessary to resort to simulations.

An example for a bunch shape reconstruction at FLASH is given in Fig. 5, taken from [18]. Here, synchrotron radiation from the first bunch compressor was transported to an experimental station outside of the accelerator tunnel, and the spectrum measured with a Martin-Puplett interferometer. The result is compared to a streak camera measurement using the visible part of the synchrotron radiation spectrum at the same beam line.

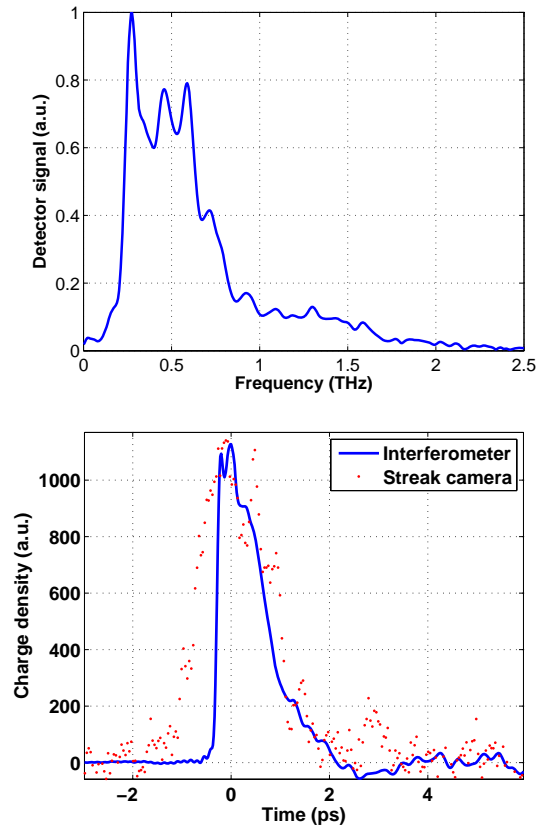


Figure 5: Example for a bunch shape reconstruction at FLASH. On top a measured synchrotron radiation spectrum, below the reconstructed charge distribution. The streak camera measurement has been made at the same synchrotron radiation beam line using visible light.

The streak camera resolution is limited to about 500 fs, the frequency-domain method mainly by the presence of a crystalline quartz window. Although an acceptable agree-

ment is found, the amount of work in correcting the measured spectrum and finding suitable extrapolations was significant, clearly indicating that full bunch shape reconstruction is still an experimental and not fully independent technique.

Another experimental result for full bunch reconstruction can be found in [19].

## SINGLE-SHOT SPECTROMETER

A high variability of the SASE intensity on a shot-to-shot basis is found at FLASH. A thorough investigation using coherent radiation diagnostics requires thus equally fast spectral information, ruling out a scanning interferometer for this tasks. A single-shot spectrometer based on staged blazed gratings was developed at FLASH, allowing a wide wavelength coverage from  $4\mu\text{m}$  up to some  $500\mu\text{m}$ . The details of the instrument are described in [20].

Measurements have been carried out at the FLASH transition radiation beamline which is located after the final bunch compression stage and equipped with a diamond window [21]. A phase scan with this instrument is reproduced in Fig. 6. Compared to the frequency-integrating scan from Fig. 4, it shows a much more complex behaviour, and especially a much stronger phase dependency (note that the phase scale in Fig. 4 has an arbitrary offset).

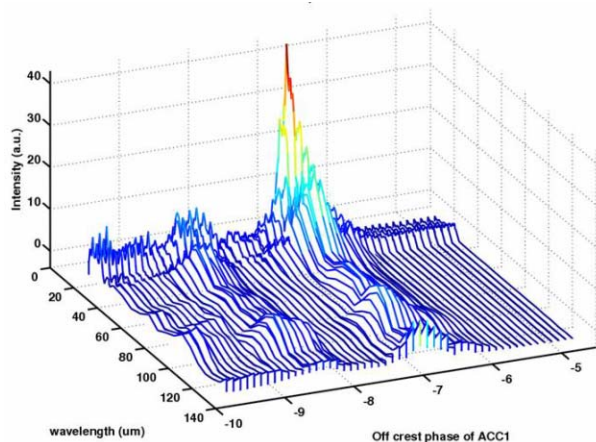


Figure 6: Phase scan with the single-shot spectrometer.

The narrow phase-band that shows high intensity at wavelengths around  $30\mu\text{m}$  is typically also a good starting point for further machine optimization. SASE performance of FLASH is influenced by many parameters, thus no optimum setting can be suggested by such a measurement alone, but tuning has in several occasions been significantly shortened and improved by using CRD for the initial set-up.

## CONCLUSION

Longitudinal bunch shape investigations using coherent radiation are by now a standard tool for nearly all machines  
06 Instrumentation, Controls, Feedback & Operational Aspects  
1-4244-0917-9/07/\$25.00 ©2007 IEEE

operating with short bunches or short bunch features. The tools employed in routine machine operation are, however, invariably non-calibrated, thus giving only relative or empirical information to help setting up a machine. Full longitudinal charge profile reconstruction is still a specialist application, and typically requires significant, dedicated work.

From the experience gained at FLASH, there is a clear benefit from having a wide wavelength coverage with a single-shot resolving spectrometer, especially at the experimental level. With increased understanding of the measured spectra and their dependence on machine parameters, it will likely be possible to restrict the wavelength coverage at a later stage. The benefit, however, comes at the price of a significantly higher hardware complexity, requiring evacuated setups, diamond windows, and well designed optics.

## ACKNOWLEDGMENTS

I'd like to thank many colleagues for their cooperation and for kindly sharing their experience and results with me: G. Doucas and V. Blackmore (Oxford), V. Schlott (PSI), J. Frisch (SLAC), E. Chiadroni (INFN), H.W. Hübers (DLR Berlin), K. Holldack (BESSY), A. Paech (TU Darmstadt), B. Schmidt and L. Fröhlich (DESY). I'd like to acknowledge especially the many useful discussions and comments of my colleagues J. Rossbach and H. Delsim-Hashemi from DESY.

## REFERENCES

- [1] J. Schwinger, LBNL-39088 (1996)
- [2] R. Lai, A.J. Sievers, Nucl. Instr. Meth. A397(1997) 221
- [3] Y. Shibata et al., Phys. Rev. E50, 1479 (1994)
- [4] A.H. Lumpkin, Phys. Rev. Lett 88, 234801 (2002)
- [5] O. Grimm, P. Schmüser, TESLA FEL 2006-03 (2006)
- [6] O. Grimm et al., Proceedings of FEL 2005, p. 183
- [7] R.A. Bosch, Nucl. Instr. Meth. A482, 789 (2002)
- [8] A. Paech et al., Proceedings of EPAC 2006, p. 1031
- [9] E.L. Saldin et al., Nucl. Instr. Meth. A398, 373 (1997)
- [10] S. Casalbuoni, B. Schmidt, P. Schmüser, TESLA 2005-15 (2005)
- [11] G. Doucas et al., Proceedings of EPAC 2006, p. 1100
- [12] C.B. Roundy, SPIE Vol. 62, 191 (1975) Infrared Technology
- [13] E. Chiadroni, TESLA-FEL 2006-09 (2006)
- [14] K. S. Il'in et al., Appl. Phys. Lett. 76, 2752 (2000)
- [15] J. Frisch, SLAC, private communication
- [16] J.S. Toll, Phys. Rev. 104, 1760 (1956)
- [17] M. Abo-Bakr et al., Phys. Rev. Lett. 90, 094801 (2003)
- [18] L. Fröhlich, DESY-THESIS 2005-011 (April 2005)
- [19] G. Schneider et al., Nucl. Instr. Meth. A396, 283 (1997)
- [20] H. Delsim-Hashemi, PhD thesis University of Hamburg, to be published
- [21] S. Casalbuoni et al., TESLA 2006-04 (2006)

## OBSERVATION OF FEMTOSECOND BUNCH LENGTH USING A TRANSVERSE DEFLECTING STRUCTURE

Markus Hüning\*, Andy Bolzmann, Holger Schlarb (DESY, Hamburg),  
 Josef Frisch, Douglas McCormick, Marc Ross, Tonee Smith (SLAC, Menlo Park, California),  
 Jörg Rossbach (Universität Hamburg, Hamburg)

### Abstract

The design of the VUV-FEL at DESY demands bunch lengths in the order of 50 fs and below. For the diagnostic of such very short bunches a transverse deflecting RF structure (LOLA) has been installed which streaks the beam according to the longitudinal distribution. Tests in the VUV-FEL yielded a rich substructure of the bunches. The most pronounced peak in the has a rms length of approximately 50 fs during FEL operation and below 20 fs FWHM at maximum compression. Depending on the transverse focusing a resolution well below 50 fs was achieved.

### INTRODUCTION

To obtain enough gain for the SASE process it is necessary to produce peak currents in the order of 4 kA. With the present setup of the machine this can only be accomplished by compressing part of the bunch to 50 fs. Diagnosing such a short pulse poses a challenge to the beam instrumentation. Therefore a transversely deflecting structure is used to streak the beam.

For this purpose a structure formerly used for particle separation in secondary beams is utilized. It has been used before at SLAC under the name LOLA IV [1]. It is an S-band structure operating at a frequency of 2.856 GHz. Operating the structure close to the zero crossing of the field the bunches acquire no net deflection but are streaked vertically. Using a horizontally deflecting kicker one bunch per pulse is steered onto an OTR-screen. This way it is possible to diagnose parasitically one bunch out of a train of several hundred bunches. At SLAC this structure has been used for the same purpose [2,3,4]

### SETUP

The setup of the VUV-FEL is depicted in figure 1. The electron bunches are created in an RF-gun and then

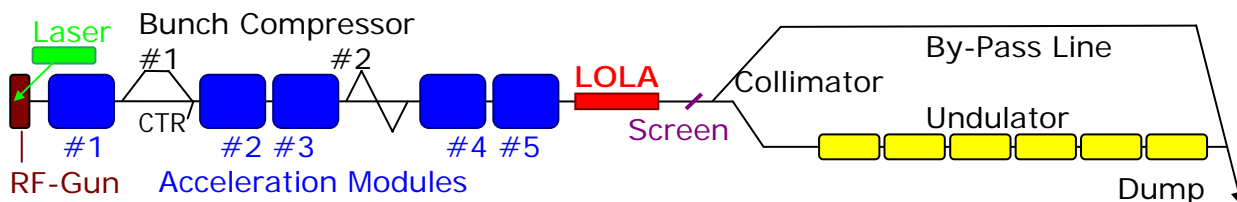


Figure 1: Schematic drawing of the VUV-FEL beam line. At the end of the accelerating section there is the transversely deflecting structure LOLA. It streaks the beam vertically so that on a downstream viewscreen the longitudinal profile of the bunches can be studied.

\*Corresponding author: markus.huening@desy.de

accelerated in 5 superconducting modules up to presently 450 MeV. Behind the first and the third module there are two bunch compressors used to shape the longitudinal profile of the bunches. The initial bunch length is 7 ps (RMS) which is already long enough to probe the nonlinear rf curvature of the 1.3 GHz L-band cavities. This results in an incomplete compression in the first bunch compressor. The out coming bunch then has two main parts: A very short spike in the head and a tail which resembles the original distribution. The tail however still has an energy correlation imprinted in the first module and reshaped in the bunch compressor. Part of the tail is then compressed in the second bunch compressor to form a short spike with high peak current and good emittance. Depending on the exact phases in the modules #1-#3 the two bunch compressors produce a single or double spike at the exit of the linac. At the end of the acceleration sections, before the collimator system of the undulators, there is the transversely deflecting structure LOLA installed.

The structure is an S-band travelling wave structure. It operates in TE-TM-hybrid mode, so that a combination of electric and magnetic field produces a transverse kick. The maximum equivalent deflecting voltage is 20 MV over a structure length of 3.6 m. The fill-time is 680 ns, so that in a 1 MHz bunch train only one bunch is affected. A downstream OTR screen is utilized to analyse the streak. It is displaced from the centre of the beam pipe so that the beam can pass through. A kicker is used to steer only the bunch in question onto the screen.

To allow for a better synchronization with the master clock, LOLA is tuned to a frequency of 2.856059 GHz, which is an integer multiple of 1/11 of the master clock frequency of 9.027775 MHz. By means of an additional synchronization circuit it is guaranteed that the machine triggers always with a fixed phase relation to this reference [5]. At 9 MHz bunch rate this frequency offset

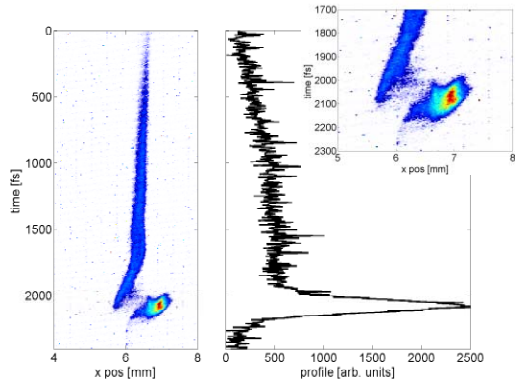


Figure 2: Image of the streaked bunch; inset: zoom on the spike at the head. The streak was approximately 4 fs/px.

results in a phase shift of  $36^\circ$  between neighbouring bunches. This way these bunches would miss the screen and not disturb the measurement.

Because an absolute calibration of the streak based on pure RF measurements did not seem precise enough, one power level was calibrated using the deflection of the beam. The calibration of the other power levels was then scaled according to the relative change of RF power. Relative power levels can be measured much more precisely than absolute levels, so that this method appeared accurate enough. For the calibration a relatively low power level was chosen, allowing for a phase shift of  $\sim 7^\circ$  before the bunch misses the screen. In this way the influence of phase jitter on the calibration is reduced. A streak of 74 pixel/degree or 13.2 fs/pixel was measured. One pixel of the CCD corresponds to  $26 \mu\text{m}$ . A maximum possible streak of 1.8 fs/pixel can be achieved. The optical setup allows for a better resolution than  $26 \mu\text{m}$ .

The beam size at this location is larger, however. The standard beam optics foresee  $200 \mu\text{m}$  spot size (RMS), which would then correspond to a resolution of approximately 15 fs. Unfortunately the spike is also the region of the largest energy spread in the bunch. An energy spread of  $\sim 1 \text{ MeV}$  (RMS) is not uncommon. In

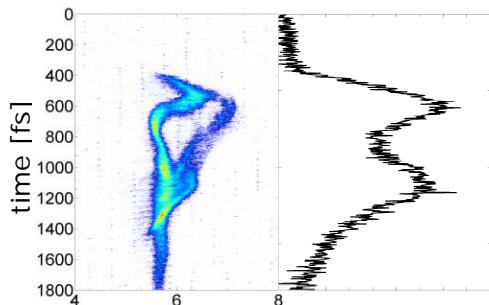


Figure 3: Bunch head with a double peak structure. There is a rich sub-structure of the bunch which shows not only longitudinally but transversely. Note that the streak is opposite to figure 2.

such a case each millimetre of vertical dispersion would contribute with 0.3 fs to above resolution.

## RESULTS

The transverse deflecting structure LOLA has been used to measure the longitudinal bunch profile while the machine was setup for SASE operation. Two examples are given in the figures 2 and 3. While the performance of the FEL was quite similar in the two cases (approximately  $1 \mu\text{J}$  photon pulse), the two profiles differ considerably. Both setups were started from a standard setting defined as follows: The acceleration in the first module was adjusted 6 degrees from the maximum compression phase, which is defined by the maximum of the coherent diffraction radiation at a station closely behind the first bunch compressor (see figure 1). The second and third module are adjusted for on-crest operation so that they do not add considerably to the longitudinal energy distribution. The second bunch compressor then creates the spike necessary for the high peak current at low emittance.

In the first case (figure 2) the module 1 phase was subsequently tuned for less compression, so that no strong peak was produced in the first bunch compressor but only in the second. This would also explain the relatively weak sub-structure of the bunch, because CSR would play a big role only after the second compression stage when it can not influence the longitudinal profile very much.

In the second case (figure 3) the phase was tuned to stronger compression in the first bunch compressor, so that both bunch compressors produce a spike. This results in the double peak structure that can be observed. At the same time there is even more structure to the bunch. This is probably due to wakefield and CSR effects in the first bunch compressor, which can then be translated into a longitudinal modulation in the second compressor stage.

In both cases the width of the peak in the projected profile is measured to be in the order of 120 fs (FWHM). This result however has to be considered preliminary because not all detrimental effects have been considered thoroughly yet. The true width will be smaller than that.

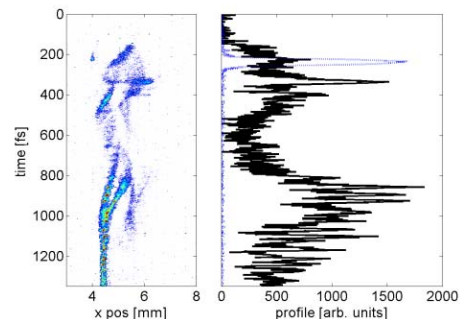


Figure 4: Bunch head with faster streak (2 fs/px) and optimized focusing. The dotted line in the right plot indicates the unstreaked beam size.

For the example in figure 4 the streak was increased and the unstreaked spot optimized for minimum vertical size. Consequently there was no lasing at that time, but the settings were somewhat close to the ones in figure 3. Exact consistency can not be guaranteed, particularly the compression might have been stronger. There is much more structure to be seen than in the previous cases. This appears in part enhanced by a lower intensity of the image which causes darker parts to vanish completely.

The effects that concern the most are the entanglement of the vertical and longitudinal structure of the bunch and the vertical dispersion. As can be seen from the figures 2 through 4 there is a strong variation of the horizontal profile along the bunch. This presumably has to be attributed to the two bunch compressors, which deflect horizontally. Nevertheless it can not be excluded that similar effects show vertically. Since the spike carries only a small fraction of the total bunch charge this can not be checked with the un-streaked beam. In this case the charge contained in the tail outshines the head.

A remedy to this problem might be a tomography in the z-y-plane. For this the voltage in the structure would have to be scanned while the change in profile would be recorded. This procedure is in preparation but is not finished yet. Likewise has the dispersion not been measured nor compensated yet.

The LOLA structure can also be used to monitor the jitter of the beam arrival time. This information is of special importance to pump-probe experiments to be

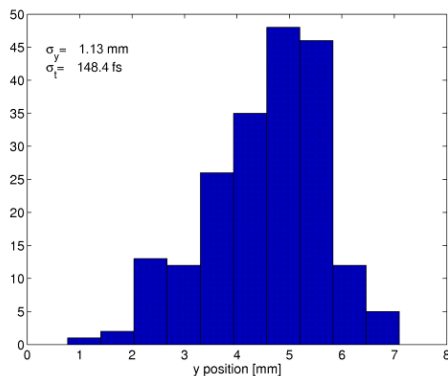


Figure 5: Phase jitter of the beam with respect to LOLA. The jitter due to the high power RF in LOLA is approx. 70 fs.

performed with external lasers synchronized to the master clock. The figure 5 shows the shot-by-shot jitter of the bunches measured with a BPM close to the viewscreen.

An RMS jitter of 145 fs (RMS) was measured. Note that this is the jitter of the beam with respect to the LOLA RF which can have a jitter by itself. The largest contribution will be the stability of the klystron, which was found to be in the order of 70 fs (RMS). A similar result for the beam jitter was found with electro-optical

sampling (EOS) at a nearby diagnostic station [6]. The main contribution to this timing jitter is expected to be the energy jitter in the first bunch compressor. Evaluation of this jitter delivered compatible results.

## CONCLUSION AND OUTLOOK

A transversely deflecting structure has been successfully applied to the beam in the VUV-FEL at DESY. Although some important contributions to the measurement error are not fully controlled yet, the achieved resolution surpasses most other methods already and it can be used in normal operation of the accelerator.

There are plans to exploit more capabilities of this measurement method as well as measurements of slice-emittances. A first attempt has already been made [7], but for best results tomographic measurements are foreseen.

In view of higher bunch repetition rates at later times and in future projects, shorter structures with a shorter fill-time are being envisioned.

## REFERENCES

- [1] O. H. Altenmueller, R. R. Larsen, and G. A. Loew, *Investigations of Traveling-Wave Separators for the Stanford Two-Mile Linear Accelerator*, The Review of Scientific Instruments, Vol. 35, Number 4, April 1964.
- [2] R. Akre, L. Bentson, P. Emma, P. Krejcik, A *Transverse RF Deflecting Structure for Bunch Length and Phase Space Diagnostics*, proceedings PAC 2001, p. 2353.
- [3] R. Akre et al, *Bunch Length Measurements Using a Transverse Deflecting Structure in the SLAC Linac*, EPAC'02, Paris, France, June 2002.
- [4] P. Krejcik et al, *Commissioning of the SPSS Linac Bunch Compressor*, proceedings PAC 2003, Portland, Oregon
- [5] A. Bolzmann, *Diploma Thesis*, Universität Würzburg
- [6] Bernd Steffen, Sara Casalbuoni, Ernst-Axel Knabbe, Bernhard Schmidt, Peter Schmüser, Axel Winter, *Spectral Decoding Electro Optic Bunch Length and Arrival Time Jitter Measurements at the DESY VUV-FEL*, this proceedings
- [7] Michael Roehrs, Markus Huening, Holger Schlarb, *Measurement of Slice-Emittance using a Transverse Deflecting Structure*, this proceedings

# FEMTOSECOND RESOLUTION BUNCH PROFILE MEASUREMENTS

S.P. Jamison / ASTeC, Daresbury  
 G. Berden / FELIX, Nieuwegein, The Netherlands  
 A.M. MacLeod / University of Abertay Dundee, Dundee, UK  
 B. Steffen / DESY, Hamburg, Germany  
 P. J. Phillips, W.A. Gillespie / University of Dundee, Dundee, UK

## Abstract

The measurement of ultrashort longitudinal bunch profiles is of growing importance to accelerator development and operation. With requirements of  $\sim 10$ fs time resolution, and a desire for non-destructive and real time diagnostics, the challenges for diagnostic development are significant. Alongside more established transverse deflecting cavity and CTR measurement techniques, new approaches arriving from the field of ultrafast lasers offer significant potential; Ultrafast electro-optic detection has now been demonstrated on several accelerators, and in many distinct forms, although challenges remain in getting to the desired time resolution. Proposed schemes combining ultrafast laser diagnostics with FEL interactions, such as the ‘‘optical replica’’ scheme also have considerable potential. Here, we discuss some of the recent developments in longitudinal diagnostics.

## INTRODUCTION

Many different approaches to ultrafast characterization of electron bunches have been explored experimentally, and with the growing importance of such diagnostics to light source machines, more schemes are proposed to be tested in the near future. Here we discuss some of the leading longitudinal diagnostics techniques, with an emphasis on recent demonstrations of their sub-picosecond capabilities; this discussion is not intended to be an exhaustive review of the all the latest developments, but rather an examination of some of the experimental issues and challenges facing sub-ps longitudinal profile diagnostics. Furthermore, the longitudinal profile diagnostics are seen as distinct from approaches that aim to provide an empirical ‘bunch-length’ monitor, which only aims to inform on the first moments of the bunch profile, or on the presence of structure on a particular time scale of interest.

We discuss techniques through a sub-classification of i) spectral techniques, where the bunch profile is inferred from the spectral intensity of a radiated field, ii) electro-optic (EO) techniques where a Coulomb or radiated field is determined through sampling (possibly single shot) with an ultrafast laser, iii) direct electron bunch techniques, where an active change to the electron bunch properties is made in such a manner that the original longitudinal profile can be inferred from the bunch. Here we restrict ourselves to a brief discussion of transverse deflecting cavities, and proposed demonstrations of the ‘optical replica’ scheme.

## SPECTRAL TECHNIQUES

Within spectral techniques we include the spectral measurements of coherent transition, diffraction and synchrotron radiation, and Smith-Purcell radiation (CTR, CDR, CSR and S-P, respectively). Such techniques have been applied to longitudinal bunch diagnostics in a considerable number of laboratories, and here we give selective examples to demonstrate the practical issues of their implementation and interpretation. These spectral techniques rely on causing the Coulomb field of the electron bunch to radiate in a controlled manner, and subsequently inferring the bunch profile from the emitted radiation spectrum. For femtosecond diagnostics it is important to address the temporal distinction in the Coulomb field and the electron bunch itself. At large distances from the bunch ( $r \gg \sigma_z/\gamma$ ) the field will have a spreading angle of  $\theta \sim 2/\gamma$ , which corresponds to a temporal spreading in the field of  $t \sim 2r/c\gamma$ . Furthermore, the field strength will fall as  $1/r$  at short distances from the electron bunch, and as  $1/r^2$  at large distances. It therefore follows that the position of the radiating structure must be sufficiently close to the electron bunch both to retain the fast time structure and to ensure that the radiated field is sufficiently large for detection. As an example, for a  $\gamma \sim 1000$  it follows that any measurements that wish to probe the bunch structure with a 10 fs resolution must be able to access the field distribution within a  $< 2$  mm radius of the bunch (this requirement is also present in electro-optic techniques). For low energy machines this may be a deciding factor in the applicability of CDR or Smith-Purcell radiation techniques. A demonstration of the relative signal strength of CTR and CDR has been given by Delsim-Hashemi et al. [1, 2]. For a CTR or CDR screen inserted into the compressed bunch of FLASH, with  $\gamma \sim 900$ , the CDR energy is approximately two orders of magnitude reduced in power density with respect to the CTR radiation. The CDR screen is intercepting the Coulomb field at a radius of 5 mm from the bunch. They also observe a cut-off in the short wavelength emission for the diffraction radiation at  $\lambda \approx 200 \mu\text{m}$ , while the transition radiation has a cutoff at the much shorter wavelength of  $\lambda \approx 50 \mu\text{m}$ . In separate experiments, with a diffraction grating spectrometer they were able to observe CTR at wavelengths at short as  $5 \mu\text{m}$ , thus identifying the presence of extremely short time structure in the bunch [3]. At SLAC, CTR has also been used to characterize the extremely short bunches available at the FFTB

facility [4]. Using a Michelson-Morely interferometer the autocorrelation of the CTR radiation was measured, from which the power spectrum of the CTR radiation is determined. In that work, Muggli et al. comment that limitations in the accuracy of the diagnostic arise from the difficulties of transporting and detecting the full spectral range of the far-infrared radiation; these effects limited the ability to infer an actual bunch profile, although bunch lengths of 210fs FWHM were however able to be determined. At the Advanced Photon Source (APS), CTR and CSR diagnostics have been demonstrated for profile reconstruction of sub-picosecond 150 MeV bunches [5, 6]. The spectrum of the CTR/CSR was obtained from a Michelson-Morely interferometer. To determine the profile of the bunch, the phase of the radiation was retrieved from the intensity spectrum from applying a “minimal phase approximation”, a numerical process that is based on Kramers-Kronig relations. For the CTR measurements [5] the retrieved bunch profiles displayed FWHM durations as short as 290fs for leading spikes of the profile.

For Smith-Purcell radiation, the radiator is a periodic structure running parallel to the beamline. In such a structure the radiated power at a specific wavelength can be enhanced in proportion to the number of periods to the structure. It also has the property of acting as a wavelength dispersing element. Korby et al. [7] have determined bunch lengths using S-P radiation of a 15 MeV beam. Their S-P gratings had periods of either 6 mm or 10 mm, and a grating length of 100 mm. Through a moveable mirror directing the S-P radiation out of the beamline, they were able to determine the angular, and hence spectral, intensity of the radiation. Separately, Blakemore and Doucas [8, 9] have undertaken S-P experiments at the FELIX FEL facility in the Netherlands. In their experiments an array of 11 detectors arranged opposite the radiator were able to simultaneously collect the S-P radiation over a large angular range. They collect radiation in the range of  $\lambda = 500 \mu\text{m}-3 \text{ mm}$ , and determine a sub-ps bunch length. In both the above examples of S-P radiation, the bunch shape was not explicitly determined from the data; instead the experimental spectra were compared to calculated spectra based on trial bunch profiles.

In determining the bunch profile from the spectral content a number of issues must be accounted for. These issues can be summarized as i) the Coulomb field temporal profile at the radiator; ii) the propagation of the radiation to the detectors (Absorption, dispersion and diffraction); iii) the detector response, which may include the dispersive characteristics of the spectrometer. Finally, the net result is a power density measurement, and it therefore does not explicitly include information about the phase of the radiation (measurements of CTR or CSR by electro-optic techniques, which do measure the radiation phase, will be discussed separately below).

The propagation issue is one of the significant experimental challenges for spectral techniques. The long wavelength radiation is significantly affected by diffraction, and

there is always some long wavelength cutoff present. The design of transfer lines will usually be specific to the particular experimental conditions (e.g. transport distance from the beamline, available window aperture at the beamline, and the beam properties themselves). These issues, and the analysis of far-infrared (FIR) beamline propagation have been described in detail by Casalbuoni et al [10]; while focused particularly on the the CTR radiation transfer line at the 140m point of FLASH at DESY, the methods and many general results are equally applicable to other experimental situations.

Of a different character is the problem of missing phase information for the field. Lia and Sievers [11] have shown that the phase of the field can be determined from the field amplitude (i.e. the power spectrum) using Kramers-Kronig relation (KK). The KK relations relate the imaginary components of an analytic function through an integral function of the real components, with an integration range extending over the full spectral range of the signal. In the context of bunch diagnostics, a fundamental issue arises as to the validity of the KK phase retrieval in the absence of some spectral amplitude information. Grimm et al. [12] have discussed this issue with examples of sub-ps bunch profiles retrieved with different levels of missing data. Specifically, they show the importance of the long wavelength data in obtaining a faithful retrieval of the bunch shape. Earlier, Lai et al. also addressed this question of retrieval validity, and noted (as do Grimm et al.) that for some bunch profiles the underlying assumption of minimal phase employed in the retrieval may not always be appropriate; an example of a truncated Lorentzian with failed retrieval is given. The conclusion of Lai, Grimm, and others, however is that for “reasonable” bunch profiles, and with sufficient extent to the data, a meaningful bunch profile can indeed be obtained.

## ELECTRO-OPTIC TECHNIQUES

Electro-optic techniques enable the ultrafast characterization of far-infrared (FIR) pulses directly in the time domain, and as such avoid the possible ambiguities associated with spectral techniques. In electron-bunch diagnostics, through carrying out the EO detection within the electron beamline, it is possible to measure the Coulomb field directly, avoiding the step of first causing the field to radiate; alternatively, the emitted CTR/CDR or CSR radiation can be measured with the EO detection outside the beamline. Unless otherwise stated, we will be referring to intra beamline measurements of the Coulomb field.

It is usual to describe the EO modulation as resulting from an electric field induced refractive index change within an EO material (such as appropriately orientated ZnTe or GaP crystals). This refractive index change can then be probed by optical means; the polarization components of a linearly polarised laser will experience a differing delay in propagating through the crystal, with the emerging pulse therefore becoming elliptically polarized.

This ellipticity can subsequently be converted into an intensity modulation by a suitable arrangement of polarisers. The net result is an intensity change in the optical probe as a function of the FIR field which is dependent on the particular arrangement of polarizers. In the two most commonly used arrangements, which we call “balanced detection” and “crossed polariser detection”, the intensity change is proportional to field or field squared, respectively.

An alternative perspective for describing the EO process has been derived by Jamison et al [13]; the ellipticity induced in the optical pulse is the result of sum and difference frequency mixing of the FIR and optical field. This is a rigorous description, and has the advantage of being a more appropriate formalism for describing the interaction with long duration (few ps) chirped optical pulses such as used in single shot EO techniques. In essence, they have shown that the optical field spectrum exiting the EO crystal, for a given polarisation component, is given by

$$\tilde{E}_{\text{out}}^{\text{opt}}(\omega) = \tilde{E}_{\text{in}}^{\text{opt}}(\omega) + i\omega a \tilde{E}_{\text{in}}^{\text{opt}}(\omega) * \left[ \tilde{E}^{\text{Coul}}(\omega) \tilde{R}(\omega) \right] \quad (1)$$

where the coefficient  $a$  is dependent on the polarization geometry.  $\tilde{R}(\omega)$  describes the material response due to the nonlinear coefficient and phase-matching. From Eqn. 1 it can be said that the far infrared spectrum of the Coulomb field is now ‘upconverted’ into the optical region. A FIR bandwidth of  $\sim 100\%$  (if that can be assigned any rigorous meaning) is exchanged for an experimentally easier optical bandwidth of  $\sim 5\%$ . Importantly, if the EO frequency conversion is done directly on the Coulomb field within the beamline, the shift to optical frequencies allows the information from the DC component to propagate and be detected. Simple Fourier transformation of Equation 1 gives the equivalent expression for the optical field in the time domain,

$$E_{\text{out}}^{\text{opt}}(t) = E_{\text{in}}^{\text{opt}}(t) + a \left[ E^{\text{Coul}}(t) * R(t) \right] \frac{d}{dt} E_{\text{in}}^{\text{opt}}(t) \quad (2)$$

We therefore see that the EO interaction has created a new optical pulse with pulse envelope described by the Coulomb field; in borrowing terminology from a quite distinct technique, we have created an “optical-replica” of the Coulomb field.

An important factor in the ultimate time resolution of EO techniques is the bandwidth of the response function, and the degree to which it is known. Fortunately, materials are available for which the response is approximately constant over the spectral region of interest. For the most commonly used crystal, ZnTe,  $\tilde{R}(\omega)$  has an approximately flat spectrum from 0-2.5 THz. Sufficiently thin GaP crystals may have a cutoff as high as 8 THz ( $\lambda \sim 37 \mu\text{m}$ ). Other EO materials with even broader response functions are known, although to date they have not been used in electron-bunch diagnostic experiments. In using materials with such a flat spectral response, time resolutions of  $< 150$  fs can potentially be obtained without the need for explicit calibration of the response; this assertion has recently been examined

through EO benchmarking experiments (as discussed below).

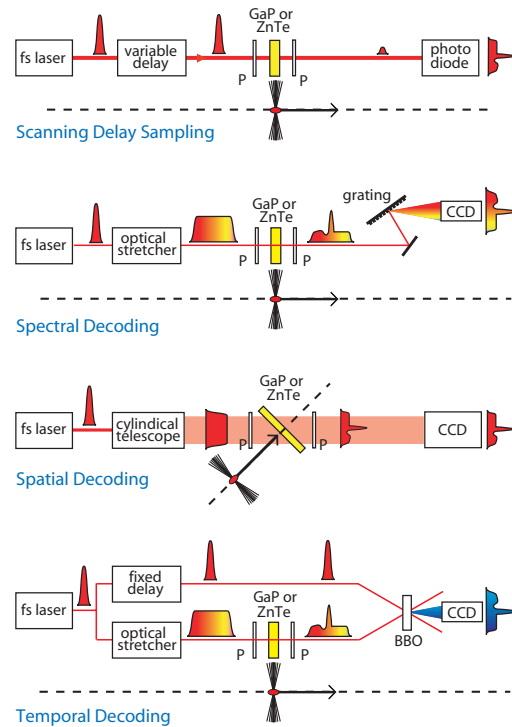


Figure 1: Schematic representations of the four EO detection techniques that have been demonstrated for detection of the bunch Coulomb field.

The above discussion describes the encoding of the Coulomb (or CTR/CSR) field into an optical pulse. The ellipticity introduced into the probe laser is converted into an intensity change with a suitable arrangement of polarisation optics. There are several demonstrated methods for observing this intensity change, each with particular merits. These methods, shown schematically in Fig. 1 are discussed in turn:

**Scanning delay sampling:** This is the simplest and first demonstrated example EO bunch diagnostics [14]. A short (sub-50fs) laser is used to sample fixed parts of the FIR pulse, and an integrated intensity change in the optical probe is measured. Scanning the relative delay between laser and electron bunch allows the build up of the profile. Multi shot measurements such as this do suffer from time jitter between the laser and electron bunch; however, in even the first demonstration, scanning rates of 2ps per  $\mu\text{s}$  were achieved, and over such short measurement periods very small timing jitter ( $< 50$  fs) can be achieved. The time resolution is in the first instance determined by the sampling pulse duration, although for very short laser pulses ( $< 30$  fs), group velocity dispersion of the optical pulse may become the dominating factor [15].

**Spectral decoding (SD):** The measurement of the optical spectrum can be used to directly infer the field temporal profile if a chirp is first applied to the optical pulse, so

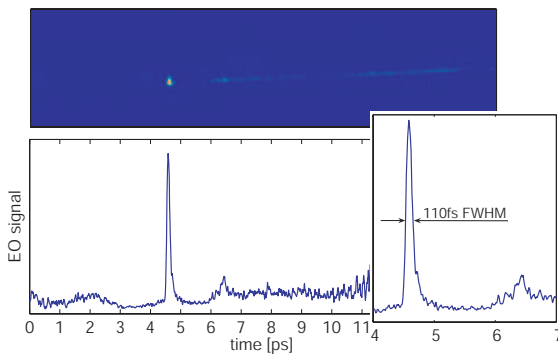


Figure 2: Single shot temporal decoding measurements at FLASH. These measurements are described further in Berden et al. [26].

that there is a known time-frequency relationship in the sampling laser pulse. A lower limit on the bunch duration for which this technique is suitable arises from the intrinsic connection between the temporal modulation of the chirped pulse, and the distortion of the initially known chirp (this limitation can also be shown to be a consequence of the convolution in Eqn. 1). For bunches shorter than this limitation, the measured bunch profile may contain significant artifacts, producing a misleading bunch profile. The limitation can be given approximately as  $\tau_{\text{lim}} = 2.6\sqrt{T_c T_0}$ , where  $T_c$  and  $T_0$  are the FWHM of the chirped and transform limited optical pulse durations, respectively [16]. SD characterization of the in-beam-line Coulomb field has been demonstrated at several facilities, including FELIX [17], NSLS [19], and FLASH[20]. The technique has also been demonstrated for single shot characterisation of CSR [21, 22], and CTR [23].

**Spatial encoding:** This approach has many similarities to the scanning delay line approach, but instead allows for a single-shot measurement. By sampling the Coulomb field with an optical pulse obliquely incident to the EO crystal and the Coulomb field propagation direction, there is a spatial to temporal mapping introduced for the relative delay of the laser arrival time at the crystal. Imaging the EO crystal, and the intensity changes as a function of spatial position, therefore allows the determination of the field induced intensity changes as a function of relative arrival time at the crystal. An important requirement for spatial encoding is spatially uniform EO materials. The tolerances of this requirement can be difficult to satisfy, with even stress induced birefringence potentially adding significant experiential difficulty. This approach has been demonstrated at SLAC FFTB [24] and at DESY on FLASH [25]. At the FFTB EO signals of 270 fs FWHM were measured, while at FLASH  $\sim 300$  fs FWHM signals have been obtained.

**Temporal decoding (TD):** Referring to the time domain description of Eqn. 2, it is apparent that for a long duration optical probe, an intensity modulation will be imposed only on portions of the the pulse envelope. TD temporally

resolves this intensity modulation through a process of optical second-harmonic generation, using a non-collinear geometry. Just as in spatial encoding, a time-space mapping is therefore achieved, although in TD this is purely with the optical fields, and is done outside the beamline. TD has been demonstrated at FELIX [18], and more recently at FLASH [26]. In these later experiments an electro-optic signals with FWHM duration of 110 fs were observed. An example of these ultrashort TD measurements is shown in Fig. 2

### Benchmarking of Electro-Optic Signals

An important recent advance in electro-optic diagnostics has been the benchmarking of the measured signal with other diagnostics. In recent experiments at FLASH, a variety of longitudinal diagnostics were used to make concurrent measurements. The EO signal has been measured by Temporal Decoding, Spectral Decoding, and Spatial Encoding, together with simultaneously transverse deflecting cavity measurements of the electron bunch immediately following in the bunch train. CTR measurements were also made during the experiments, although not generally simultaneously. The Temporal decoding and transverse cavity measurements have in particular provided explicit confirmation of the exceptional time resolution achieved in the latest TD experiments, and in the faithful reproduction of the bunch profile.

## DIRECT ELECTRON BUNCH TECHNIQUES

Direct electron bunch techniques rely on a change to the electron bunch phase space so that the longitudinal projection is converted to a more easily observed projection, such as transverse profile or energy.

### Transverse Deflection Cavities: Lola

In RF transverse deflecting cavities, a transverse kick is applied to the bunch which is dependent on the relative phase of the RF with respect to the electron arrival time. Extremely fast temporal resolution can be obtained with a sufficiently rapidly varying deflecting force. Cavities capable of producing such a rapidly varying deflecting force were developed at SLAC in the 1960's, and were prosed for particle separates, as well as for fast bunch diagnostics.

More recently these original SLAC cavities have been installed and operated at the SPPS facility, and at FLASH. The transverse deflection cavity at FLASH, known as "Lola" after its original developers, is currently producing the highest time resolution of all the longitudinal diagnostics. Lola operates in a hybrid mode for which the net deflection produced by the combination of electric and magnetic fields is independent of the transverse position of the beam within the cavity (although the individual contributions from magnetic or electric fields does vary across the cavity aperture). The RF-bunch phase is operated at the

zero-deflection point, so that the longitudinal phase space of the bunch is streaked transversely, but does not have a mean deflection. At FLASH the Lola cavity is preceded by a kicker that adds an additional mean deflection, so that a single bunch can be deflected onto an off-axis OTR screen. An example of the Lola image, and the projected longitudinal profile is shown in Fig. 3. The temporal resolution of TDC is ultimately restricted by the unstreaked transverse beam size on the OTR screen; for Lola this is  $\approx 200 \mu\text{m}$  in normal SASE operation conditions, and the maximum streak is  $72 \text{ fs/mm}$ , from which an ultimate resolution of  $15 \text{ fs}$  has been inferred [27].

Transverse deflecting cavities such as Lola are intrinsically destructive measurements. They also have large infrastructure requirements, and may require significant beamline space; the Lola cavity is  $3.6 \text{ m}$  in length, compared to the requirement of  $\sim 10 \text{ cm}$  for CTR or electro-optic diagnostics. However, the added capability for measuring slice parameters, such as emittance, energy, or z-y correlations, makes them a more versatile diagnostic than longitudinal profiling by itself.

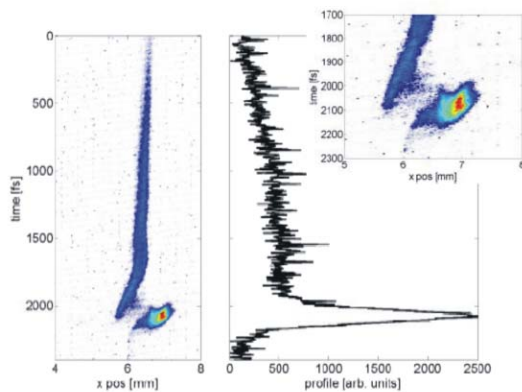


Figure 3: An example of a Lola transverse deflecting cavity measurement (from Hüning et al. [27]).

### Optical Replicas

A new technique known as ‘optical replicas’ has been proposed as a means to obtain femtosecond resolution longitudinal profile diagnostics [28]. The basic concept of the scheme is to impose an optical wavelength density modulation on the electron bunch under investigation, and then cause the bunch to radiate optically by passing this modulated bunch through a resonant undulator.

The full scheme consists of i) an initial undulator resonant at  $\lambda = 800 \text{ nm}$ , which is synchronously seeded with an  $800 \text{ nm}$  Ti:S laser pulse. The interaction of the bunch with the seeded undulator will result in an energy modulation on the bunch with a period of  $800 \text{ nm}$ , or  $2.7 \text{ fs}$ . The bunch is taken through a drift space to allow the energy modulation to develop into a longitudinal density modulation, again with a period of  $800 \text{ nm}$ . This modulated bunch then

enters a second undulator also resonant at  $\lambda = 800 \text{ nm}$ . The pre-modulated bunch will therefore coherently radiate at  $800 \text{ nm}$ , with a radiated intensity dependent on the local charge density of the bunch. Simulations indicate that there will be sufficient intensity in the radiated optical pulse for it to be separately diagnosed with standard ultrafast laser diagnostics. An ultimate time resolution to this technique will be associated with the slippage length of the bunch with respect to the radiation field in the second undulator.

Experimental implementation of a demonstration of the optical replicas concept is currently underway [29]. The system will be installed on FLASH. With a proposed 5 period undulator the achievable time resolution will potentially be 5 cycles of the  $800 \text{ nm}$  resonant wavelength, or  $13 \text{ fs}$ .

### REFERENCES

- [1] H. Delsim-Hashemi, et al., EPAC 2006, MOPCH016.
- [2] H. Delsim-Hashemi, B. Schmidt. Private communication.
- [3] H. Delsim-Hashemi, et al., FEL 2005, p. 514.
- [4] P. Muggli et al., PAC 2005, p. 4102
- [5] A. H. Lumpkin, et al., PAC 2003, p. 2420
- [6] A.H. Lumpkin, et al., FEL 2005, p. 608
- [7] S. E. Korbly, et al., Phys. Rev. ST Accel. Beams **9** 022802 (2006)
- [8] V. Blackmore, et al., EPAC 2006, TUPCH042.
- [9] G. Doucas, et al., EPAC 2006, TUPCH043
- [10] S. Casalbuoni, et al., TESLA-FEL report 2006-04.
- [11] R. Lai, A.J. Sievers, Nucl. Instr. and Meth. A **397** 221 (1997).
- [12] O. Grimm, P. Schmüser. Tesla-FEL report 2006-3
- [13] S. P. Jamison, et al., Opt. Lett. **31** 1753 (2006)
- [14] X. Yan, et al., Phys. Rev. Lett. **85** 3404 (2000)
- [15] S. Casalbuoni, et al., PAC 2005, p. 3070.
- [16] S.P. Jamison et al., to be published.
- [17] I. Wilke, et al., Phys. Rev. Lett. **88**, 124801 (2002).
- [18] G. Berden, et al., Phys. Rev. Lett. **93**, 114802 (2004).
- [19] H. Loos et al., PAC 2003, p. 2455.
- [20] B. Steffen, et al., FEL 2005, p. 549.
- [21] S.P. Jamison, et al., Nucl. Instr. and Meth. A **557**, 305 (2006).
- [22] G. Berden, et al., DIPAC 2005, p. 69.
- [23] G. Berden, et al., EPAC 2006, TUPCH027.
- [24] A. L. Cavalieri, et al., Phys. Rev. Lett. **94**, 114801 (2005).
- [25] H. Schlarb et al. EPAC 2006, TUPCH024
- [26] G. Berden, et al., EPAC 2006, TUPCH026.
- [27] M. Hüning, et al., FEL 2005, p. 538.
- [28] E.L. Saldin, E.A. Schneidmiller, M.V. Yurkov, Nucl. Instr. and Meth. A **539** (2005) 499
- [29] V. Ziemann, et al., EPAC 2006, TUPCH081.

## **Chapter 6**

### **Writeup of instrumentation and diagnostics lectures: CAS2009**

#### **6.1 Introduction to Beam Instrumentation and Diagnostics**

# INTRODUCTION TO BEAM INSTRUMENTATION AND DIAGNOSTICS

*R. Jones & H. Schmickler*  
CERN, Geneva, Switzerland

## **Abstract**

These lectures aim at describing instruments and methods used for measuring beam parameters in circular accelerators. Emphasis will be given to new detection and analysis techniques in each field of accelerator instrumentation. The clear distinction is made between “instrumentation”, i.e. the design and construction of the instruments themselves and “diagnostics”, the use of the data from these instruments for running and improving the performance of the accelerator.

## **INTRODUCTION**

Beam instrumentation and diagnostics combines the disciplines of accelerator physics with mechanical, electronic and software engineering, making it an extremely interesting field in which to work. The aim of the beam instrumentation physicist or engineer is to design, build, maintain and improve the diagnostic equipment for the observation of particle beams with the precision required to tune, operate and improve the accelerators and their associated transfer lines.

This introduction is intended to give an overview of the instrumentation in use in modern synchrotrons. The choice available today is so vast that inevitably it will not be possible to cover them all. Many of the standard instruments have been covered in previous CAS schools (see for example Ref. [1] which also contains a comprehensive list of references) and will therefore be touched upon only briefly, with more emphasis being given to new and innovative measurement techniques and their use in beam diagnostics. The following subjects will be discussed:

1. Beam position measurement
2. Beam current measurement
3. Diagnostics of transverse beam motion (tune, chromaticity and coupling)
4. Emittance measurement
5. Beam loss monitoring
6. Luminosity measurement
7. Some examples of beam diagnostics

## **1. BEAM POSITION MEASUREMENT**

The Beam Position Monitor (BPM) can be found in every accelerator. Its role is to provide information on the position of the beam in the vacuum chamber at the monitor location. For linacs and transfer lines the BPMs are used to measure and correct beam trajectories, while for synchrotrons such monitors are distributed around the ring and used to calculate the closed orbit. In circular machines, their location is usually chosen close to the main quadrupole magnets where the  $\beta$ -functions are largest and so any orbit distortion a maximum. For  $90^\circ$  lattices a typical layout involves placing horizontal monitors near the focusing quadrupoles (where the horizontal  $\beta$ -function is large) and the vertical monitors near the defocusing quadrupoles (where the vertical  $\beta$ -function is large). Apart from closed orbit measurements, the BPMs are also used for trajectory measurements (the first turn trajectory is particularly important for closing the orbit on itself) and for accelerator physics experiments, where turn-by-turn data, and even bunch-to-bunch data is often required.

In the early days a BPM monitoring system simply consisted of an oscilloscope linked directly to the pick-up signals. Since then, enormous advances in the acquisition and processing electronics have been made, turning beam position monitors into very complex systems. Modern BPMs are capable of digitising individual bunches separated by a few nanoseconds, with a spatial resolution in the micron range, while the resulting orbit or trajectory collected from several hundred pick-ups can be displayed in a fraction of a second.

### 1.1 Pick-ups

The measurement of beam position relies on processing the information from pick-up electrodes located in the beam pipe. Five pick-up families are commonly employed:

- Electrostatic – including so-called ‘button’ and ‘shoe-box’ pick-ups
- Electromagnetic – stripline couplers
- Resonant cavity – especially suited for high frequency linacs
- Resistive
- Magnetic

An excellent in depth analysis of most of these pick-ups is presented in Ref. [2]. Here we will briefly describe the two most commonly used, namely the electrostatic and electromagnetic pick-up.

#### 1.1.2 Electrostatic (Capacitive)

The electrostatic or capacitive pick-up is the most widely used in circular accelerators. It consists of metallic electrodes situated on opposite sides of the vacuum chamber at the location where the beam is to be measured. As the beam passes through, electric charges are induced on the electrodes, with more induced on the side which is closer to the beam than the one furthest from the beam. By measuring the difference in the charge induced, the position can be calculated. Let us analyse the properties of button pick-ups (see Fig. 1) since they are the most popular due to their cheapness and ease of construction.

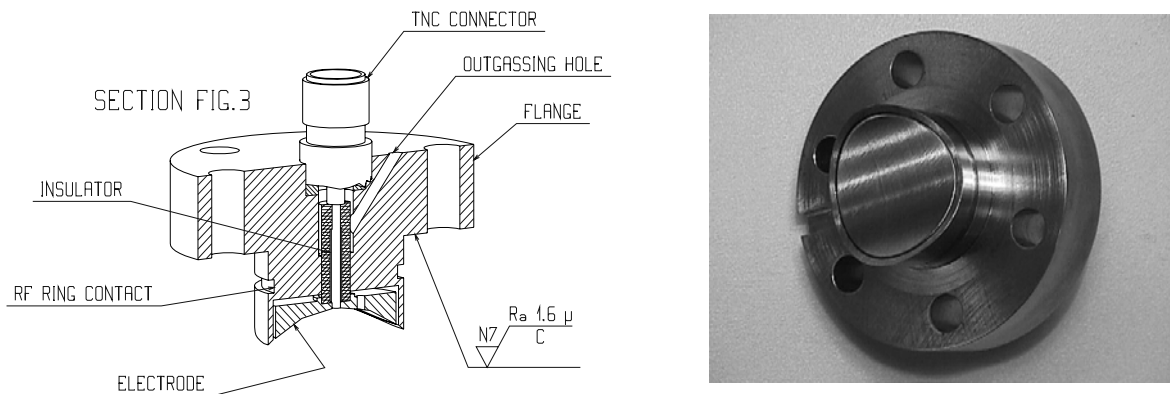


Fig. 1 Cross-section and photo of an LHC button electrode.

The image current associated with the beam will induce charges on the button which are proportional to the beam intensity and inversely proportional to the position of the beam from the electrode. A schematic representation is given in Fig. 2.

The figure of merit for any electrode is its transfer impedance (the ratio of the pick-up output voltage,  $V$ , to the beam current,  $I_B$ ). For a capacitive pick-up the signal is proportional to the rate of change of beam current at low frequencies, while for high frequencies the capacitance ‘integrates’ the signal and the transfer impedance tends to its maximum. For the case of a button electrode of area  $A$  and capacitance  $C$  situated at a distance  $d$  from the beam the maximum transfer impedance (i.e. the

value it tends to at high frequency) can be approximated by:

$$Z_{T\infty} = \frac{A}{2\pi d(\beta c) C}$$

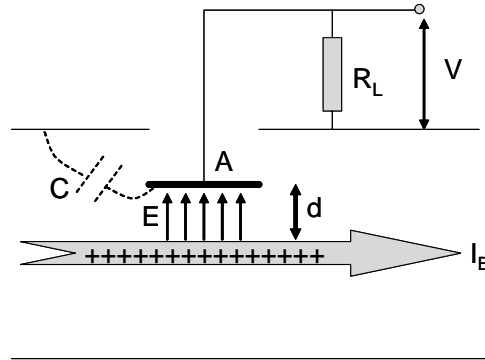


Fig. 2 Schematic of a capacitively coupled electrode.

Button electrode capacitances are typically in the 10pF range. Impedance transformation can be used to improve the low frequency response at the expense of that at high frequency. Figure 3(a) shows the frequency response of an 8pF button electrode for the matched 50Ω impedance case (1:1) and after two different impedance transformations. The time response of the button for different bunch lengths can be seen in Fig. 3(b).

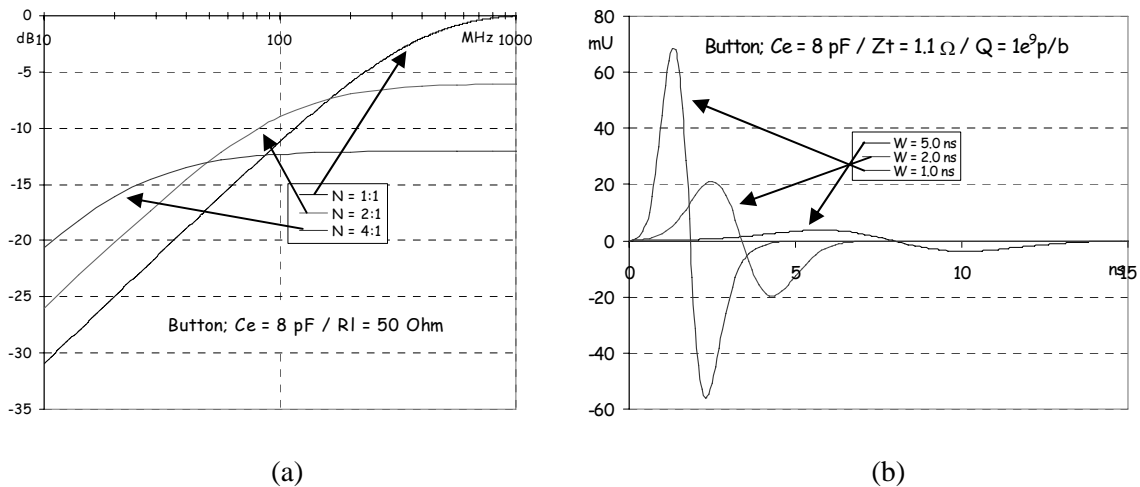


Fig. 3 Frequency (a) and time (b) response of a button electrode.

When designing such pick-ups care must be taken to limit the impedance variations when the transmission line used for signal extraction passes from the vacuum to a feedthrough or cable dielectric (such as ceramic, glass or air). Any such mismatch will produce unwanted reflections, often at high frequency, which could perturb the processing electronics. For this reason most processing chains introduce a low-pass filter on the button output. Special care must also be taken to pair the electrodes on opposite sides of the chamber to minimise offsets in the position reading. This pairing can be made less sensitive to capacitance variations if the high frequency cut-off for the processing electronics sits on the linear part of the button response, with the disadvantage that the overall signal amplitude is reduced.

### 1.1.3 Electromagnetic (stripline)

The electromagnetic pick-up is a transmission line (stripline) which couples to the transverse electromagnetic (TEM) field of the beam. The transmission line is formed between the stripline and the wall of the vacuum chamber and is excited by the beam only at the gaps on either end of the stripline where a longitudinal field occurs. Fig. 4 shows the layout of such an electromagnetic stripline electrode.

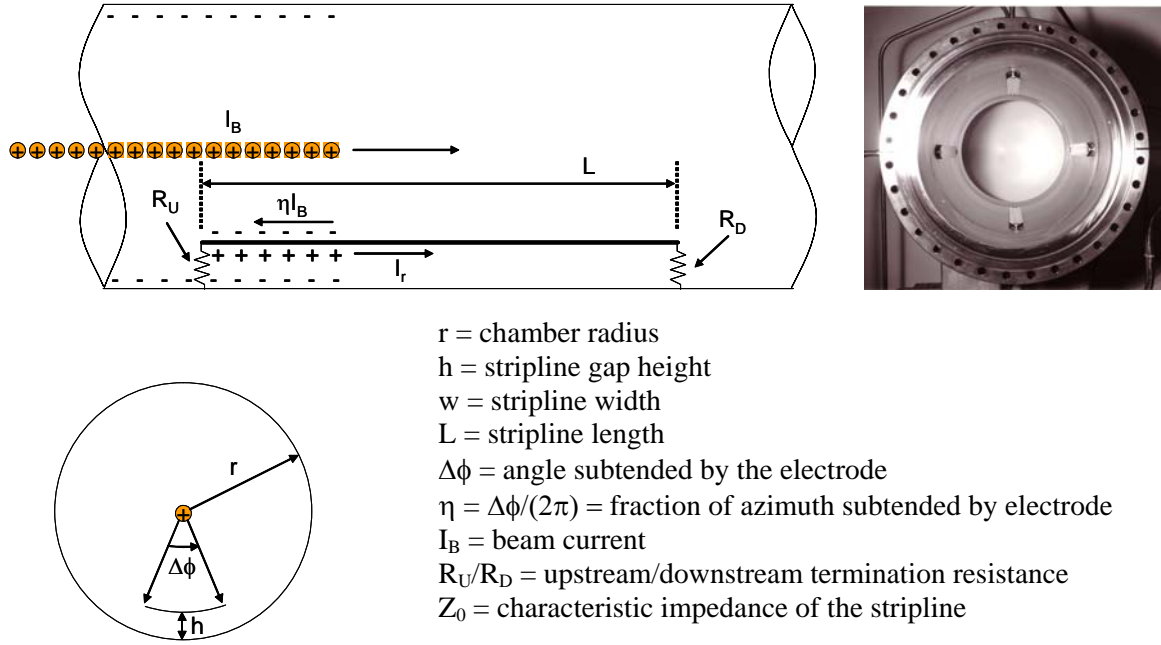


Fig. 4 Schematic and photo of an electromagnetic stripline pick-up.

Consider a bunch travelling from left to right (upstream to downstream). While it is over the upstream port there is a voltage  $V_r$  across  $R_U$ , causing a voltage wave of that amplitude to be launched to the right. The stripline forms a transmission line with the wall of the vacuum chamber of characteristic impedance  $Z_0$ . The voltage wave is therefore accompanied by a right travelling current wave of amplitude  $I_r = V_r / Z_0$ . This current flows along the bottom surface of the electrode whilst an equal and opposite current flows along the chamber wall. In addition an image current of amplitude  $\eta I_B$  travels along the top surface of the electrode. The voltage  $V_r$  across  $R_U$  can therefore be expressed as

$$V_r = (-I_r + \eta I_B) R_U = \eta I_B \frac{R_U Z_0}{R_U + Z_0} \Rightarrow V_r = \frac{1}{2} \eta I_B Z_0 \text{ for a matched stripline } (R_U = Z_0)$$

When the beam is over the downstream port it produces a voltage  $-V_r = -\frac{1}{2} \eta I_B Z_0$  across  $R_D$  in the same way as it produced a voltage  $+V_r$  across  $R_U$ . This launches a left-travelling wave of the same magnitude, but different sign to the right-travelling wave, which propagates along the transmission line formed by the stripline and the chamber wall and will produce an inverted signal upon arrival at the upstream port a time  $L/c$  later. The final signal observed at the upstream port will therefore be a bipolar pulse with the maxima separated by  $2L/c$  (see Fig. 5(a)).

When the RF wavelength of the beam is equal to multiples of  $2L$ , the reflection and the signal from next bunch will cancel and there will be no net signal from the stripline. A maximum in the frequency response will be observed when  $L$  is a quarter of an RF period, and hence the stripline pick-

up length is usually chosen accordingly. The full frequency response of a 60cm long stripline is shown in Fig. 5(b) and has a lobe structure, with the minima located at multiples of  $c/(2L)$ .

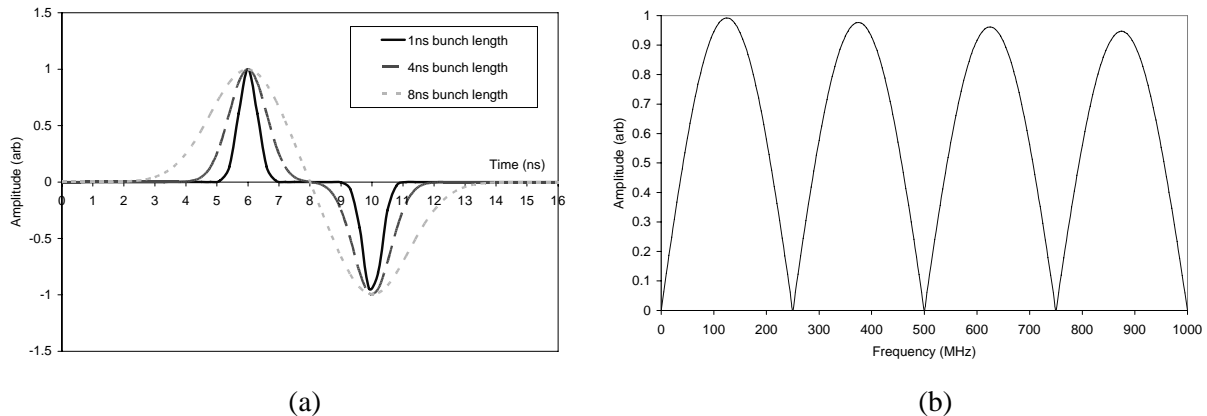


Fig. 5 Time (a) and frequency (b) response of a 60cm long electromagnetic stripline pick-up.

For a relativistic beam the voltage due to the beam passing the downstream port is produced at the same time as the right-travelling wave propagating between the stripline and the wall arrives at the downstream port. The two equal and opposite voltages therefore cancel producing no net signal at the downstream port. The electromagnetic stripline pick-up is therefore said to be “directional”, i.e. a signal is only observed on the upstream port with respect to the beam direction. These pick-ups are therefore used in all locations where there are two counter rotating beams in the same vacuum chamber. Due to the imperfections in the stripline and feedthrough impedance matching, the best directivity one can hope to obtain for a real stripline is generally around 25-30dB (i.e. the voltage signal of one beam with respect to the other is attenuated by a factor between 18-32).

### 1.2 Beam Position Acquisition Systems

Once the signals from the opposite electrodes of a pick-up have been obtained, the next step is to convert these signals into a meaningful beam position. The first thing to do is to normalise the position, i.e. to make it independent of the signal amplitude (or beam intensity). This is generally done using one of three algorithms, whose response curves can be seen in Fig. 6.

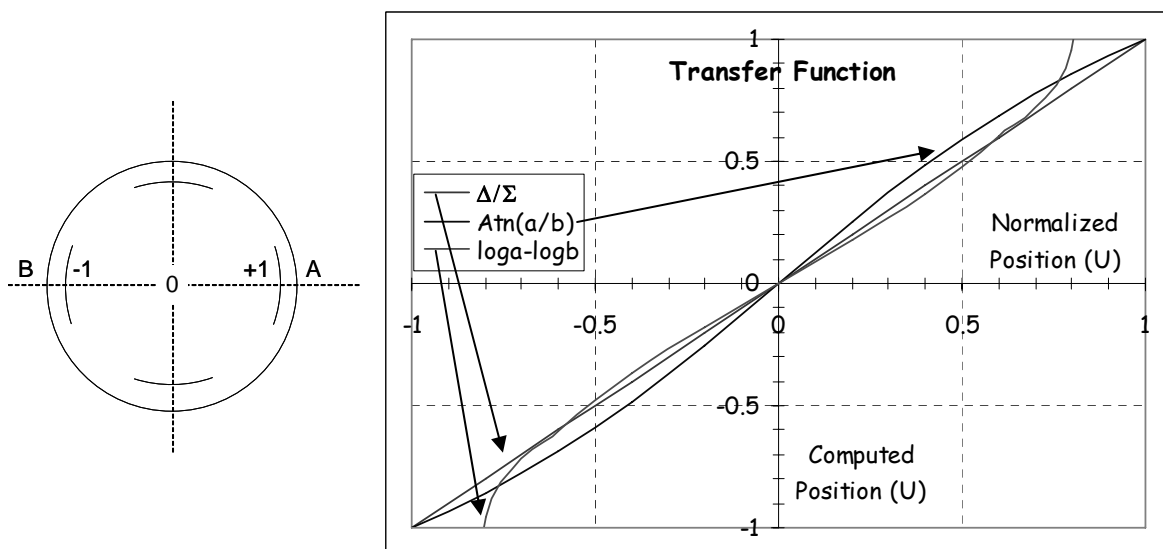


Fig. 6 Transfer functions for three commonly used position normalisation algorithms.

- **Difference over sum ( $\Delta/\Sigma$ )** - The sum and difference can be obtained either using a  $0^\circ/180^\circ$  passive hybrid, a differential amplifier or calculated by software (after digitising), to give:

$$\text{Normalised Position} = \frac{A - B}{A + B}$$

The transfer function of this algorithm can be seen to be highly linear.

- **Logarithmic ratio** - The two input signals are converted into their logarithmic counterparts and subtracted. In practice this is done using logarithmic amplifiers followed by a differential amplifier. This gives:

$$\text{Normalised Position} = \text{Log}(A) - \text{Log}(B) \left( = \text{Log} \left[ \frac{A}{B} \right] \right)$$

whose response curve is seen to be an reversed S-shape, which becomes highly non-linear when exceeding 70% of the normalised aperture.

- **Amplitude to Phase** - The two input signals are converted by a  $90^\circ$  passive hybrid into signals of equal amplitude but varying phase, with the position dependence of this phase given by:

$$\text{Normalised Position} = \phi = 2 \times \text{ArcTan}(A/B)$$

Here the transfer function again deviates from the linear in an S form, but does not diverge for large excursions. In addition, the gradient is larger around zero, making it more sensitive towards the middle of the pick-up. A variation on the amplitude to phase algorithm is amplitude to time conversion, which will be discussed in more detail below.

The type of algorithm to be used will depend on the choice of processing electronics. In all cases the non-linearity is taken into account by calibration circuits and correction algorithms. A summary of commonly used beam position acquisition systems is given in Fig. 7.

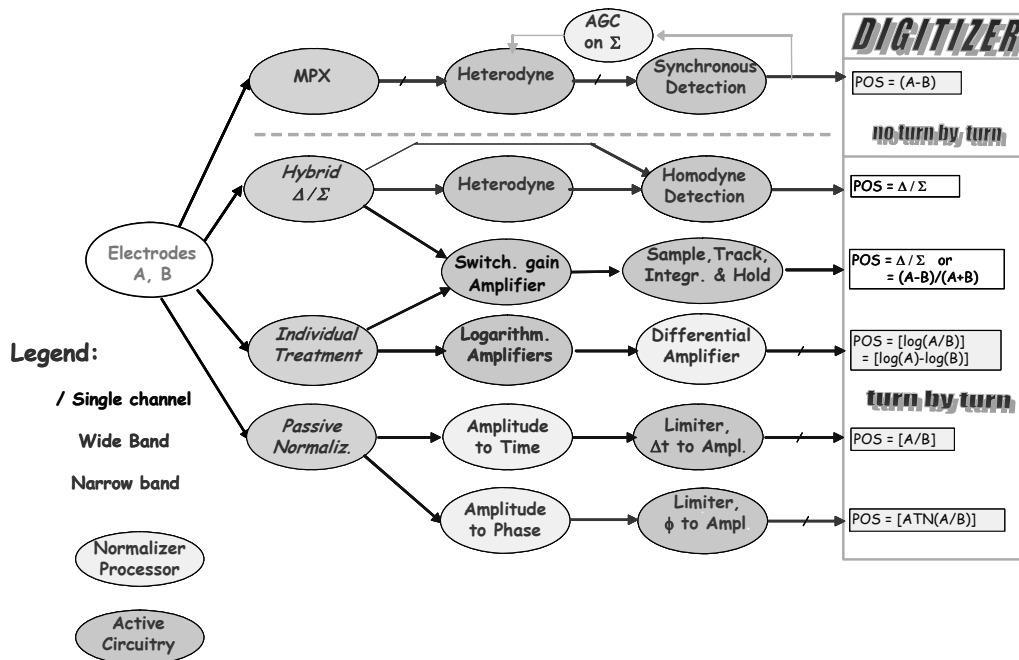


Fig. 7 Schematic representation of the various beam position processing families. ( courtesy of G. Vismara, CERN )

Here we will only briefly mention the various families in passing, but detailed descriptions along with the advantages and disadvantages of each system can be found in ref [3].

**MPX (multiplexed)** – each of the BPM electrodes is multiplexed in turn onto the same, single acquisition electronics chain. This eliminates channel to channel variations, but since the switching is generally quite slow such an acquisition tends to be used in circulating machines where only the average orbit is of importance.

**Hybrid (Sigma & Delta)** – here a  $0^\circ/180^\circ$  passive hybrid is usually used to give the sum ( $\Sigma$ ) and difference ( $\Delta$ ) signal from the two electrodes. The position (or ratio of the sum and difference signals) can then be obtained in many ways including: direct digitisation, homodyne detection (mixing the sum and delta signals with the sum signal itself) or heterodyne detection (mixing sum and delta signals with an external reference).

**Individual Treatment** – in this case each electrode is treated separately, but in parallel. The acquisition can either consist of directly digitising each signal or using logarithmic amplifiers as outlined above. The disadvantage of this method is that it requires two (or four depending on the pick-up orientation) very well matched chains of electronics, since the combination of the signals to obtain a position is performed at the very end of the chain.

**Passive Normalisation** – here the amplitude difference (i.e. position information) in the input signals is directly converted into a phase or time. Intensity information is lost in this procedure, but the result is a varying phase or time which is directly proportional to the position.

### 1.2.1 Wide-Band Time Normalisation

The LHC beam position system will be based on a new concept of amplitude to time normalisation, so-called “wide-band time normalisation” or WBTN (see ref [4]). This was developed with two main aims in sight; to provide bunch by bunch beam position information (requiring one measurement every 25ns for the LHC) and to avoid the necessity of gain switching (requiring that one chain of electronics cope with a factor 40 difference in single bunch intensity). The principle of the WBTN technique is outlined in Fig. 8.

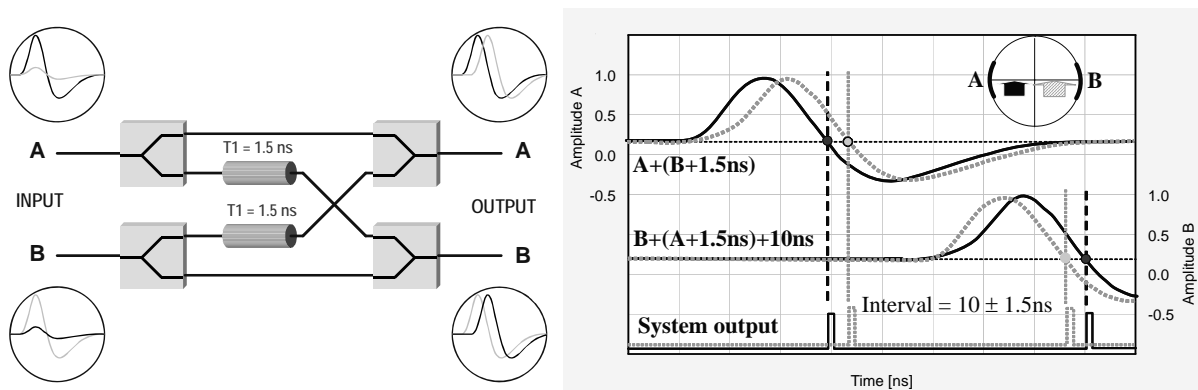


Fig. 8 The wide band time normalisation principle.

The signal from a single pick-up electrode is split and recombined with a delayed signal from the other electrode. This results in two signals where the relative zero crossing time depends on the position of the beam. In the case of the LHC the position information is converted into two pulses separated by  $10 \pm 1.5 \text{ ns}$  (the position being encoded into the  $\pm 1.5 \text{ ns}$ ). To obtain the required resolution and linearity using such a system requires precision high frequency electronic engineering. For example in order to achieve the 0.1% single shot resolution requested for the LHC ( $50 \mu\text{m}$  on a 50mm diameter pick-up) a stability and reproducibility at the 3ps level is required. One advantage of this system is that once the position has been encoded into these two pulses, it can be transmitted in a digital manner over a fibre optic network. This is important for machines such as the LHC where the

amount of electronics in the tunnel, in particular digital electronics, has to be minimised due to radiation levels. Fibre-optic transmission allows all the digital processing electronics, which finally extract the position from the time difference, to be regrouped in surface buildings, where they are accessible and free from radiation concerns. The final implementation layout for the LHC WBTN system is shown in Fig 9.

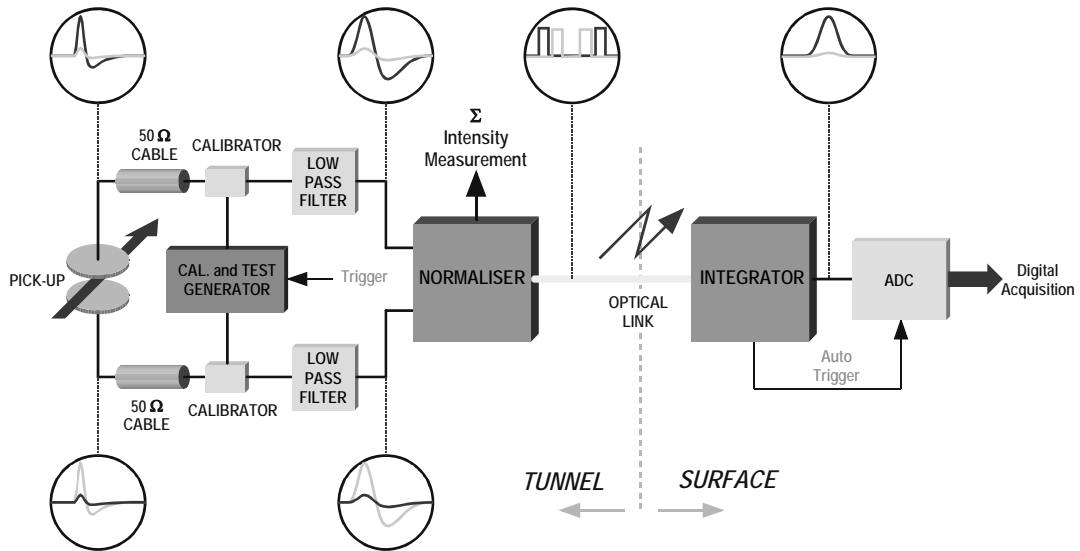


Fig. 9 Implementation of the Wide Band Time Normalisation electronics for the LHC. ( courtesy of D. Cocq, CERN )

**2. BEAM CURRENT AND INTENSITY MEASUREMENT**

The measurement of beam current or bunch intensity is one of the most basic measurements performed at any accelerator. This is usually done by means of a “beam current transformer” or BCT. In order for the transformer to interact with the magnetic field of the beam it has to be placed over a ceramic gap in the vacuum chamber. To keep the impedance seen by the beam as low as possible an RF bypass (either a thin metallic coating or external capacitors on the ceramic) is required for the high frequency wall current components. In addition, to keep the vacuum chamber continuity, an Ohmic bypass external to the transformer is needed.

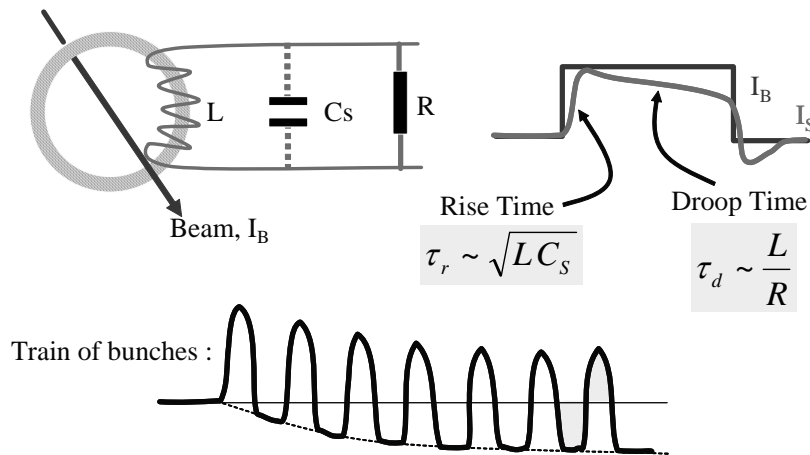


Fig. 10 The beam current transformer.

### 2.1 The Beam Current Transformer

The beam current,  $I_B$ , can be considered as the primary winding of the transformer, with the output voltage from the secondary windings given by  $V = L \, dI_B/dt$ . An ideal transformer would give a differentiated response, with the integrated charge being zero, which is not of much use as a measuring device. In reality the secondary windings have some stray capacitance, and are terminated by some finite resistance. This leads to signals of the form shown in Fig. 10. The transformer output now closely resembles the beam intensity distribution, with the added inconvenience of a DC offset due to the transformer droop. This DC offset can be corrected for either electronically or, in this modern era, by software treatment of directly digitised data.

A transformer with a bandwidth from 200Hz to 1GHz has recently been installed in the CERN-SPS [5]. Such a bandwidth is obtained by using a ferromagnetic core wound of high permeability metal tape to avoid eddy currents. With this instrument, operators can observe the bunch-by-bunch intensity evolution of beams destined for the LHC throughout the SPS acceleration cycle. In order to obtain the total charge in each bunch, fast integrators are required which are capable of working at repetition frequencies of up to 40MHz. Such an integrator chip has been developed by the Laboratoire de Physique Corpusculaire, Clermont-Ferrand, France, for capturing photomultiplier signals in the LHC-b experiment [6], and is now also used for bunch intensity measurements. A schematic of the integration principle and the resulting signals as measured in the CERN-SPS are shown in Fig. 11. The chip works using two integrators in parallel. As one integrates the other is discharged, with the output switched from one to the other on each clock cycle. The resulting integrated amplitude (voltage) is directly digitised, with all gain linearisation and DC offset subtraction performed by software.

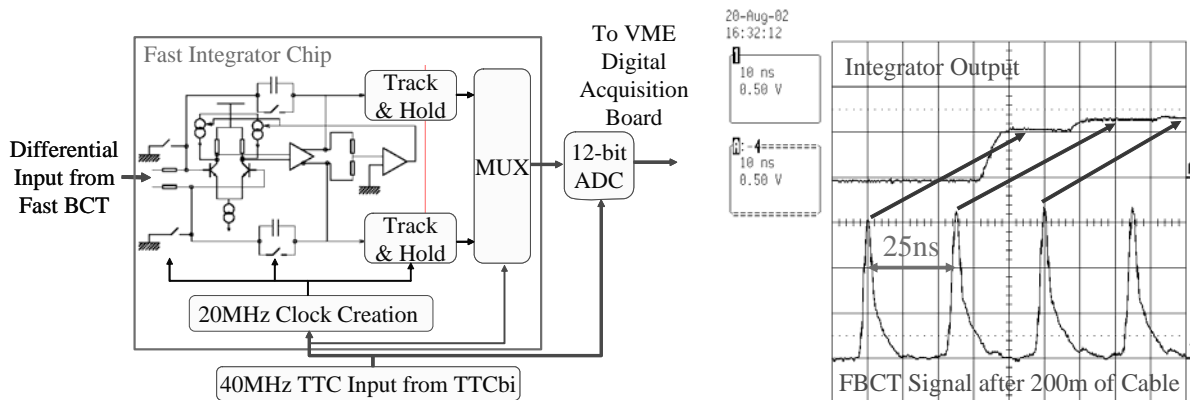


Fig. 11 The principle and measurement of the CERN-SPS fast beam current transformer.

### 2.2 The DC Beam Current Transformer

In storage rings and accelerators with cycle times of several seconds, a DC beam transformer can be used to measure the total current. Such an instrument was developed for the CERN-ISR (Intersecting Storage Rings), the first machine to sustain beams for hours [7]. A DC transformer is based on a pair of matched, toroidal, ferromagnetic cores, which are driven into saturation by a modulation current at frequencies of up to a few kHz. The principle of operation is shown in Fig. 12, and makes use of the hysteresis loop of the toroid. If an equal but opposite modulation current (the triangular waveforms in Fig. 12) is applied to both cores with the beam not present, then the voltage induced in the detection windings on each core will also be equal but opposite. When, however, there is a beam current  $I_B$  present, the starting point in the hysteresis loop for zero modulation current is offset due to the static magnetic field generated by the beam current. Since the modulation is opposite in each toroid, the time spent in saturation will be different for the two branches of the hysteresis loop. This results in the

generation of voltage pulses at twice the modulation frequency when the induced voltage in the detection windings on each core is combined. The demodulation of this signal gives a train of pulses, with the width of each pulse being a direct measure of the beam current, i.e. by how much the hysteresis curves are offset.

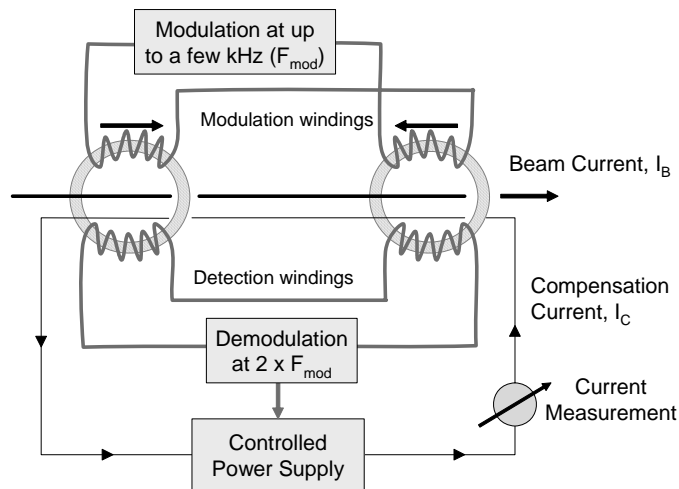
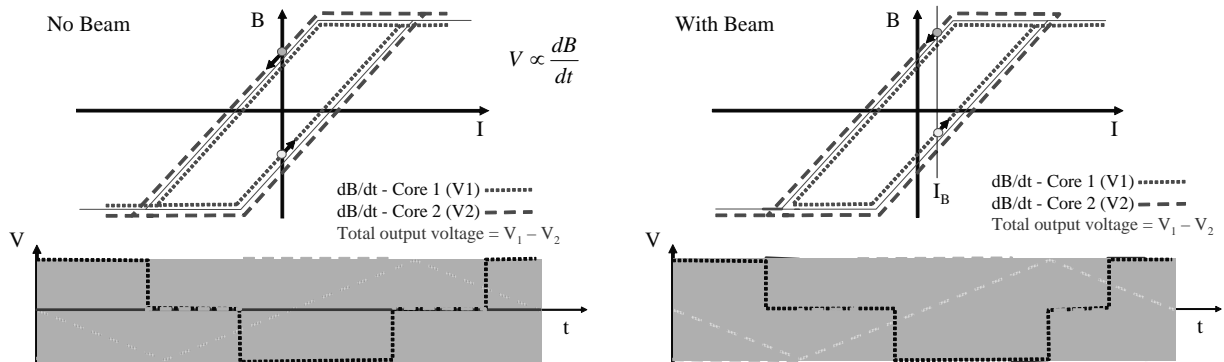


Fig. 12 The principle and schematic of a DC beam current transformer.

In the “zero flux detector” implementation of the DC beam transformer, the result of the demodulation is fed back into a compensating current loop (see Fig. 12). Once the compensation current and the beam current are identical the net static magnetic field seen by the toroids is zero (hence zero flux) and the output from the demodulator is also zero. The beam current can then be obtained by simply measuring the voltage produced by this compensation current across a know resistor.

For modern DC transformers such a zero flux detector is used to compensate the droop of the simple beam current transformer described in section 6.2. This significantly increases the bandwidth of the system, allowing measurement from DC to a few MHz.

### 3. DIAGNOSTICS OF TRANSVERSE BEAM MOTION

The instrumentation used to look at transverse beam motion is very important to the efficient operation of any circular accelerator [8]. There are three main parameters which can be measured using such diagnostics, namely the betatron tune, chromaticity and coupling, all of which are discussed in detail below.

### 3.1 Tune Measurement

All betatron tune measurements are based on applying a transverse excitation to the beam and looking at the resulting beam response. The most common methods of performing such measurements are presented in this section.

#### 3.1.1 Fourier Transform (FFT) of beam motion

In the simplest case the beam is given a single kick using a powerful stripline or magnetic kicker, and allowed to oscillate freely (alternatively white noise can be injected onto the beam). The observation of the resulting beam motion is usually carried out using one of the types of position pick-ups covered in Section 1. Once the data has been recorded, the power density spectrum in frequency domain can be computed using a Fast Fourier Transform (FFT). The betatron tune is determined as the frequency which has the highest amplitude response. If there is enough external excitation from other sources (ground motion, power supply ripple etc) or the beam is slightly unstable by itself, the method also gives useful information without any specific beam excitation.

What is usually of most interest for particle colliders is to be able to track the tune evolution during the whole of the accelerator cycle. The simplest way of achieving this is to repeat the tune measurement outlined above at regular intervals. By displaying such data as a spectrograph (Fig. 13(a)) the complete history of the tune during the machine cycle can be tracked.

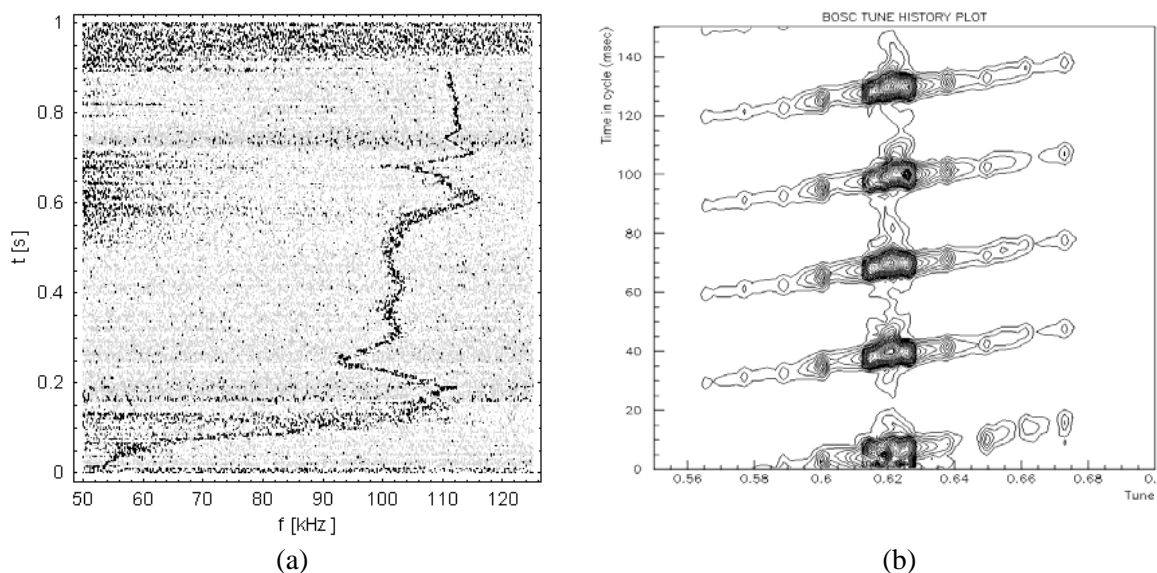


Fig. 13 (a) A spectrograph showing tune evolution in the CERN-PS.  
(b) Chirped tune measurements from the CERN-SPS.

#### 3.1.2 Chirp Excitation

In order to minimise the frequency range over which power is put into the beam, swept frequency or “chirp excitation” is often used (so-called because if listened to at audio frequencies such a signal sounds like the chirp of a bird). The chirp range is set around the expected betatron tunes and the sweep time is determined depending on the requested time resolution and precision of the tune measurement. The advantage of this technique is that in addition to an amplitude response it also gives phase information, as the phase difference between the observed motion and the applied sine wave is easily measured. This makes it more sensitive than the single kick method and so allows smaller excitation amplitudes to be used. Fig. 13(b) shows a result from the CERN-SPS where a chirp was

performed every 30ms. The sine wave can be seen to sweep from low to high frequency, with the main tune peak and the synchrotron satellites clearly visible.

### 3.1.3 Swept Frequency Analysis

For this method (often called “Network Analysis”) the beams are excited with a steady sinusoidal wave. The amplitude and phase of the resulting oscillation are precisely determined by means of harmonic analysis. Thereafter the excitation frequency is increased in steps until the range of interest is covered. This represents a very precise measurement yielding the full information of the beam transfer function. The disadvantage is the long measurement time, which renders the method of little use for the study of dynamic phenomena.

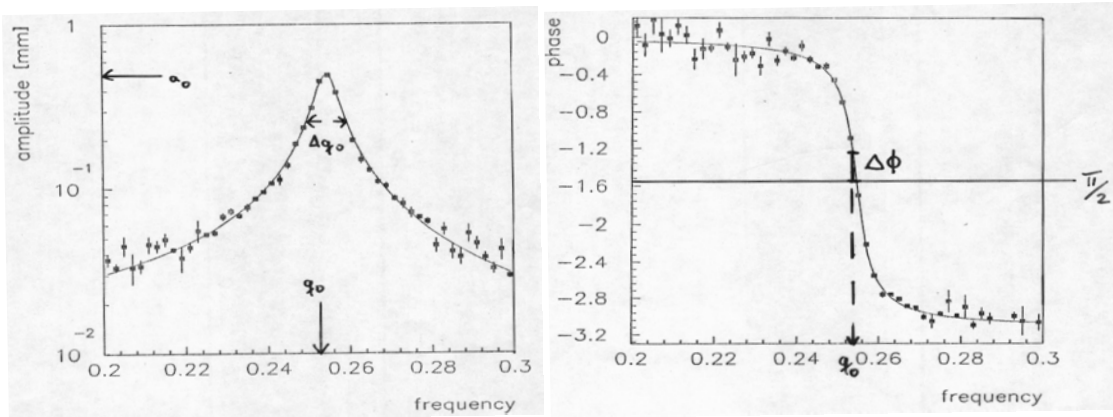


Fig. 14 Complete beam transfer function measured using swept frequency analysis in the CERN-LEP.

Such a complete beam transfer function is shown in Fig. 14. Notice how the phase jumps by  $180^\circ$  as the excitation sweeps across the betatron tune frequency. Such a response is typical of any harmonic oscillator. Since the rate of change of the phase change is a maximum at the peak of the amplitude response, measurements performed using the phase response of the beam are in general more sensitive than those relying on amplitude response.

### 3.1.4 Phase Locked Loop Tune Tracking

In order to have a fully continuous measurement of the tune a Phase Locked Loop (PLL) needs to be implemented. The basic principle of the PLL is sketched in Fig. 15. A voltage or numerically controlled oscillator (VCO or NCO) is used to put a sine wave excitation,  $A \cdot \sin(\omega t)$ , on the beam. The beam response to this signal is then observed using a pick-up, and will be of the form  $B \cdot \sin(\omega t + \phi)$ , where  $\phi$  is the phase difference between the excitation and the observed signal. In the phase detector the excitation signal and the observed signal are multiplied together, resulting in a signal of the form  $A \cdot B \cdot \sin(2\omega t + \phi) \cdot \cos(\phi)$ , which is seen to have a DC component proportional to the cosine of the phase difference. This will therefore be zero when the phase difference is  $90^\circ$  which, as was seen above, is where the amplitude response is a maximum, i.e. at the tune frequency. The aim of the PLL is to “lock-in” to this  $90^\circ$  phase difference between excitation and observed signal by correcting the VCO frequency until the DC component of the phase detector output is zero. Since the PLL will always try to maintain this  $90^\circ$  phase difference, the VCO frequency will track any tune changes, so giving a continuous tune measurement.

In practice things are not quite as simple. Many parameters have to be optimised in order for the PLL to find, lock-in and subsequently track the tune peak. The beam spectra and dynamics also have to be well understood if the PLL is not to lock or jump to a spurious line, resonance, synchrotron sideband etc. In addition, for hadron machines, the continuous excitation will lead to emittance blow-up. In order for this to be kept to a minimum the applied excitation has to be small and therefore the

observation pick-up and following electronics very sensitive. This is less of a problem for lepton colliders where radiation damping takes care of any emittance blow-up caused by the excitation, making PLL systems much easier to implement on such machines.

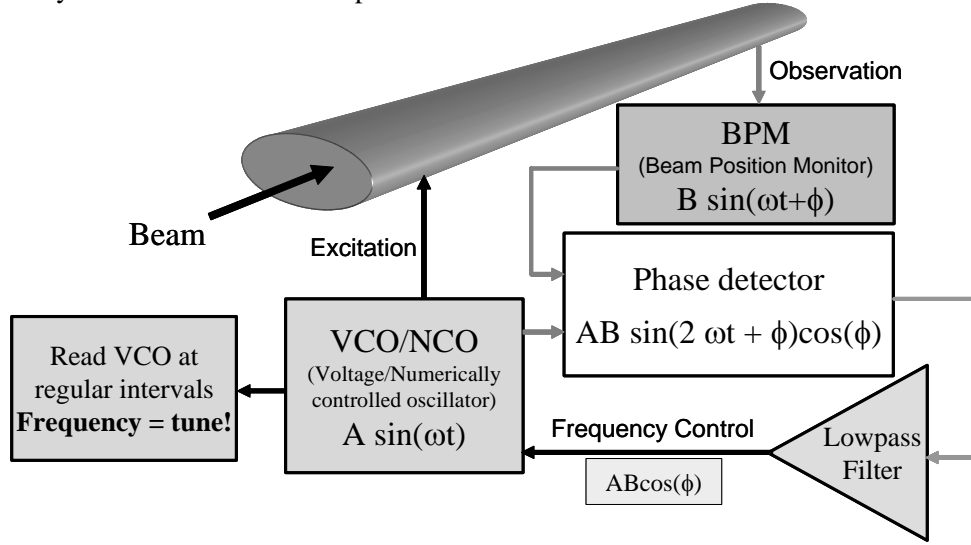


Fig. 15 Principle of a phase locked loop tune tracker.

### 3.2 Chromaticity Measurement

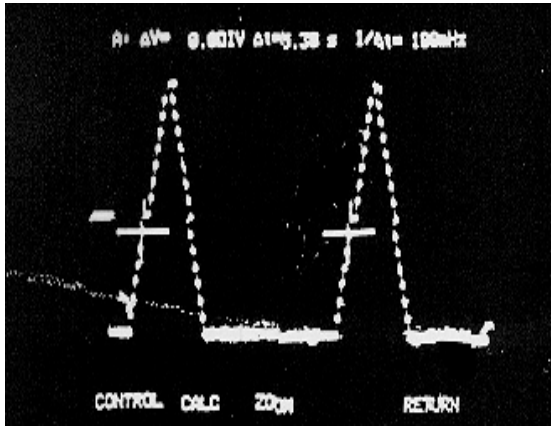
For any high energy synchrotron, the control of chromaticity is very important. If the chromaticity is of the wrong sign (corresponding to positive below the transition energy or negative above it) then the beam quickly becomes unstable due to the head-tail instability. If the chromaticity is too big then the tune spread becomes large and some particles are inevitably lost as they hit resonance lines in tune space. The most common method of measuring the chromaticity of a circular machine is to measure the betatron tune as a function of the beam energy and then to calculate the chromaticity from the resulting gradient. This is usually done by varying the RF frequency, keeping the magnetic field static. The equations of interest are:

$$\Delta Q = (\xi Q) \frac{\Delta p}{p} = Q' \frac{\Delta p}{p} = Q' \gamma_t^2 \frac{\Delta R}{R} = Q' \left( \frac{-\gamma_t^2 \gamma^2}{\gamma^2 - \gamma_t^2} \right) \frac{\Delta f}{f} \quad (3.1)$$

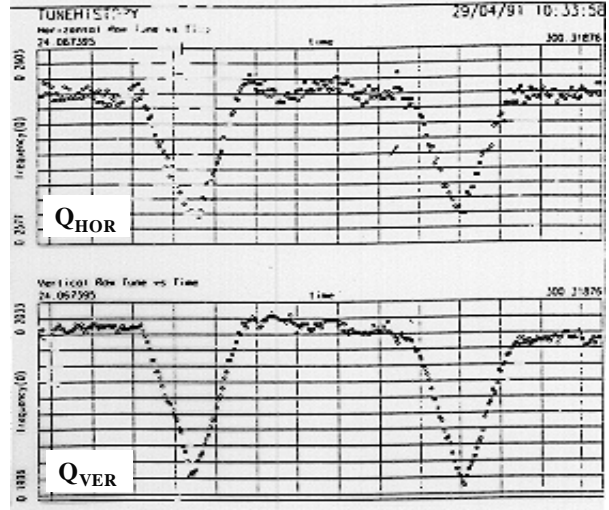
where  $\Delta Q$  is the change in tune,  $\Delta p/p$  the momentum spread (or relative change in momentum),  $\Delta R/R$  the relative change in radius,  $\Delta f/f$  the relative change in RF frequency and  $\xi$  the chromaticity. Please note that the chromaticity,  $\xi$ , is often expressed as  $Q' = Q \xi$ , where  $Q$  is the total betatron tune including the integer part.

In the CERN-SPS, for example, a chromaticity measurement consists of performing a tune measurement for three different RF frequency settings. Instead of noting the exact RF frequency, what is actually measured is the change in closed orbit, from which the relative change in radius can be calculated. These three points are then plotted, with the gradient giving the chromaticity.

In order to obtain continuous chromaticity measurements this technique of RF modulation is combined with the PLL tune measurement outlined in the previous section. The RF frequency is usually programmed with a small asymmetric function which periodically varies about the mean RF frequency. By tracking the tune during this time using the PLL and knowing the magnitude of the RF change, the chromaticity can be calculated and tracked. An example of such a measurement performed at the CERN-LEP is shown in Fig. 16.



(a)



(b)

Fig. 16 Example of a LEP chromaticity measurement. (a) shows the applied RF frequency shift and (b) shows the response of the horizontal and vertical betatron tunes measured by PLL tune tracking.

### 3.2.1 Head-Tail Chromaticity Measurement

The methods outlined above do not allow instantaneous chromaticity measurements, for instance during energy ramping or beta squeezing and are limited to repetition intervals in the Hz range. In preparation for the LHC a new approach has been developed which uses the energy spread in the beams for a chromaticity measurement. Transverse oscillations are excited with a single kick and the chromaticity is calculated from the phase difference of the individually sampled head and tail motions of a single bunch. Using this method the chromaticity can be calculated using the data from only one synchrotron period (about 15-50 milliseconds in the case of the LHC). In addition, this technique does not rely on an accurate knowledge of the fractional part of the betatron tune and, for a machine operating well above transition, the calculated chromaticity is virtually independent of beam energy.

Assuming longitudinal stability, a single particle will rotate in longitudinal phase-space at a frequency equal to the synchrotron frequency. During this longitudinal motion the particle also undergoes transverse motion. If the chromaticity is zero, then the particle will have the same tune wherever it is in the bucket. As soon as chromaticity is non-zero, however, the particle's tune will change depending on where it happens to be longitudinally. If a whole bunch of particles is kicked transversely, then the resulting transverse oscillations for a given longitudinal position within the bunch can be shown [9] to be given by

$$y(n) = A \cos(2\pi n Q_0 + \omega_\xi \hat{\tau} (\cos(2\pi n Q_s) - 1)) \quad (3.2)$$

where  $n$  is the number of turns since the kick,  $Q_0$  is the betatron tune,  $Q_s$  is the synchrotron tune,  $\hat{\tau}$  is the longitudinal position with respect to the centre of the bunch and  $\omega_\xi$  is the so-called chromatic frequency given by

$$\omega_\xi = Q' \omega_0 \frac{1}{\eta} \quad (3.3)$$

Here  $Q'$  is the chromaticity,  $\omega_0$  is the revolution frequency and  $\eta = 1/\gamma^2 - 1/\gamma_{tr}^2$ . If we now consider the evolution of two longitudinal positions within a single bunch separated in time by  $\Delta\tau$ , then from (3.1) it follows that the phase difference in the transverse oscillation of these two positions is given by

$$\Delta\psi(n) = -\omega_\xi \Delta\tau (\cos(2\pi n Q_s) - 1) \quad (3.4)$$

This phase difference is a maximum when  $nQ_s = 1/2$ , i.e. after half a synchrotron period, giving

$$\Delta\psi_{\max} = -2\omega_\xi \Delta\tau \quad (3.5)$$

The chromaticity can therefore be written as

$$Q' = \frac{-\eta \Delta\psi(n)}{\omega_0 \Delta\tau (\cos(2\pi n Q_s) - 1)} = \frac{\eta \Delta\psi_{\max}}{2\omega_0 \Delta\tau} \quad (3.6)$$

A schematic layout of the CERN-SPS Head-Tail monitor [10] set-up is shown in Fig. 17(a). A straight stripline coupler (see section 1.1.3) followed by a  $180^\circ$  hybrid is used to provide the sum and difference signals for a given measurement plane. These signals are fed into a fast-sampling (2GS/s on each channel), high bandwidth (2GHz) digital oscilloscope. A VME front-end acquisition crate then retrieves the data via a GPIB link and provides the bunch synchronous timing. Using the ‘‘Fast-Frame’’ capabilities of the oscilloscope the data from the same bunch can be captured over several hundred turns. Fig. 17(b) shows the result of such a head-tail chromaticity measurement. The top two plots show the transverse movement of the head and tail respectively of a single bunch after the beam is kicked. The lower left plot shows the evolution of the phase of the head and tail and the phase difference. It can be seen that the signals are re-phased after one synchrotron period, with the phase difference a maximum after  $1/2$  a synchrotron period. The final plot (lower right) shows the calculated chromaticity (using equation 3.6) for all turns where the phase difference is well defined.

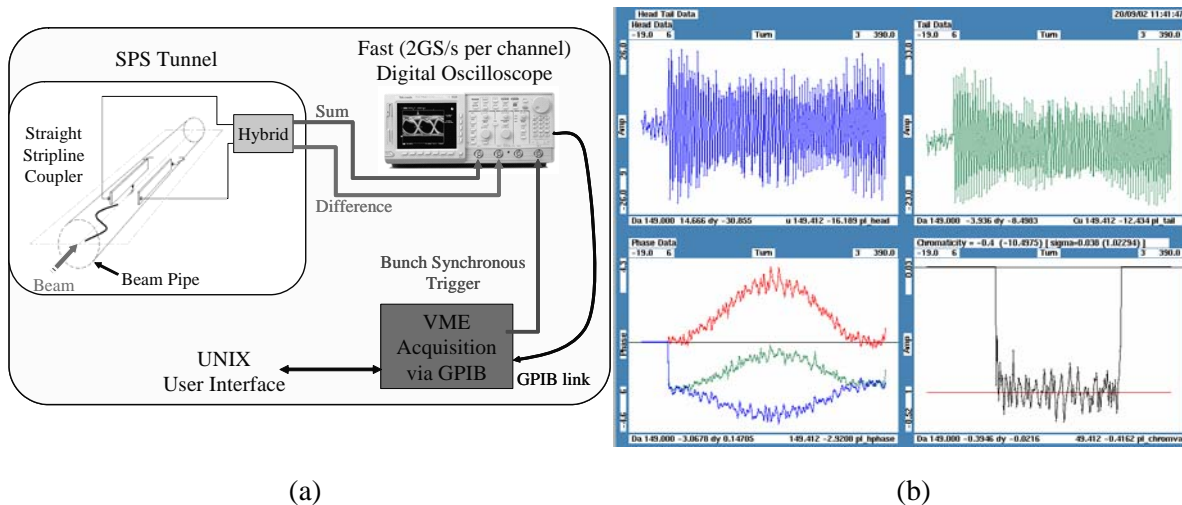


Fig. 17(a) Layout of the CERN-SPS head-tail monitor. (b) Head-tail monitor acquisition.

### 3.3 Coupling Measurement

The control of coupling (the degree to which horizontal and vertical betatron motion is linked) is also important for circular accelerators. Excessive coupling will make tune and chromaticity measurements almost impossible, as the information from both planes are mixed-up in the observed signal. A very good and comprehensive summary of linear betatron coupling can be found in [11].

#### 3.3.1 Closest Tune Approach

For this method, both betatron tunes are measured during a linear quadrupole power converter ramp which crosses the values of the horizontal and vertical tunes. The remaining separation of the tune

traces is a direct measure for the total coupling coefficient  $|c|$ . A measurement example from the CERN-LEP, using a phase locked loop tune measurement is shown in Fig. 18. In order to ensure that the PLL keeps tracking both tunes, even when they approach each other, the measurements are performed on two different bunches.

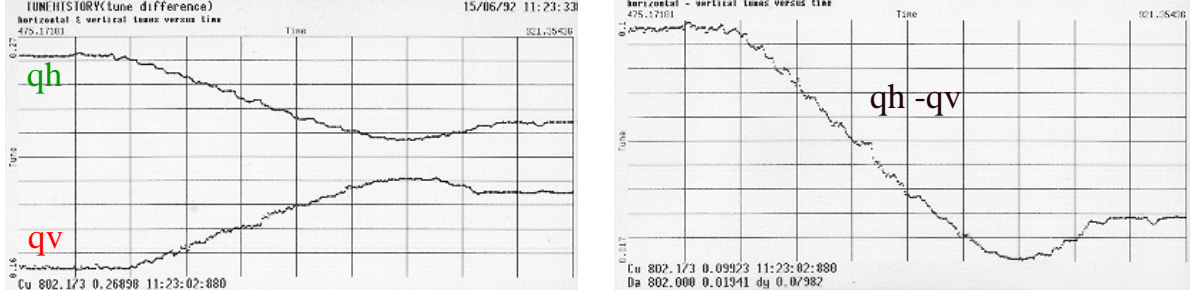


Fig. 18 LEP coupling measurement.

### 3.3.2 Kick Method

The above method does not allow for diagnostics during machine transitions. A better tool for the measurement of small coupling coefficients, although demanding quite large beam excitations, consists of applying a single kick in one plane and observing the time evolution of the betatron oscillations in both planes. This method is described in Ref [11].

## 4. EMITTANCE MEASUREMENT

The ultimate luminosity of any collider is inversely proportional to the transverse emittance of the colliding beams. Preservation of emittance and hence emittance measurements are of particular importance in the long chain of accelerators and storage rings of big hadron colliders as the emittance of a hadron bunch is not appreciably reduced through mechanisms such as the radiation damping associated with lepton machines. Good explanations of emittance can be found in Refs [12, 13].

The emittance which includes about 98 % of the beam-particles can be defined as

$$\varepsilon(98\%) = \frac{\text{beamwidth}^2 - \left(\frac{\Delta P}{P} \cdot D_m\right)^2}{\beta_m} = \frac{\text{FWHM}^2 - \left(\frac{\Delta P}{P} \cdot D_m\right)^2}{\beta_m} \quad (4.1)$$

where FWHM is the measured full width at half height ( $2.35\sigma$ ) of the beam,  $\Delta P/P$  the FWHM of the momentum spread,  $D_m$  the value of the dispersion-function and  $\beta_m$  the value of the beta-function at the monitor position.

From this equation one can immediately see that the measurement of emittance depends on many parameters. This limits the accuracy to which emittance can be calculated, which is generally with a precision no better than around 10%. A number of instruments are capable of measuring the beam profile quite precisely, but in calculating the emittance one also relies on knowledge of the beam optical parameters at the place of the instrument and these are often fraught with considerable uncertainties.

#### 4.1 Scintillator and Optical Transition Radiation Screens

Scintillator screens have been used for nearly a century and are the simplest and most convincing device when one has to thread a beam through a transfer line and into and around an accelerator. The modern version consists of a doped alumina screen which is inserted into the beam and can stand high intensities and large amounts of integrated charge. In its simplest form a graticuled screen is observed using a TV-camera. It can deliver a wealth of information to the eye of an experienced observer, but only in a semi-quantitative way. Much can be done about that with modern means of rapid image treatment, but questions concerning the linearity of these screens at high beam densities remain.

Optical Transition Radiation (OTR) screens are a cheap substitute for scintillator screens. OTR radiation is generated when a charged-particle beam transits the interface of two media with different dielectric constants (e.g. vacuum to metal or vice versa) [14]. Since this is a surface phenomenon, the screens can be made of very thin foils which reduces beam scattering and minimises heat deposition. The radiation produced is emitted in two cones around the angle of reflection for backward (vacuum to metal) OTR so that if the foil is placed at  $45^\circ$  to the beam direction, the radiation produced is at  $90^\circ$  to the beam direction. In addition two cones of forward OTR (metal to vacuum) are produced around the beam direction (see Fig. 19). The angular distribution of the emitted radiation has a central hole and a peak located at  $1/\gamma$ . The higher the value of  $\gamma$  the sharper the peaks and the more light can be collected, which is why OTR is generally suited to lepton or high energy hadron machines.

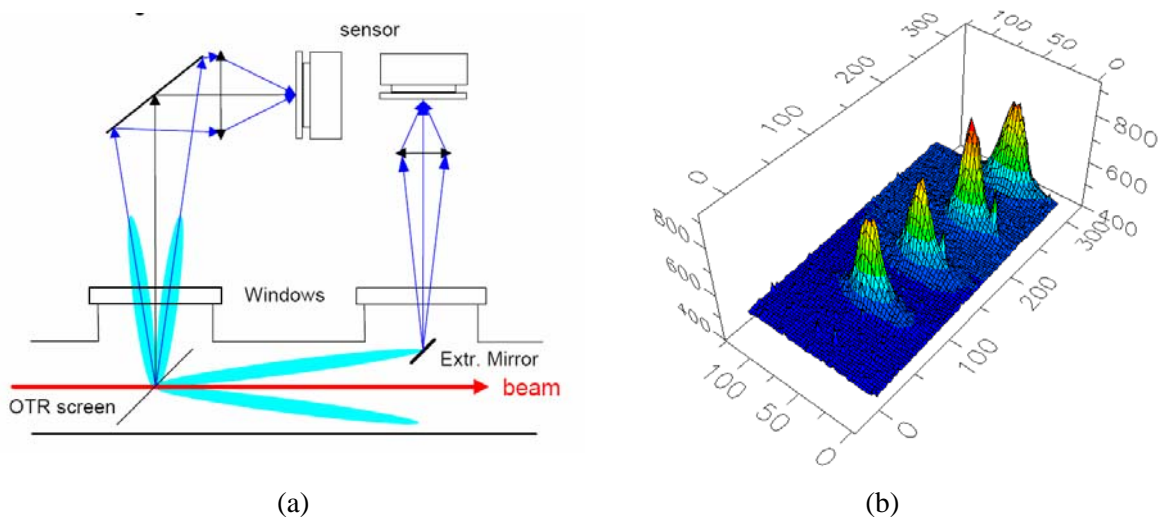


Fig. 19 (a) Backward and forward OTR patterns with their imaging schemes.  
(b) Example of 2D OTR images taken every four turns at injection in the CERN-SPS.

#### 4.2 SEM-Grids

Secondary Emission (SEM) Grids, also known as harps, consist of ribbons or wires which are placed in the beam. As the beam intercepts the grid, secondary emission occurs leading to a current in each strip which is proportional to the beam intensity at that location. By measuring this current for all strips a beam profile is obtained. SEM-grids are the most widely used means to measure the density profile of beams in transfer lines. In addition, sets of three, properly spaced (i.e. with the right phase advance between monitors), allow a determination of the emittance ellipse. What makes them popular is their simple and robust construction, the fact that there is little doubt about the measured distribution, and their high sensitivity, in particular at low energies and for ions. At higher energies they can be considered semi-transparent. Amongst their drawbacks are the limited spatial resolution (difficult to get the wire spacing much below 0.25mm) and the rather high cost for the mechanisms and electronics.

### 4.3 Wire Scanners

Of all the instruments used for measuring the emittance of circulating beams, wire-scanners are considered to be the most trustworthy. They come in two different types; rotative and linear. Rotative wire scanners consist of a thin wire (some tens of microns in diameter) mounted on a fork which is attached to a rotating motor (see Fig. 20), while linear scanners use motors which push/pull the wire across the beam. There are two ways of obtaining a beam profile with wire scanners; by measuring the secondary emission current as a function of wire position (similar to the SEM-grid acquisition mentioned above) or by measuring the flux of secondary particles created as the beam interacts with the wire. This latter technique is often used for high intensities, where the heating of the wire produces thermal emission which falsifies the secondary emission results. It relies on the use of radiation detectors, typically scintillators followed by photo-multipliers, placed downstream of the wire scanner to detect the  $\gamma$ -radiation and secondary particles produced when the wire intercepts the beam. To make the flux collected independent of the wire position may require the summation of the signals from two or more detectors positioned around the beam chamber.

Fast wire scanners are nearly non-destructive over a wide range of energies. Their spatial resolution can reach the micrometer range and, with fast gated electronics, the profiles of individual bunches can be observed. Their great sensitivity also allows them to be used for the study of beam halos.

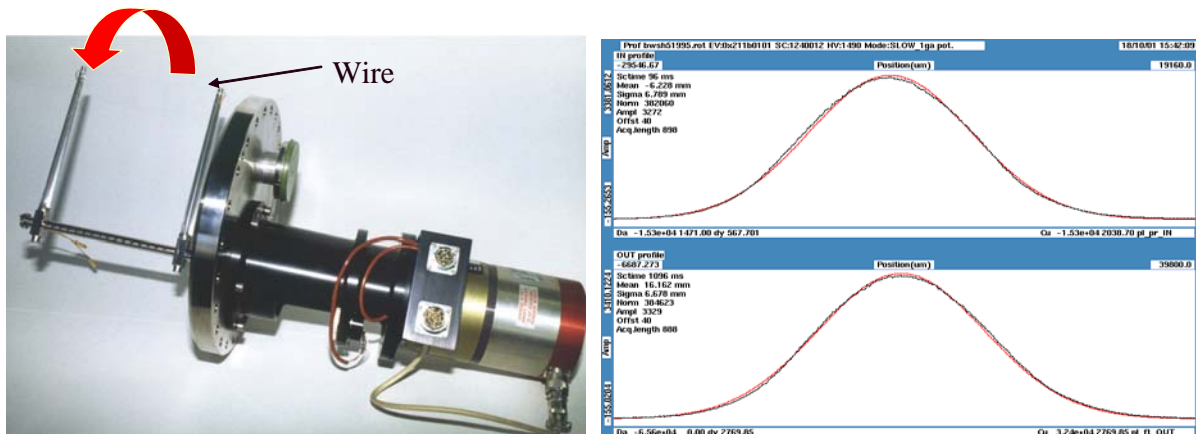


Fig. 20 Rotative wire scanner and an example of a wire scanner profile measurement.

### 4.4 Residual Gas and Luminescence Monitors

Rest gas monitors are used in many high energy accelerators in order to reconstruct transverse beam distributions (see e.g. Ref. [15]). The signal results from the collection of either the ions or the electrons produced by the beam ionising the small amount of residual gas in the vacuum chamber. These ions or electrons are accelerated using a bias voltage of several kilovolts and collected on a micro channel plate (MCP). The avalanche of electrons produced by the MCP then hits a phosphor screen, giving an image of the beam profile which can be monitored using a CCD camera (see Fig. 21). Due to their rigidity, ions are less sensitive to the distorting effects of the space charge from the circulating beam, but their slow drift time, even with high bias voltages, means that they spend a long time in this beam field, making it difficult to analyse rms beam dimensions smaller than one millimetre. In order to use electrons to produce an image, a transverse magnetic field needs to be added around which the electrons spiral on their way to the MCP. This eliminates, to a large extent, the space charge effects of the beam and allows sharper images to be produced than with ions. This additional magnetic field, however, is also seen by the beam and has to be compensated by two corrector magnets either side of the ionisation profile monitor.

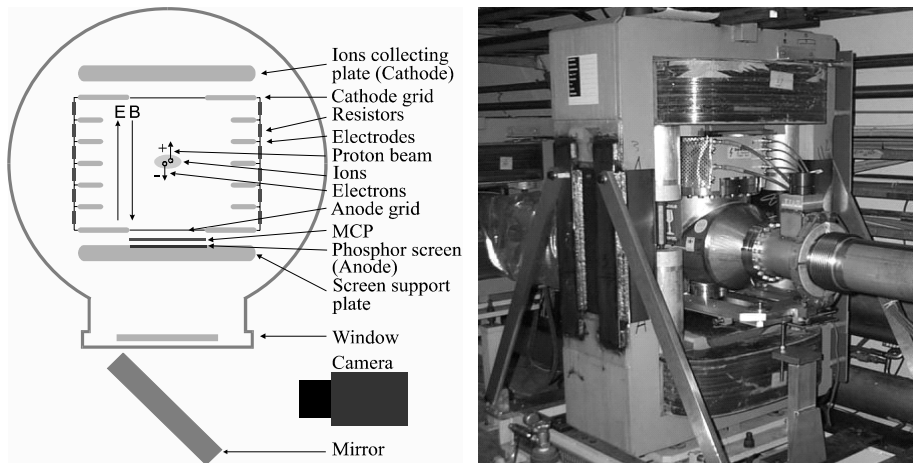


Fig. 21 Principle of a residual gas ionisation profile monitor and an example from the CERN-SPS.

Luminescence monitors (see e.g. Ref. [16]) also rely on the interaction of the beam with a gas in the vacuum chamber. In this case the gas of interest is nitrogen, in which electrons are excited from the ground state to a higher energy level by the passing beam. Once the beam has passed the electrons return to the ground state and emit photons. In the case of nitrogen the dominant photon wavelength is 391.3nm, corresponding to light at the lower end of the visible range, for which many detectors are available. In general, the residual gas alone does not produce enough photons for accurate imaging and hence a local pressure bump is usually created by injecting a small amount of nitrogen to enhance the photon production. The principle of luminescence monitoring and a schematic layout of such an instrument are shown in Fig. 22. Also shown in Fig. 22 is an example of a continuous measurement performed at the CERN-SPS, showing the ability of such an instrument to track the evolution of the beam size through the various acceleration stages with little effect on the beam.

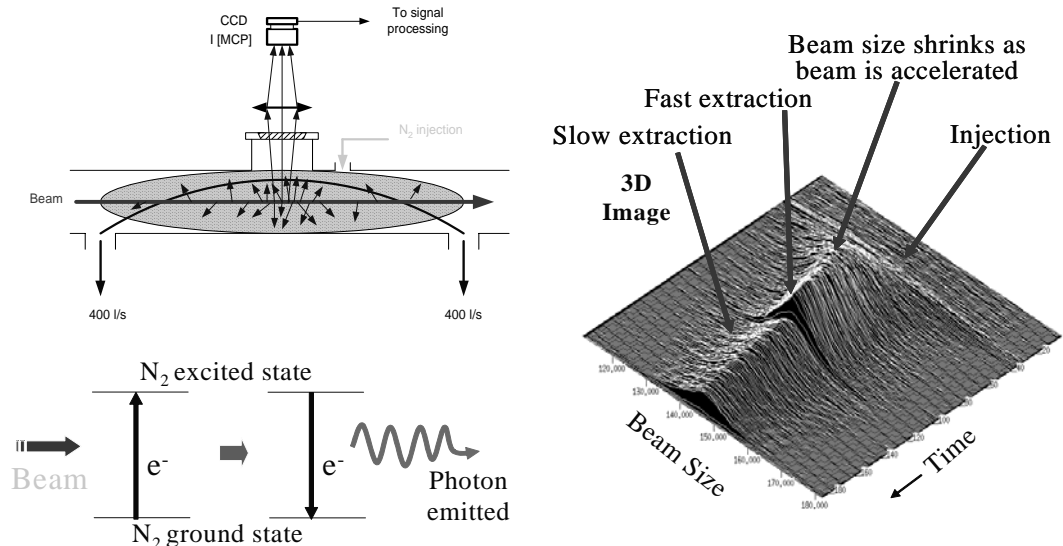


Fig. 22 Principle of luminescence monitoring and a beam measurement example from the CERN-SPS.

Most users consider both the residual gas ionisation and luminescence profile monitors to be semi-quantitative and not be relied upon for absolute emittance measurements, even after calibration

against some other instrument such as a wire scanner. Their virtual transparency for the beam, however, makes them useful for the continuous on-line tracking of beam size.

### 4.5 Synchrotron Radiation Monitors

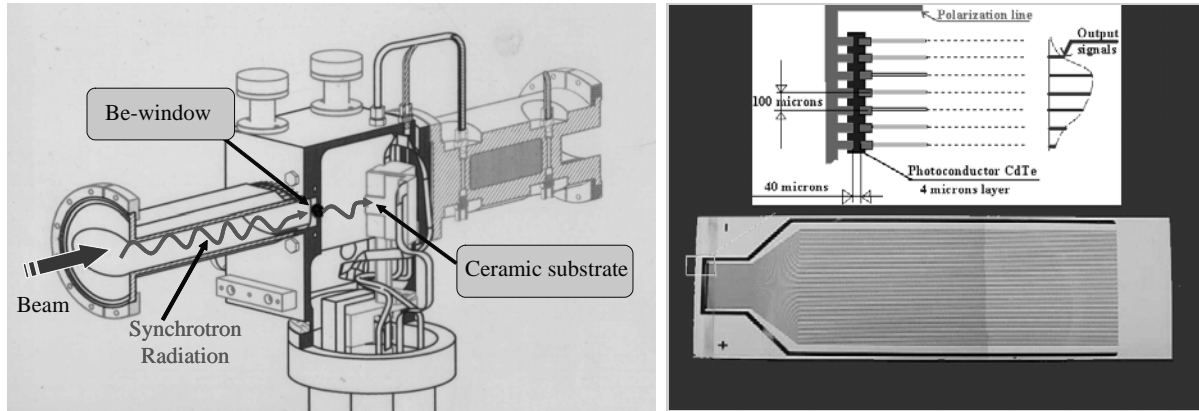


Fig. 23 The CERN-LEP BEXE detector based on cadmium telluride photo-conductors.

Synchrotron radiation monitors are limited to highly relativistic particles and offer a completely non-destructive and continuous measurement of the 2-dimensional density distribution of the beam. These monitors make use of the light produced when highly relativistic particles are deflected by a magnetic field. They are therefore usually positioned to make use of parasitic light produced by a dipole magnet in the machine or behind a purpose built “wiggler” magnet in which the beam is deflected several times to enhance the photon emission.

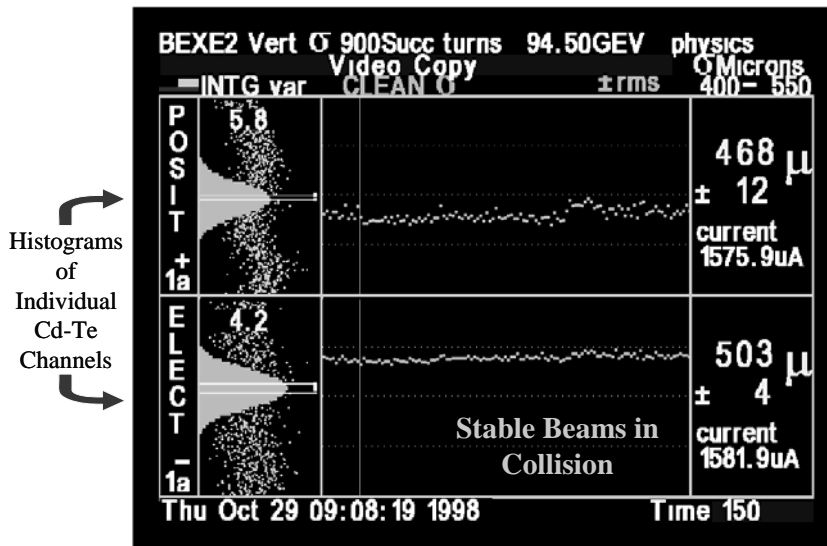


Fig. 24 Tracking vertical beam sizes with the BEXE detector during electron-position collisions.

The most common way of measuring the beam size with synchrotron radiation is to directly image the extracted light using traditional optics and a camera. The spatial resolution for such systems is usually limited by diffraction and depth-of-field effects. If the beam is sufficiently relativistic then the photon emission extends into the hard X-ray region of the spectrum and X-ray detectors can be used, for which diffraction effects can be completely disregarded. Such an instrument, based on

cadmium-telluride (CdTe) photo-conductors, was used at the CERN-LEP [17] to measure rms beam sizes down to  $300\mu\text{m}$  with a resolution of some  $10\mu\text{m}$  (see Fig. 23). The detector consisted of 64 voltage biased CdTe photo-conductors of  $4\mu\text{m}$  thickness and spaced by  $100\mu\text{m}$  on a ceramic substrate. Each photo-conductor was followed by its own individual charge amplifier. By reading out the signal from each cell the beam profile could be reconstructed. The interesting feature about such photo-conductors is that they allow real-time measurements with data acquisition rates up to  $100\text{kHz}$ . In addition they are extremely radiation resistant, accepting doses beyond  $10^{12}$  Grays. These detectors were heavily used towards the end of CERN-LEP operation to optimise the luminosity by tracking the electron and positron vertical beam size during collision (see Fig. 24).

## 5. BEAM LOSS MONITORING

Beam loss monitors (BLMs) have three main uses in particle accelerators:

- **Damage prevention** - Beam loss may result in damage to accelerator components or the experimental detectors. One task of any BLM system is to avoid such damage. In some accelerators it is an integral part of the protection system, signalling the beam abort system to fire if a certain loss rate is exceeded. This is of vital importance to the new generation of superconducting accelerators, for which even fairly small beam losses in the superconducting components can lead to magnet quenches.
- **Diagnostics** - Another task of BLM systems is to identify the position (and time) of unacceptable beam losses and to keep the radiation level in the accelerator and its surroundings as low as possible.
- **Luminosity optimisation** - BLMs can also help in the tuning of the machine in order to produce the long lifetimes necessary for improved luminosity.

The job of the BLM system is to establish the number of lost particles at a certain position within a specified time interval. Most BLM systems are mounted outside the vacuum chamber, so that the detector normally observes the shower caused by the lost particles interacting in the vacuum chamber walls or in the materials of the magnets. The number of detected particles and the signal from the BLM should be proportional to the number of lost particles. This proportionality depends on the position of the BLM with respect to the beam, the type of lost particles and the intervening material. It also, however, depends on the momentum of the lost particles, which may vary by a large amount during the acceleration cycle. One has to distinguish between two types of losses:

- **Fast losses** – where a large amount of beam is lost over a very few turns.
- **Slow losses** – where partial beam loss occurs over some time (circular machines) or distance (LINAC, transport lines). In storage-rings, the lifetime is defined by slow losses. There are many reasons for these losses and a BLM system is very helpful for finding out what is happening in the machine. In superconducting accelerators a BLM system can also prevent beam loss induced quenches caused by these slow losses.

The fact that BLM systems have to cover both of these cases means that they are required to function over a very large dynamic range, typically in the region of  $10^4$  to  $10^6$ .

### 5.1 Long Ionisation Chambers

In 1963, Panowsky [18] proposed a BLM system for SLAC which consisted of one long (3.5 km) hollow coaxial cable filled with Ar (95%) +  $\text{CO}_2$  (5%), mounted on the ceiling along the LINAC, about 2m from the beam. When a beam loss occurs, an electrical signal is produced which propagates to both ends of the cable. Position sensitivity is achieved by comparing the time delay between the direct pulse from one end and the reflected pulse from the other. The time resolution is about 30ns ( $\sim 8\text{m}$ ) which, for shorter versions, can be reduced to about 5ns. This principle of space resolution works for linear accelerators and transport lines with a bunch train much shorter than the machine and with relativistic particles. For particles travelling significantly slower than the signal in the cable the

resolution of multiple hits in the cable becomes difficult. In this case, and for circular machines, it is necessary to split the cable. Each segment has to be read out separately, with a spatial resolution which becomes approximately equal to their length.

### 5.2 Short Ionisation Chambers

Short ionisation chambers are used in many accelerators (see e.g. Ref. [19]). They are more or less equally spaced along the accelerator with additional units at special positions such as aperture restrictions, targets, collimators, etc. The chamber provides some medium with which the secondary particles created by the beam loss can interact, typically a gas such as nitrogen or argon. This interaction produces electron-ion pairs which are collected by a series of high voltage gaps along the length of the chamber. The resulting current is then measured and is proportional to the beam loss at the location of the monitor. An example of a CERN-SPS ionisation chamber is shown in Fig. 25.

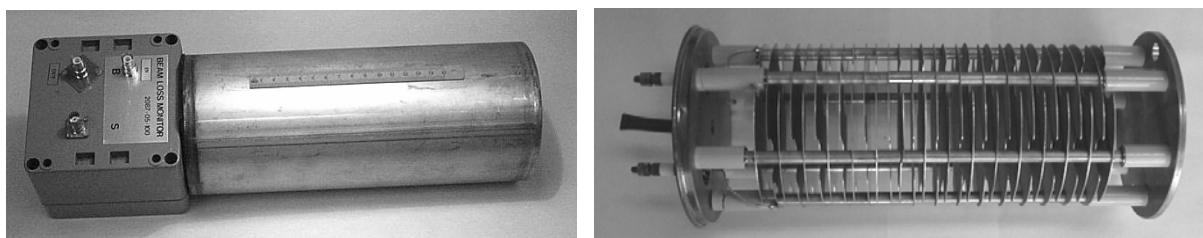


Fig. 25 A CERN-SPS ionisation chamber used for beam loss monitoring.

### 5.3 Scintillation Counters

In the case where losses occur in a machine without a full BLM system, a plastic scintillator with photomultiplier readout is often temporarily installed. Such systems have a well known behaviour, but the radiation damage of the plastic scintillator restricts their long term use. Liquid scintillators are not susceptible to such damage and have been installed in some accelerators [20, 21]. Such BLMs can be very fast, with pulse rise times of around 10ns, but suffer from drift in the photomultiplier gain.

### 5.4 Aluminum Cathode Electron Multipliers

In such detectors the sensitivity of photomultipliers to ionising radiation is increased by replacing the photocathode with an aluminium foil. This foil then works as a secondary electron emitter when irradiated. A BLM system consisting of Aluminum Cathode Electron Multipliers (ACEMs) is installed in the CERN-PS and PS-Booster [22]. It is very fast, with signal rise times in the order of 10ns, but is rather expensive since the ACEM is not a standard tube of photomultiplier manufacturers.

### 5.5 PIN Photodiodes

For circular electron accelerators which emit hard synchrotron radiation it is difficult to distinguish between the beam loss distributions and the synchrotron radiation background using traditional BLM techniques. In DESY-HERA, an electron-proton collider, the warm electron and a superconducting proton rings are in the same tunnel. Protection of the superconducting proton beam magnets from beam loss induced quenches must therefore rely on a BLM system which sees only the proton beam losses and not the synchrotron radiation background. In this case back to back PIN photodiodes are used to distinguish between the hadronic shower created by beam losses and the synchrotron radiation [23]. The charged particles will interact with both photodiodes, giving a coincidence signal, while the photons will be absorbed by the first diode. In contrast to the charge detection of most other BLM systems, PIN photodiode detection depends on counting coincidences, with the count rate proportional to the loss rate so long as the number of overlapping coincidences is small.

## 6. LUMINOSITY MONITORING

Luminosity Monitors are specific to colliders, since they measure the collision rate of the two counter-rotating particle beams. The following formulae define luminosity and related quantities:

Luminosity: 
$$L = f_{rev} \frac{MN^2}{4\pi\sigma_*^2}$$

Normalized emittance: 
$$\varepsilon_N = \gamma \frac{\sigma_*^2}{\beta_*}$$

Beam-beam tune shift: 
$$\Delta\nu_{bb} = \frac{Nr_p}{4\pi\varepsilon_N}$$

where  $f_{rev}$  is the revolution frequency,  $M$  the number of bunches,  $N$  the number of particles per bunch,  $\sigma_*$  the rms beam size at the collision point,  $\beta_*$  the beta function at the collision point and  $r_p$  the particle radius.

Since the counting rates of the experiments are directly proportional to the luminosity, the aim of the accelerator operators is to maximise the luminosity. This can be done by having a large number of particles per bunch, many bunches and small beams sizes at the interaction point.

In this section, luminosity monitoring will be taken as an example of beam instrumentation engineering, i.e. the whole process from selecting an appropriate physics process to system design. The system presently under development for the LHC has been chosen for this case study, as all the documents and figures are easily at hand. The following steps will be treated:

- Functional requirements
- Choice of physics process
- Location of the sensor
- Choice of the sensor

### 6.1 Functional requirements of the LHC luminosity monitor

The monitor under discussion is aimed at giving a relative luminosity reading for machine optimisation, but it is not required to give the absolute luminosity (as defined above) for the calculation of the underlying cross-section of the experimental physics processes. Hence the system does not need an absolute calibration. In addition, the monitor is to be used to study the variation in luminosity between the individual bunches of the LHC. This means that the detector has to have the bandwidth of the individual bunch crossings, which is 40 MHz. The expected difference in luminosity between bunches is very small, so a resolution of 1% is required.

### 6.2 Choice of the physics process for the detector

Since any count-rate coming from the collision point of the beam particles can be used as a signal for luminosity monitoring there is a wide choice of physics processes that could be used for this measurement. Due to both cost and integration issues the detector has to be small in size, hence huge detector arrays covering a large solid angle of secondary particle production can be excluded. This eliminates all well identified physics processes producing particles with large transverse momenta. Diffractive beam particle interactions, for which at least one of the incoming protons dissociates into a leading (high energy) neutron plus other secondary particles have therefore been considered as a source for the luminosity signal. Due to the nature of this process, most of the secondary neutrons are emitted into a very small solid angle in the forward direction. The properties of this interaction are pretty well known from lower energies, so that the cross section can be assumed to within a 10% accuracy. This process has been chosen as the basis for LHC luminosity monitoring.

### 6.3 Location of the sensor

Since the neutron production is in the very forward region, a monitor located close to the interaction point would have to be inside the vacuum chamber. In order to measure the forward neutron flux outside the vacuum chamber one also needs at least one intervening deflecting dipole to bend away the charged beam particles. Looking at the design of one of the high luminosity LHC interaction regions (Fig. 26) one can spot two large metallic objects, which are introduced to shield the superconducting elements from the particle flux of the collision products. The TAS is intended to shield the inner triplet from secondary particles, while the TAN is designed to absorb the forward neutron flux, which is just the signal required for luminosity monitoring.

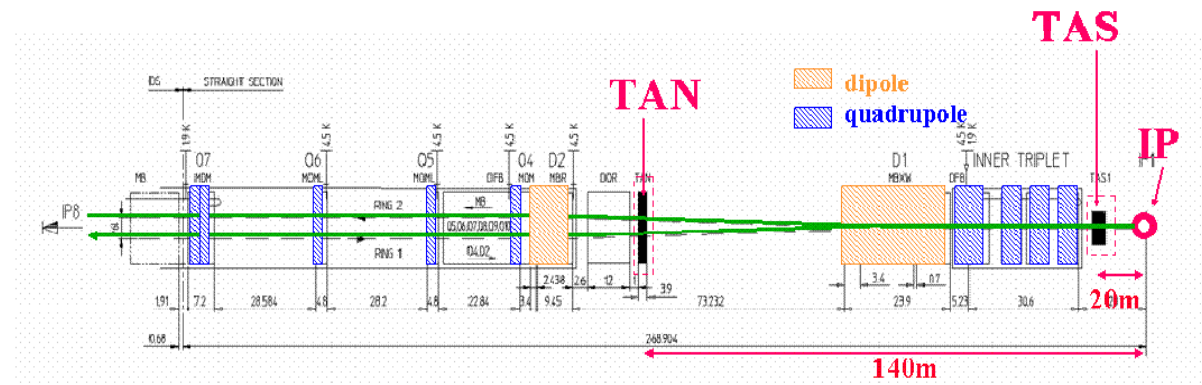


Fig. 26 Layout of one of the LHC interaction regions.

Fig. 27 shows the simulated secondary particle flux at location of the TAN. The circles indicate the location of the two beam pipes. If the neutron flux (centre image) is weighted with the average particle energy, it becomes the dominant signal at this location. The luminosity detector will therefore be located inside the TAN (a 4m long copper block) between the two beam pipes.

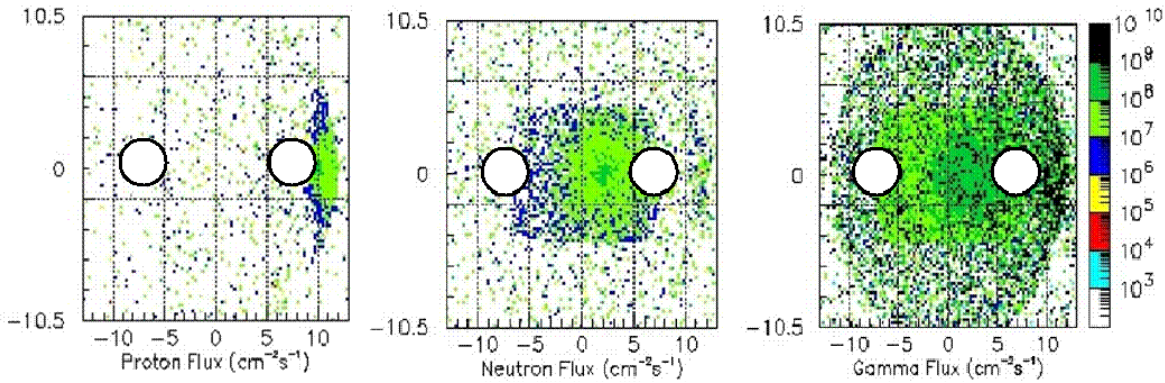


Fig. 27 Simulated secondary particle flux distribution at the location of the TAN.

### 6.4 Choice of the sensor

Having selected the location, the physical dimensions of the detector are limited by installation constraints. Moreover, since the TAN absorber is designed to shield the superconducting elements from an enormous flux of secondary particles, the luminosity detector will have to withstand a very high radiation dose. If one assumes 20 years of operation at nominal luminosity, the integrated neutron flux will be  $10^{18}$  n/cm<sup>2</sup>. This is about 3 orders of magnitude larger than normal so-called “radiation hard” semiconductor sensors can withstand. It should also be kept in mind that after some running time the whole installation will be so radioactive, that human intervention for repair will be nearly

impossible. This, in addition to the other stringent requirement of a bandwidth of 40MHz meant that only two different detector technologies were retained and studied in detail:

1. A polycrystalline cadmium telluride (CdTe) detector array [24]
2. A pressurised ionisation chamber with continuous gas exchange [25]

The first option has the advantage of high bandwidth, but the radiation hardness is not completely demonstrated. The second option is believed to withstand the high radiation levels but, even after some years of optimisation, the bandwidth is still somewhat too low. Due to the high radiation doses expected, however, the most likely choice will be the ionisation chamber. Fig. 28 shows the design of the ionisation chamber presently used with test beams.

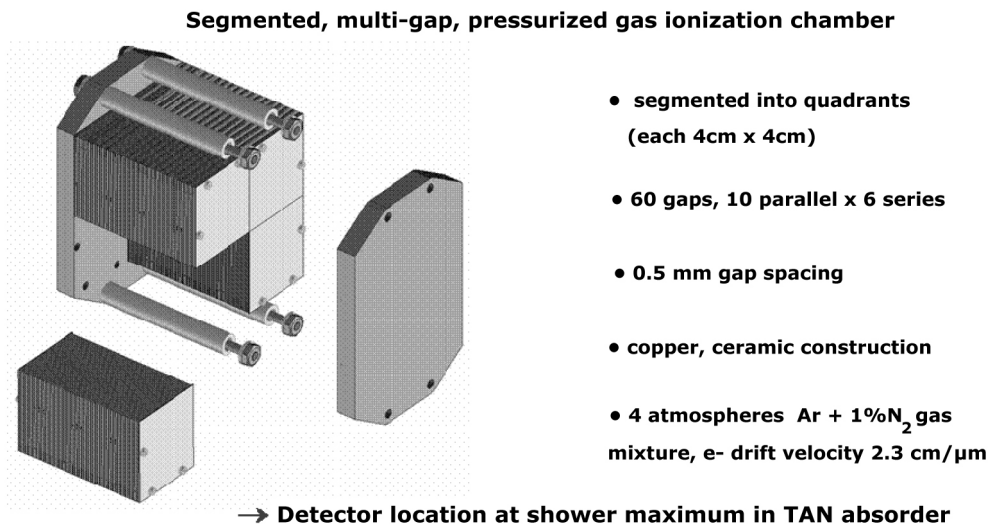


Fig. 28 Schematic of the ionisation chamber for LHC luminosity monitoring.

## 6.5 Electronics

The most critical element in the system is the detector itself, due to the requirements for bandwidth and radiation hardness. Once a signal is produced, it will be sent out of the TAN block via special radiation hard cables (stainless steel with a mineral insulator) to standard preamplifiers and digitising electronics. The signals will be recorded for each individual bunch crossing and averaged over many machine turns in order to produce the luminosity information for the control room.

## 7. SOME EXAMPLES OF BEAM DIAGNOSTICS

This section is meant to serve as general entertainment for those readers who have made it to here with their reading! Two examples from CERN-LEP operation have been selected, and show how difficult it can be to interpret primary measurements and decide on the right actions for solving a problem in an accelerator.

### 7.1 The CERN-LEP beam does not circulate!

The schedule for the CERN-LEP accelerator had a very regular structure. Every year LEP was used for about 8 months for physics beams followed by a 4 month maintenance and upgrade shutdown. During this shutdown major intervention work was sometimes carried out on the machine. At the next start-up it was therefore often expected that typical problems such as inverted magnet polarities would have to be overcome. One year, the start-up was particularly bad, with neither the electron beam nor the positron beam capable of being injected and made to circulate. Several hours were used to check all vacuum conditions, power supply currents, settings of the radio frequency system, injection deflectors

and so on, but nothing indicated a severe problem. Finally people started to look in detail at the measured beam trajectory from the injection point onwards. A typical example for the positron beam is shown in Fig. 29.

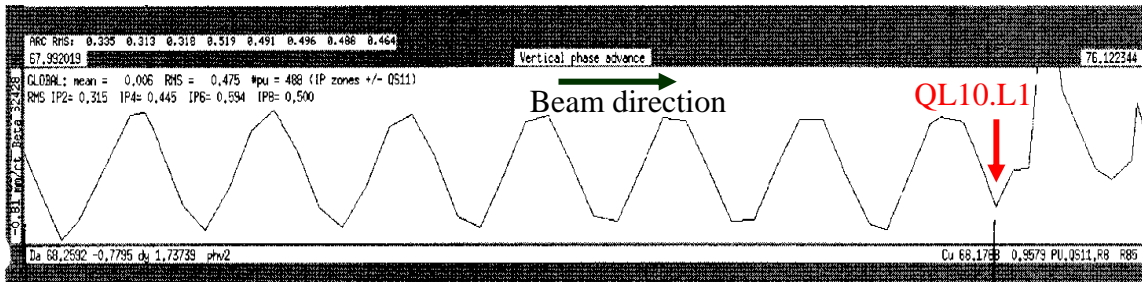


Fig. 29 Measurement of the LEP phase advance when beams did not circulate.

What is actually shown in Fig. 29 is the phase advance from one beam position monitor to the next, as calculated from the measured beam trajectory. At a particular quadrupole (QL10.L1) the regular pattern is distorted. Additional measurements also indicated that most of the beam was lost at this point. The first conclusion was to suspect a problem with this quadrupole. People went in, measured the current in the quadrupole, checked its polarity, inspected its coils, but could not find anything abnormal. The indications of the beam measurements, however, clearly pointed to a problem at this location. After many discussions and potential hypotheses it was decided to open the vacuum chamber. It should be noted that this was a major intervention, causing a stop of the accelerator for at least one day. One can understand the surprise of the intervention team when they looked into the open vacuum chamber and saw a beer bottle!!!

During the shutdown intervention, somebody had sabotaged the LEP accelerator and had inserted a beer bottle into the beam pipe (Fig. 30)! What had upset the operation team most at the time was the fact that it was a very unsocial form of sabotage - the bottle was empty!

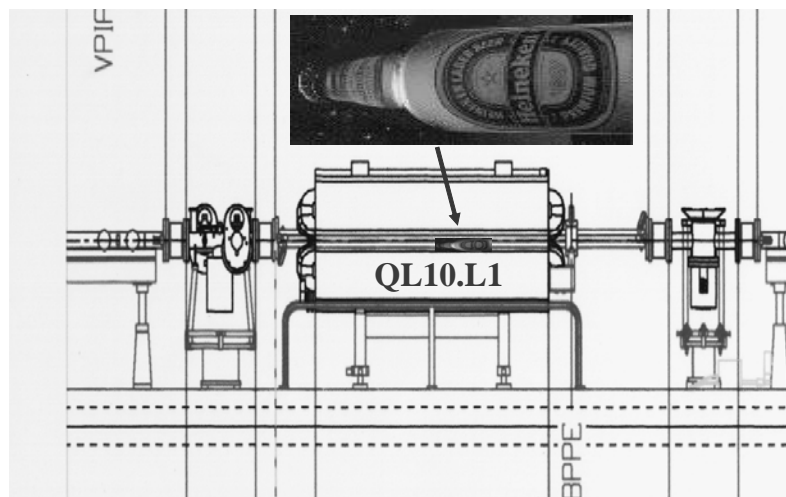


Fig. 30 The mystery of the beam circulation problem in LEP is solved!

## 7.2 The beam gets lost during the beta squeeze

This again is one of the stories from LEP operation which took several hours of beam diagnostics to solve. The problem in itself is pretty complex, and therefore requires some additional explanations beforehand.

The acceleration of the particle beams and the change of the lattice function in the insertion regions in order to get smaller values of the beta-function at the crossing point (hence higher luminosity) are so called “dynamic processes”. The presence of the beam requires that all actions are well synchronised. For example, the power converters of all relevant magnetic circuits have to be controlled such that beam parameters like the closed orbit, tunes and chromaticities stay within tolerance during the dynamic process. In order to achieve this, the behaviour of these beam parameters is periodically measured as a function of time and the corresponding power converter tables are updated.

During one period of LEP operation it was found that the beams were lost during the beta squeeze. Shortly before the total loss of the beams a significant beam loss was measured. As standard practice when encountering such problems, the engineer in charge (EIC) launched a new machine cycle with diagnostics facilities such as “tune history” (the measurement of the betatron tunes as a function of time – see Section 3) switched on. This indicated that the vertical tune moved out of tolerance during the beta squeeze. Fig. 31 shows an excerpt from the actual LEP logbook entry of this event.

01:40 Straight through to 98 GeV.  
 At ~97-98 GeV  $e^-$  large vertical oscillation  
 OPAL trigger. Maybe a bit too ambitious  
 Tune history 01-12-40 fill 7065  
 → nothing particularly nasty.  
 Big radiation spikes in all expts.  
 22 GeV 4Q50 Breakpoint at 93 GeV.  
 640  $\mu$ A .234 / .164 5.27 mA  
 93 GeV 4Q50 01-58-36 VEMS nic  
 Tune history 01-50-25 fill 7066

Fig. 31 Excerpt from the LEP logbook when beams were lost during the beta squeeze.

As a result of this observation, the EIC launched another cycle, but inserted a breakpoint (to stop the accelerator cycle) just before the critical moment in the beta squeeze when the deviation in tune occurred. Having reached that breakpoint the tunes were measured statically and found to be perfectly within tolerance. The beta squeeze was then executed step by step, and to the big surprise of the operations crew, the tunes were found to be correct at all times. The beam had passed the beta squeeze like on an ordinary day! But on the next attempt, without a break in the cycle, the beam was again lost at the same moment, and several people scratched their heads to find an explanation.

Finally, the following measurement was made. The machine was prepared and a breakpoint again inserted just before the critical beam loss. Once this point was reached, the EIC requested the execution of one further step in the beta squeeze. The facility by which one could execute a single step in a dynamic process had the additional feature that one could specify the rate of current change of any machine element. This current rate limitation was changed from 25 A/s (nominal) down to 2.5 A/s on consecutive steps. The corresponding tune history (the result from the vertical plane is plotted on the lower graph) is shown in Fig. 32.

One can clearly see that a huge (negative) tune excursion occurred when the step was executed at the nominal rate. This observation led the EIC to the right conclusion, which was that one of the power supplies was able to deliver the demanded current statically, but not dynamically. When this

was discussed with experts from the power converter group, they indicated that the power supplies for the superconducting insertion quadrupoles were built as two blocks in series, each of them able to deliver the necessary current (each block typically 1000 A/10 V). Both of these blocks were required to have enough voltage margins to enforce a current change against the inductance of the quadrupole coil. This then explained the whole story. One of these blocks was faulty, but since the power converter could deliver its (static) current, it was not detected by an alarm or surveillance circuit. In the static case the working, single block could deliver the requested current. If the dynamic rate was too high, however, this single block could not provide enough current leading it to lose synchronism with the other power converters. This resulted in the large tune change observed and ultimately the total beam loss.

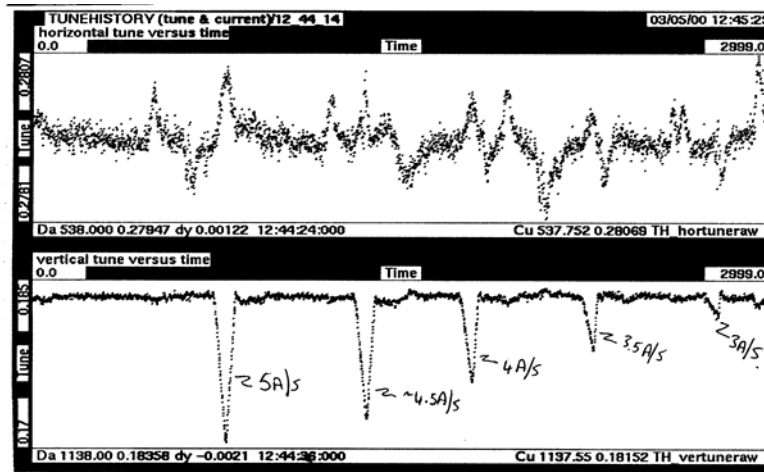


Fig. 32 The LEP tune history during the beta squeeze for various power converter ramp rates.

These two examples show the enormous potential of beam instrumentation if they are used in the right combination by intelligent people.

## REFERENCES

- [1] H. Koziol, "Beam diagnostics for accelerators", CAS 1992, Fifth General Accelerator Physics Course, Jyväskylä, Finland, 7-18 Sept. 1992. CERN Yellow Report 94-01, p565.
- [2] D.A. Goldberg, G.R. Lambertson, "Dynamic devices : a primer on pickups and kickers ", US Part. Acc. School, 1991. AIP Conf. Proc., 249,1992.
- [3] G. Vismara, "Signal Processing for Beam Position Monitors", 9th Beam Instrumentation Workshop, BIW 2000, Cambridge, MA, USA , May 2000, AIP Conf. Proc. 546, pp36-60.
- [4] D. Cocq, "The Wide Band Normaliser : a New Circuit to Measure Transverse Bunch Position in Accelerators and Colliders", Nucl. Instrum. Methods Phys. Res., A 416 (1998) 1.
- [5] H. Jakob et al., "A 40 MHz Bunch by Bunch Intensity Measurement for the CERN SPS and LHC", 6th European Workshop on Beam Diagnostics and Instrumentation for Particle Accelerators, DIPAC 2003, Mainz, Germany , May 2003.
- [6] G. Bohner et al., "Very front-end electronics for the LHCb preshower", LHCb-2000-047, CERN, 2000.
- [7] K. Unser, "A toroidal dc beam current transformer with high resolution", IEEE Trans. Nucl. Sci.: 28 (1981) pp.2344-2346.

- [8] H. Schmickler, “Diagnostics and Control of the Time Evolution of Beam Parameters”, 3rd European Workshop on Beam Diagnostics and Instrumentation for Particle Accelerators, DIPAC '97, Frascati, Italy, Oct 1997.
- [9] D. Cocq et al., “The Measurement of Chromaticity via a Head-Tail Phase Shift”, 8th Workshop on Beam Instrumentation, BIW '98, Stanford, CA, USA, May 1998.
- [10] R. Jones et al., “The measurement of  $Q'$  and  $Q''$  in the CERN-SPS by head-tail phase shift analysis”, IEEE Particle Accelerator Conference, PAC '01, Chicago, IL, USA, June 2001.
- [11] P. Bryant, “A simple theory for weak betatron coupling”, CAS, CERN 89-03, 1989.
- [12] E. Wilson, “Transverse Beam Dynamics”, CAS, CERN 85-19, Vol. 1, 1985.
- [13] J. Buon, “Beam Phase Space and Emittance”, CAS, CERN 91-04, 1991.
- [14] J. Bossert et al., “Optical Transition Radiation Proton Beam Profile Monitor”, CERN/SPS 84-17, (1984).
- [15] C. Fischer et al., “Measurements made in the SPS with a Rest Gas Profile Monitor by collecting Electrons”, 9th Beam Instrumentation Workshop, BIW 2000, Cambridge, MA, USA, May 2000.
- [16] G. Burtin et al., “The Luminescence Profile Monitor of the CERN SPS”, 7th European Particle Accelerator Conference, EPAC 2000, Vienna, Austria, June 2000.
- [17] C. Bovet et al., “Measurement Results with the BEXE Detector at LEP”, 3rd European Workshop on Beam Diagnostics and Instrumentation for Particle Accelerators, DIPAC '97, Frascati, Italy, Oct 1997.
- [18] W. Panofsky, SLAC Internal Report TN-63-57, (1963).
- [19] V. Agoritsas, “Air Ionisation Chamber as Detector of the Beam Losses in the CPS Ring”, Internal Report CERN MPS/Int.CO 66-23, (1966).
- [20] J.R. Parker et al., “A Beam-Spill Monitor for LAMPF”, IEEE Trans. on Nucl. Science Vol. 18 No. 3, (1971), p. 825-826.
- [21] R.A. Lundy et al., “A System for Monitoring Proton Losses from the NAL Main Accelerator”, IEEE Trans. on Nucl. Science Vol. 20 No. 3, (1973), p. 596-598.
- [22] V. Agoritsas et al., “Aluminum Cathode Electron Multipliers: CERN TESTS”, CERN MPS/CO Note 71-51, (1971).
- [23] S. Schlögl et al., “A Beam Loss Monitor System for HERA”, Proc. 15th Int. Conf. on high Energy Accel., Hamburg, (1992), p. 254-256.
- [24] P. Datte et al., “Initial Test Results of an Ionization Chamber Shower Detector for a LHC Luminosity Monitor”, IEEE Transactions on Nuclear Science, Vol. 50, No.2, April 2003.
- [25] E. Rossa et al., “CdTe Photoconductors for LHC luminosity monitoring”, NIM, Vol. 480, Issues 2-3, 21 March 2002, p. 488-493.



